Physicochemical analysis of South African metamorphosed coal

JOHN BUSSIO

University of Pretoria

Faculty of Natural and Agricultural Sciences

Department of Geology

This thesis is submitted for the degree of Doctor of Philosophy

January 2020

REPORT DECLARATION

I, John Paul Bussio declare that the thesis/dissertation, which I hereby submit for the degree PhD Geology at the University of Pretoria, is my own work and has not previously been submitted by me for a degree at this or any other tertiary institution.

SIGNATURE: .....

DATE: .....

ABSTRACT

An in-depth understanding of the physico-chemical nature of coal is required in order to meet ever-increasing energy demands and environmental legislature. New and classical coal analysis techniques were used on thermally-affected coals from a working coalfield in Secunda, South Africa. The study area has ubiquitous dolerite intrusions that have large-scale impacts on the minable coal resource.

A combination of five modern and classical analysis techniques, namely Schmidt hammer testing, three-dimensional X-ray tomography, proximate analysis, petrographic analysis with reflectance analysis, and two-dimensional gas chromatography time of flight mass spectrometry (GC*GCTOFMS) were used to model the mechanics of metamorphism of coal intruded by an igneous body. Freshly exposed coalface with an intersecting dolerite was analysed. The data produced from GC*GCTOFMS, reflectance, and tomographic analysis produced no strong linear correlations. Thermal dolerite influence was capped at approximately 5m from the dolerite intrusion and of note was a secondary trend that identified peaks throughout the transect correlating across GC*GCTOFMS, reflectance, and tomographic analysis. To reconcile the non-linear correlation a model using a combination of hydrothermal and thermal influences was produced to explain the mechanics of the metamorphic environment. A schematic representation of this model can be seen in the Figure below:

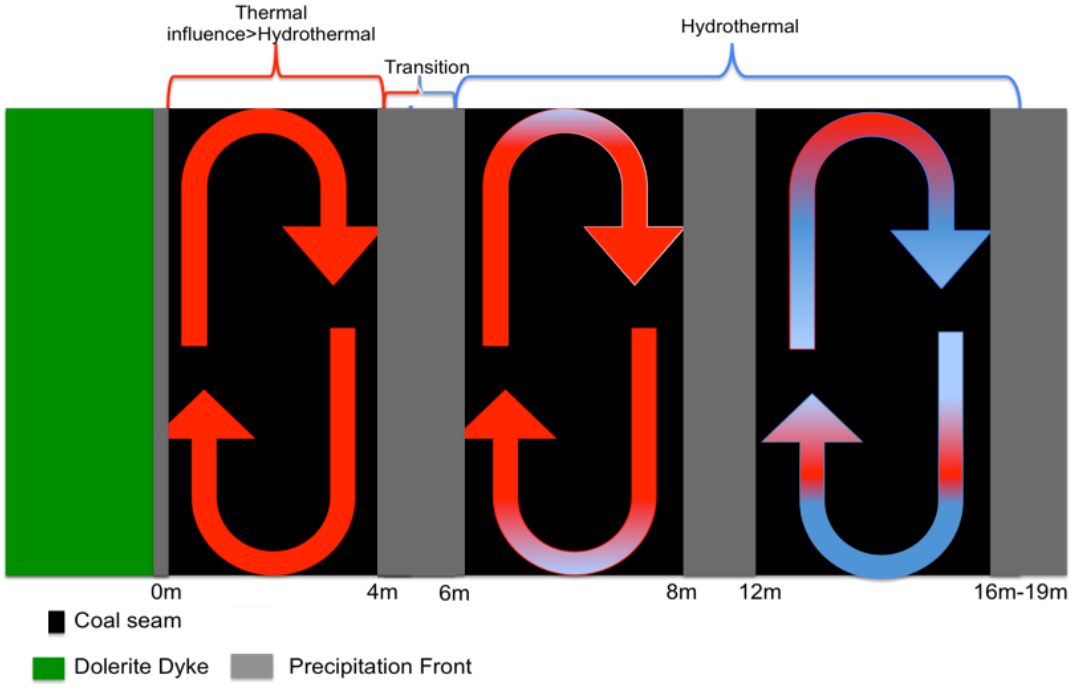

ACKNOWLEDGEMENTS

Many thanks must be given to Coaltech for sponsoring this project and granting access to the sampling sites. The National Research Foundation (NRF) must also be acknowledged for funding this work—without which much of the analytical work done here would not have been accomplished.

Thanks must be given to both Dr R.J. Roberts and Prof. N.J. Wagner for supervising this work and guiding it through to completion. A special thanks to my mother and father for the amazing support base they granted me—without which I would not be where I am today. Special thanks must go to my wife, who has stood by me throughout the final days of this work. Without her support, it may still have been in progress.

CONTENTS

LIST OF FIGURES

LIST OF TABLES

CHAPTER 1: INTRODUCTION

The finite nature of fossil fuels means that commodities such as coal are becoming more difficult to mine and refine. A detailed understanding of the physical and chemical properties of coal is required in order for the coal industry to optimise and meet future energy needs. This is hampered by the complexity and heterogeneity of coal. It is the focus of this work to apply collaborative, modern, and novel techniques to derive a more holistic understanding of the physicochemical nature of coal. The following work focuses on coal exposed to thermal intrusion and the effect this has on both the physical and chemical properties of the coal. These thermally-affected areas are becoming increasingly important as potential coal sources, so understanding the physicochemical properties of the coal and the mechanics of thermal influence are crucial in determining the potential uses and mineability of these areas.

1.1. Coal as an energy resource for the future

Coal as a modern source of energy has come under some scrutiny which can be attributed to the environmental implications of its combustion. Overshadowing these concerns is the urgent need for cheap usable energy resources in emerging markets (Heinberg & Fridley, 2010). Coal production has recently been de-emphasised due to the surge in global shale gas production. However, the forecast use of coal as an energy production resource shows that it will be in global demand for the foreseeable future due to its low cost, ease of mining and already available infrastructure (Höök *et al*., 2010).

The global focus on clean energy has placed pressure on the fossil fuel market. This urges research to focus on a greater understanding of the molecular make up of coal. Additionally, the implementation of improved mitigation measures of undesired by-products is reliant on a detailed understanding of the components of the combusted material. A large focus of industry is also on the method of energy production from a coal source, focussing on optimisation and efficiency (Höök *et al*., 2010). Both mitigation and efficiency rely on an improved understanding of coal.

1.2. Economic climate of coal

Present global proven coal reserves stand at approximately 861 Gt (Fig. 1). Fossil fuels are currently responsible for a large degree of world energy needs and coal is a significant contributor. Coal is projected to remain a major source of global energy well beyond 2020 (Fig. 2).

Figure 1: Global proven coal reserves *circa 2008* (Heinberg and Fridley, 2010).

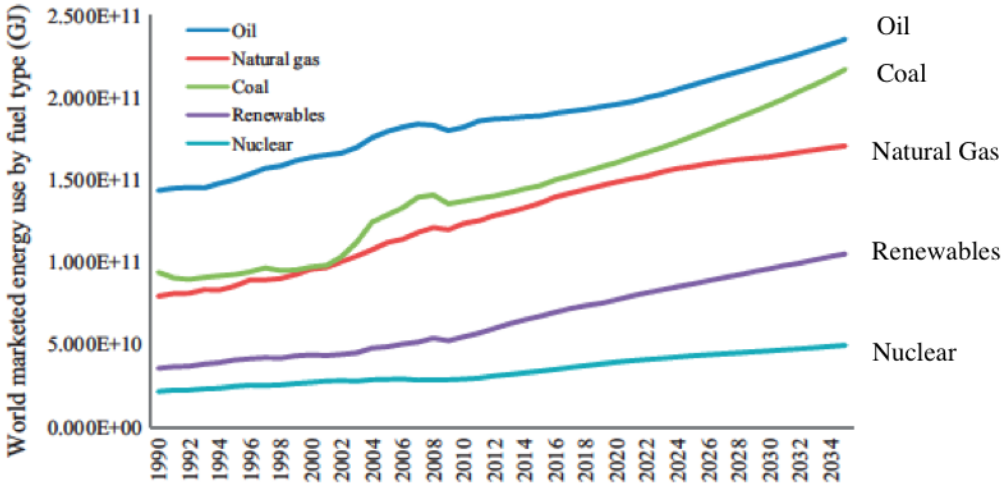

Figure 2: Global predicted energy output by fuel type 1990-2034 (Saidur *et al.,* 2011).

With global requirements of coal as an energy source projected to increase, global producers will come under pressure to exploit reserves in more difficult environments. The "big six" producers (Fig. 3) (namely USA, Russia, China, India, Australia and South Africa) will become increasingly pressured to produce coal for both their local needs and international demand (Höök *et al*., 2010; Eberhard, 2011). In light of market pressures, forecasts predict peak outputs will be reached as early as 2025 (Fig. 4) (Saidur *et al.,* 2011). The forecasts are inherently linked to technological developments and rate of implementation, which may augment these figures (Höök *et al*., 2010).

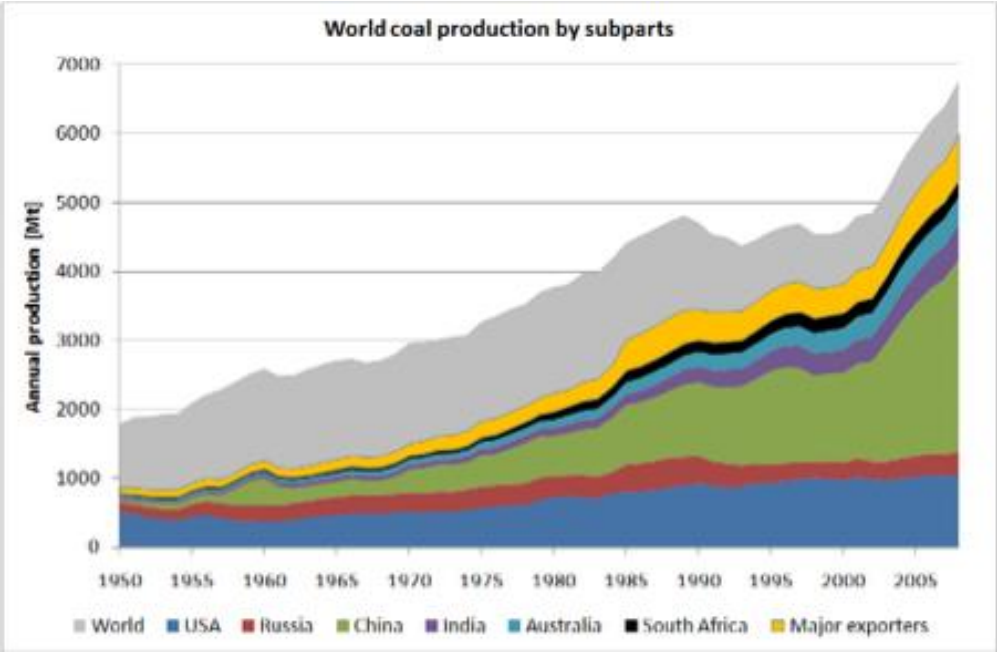

Figure 3:Global annual coal production by location (Höök *et al*., 2010)

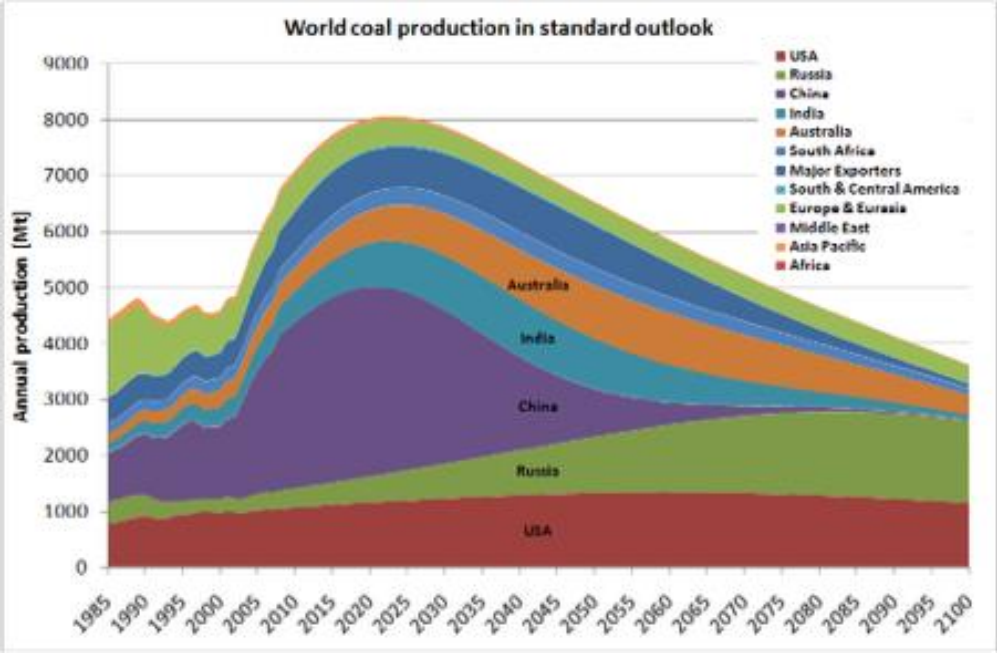

Figure 4:Global coal production by location (Höök *et al*., 2010).

The two main deliverables linked to future industries are increased production in the face of more difficult mining conditions, and reduced environmental impact in line with current and future legislation. According to Franco and Diaz (2009), the future clean coal technologies (CCT) must comply with two factors:

1. **Pollutant emission control:** Limiting the expulsion of harmful by-products and/or the capture and use/disposal of harmful by-products.
2. **Efficiency:** All CCT must improve on their current outcomes regarding the amount of energy produced per ton of coal consumed. This is expected despite the decreasing quantities of higher quality coals.

Improved performance of CCT is essential due to increasing pressure from developed nations, climate change and tax legislation. A reduction in undesirable combustion, mining and processing related by-products is fundamental to the economic growth and global image of the coal industry (Wang & Nakata, 2009). In response to this, the development and implementation of new CCT have produced varied degrees of success and efficacy (Wang & Nakata, 2009).

From an environmental standpoint, the focus is placed on 5 major pollutants: SO_x, NO_x, CO_2, particulate matter (airborne and waterborne) and acid mine drainage (Saidur *et al.,* 2011). The focus of CCT is to either mitigate the release of these materials or to capture and store them in a safe manner (Chen & Xu, 2010).

To efficiently implement CCT it is fundamental to understand the geochemical and physical properties of the processed coal material (Wang & Nakata, 2009). The physicochemical understanding of coals will become critical as reserves and resources become depleted and industry is forced to use poorer quality coals such as those affected by igneous intrusions.

In Southern Africa, igneous dykes and sills have dramatically altered a large proportion of the coalfields. The influence of these intrusions on the energy production capacity of Southern African coal reserves will become more dramatic as reserves diminish and energy requirements increase (Hancox & Gotz, 2014). The implications of these thermally affected coals on CCT's operations will be dramatic, due to the current lack of understanding of these coals in terms of their physicochemical nature. In light of this, the works of authors such as Tsai and Scaroni, (1987); Murchison (1991); Wall *et al.,* (1992); Thomas *et al.,* (1993) and Alonso *et al.,* (2001) will become increasingly important as the anthropogenic combustion of coals discussed by these authors can give insight into the degradation and devolatilisation of coal.

1.3. Problem Statement

The economic importance of poorer quality coal within a South African framework cannot be understated (Hancox & Gotz, 2014). With many of the easily minable reserves already exploited, regions previously thought of as undesirable will become areas for future exploitation (Hancox & Gotz,

2014). In the geological setting of South Africa common problem areas for coal exploitation are regions deemed to be devolatilised, that is in close proximity to dolerite intrusions (Hancox & Gotz, 2014). These metamorphosed zones have been extensively investigated in efforts to obtain a simplistic formula to evaluate areas affected by these intrusions (Bussio & Roberts, 2016). Research seems to reveal that formulae applied in one region may not be applicable universally as geochemical and physical data are highly variable (Bussio & Roberts, 2016).

The following work provides novel and holistic analysis of thermally affected poor quality coal, to provide insight and understanding of its physicochemical history and properties. Due to the more precise parameters under which new CCT operate, it will become fundamental that a greater understanding of poorer quality coals is available.

1.4. Aims

The aim is to provide a holistic view of the macroscopic physicochemical properties of coal, with a specific focus on areas affected by dolerite intrusions. New analytical methods are paired with classical techniques to provide results that will enable a comprehensive understanding of the mechanics and effects of metamorphic processes acting upon coal intruded by igneous bodies.

1.5. Project scope

The thesis describes each technique individually and reports the results of each, followed by a section discussing the links between the results of the various techniques to evaluate the physicochemical properties of the coal. It concludes with a detailed discussion of the physicochemical nature of coal and a model is suggested to describe the processes and mechanics acting on coals affected by dolerite intrusions.

CHAPTER 2: SOUTH AFRICAN COAL AND COALIFICATION PROCESSES

In order to adequately understand the structure and organic chemistry of coal it is crucial to understand the coalification process. The properties of coal are directly linked to the paleo-climatic environment of the region where the coal is found, and the organic material that was originally deposited here (Speight, 2005). For the purpose of this study, a focus is placed on the coalification of South African coals of the Permian age.

This chapter discusses the geological setting of the coalfields in South Africa and provides an overview of the processes of coal formation. An understanding of the broader differentiation of macerals and their botanical origins is necessary for this discussion, as this provides a basis from which to understand how the various particles involved will react to heating. To illustrate the physicochemical alterations of macerals that take place during heating, an anthropogenic example of coal chars is discussed.

2.1. Geological setting of South African coals and the process of coal formation

South African coals are hosted within the Karoo sedimentary basin (Cadle *et al.,* 1993). Of the 550 000 km^2 extent of the basin, seen in Figure 5, the vast majority of coal is found in the north-eastern regions of the basin and only the Ecca and Stromberg Groups are coal bearing, as shown in the cross section in Figure 6 (Cadle *et al.,* 1993).

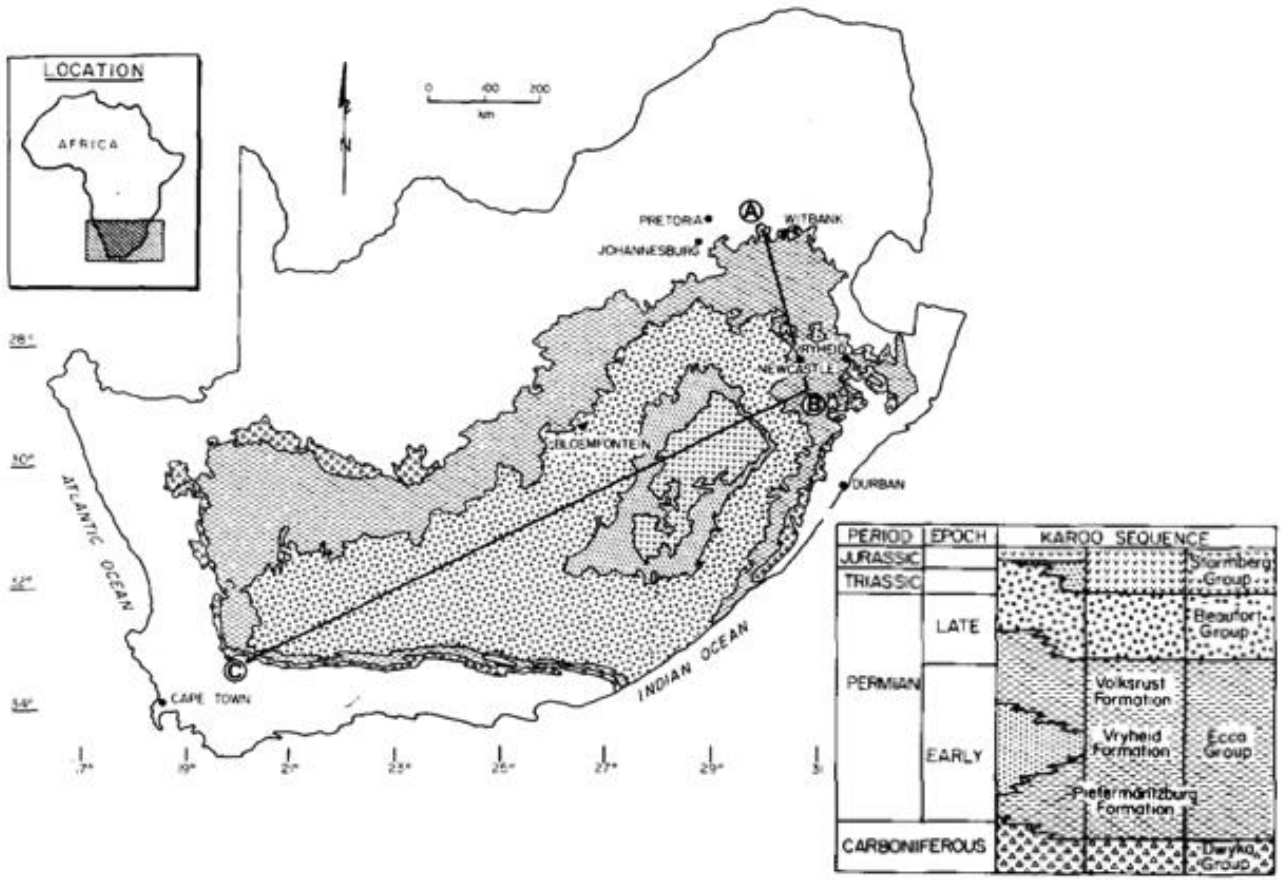

Figure 5:Karoo Basin stratigraphy and extent over South Africa (Cadle *et al.,* 1993)

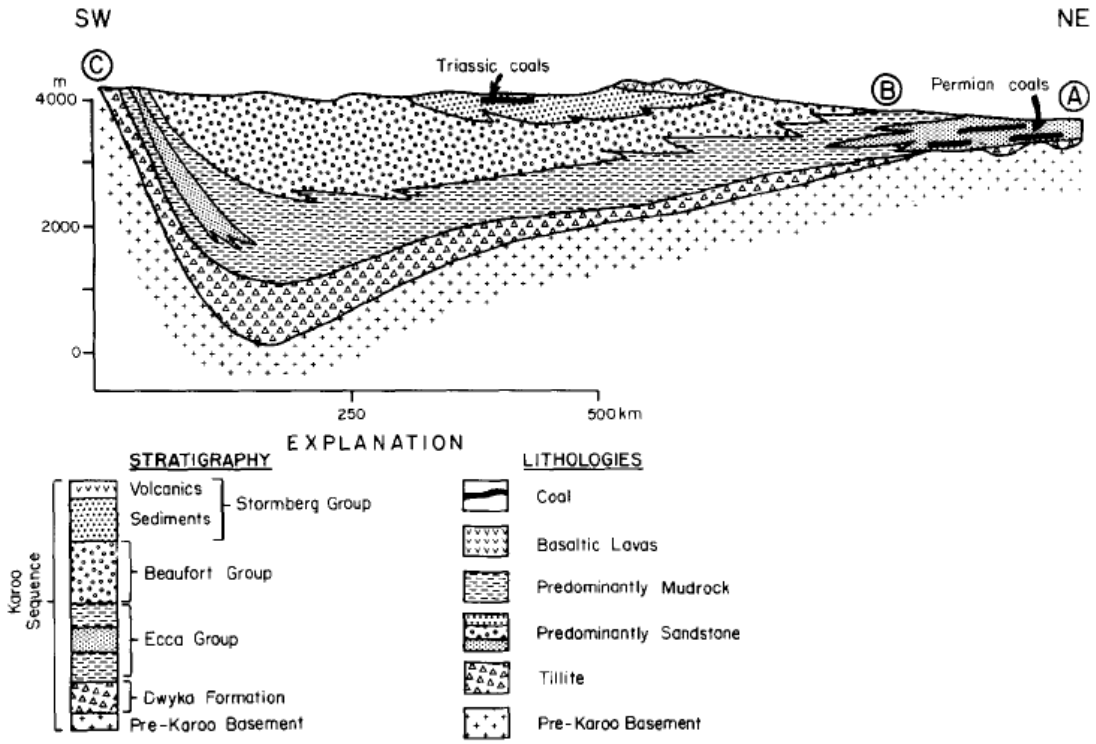

Figure 6:Cross-section of the Karoo basin displaying stratigraphic sequences and coal bearing regions. The cross-sectional points A, B and C are noted in Figure 5 (Cadle *et al.,* 1993).

The north-eastern coal-bearing region is segmented into 19 coalfields (Fig. 8), all of which host their seams within the Vryheid Formation with the exception of the Waterberg Coalfield, which is hosted within the Volksrus Formation (Jeffery, 2005). The coalfields are separated based on structural and minor geological variations (Jeffery, 2005). In terms of the paleo-vegetative and -climatic conditions, the stratigraphy (Fig. 6) shows a Perm-Carboniferous base (the Dwyka Group) (Snyman & Barclay, 1989). This is then followed by a period of intra-cratonic basinal and marine sedimentation (the Ecca Group), which is the host of the coal-bearing Vryheid Formation. A general increase in aridity follows the Ecca Group, as represented by the terrestrial sedimentation of the Beaufort Group (Snyman & Barclay, 1989). The basic basin structure of the coal bearing regions in the northeast is well displayed in Figure 7 (Cadle *et al.,* 1993).

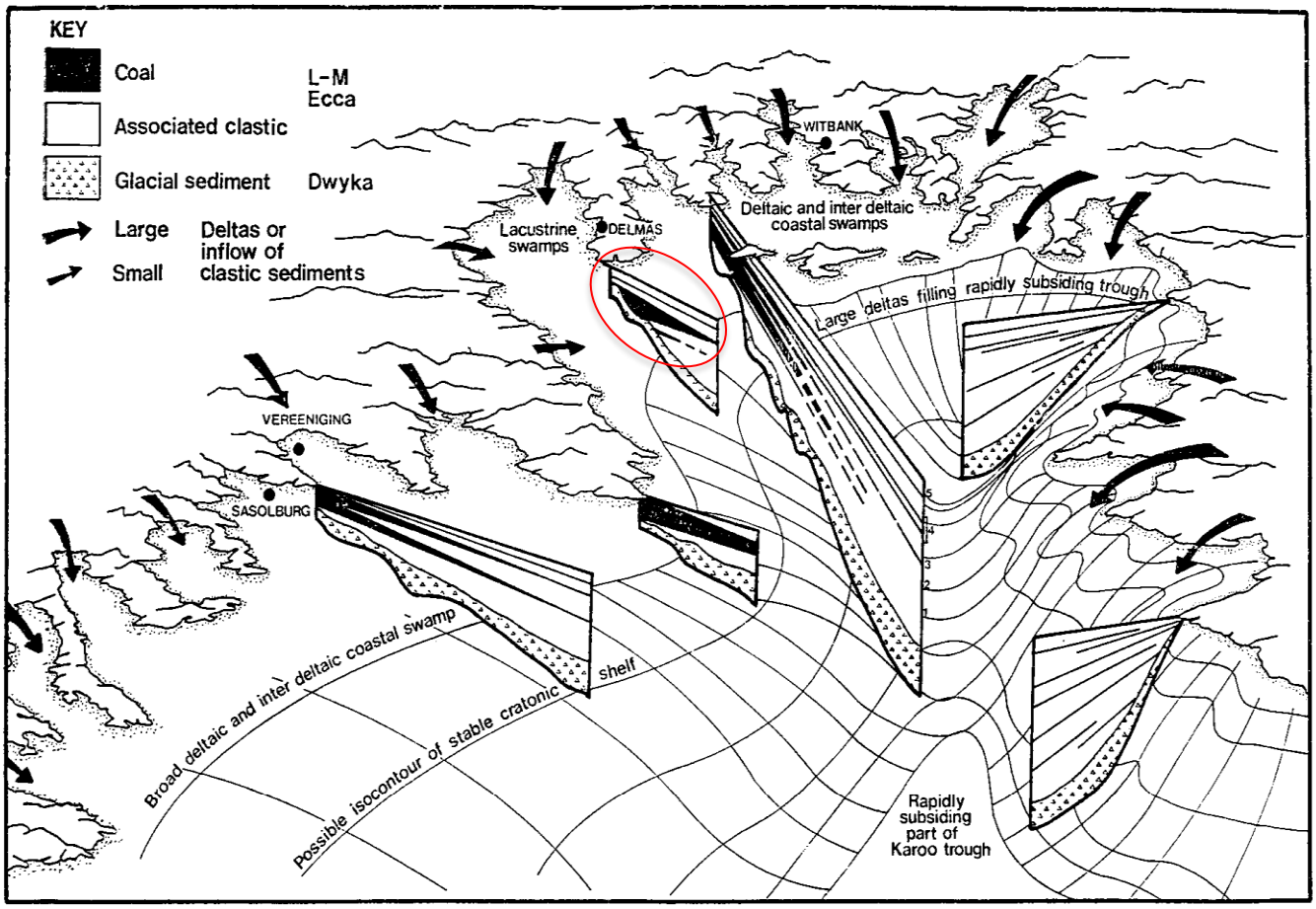

Figure 7:Diagrammatic distribution of the seams in the main coalfields of the Karoo Basins northeastern extent (Falcon and Ham, 1988). Highlighted in red is the location of the Secunda coalfield.

The geology of the Vryheid Formation is dominated by coarse fluviodetalic deposits formed from the glacial retreat of the Dwyka ice sheets (Snyman & Barclay, 1989). Capping and intruding throughout the Karoo sedimentary sequence are basaltic lavas and doleritic intrusions of the Drakensberg flood basalts. These ~180 Ma magmatics are highly pervasive and continuous over the extent of the Karoo Basin, with the exception of the lower southern extent that borders the Cape Fold Belt (Jourdan *et al.,* 2007).

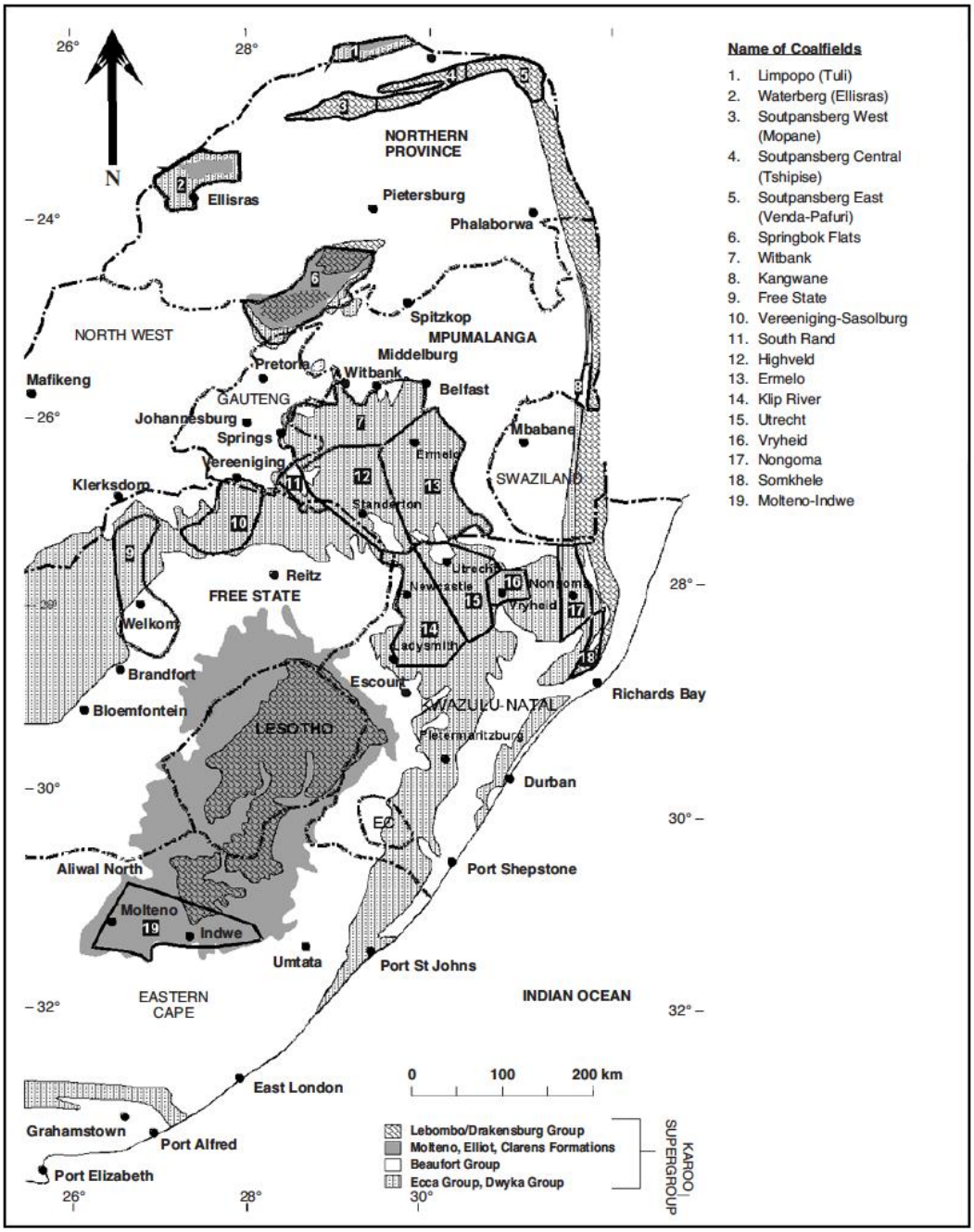

Figure 8:Locations of the 19 coalfields of South Africa (Jeffrey, 2005).

Taking into account the paleo-environment during deposition, the coal formation process requires the sedimentation of large quantities of vegetative organic matter. The deposition of this into a hydrous anoxic environment allows for the formation of peat: a hydrous, heterogeneous accumulation of vegetative organic material (Speight, 2005). With time, pressure, and temperature, the basal peat material is dehydrated and cemented together to form coal (Speight, 2005). The extent to which this process takes place is reflected in the rank of coal (Teichmüller, 1989). Rank variations are based on the fixed carbon content, volatile matter %, and calorific value (Speight, 2005). Table 1 below displays the limiting values of each of these components:

Table 1: Limiting percentages of coal ranks from Speight, (2005).

Class	Group	Fixed Carbon Limits (%, Dry, Mineral-Matter-Free Basis)		Volatile Matter Limits (%, Dry, Mineral-Matter-Free Basis)		Calorific Value Limits (Btu/lb, Moist, Mineral-Matter-Free Basis)[b]		Agglomerating Character
		Equal to or Greater Than	Less Than	Greater Than	Equal to or Less Than	Equal to or Greater Than	Less Than	
I. Anthracitic	1. Metaanthracite	98	—	—	2	—	—	Nonagglomerating
	2. Anthracite	92	98	2	8	—	—	
	3. Semianthracite[c]	86	92	8	14	—	—	
II. Bituminous	1. Low-volatile bituminous coal	78	86	14	22	—	—	Commonly agglomerating[e]
	2. Medium-volatile bituminous coal	69	78	22	31	—	—	
	3. High-volatile A bituminous coal	—	69	31	—	14,000[d]	—	
	4. High-volatile B bituminous coal	—	—	—	—	13,000	14,000	
	5. High-volatile C bituminous coal	—	—	—	—	11,500	13,000	
						10,500	11,500	Agglomerating
III. Subbituminous	1. Subbituminous A coal	—	—	—	—	10,500	11,500	Nonagglomerating
	2. Subbituminous B coal	—	—	—	—	9,500	10,500	
	3. Subbituminous C coal	—	—	—	—	8,300	9,500	
IV. Lignite	1. Lignite A	—	—	—	—	6,300	8,300	
	2. Lignite B	—	—	—	—	—	6,300	

The progression from low-rank lignite (brown coal) to high-rank anthracite correlates with the extent of expulsion of moisture and reduction in volatile components (Lowry, 1963). This progression of rank is a direct function of the geological environment, *i.e.* the extent to which the sedimentary sequence containing the organic material is exposed to diagenetic pressures and temperatures (Lowry, 1963). In addition to this, rank advancement may be induced through post depositional igneous thermal intrusions (Lowry, 1963). The pressures and temperatures involved in increasing coal rank have a noted effect on the macro- and micro-physical properties of the coal (Teichmüller, 1989). These properties are linked to the development and alteration of the maceral components hosted within the coal (Lowry, 1963). The chemical and physical processes involved in the peatification, coalification, and rank advancement of the parent vegetative organic materials are decisive in the development of both appearance and morphology of these maceral components (Teichmüller, 1989).

Southern African coals, including those formed in the Gondwana provinces, are characteristically mineral rich with a highly variable level of maturity and organic composition. The composition and characteristics of the Gondwana coals stem from the geological setting, overarching climatic conditions and the flora associated with this (Falcon & Ham, 1988). Coal bearing sediments in the Gondwana provinces are set in stable continental depressions along the margins of glacial valleys, continental lakes and shallow inter-continental seas. The Vryheid Formation is an example of a stable continental depression along the margin of a glacial valley; this is well displayed in Figure 7 (Snyman & Barclay, 1989). The stratigraphy is characterised by an upward warming climate with vegetation ranging from sub-arctic flora, deciduous forests and savannah like woodlands to swamps. Such varied vegetation results in the deposition of a range of plant organs from which macerals develop, as seen in Figure 9 (Falcon and Ham, 1988).

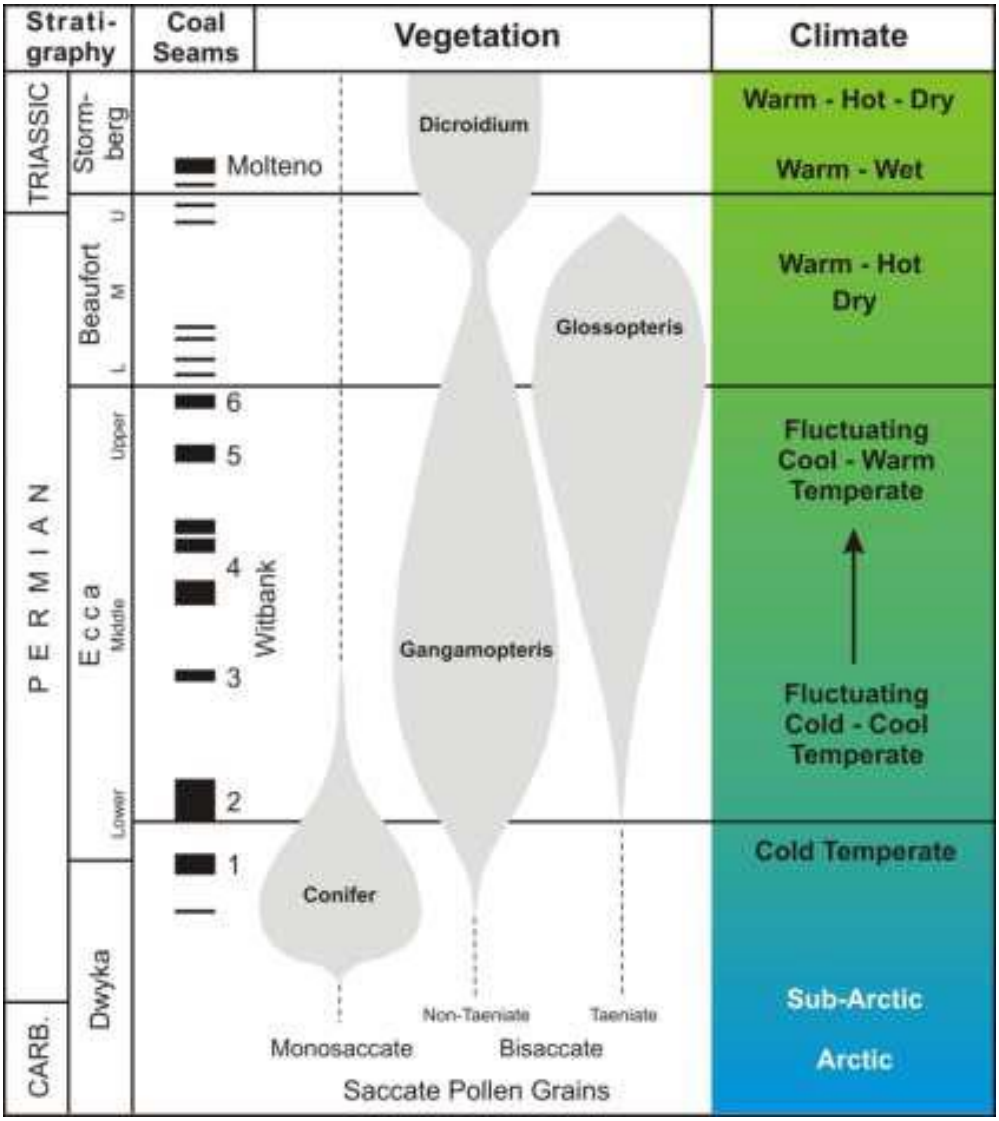

Figure 9: Gondwana climate history based on palynological record of the Karoo coal-bearing deposits (Hancox and Gotz, 2014).

The plant organs (leaves, pollen and waxy excreta) deposited in northern sectors of the Karoo Basin form the basis for the coalification process in the area. During peatification and further compression and dehydration over time these plant organs transition into macera. Coal macerals can be likened to minerals in other geological material and the evolution of these structures aids in the understanding of coal as well as the identification of its geological history. These components become progressively removed from their original flora-based structures as peatification and coalification continues (Teichmüller, 1989).

Identification of differing maceral groups is made through the discrimination of morphology and reflectance under incident light microscopy (Teichmüller, 1989). The modern maceral classification system is based on the Stopes-Heerlen System (Mukhopadhyay & Hatcher, 1993). From the system three main maceral groups are generally identified: huminite/vitrinite, liptinite (previously exinite), and inertinite. Table 2 details the three prominent maceral groups and their properties. Liptinite

macerals are derived from the lipid components of plants and have the lowest reflectance. Vitrinites have moderate reflectance values and originate from the lingo-cellulosic components of plants. Inertinite have the highest reflectance values and are derived from the oxidised components of plant lignin, cellulose, exine, fungi, lipid, and faunal remnants (Mukhopadhyay & Hatcher, 1993).

As seen in Table 2, the various maceral types are associated with specific botanical materials; this has a direct impact on their morphological characteristics, which show that they are remnants of the original plant material (Lowry, 1963). The maceral groups have differing reactive properties (Table 2), and as the basic components of coal they determine the properties of the coal in which they are hosted. Thus, the abundance of a specific maceral group will govern the way that a coal reacts to pressure and temperature, as well as its ability to combust (Lowry, 1963; Teichmüller, 1989; Wall *et al.,* 1992).

Table 2: Summary table of the major maceral groups within hard coals (adapted from Falcon and Ham, 1988).

Group	Maceral	Reflectance			Chemical Properties		Plant origins and characteristics
		Description	Rank	Reflected Light %	Characteristic element	Typical products on heating	
Vitrinite	Telinite Collinite Corpoeollinite Vitrodetrinite Collotelinite	Dark to medium grey	High volatile to medium volatile bituminous	0.5 to 1.1 1.1 to 1.6	Oxygen-rich light hydrocarbons	Decreasing amoutns of volatiles	Woody trunks, branches, twigs, stems, stalks, bark, leaf tissue, shoots
		Pale Grey	Low volatile Bituminous	1.6 to 2.0			
		White	Anthracite	2.0 to 10.0			
Liptinite	Cutinite Suberinite Sporinite Resinite Exsudatinite Chlorophyllinite Alginite Liptodetrinite Bituminite	Black Brown	High volatile Bituminous	0.0 to 0.5 -0.5 to 1.1	Hydrogen-rich	Early methane gas, Oil, Condensates	Cuticles, spores, resin bodies, algae
		Dark grey	Bituminous	-0.5 to 1.1			
		Pale Grey	Medium Volatile Bituminous	-1.1 to 1.6			
		Pale grey to white	Low volatile Bituminous to Anthracite	-1.6 to 10.0			
Inertinite	Fusinite Semifusinite Funginite Secretinite Macrinite Micrinite Inertodetrinite	Medium Grey	High volatile Bituminous	0.7 to 1.6	Carbon-rich		Oxidized detrital organic humas from woody trunks, branches, twigs, stems, stalks, bark, leaf tissue, shoots
		Pale Grey	All Bituminous coals and anthracite	1.6 to 10.0			
		White					
		Yellow white					

CHAPTER 3: GEOLOGICAL HEATING OF COAL

The coalfields of the Highveld region in South Africa are intersected by a vast and intricate dolerite network. It is generally assumed that these intrusive dolerites metamorphose the surrounding material through contact metamorphism (Abu El-Enen *et al.,* 2003; Golab & Carr, 2004; Fredericks *et al.,* 1985). The metamorphic effects of these igneous intrusions on coal has been studied previously by authors such as Fredericks *et al.* (1985), Golad and Carr (2004), and by many others. These authors investigated the thermal metamorphic effects of specific intrusions on a specified section of coal.

3.1. Dolerites of the Drakensberg Group

A final subdivision of the Karoo Supergroup is the Drakensberg Basalt Group; this caps most of the basin with basaltic lavas which show features such as pillow lavas and additional pyroclastic outflows. Associated with this group are the ubiquitous dolerite swarms of the Karoo Basin which are generally accepted as the plumbing system for the Drakensberg flood basalts (Jourdan *et al.,* 2004). Seen in Figure 10, the Drakensberg group is wide spread over Southern Africa. The dolerites of the Secunda study area are associated with the north eastern region of the Karoo large igneous province (LIP). The dolerite metric is seen as the plumbing system through which magma from the Weddell sea triple junction plume flowed (Jourdan *et al.,* 2004*;* Riley *et al.,* 2006). This plume is considered as the source of many LIP's such as the Karoo, Ferrar and Lebombo, as seen in Figure 11.

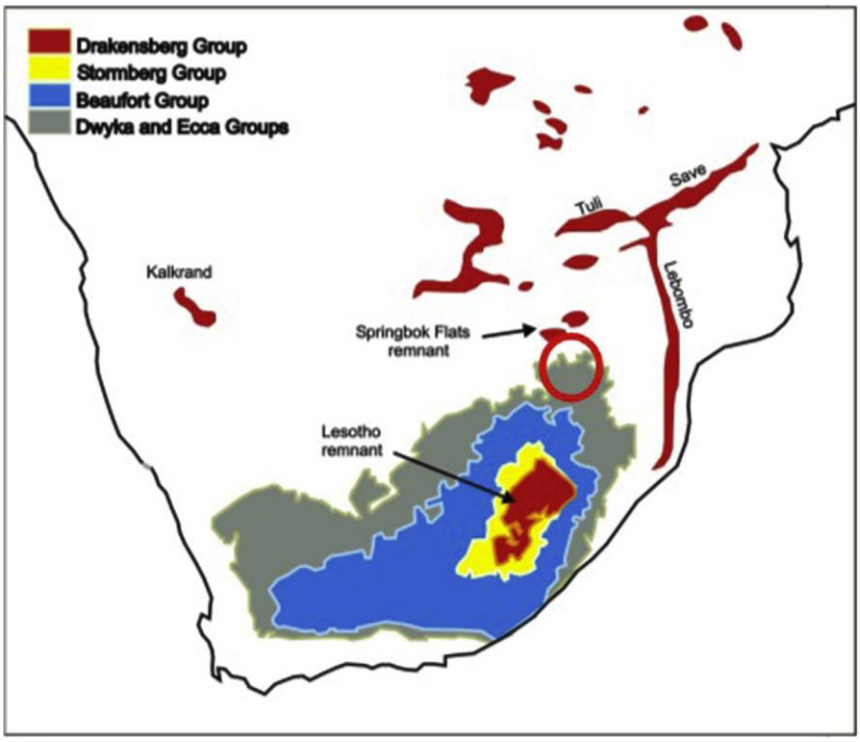

Figure 10: Karoo lavas and intrusions in Southern Africa. Highlighted in red is the Secunda study area (modified from Hancox and Rubidge, 2001*).*

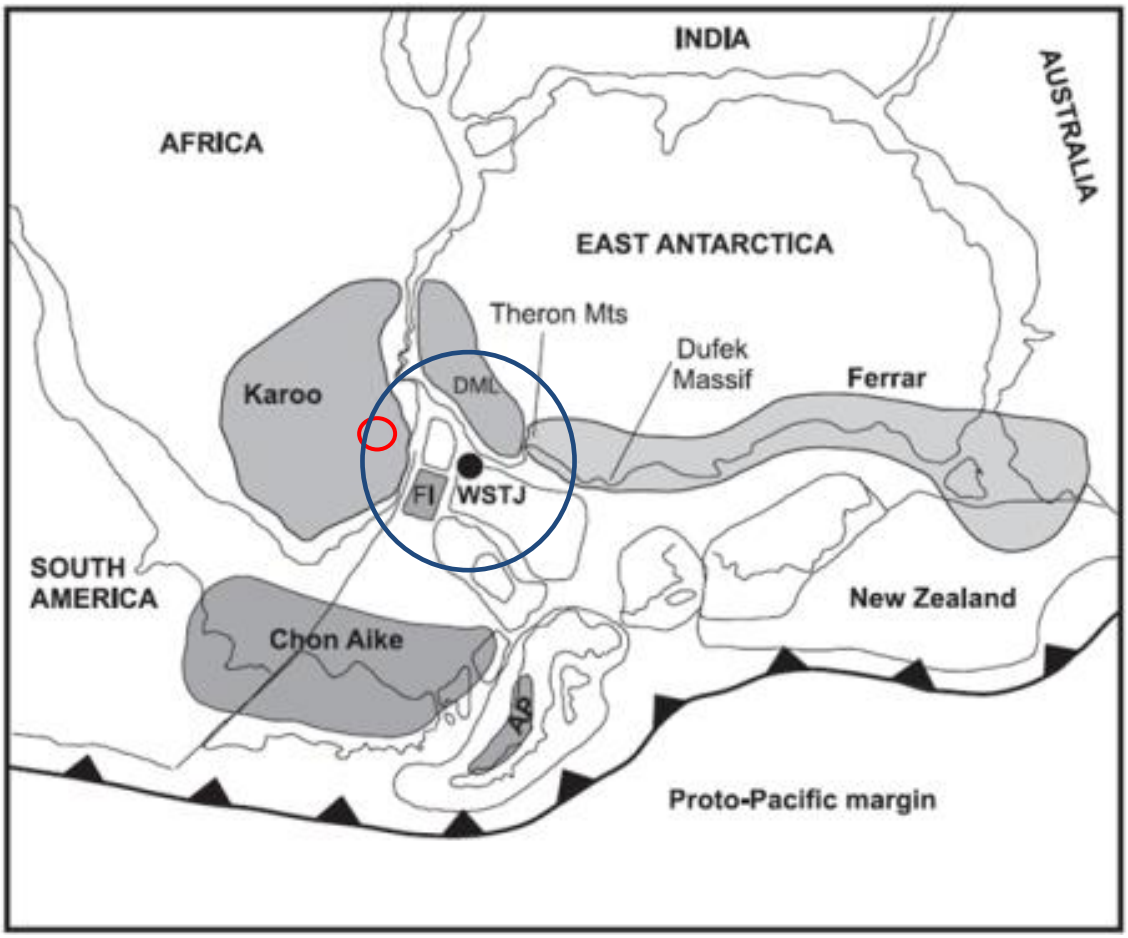

Figure 11: Paleomap of Gondwanaland at ~178-184Ma (adapted from Riley *et al.,* 2006). Highlighted in red is the study area. Highlighted in blue is an approximation of the Plume head size and dimensions based on White and McKenzie, 1989. FL Falkland Islands, DML Dronning Maud Land, AP Antarctic Peninsula and WSTJ Weddell Sea Triple Junction

Numerous age determinations have been performed on the Karoo, Lebombo, and Ferrar volcanics, with most showing an approximate age of peak volcanism to be between 178 Ma-184 Ma. The eruptive sequence of the LIP's is a point which has been highly contested (Encarnacion *et al.,* 1996; Le Gall *et al.,* 2002; Jourdan *et al.*, 2004). Authors like Jourdan *et al.* (2004) suggest that there are much earlier dates for some of the Lebombo region dykes, thus implying separate source regions for the magmatism. This age overlap and geographic relationship (Fig. 11) have propagated the single source theory and have allowed the position and dimensions of the Wedall sea triple junction, its associated plume, and the dimensions thereof to remain relatively constant since White and McKenzie (1989).

The focus of this study is on a region situated between the Lebombo and Karoo sequences (Fig. 10). The dolerites of this region of the Ecca Group are classified mainly based on the depth, intrusive character, and basic mineralogical textures (van Niekerk, 1995). The intrusion of these dolerite dykes and sills has been studied with regard to the complex emplacement and geometry of the dolerite swarms. Five dolerite types are distinguished by Sasol mining within the study area: the DO4, DO6, DO8, DO10 and DO12 sills (van Niekerk, 1995). The chemical and mineralogical character of the dolerites and lavas of the Drakensberg Group have been intensively studied in the works of Duncan *et al.* (1984), Marsh and

Eales (1984), Marsh (1984), and Marsh and Mndaweni (1998). From these works, it can be noted that the geochemical nature of the Drakensberg volcanics and intursions varies primarly in terms of TiO concentrations. There is also a general acceptance that the multiple injections within dykes and sills of the regions acted as the feeder for the flood basalts produced. In the Secunda area, Bussio (2012) investigated the geochemistry of the dolerites of the region to find little variation.

3.2. Contact metamorphism and the concept and effects of devolatilisation

The effect of igneous bodies on coal quality and morphology is a field widely investigated due the numerous occurrences of magmatic intrusions influencing coal (Finkelman *et al.,* 1998). Generally, studies focus on the thermal effects on maceral components as well as quality effects measured through proximate and ultimate analysis (Finkelman *et al*., 1998).

Works such as those of Gurba and Weber (2001) looked at the direct effects of dolerite intrusions on coal bed methane potential in New South Wales, Australia. The work showed greater gas content within the thermal-metamorphic areas of heat-affected coal seams than in coals unaffected by heat, with little effect on the gas quality. With the gas increase, Gurba and Weber (2001) also noted a reduction of oil within the coal; they postulate that this may have been reacted to form methane. Golab and Carr (2004) performed similar research, focusing on the mineralogy and geochemistry of thermally altered coals. Their work concludes that the size of the thermally altered area is a multiple of the size of the intrusion; in addition, they note that the appearance of minerals such as siderite is linked to thermally altered coals.

In both Gurba and Weber (2001) and Golab and Carr (2004), the effect of dolerite intrusions varied from site to site. The variation in metamorphic effect from dolerites was further investigated by Bussio and Roberts (2016) who showed massive variability in the metamorphic influence of dolerite sills on the C4 lower coal seam in Secunda, South Africa. The work encompassed analysis of over 15 000 borehole samples to display that there was no linear correlation between the distance from intrusion to coal seam, the dimensions of the intrusion, and the quality parameters of coal measured through proximate analysis. This is effectively displayed in figures 12, 13 and 14. Bussio and Roberts (2016) postulate that the variability is due to a more complex metamorphic environment with multiple injection scenarios and the presence of hydrothermal metamorphism that create a deviation from the expected linear relationship of proximate analysis results, distance, and intrusion dimensions.

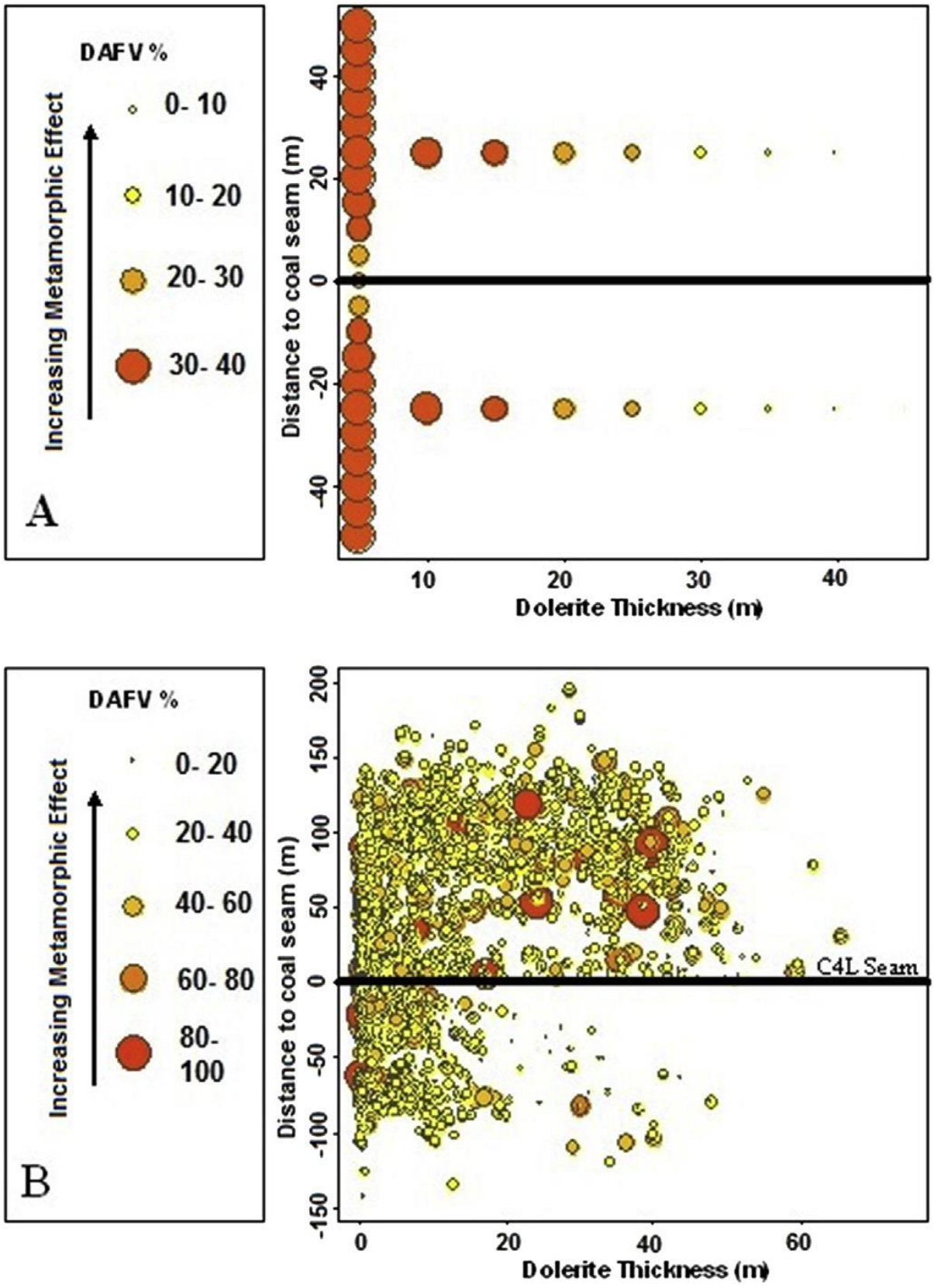

Figure 12: Dry ash free volatile percentage (DAFV %) values in relation to the thickness of dolerite and the interval between the dolerite and the coal seam. Image A displays the expected linear trend and image B the values from the sampled area (Bussio and Roberts, 2016).

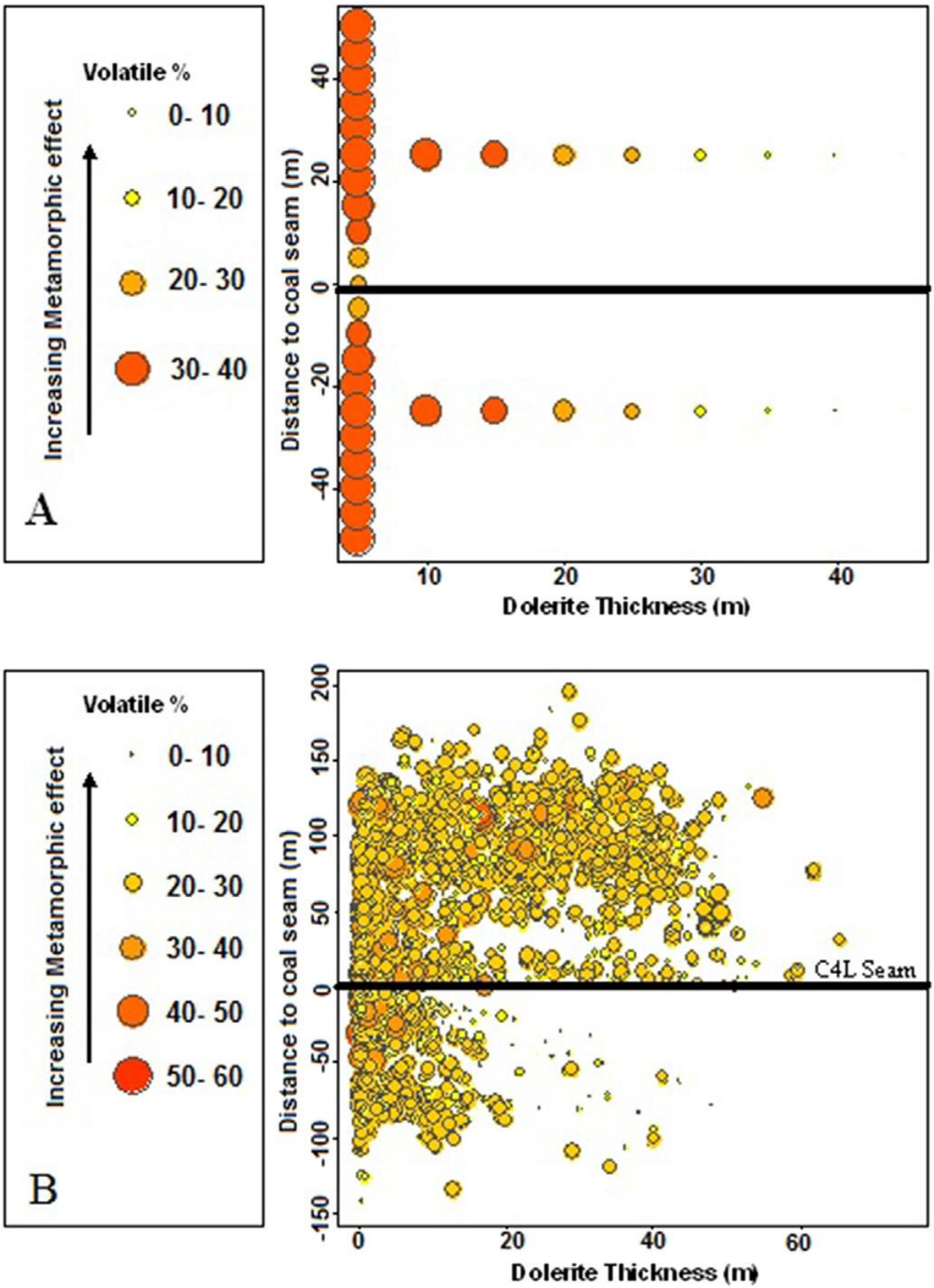

Figure 13: Volatile matter percentage (Volatile %) values in relation to the thickness of dolerite and the interval between the dolerite and the coal seam. Image A displays the expected linear trend and image B the values from the sampled area (Bussio and Roberts, 2016).

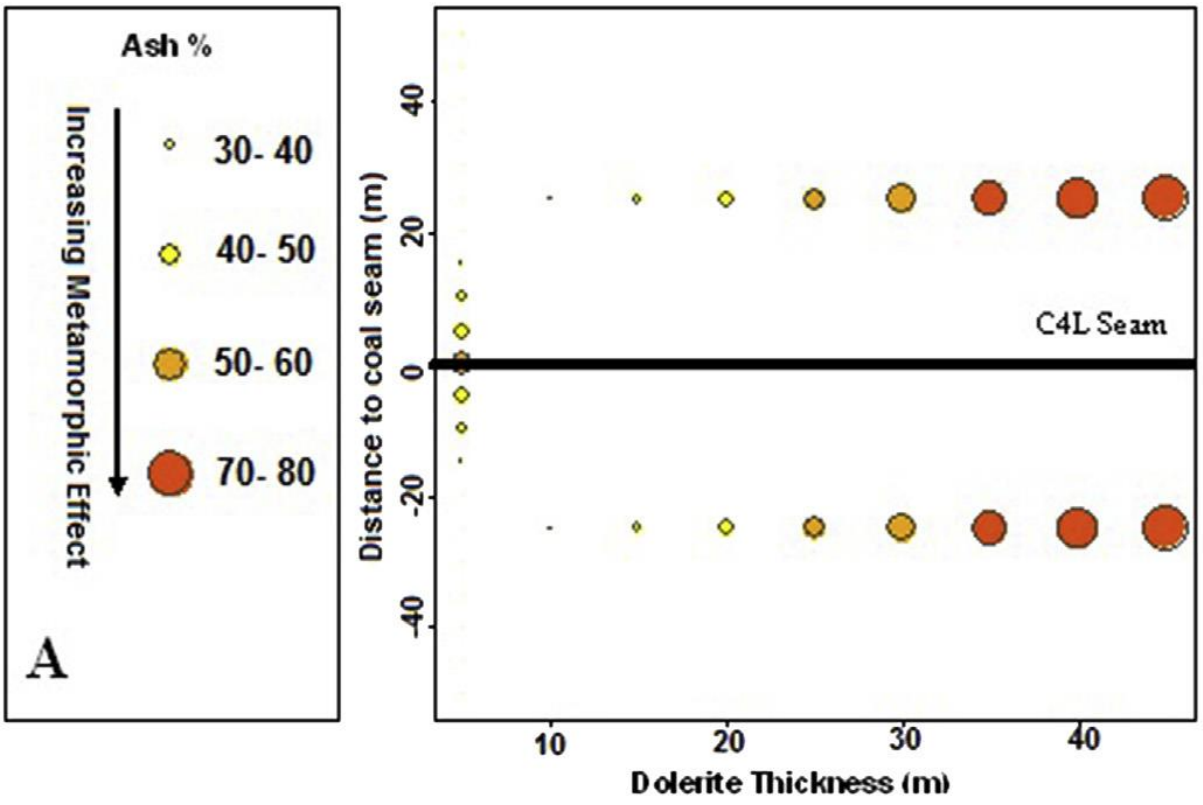

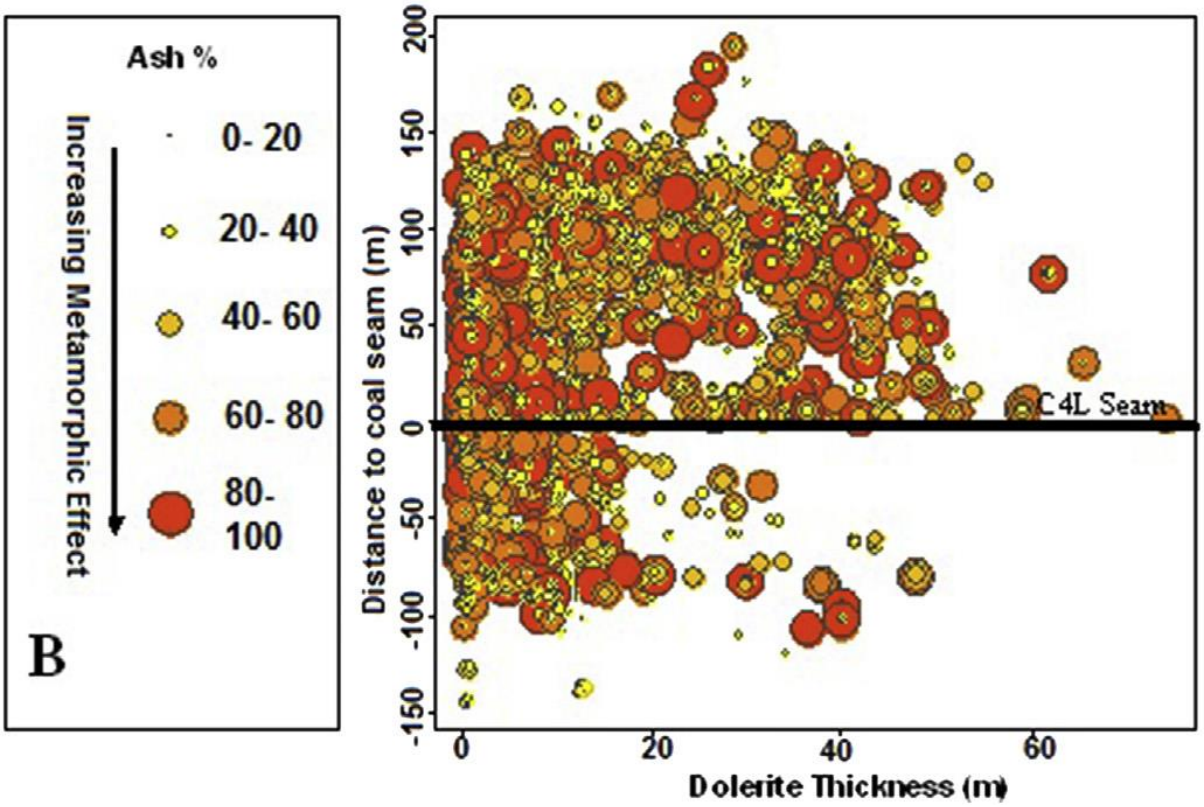

Figure 14: Ash percentage (Ash %) values in relation to the thickness of dolerite and the interval between the dolerite and the coal seam. Image A displays the expected linear trend and image B the values from the sampled area (Bussio and Roberts, 2016).

Gurba and Weber (2001), Golab and Carr (2004), and Bussio and Roberts (2016) all found that on the macro-scale the effects of intrusions on coal properties is variable from site to site—even with low levels of mineralogical, geochemical and dimensional variations of the intrusions affecting the coal.

The primary maceral components of any coal have varying physicochemical properties, as seen in Chapter 2. As a function of these variations, the manner in which macerals react to geological heat is variable. With *in situ* maceral, morphological changes seem to be directly linked to contact metamorphic effects, with the development of devolatilisation vacuoles (Stewart *et al.,* 2005; Rimmer *et al.,* 2009; Gröcke *et al.,* 2009). These vacuoles have been mostly noted within vitrinite macerals that have been thermally altered to coke particles (Stewart *et al.,* 2005; Rimmer *et al.,* 2009). This transition shows not only a physical change but also a chemical alteration of the maceral and has been used as a geothermometer to identify peak metamorphic temperatures in excess of 500 °C, *in situ* (Rimmer *et al.,* 2009). The chemical alteration of these contact metamorphosed coals is most commonly investigated using proximate and ultimate data—the most commonly used parameters being volatile matter, ash and fixed carbon (Fredricks *et al.,* 1985; Stewart *et al.,* 2005; Rimmer *et al.,* 2009; Gröcke *et al.,* 2009; Mastalerz *et al.,* 2009).

Devolatilisation is explained as the process of alteration and/or removal of volatile matter from coal through thermal or hydrothermal influence (Fredricks *et al.,* 1985; Stewart *et al.,* 2005; Rimmer *et al.,* 2009; Gröcke *et al.,* 2009; Mastalerz *et al.,* 2009; Bussio, 2012). Work on devolatilisation has shown the development of vacuoles in maceral components, which has also aligned with volatile matter decrease and fixed carbon increases (Rimmer *et al.,* 2009; Stewart *et al.,* 2005; Gröcke *et al.,* 2009).

The work done by Gröcke *et al.* (2009), focusing on the C4 lower coal seam of the Highveld Coalfield, was a systematic review of the petrographical and geochemical analysis of thermally altered coal. From this and several other works (Stewart *et al.,* 2005; Rimmer *et al.,* 2009), it has become recognised that the extent to which devolatilisation vacuoles (Fig. 15) occur is a function of the size of the magmatic intrusion (Gröcke *et al.,* 2009). Rimmer *et al.* (2009) note that the approximate thermal range of the dolerite intrusion is 1.2 to 1.5 times the crossectional width of the intrusion. However, this ratio is not universally applicable, specifically when reviewing the proximate and ultimate analysis percentages for coal in close proximity to these thermal intrusions (Rimmer *et al.,* 2009; Hancox an Gotz, 2014; Bussio and Roberts, 2016).

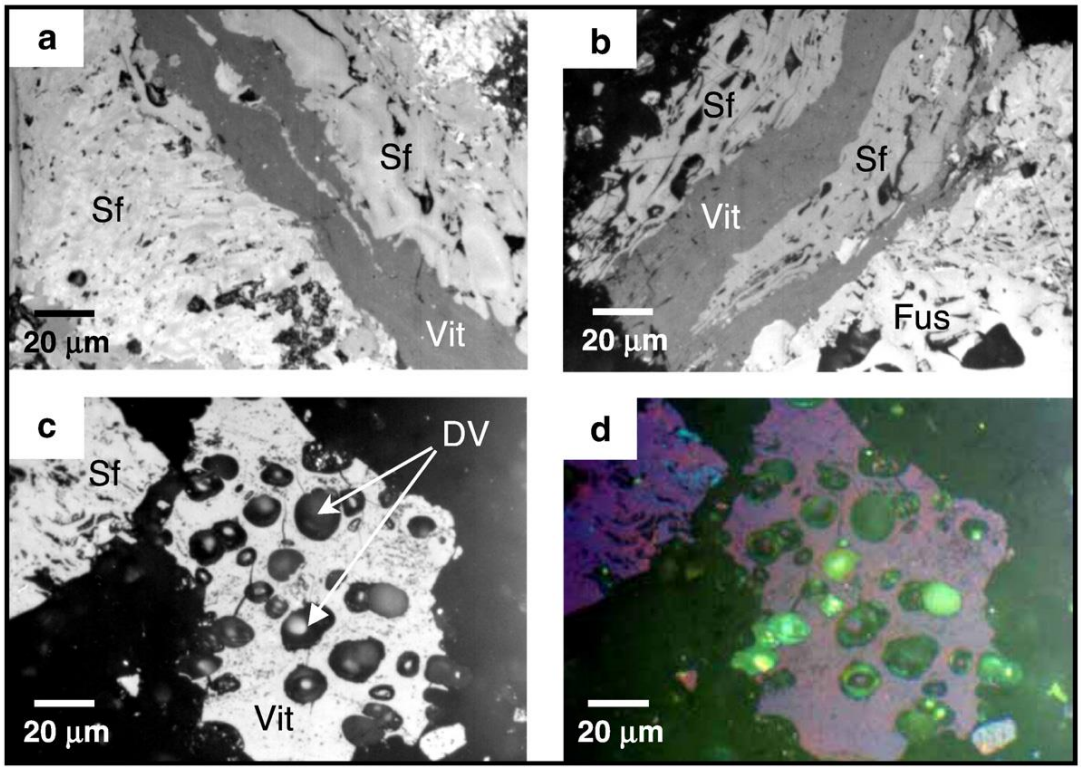

Figure 15: Photomicrographs of unaltered coal samples (a) and (b) and thermally altered (due to dolerite intrusion) sample (c) with image (d) taken under crossed polarisers. Semifusinite (Sf), fusinite (Fus), vitrinite (Vit), devolatilisation vacuoles (DV) (from Gröcke *et al.,* 2009).

To explain the variable proximate and ultimate analysis figures, Bussio and Roberts (2016) highlighted the influence of hydrothermal fluids reacting with and redistributing the volatile material. These insights correspond with work done by authors such as Wahyudiono *et al.* (2011), Fedyaeva and Vostrikov (2012) Daniels *et al.* (1990) and others, who have shown the potential for hydrothermal saline fluids to break down and mobilise organic compounds in *in situ* coal materials. The contribution of hydrothermal influences helps to describe the variations noted in the proximate and ultimate data of coal in areas affected by thermal intrusions.

The textural variation (*i.e.* development of vacuoles) on a micro-scale has further been investigated and correlated to the structural coherency of coal particles. Hower *et al.,* (2008) investigated the Vickers micro-hardness of specific macerals and showed that individual macerals such as pseudovitrinite and telovitrinite had differing micro-hardness values that dependend on the location of the sample. The work of Das (1972) described the variations in micro-hardness between thermally altered coal or "abnormal metamorphism" and normal coalification. Das (1972) describes a dramatic variation in micro-hardness between coals of the same volatile matter concentrations that are found in different metamorphic environments, and therefore at different proximities to magmatic material. Both these cases substantiate the physicochemical link within coal: the fundamental idea that the geochemical properties cannot be disconnected from the morphological and physical characteristics of coal.

3.3. Maceral reactivity in a controlled environment

Due to the heterogeneous nature of natural environments, the study of specific maceral reactivity is difficult. To circumvent this, several studies have approached maceral reactivity analysis through the study of chars produced from pyrolysis and combustion (Tsai and Scaroni, 1987; Murchison, 1991; Wall *et al.,* 1992; Thomas *et al.,* 1993; Alonso *et al.,* 2001). This vast body of work on char formation in oxygen rich environments provides a definitive display of the link between maceral groups and maceral morphology to the physicochemical reactivity of coals. The majority of these works focused on the investigation of specific maceral types and maceral concentrates to understand the distinctive properties of these macerals during combustion. The anthropogenic combustion of coal macerals in a controlled heating process that was utilized in the works of Tsai and Scaroni (1987), Murchison (1991), Wall *et al.* (1992), Thomas *et al.* (1993) and Alonso *et al.* (2001) resulted in a greater understanding of the physicochemical reactions and mechanisms of physical change within char components. Although this process takes place in an oxygen rich environment, it provides insight into the physicochemical behaviour of macerals during heating and displays the distinctive variations in the physicochemical properties of maceral groups.

An example of this physicochemical variation is described in Wall *et al.* (1992), who used concentrates of vitrinite rich coal (clarain) and inertinite rich coal (durain), is seen in Table 3. These coals were pulverised to a size range of 90-125 μm, then injected into a flow reactor and combusted. Several measurements were taken, most diagnostic of them being particle temperature. The variation in temperatures during combustion of the clarain and durain concentrates was ~250 °C. This temperature range was 100 °C greater than the theoretically calculated value of combustion of these concentrates. The ~250 °C variation in combustion temperature between the clarain and durain concentrates was shown to have some link to particle size but this was dismissed as the sole factor in the temperature variation. Wall *et al.* (1992) explains that the variation in temperatures may be due to the amount of vitrinite and inertinite macerals within each of the concentrates.

Table 3: Maceral concentrate analysis (Derived from Wall *et al.* (1992)).

	Clarain	*Durain*
Moisture %	3.1	3.3
Ash %	8.8	19.2
Volatile matter % (dry ash free)	39.8	30.6
Fixed carbon %	53	53.7
Maceral analysis %		
Vitrinite-rich	98.7	9.5
Inertinite-rich	5	89.2
Mineral-rich	1.3	1.5

The variation in reactivity between maceral types was further investigated by Thomas *et al.* (1993)—the focus of the paper was the discrimination of inertinite macerals in pulverised fuel conditions. The study expressed the need to delve into more detail when examining the maceral groupings by exposing the dramatic variations in maceral reactivity within the inertinite group. Tables 4 and 5 and figures 16-18 display the distinctive variations between macerals of the inertinite group. Noteworthy are the pyrolysis temperatures measured by Thomas *et al.* (1993) (Table 4), which range from 1300 to 1800 ℃, with single maceral concentrates varying up to 200 ℃.

Table 4: Maceral descriptions of images 2.1- 2.24 adapted from Thomas *et al.* (1993). Maceral type and char type abbreviations described in Table 5.

Fig No	*Maceral*	*Maceral Type*	*Pyrolysis Temp*	*Char Type*
2.1	VT	Telocolinite	1420	FD.TN.CE
2.2	VT	Telocolinite	1500	FD.TN.CE
2.3	VT	Telocolinite	1300	FD.TK.CE
2.4	VT	Telocolinite	1410	FD.TK.CE
2.5	SF	PG.FE.CS	1420	FD.TN.CE
2.6	SF	PG.CS	1460	FD.TN.CE
2.7	SF	PG.FE.CS	1730	FD.TN.NK
2.8	SF	PG.FE.CS	1820	FD.TN.NK
2.9	SF	WP.CS	1430	FD.MX.NK
2.10	SF	PG.CS	1400	FD.TK.NK
2.11	SF	PG.CS	1625	FD.MX.NK
2.12	SF	WP.CS	1230	FD.MX.NK
2.13	SF	WP.CS	1580	FD.MX.NK
2.14	SF	WP.TK.CS	1300	TRANS
2.15	SF	PG.FE.CS	1790	TRANS
2.16	SF	WP.FE.CS	1500	TRANS
2.17	SF	WP.FE.CS	1800	UF.OS
2.18	SF	WP.CS	1540	UF.OS
2.19	SF	WP.TK.CS	1620	UF.OS
2.20	F	BOGEN.CS	1550	UF.OS
2.21	SF	WP.TK.CS	1650	UF.OS
2.22	SF	WP.CS	1320	UF.S
2.23	SF	WP.TK.CS	1550	UF.S
2.24	F	WP.TK.CS	1600	UF.S

Table 5: Abbreviations for maceral descriptions adapted from Thomas *et al.* (1993).

Maceral		*Char*	
VT	Vitrinite	FD	Fused
F	Fusinite	UF	Unfused
SF	Semifusinite	CE	Cenosphere
CS	Cell structure	TN	Thin
WP	Well preserved	TK	Thick
PG	Part gelification	NK	Network
FE	Fine	MX	Mixed
TK	Thick	TRANS	Transitional
		S	Solid
		OS	Open solid

The photomicrographs in figures 16-18 display the dramatic variation in the char textures produced from macerals of the same group. Within figures 16-18 the variations of chars resulting from the pyrolosis of, vitrinite in images 2.1 -2.4, semi-fusinite in images 2.5-2.19; 2.21-2.23 and finally fusinite in images 2.20 and 2.24 (Thomas *et al.* 1993). The variations in single maceral groups clearly displays that there are inherent variations in the reactivity of maceral groups. The conclusion drawn from these results is that a more descriptive analysis of the maceral groups is needed in order to understand the reactivity of coals and specifically maceral groups (Thomas *et al.,* 1993).

Analysis of single macerals and concentrates in combustion and pyrolysis experiments have shown that there are large reactivity variations between maceral groups, and that these variations directly influence the reactivity of the host coal (Tsai and Scaroni, 1987; Murchison 1991; Wall *et al.,* 1992; Thomas *et al.,* 1993; Alonso *et al.,* 2001). The variations are not limited to the chemical reactivity; they are also clearly present in the structural properties of the coal, where variable levels of fusing of chars (as a measure of the reactivity of macerals) reveal a distinctive link between the chemical and physical nature of these particles (Tsai and Scaroni, 1987; Murchison 1991; Wall *et al.,* 1992; Thomas *et al.,* 1993; Alonso *et al.,* 2001).

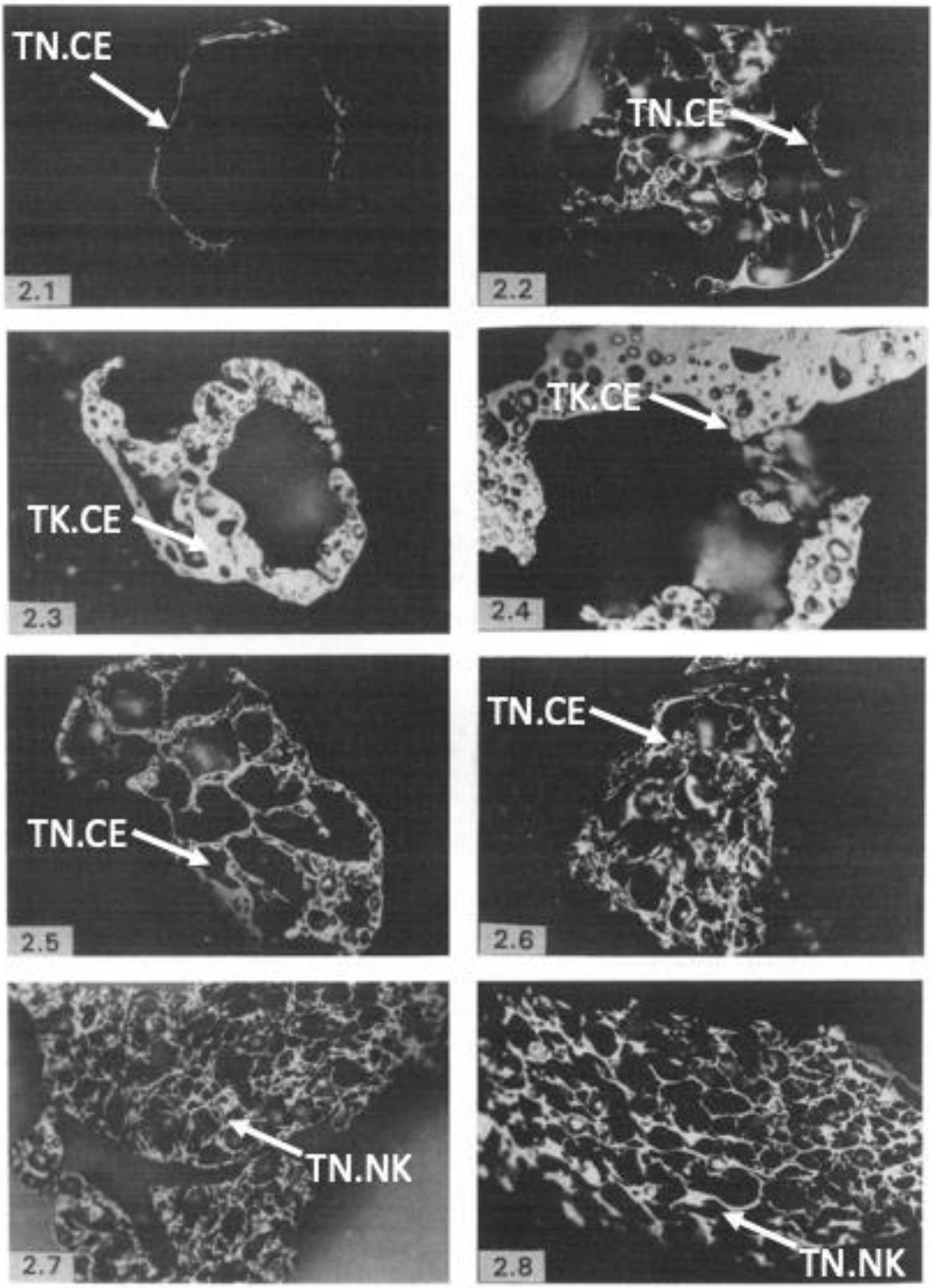

Figure 16: Photomicrographs of chars 2.1-2.8 (Thomas *et al.,* 1993). 2.1-2.4 chars produced from the pyroloysis of Vitrinite macerals. Chars in 2.1 and 2.2 show thin walled cenosphere (TN.CE). 2.5-2.8 are chars produced from semifusinite. 2.5 and 2.6 chars show thin walled cenoshperes (TN.CE); 2.7 and 2.8 show thin networks (TN.NK).

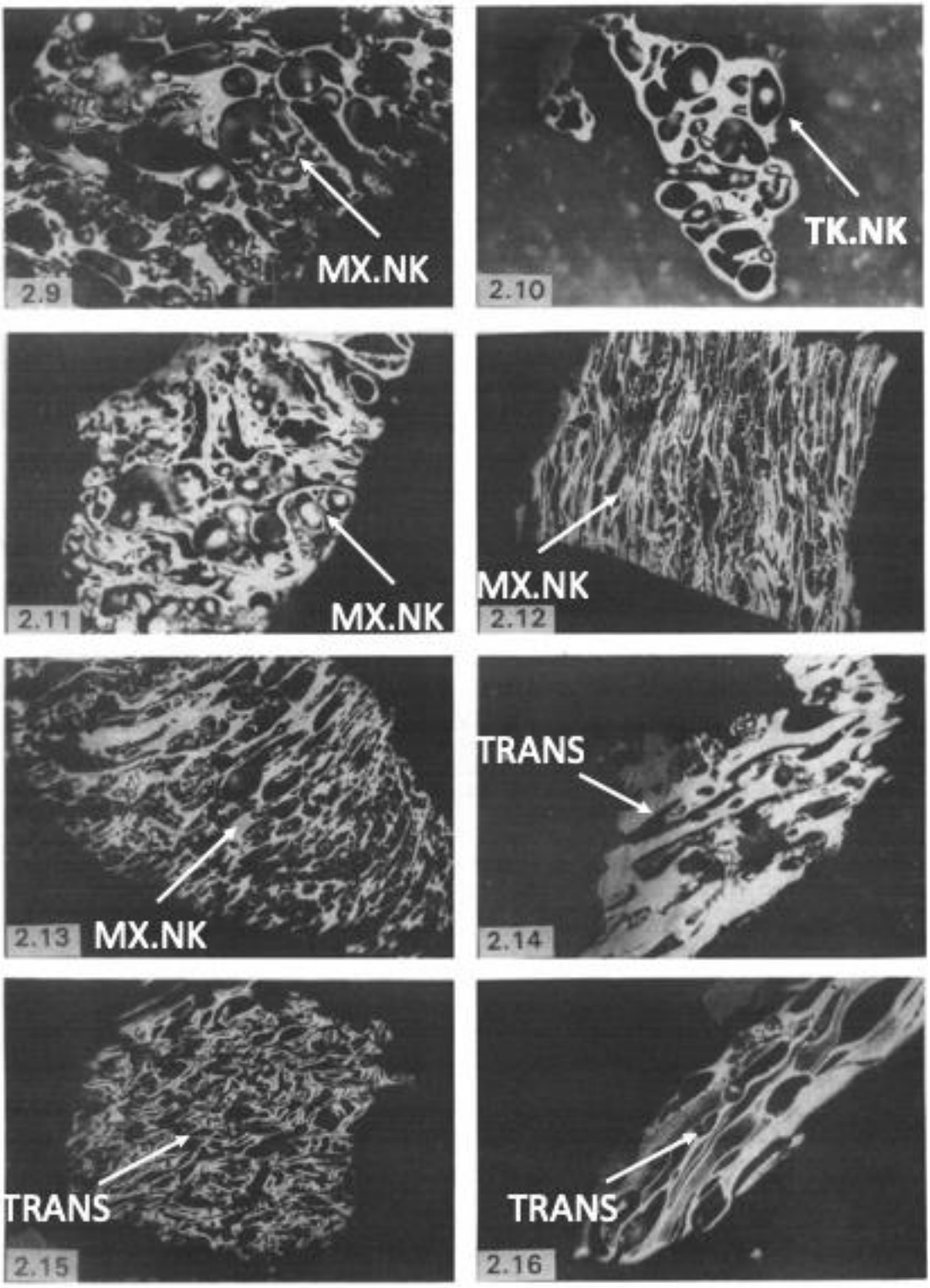

Figure 17: Photomicrographs of chars 2.9-2.16 (Thomas *et al.,* 1993). Imagies 2.9-2.16 are chars resulting from the pyrolysis of semifusinite macerals. Chars in 2.9 and 2.11-2.13 display a mixed network texture (MX.NK). Image 2.10 displays a thick network texture (TK.NK). Images 2.14-2.16 displays a transitional texture (TRANS).

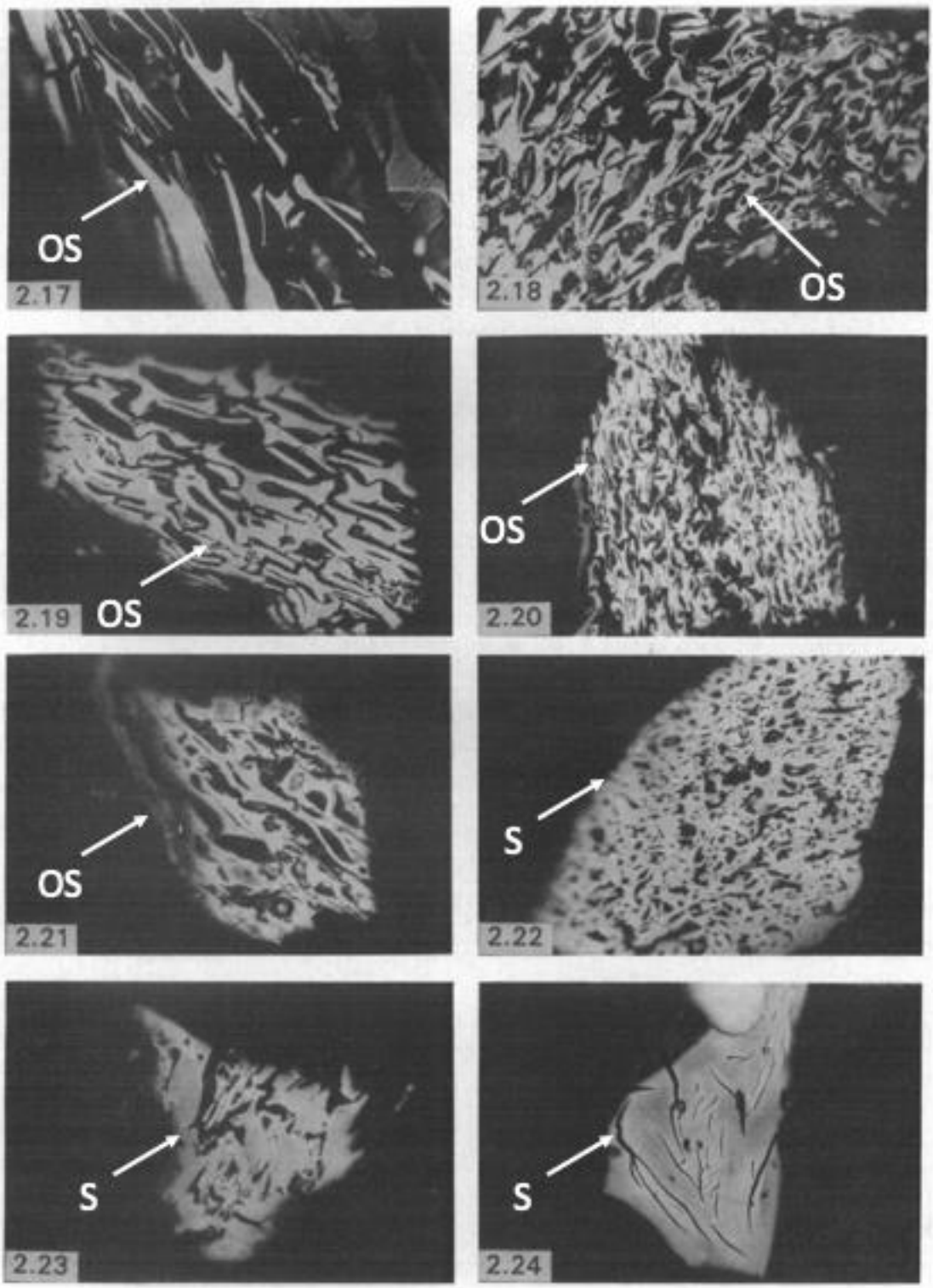

Figure 18: Photomicrographs of chars 2.17-2.24 (Thomas *et al.,* 1993) Imagies 2.17-2.19 and 2.21-2.23 are chars resulting from the pyrolysis of semifusinite macerals, while 2.20 and 2.24 are produced from fusinite macerals. Images 2.17-2.21 open solid (OS) char textures while 2.22-2.23 display solid (S) char textures.

CHAPTER 4: MACERAL STRUCTURE

It has become necessary to understand the micro-structural properties and molecular make up of maceral groups and coal, in order to further understand the variations between them. At the forefront of this is the investigation of the bonding between molecules, microstructural analysis and organic chemistry (Fabiańska *et al.,* 2013).

As mentioned, coal and its macerals are the remnants of the original organic material deposited and compressed over millions of years. The question arising from this is: what components of that original material contribute to the final geochemical and physical properties of coal?

Geochemically, coalification is still a poorly understood process. Hatcher and Clifford (1997) reviewed the coalification process on a molecular and microstructural level with Scanning Electron Microscopy (SEM), Pyrolysis Gas Chromatography Mass Spectrometry (py-GC-MS) and Cross-Polarisation Magic Angle Spinning ^{13}C Nuclear Magnetic Resonance (CPMAS NMR) data. This investigation of coalification from lignite to bituminous coals provides a detailed review on the structures and possible chemical reactions taking place during the rank progression from lignite to bituminous coal. Hatcher and Clifford (1997) simplified the process of coalification and what materials contribute to the final coal product as depicted in Figure 19.

The essential conclusions that Hatcher and Clifford (1997) propose are that the most resistant structural parts of the original plant material will better retain their geochemical and physical character, whereas more labile components will be broken down and geochemically altered during the maceration and coalification process.

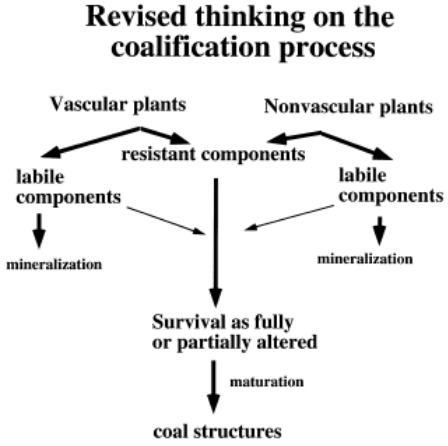

Figure 19: Unified modern view of the coalification process (Hatcher and Clifford, 1997)

Wood or secondary xylem and its cellulose are initially broken down to form lignin, the primary precursor for vitrinite macerals (Lowry, 1963; Hatcher and Clifford, 1997). This process involves several progressive chemical reactions as rank increases (Fig. 20). The reactions initially have little effect on the physical characteristics at subbituminous coal rank—the cell walls of the wood material

show significant pressure distortion on the micro-scale but retain the macro-scale morphological character despite the loss of the major component of cellulose, which is replaced by lignin biopolymers. However, this changes as rank advances to bituminous, as more significant chemical changes occur and phenol-like structures begin to dominate over the liginitic catechol-like rings. The catechols condense to diaryl ethers, which then pyrolyse to give phenols, catechols, alkyl phenols, and guaiacols. These structures condense once again to either lose another oxygen molecule or to produce diaryl ethers (Hatcher and Clifford, 1997).

These changes are displayed on the macro-scale as the coal's physical morphology becomes more lustrous, and on the micro-scale as lignin is transformed into vitrinite and becomes more homogenous (Hatcher and Clifford, 1997). If the coal advances further in rank, aromaticity increases with a reduction in oxygen content and by this point little semblance of the original cellular wood structure remains (Hatcher and Clifford, 1997).

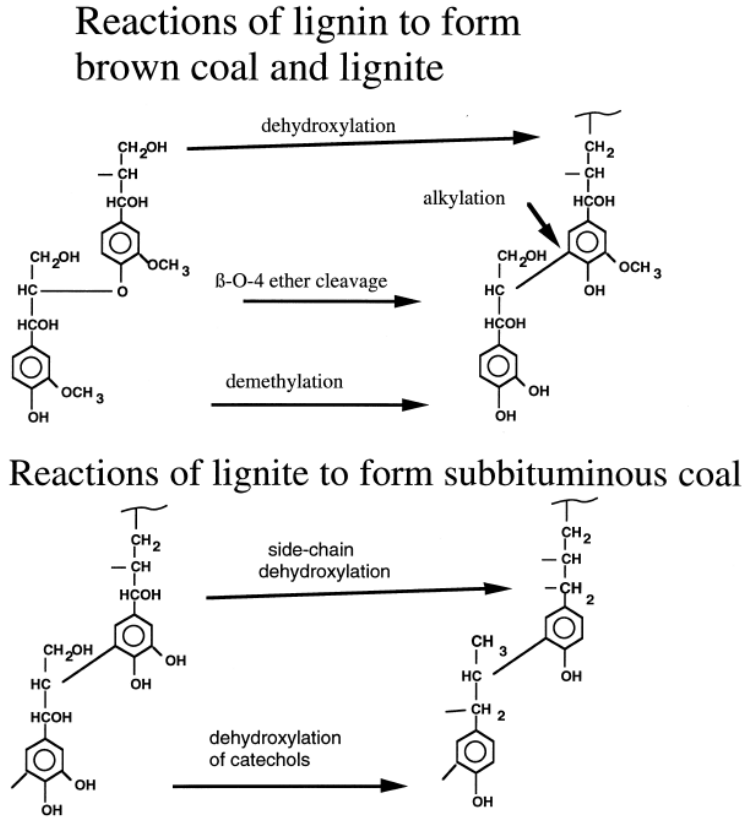

Figure 20: Reactions describing the transformation of lignin units to subbituminous coal (Hatcher and Clifford, 1997)

When looking at resinities of the liptinite maceral group, the chemical changes have been investigated and two classes of resinites are described (Hatcher and Clifford, 1997):

- Class I: Derived from the polymerisation of labdatriene diterpenoids.
- Class II: Derived from the polymerisation of cadinene sesquiterpenoids.

Of these two classes, Class II has been inferred to undergo similar maturation processes to those of crude oil, where reduction and aromatisation reactions are dominant. With increasing maturity these

resinites have increased concentrations of thermodynamically stable cadinane dimers. Class I resinites have been extensively studied and several theories exist with regard to their maturation path; however, it is generally agreed that a combination of both inter- and intramolecular cyclisation reactions occur along with isomerisation (Hatcher and Clifford, 1997).

Leaf material, represented by liptinite, is readily identified in petrographic assessments of coals, but the chemistry of this material is dramatically different from modern cuticles (Teichmüller, 1986., Hatcher and Clifford, 1997). The cutin and waxes of modern cuticles do not survive the diagenetic processes, while the biopolymer cutan has been proposed to survive unchanged during coalification (Hatcher and Clifford, 1997). The cellulosic structure is thought to act as a structural backbone for the aliphatic compounds that attach to it via ether bonds (Hatcher and Clifford, 1997).

The pollen and spore components of vascular plants are tools often used in palynological assessments of sediments; they are capable of surviving the coalification process with little physical alterations (Lowry, 1963; Hatcher and Clifford, 1997). This structural resilience has been linked to the primary chemical constituent sporopollenin (Hatcher and Clifford, 1997). Fossil sporopollenin has been found to contain aromatic and aliphatic compounds as well as labile substances (Hatcher and Clifford, 1997). With increasing maturation, the sporopollenin is converted to have a more aromatic affinity, possibly due to the pyrolysation of aliphatic structures. Further aromatic structures, such as benzene, toluene, phenol, and acetophenone, are produced as a product of the pyrolysis during py-GC-MS (van Bergen *et al.,* 1993; Hatcher and Clifford, 1997).

Algae and its remnants have been often documented as minor components of coal; this, however, may be due to the lack of physical microscopic observations rather than an accurate representation of the algal component (Hatcher and Clifford 1997). The resistant biopolymer algaenan is responsible for the preservation of structure of the algal fossils within coal, as it survives relatively unaltered during the maceration and coalification processes (Hatcher and Clifford, 1997). Chemically, the algaenans vary based on the original algal types, but the majority are highly aliphatic (Hatcher and Clifford, 1997).

Each of these components shows alterations of both structure and chemistry during the maceration and coalification processes (Hatcher and Clifford, 1997). The more resistant compounds of each discussed group often create the backbone on which reactive compounds bond. These more reactive compounds are often derived from the labile material that has broken down during maceration (Hatcher and Clifford, 1997). The coalification process and rank advancement have obvious and dramatic effects on both the physical structure and chemical nature of the original plant material (Hatcher and Clifford, 1997).

With a basic view of how macerals alter during coalification, authors such as Mathews and Chaffee (2012), Barsky *et al.* (2009), Gamson *et al.* (1993), Mastlerz and Glikson (2000), Van Niekerk *et al.* (2008), and Van Niekerk and Mathews (2010) have focused on understanding the molecular structural

properties of coal particles. The two-dimensional graphics displayed in Hatcher and Clifford (1997) have made way for a more complex, three-dimensional understanding of coal molecules.

The modern viewpoint is that coal is made up of a three-dimensional macromolecular network of polyaromatic and alkyl-substituted aromatic units bonded together (Van Niekerk and Mathews, 2010). Many of the molecular models the structures described constitute hundreds of atoms. Progress and improvements in computational abilities and analytical techniques have allowed for larger, more complex models that are more representative of coal behaviours (Mathews and Chaffee, 2012). However, this work has been largely focused on bituminous coals, with lesser work on brown coals, subbituminous coals, and anthracite (Mathews and Chaffee, 2012). This skewed analysis is due to the economic importance of bituminous coals as well as their ubiquity (Mathews and Chaffee, 2012).

Although the focus of models has been on bituminous coals, the basic structure of coal is that of a framework of aromatic and hydroaromatic macromolecules (Matthews and Chaffee, 2012). These frameworks are then bonded together through a series crosslinks of, most commonly, methylene, oxygen, and sulphur (Van Niekerk and Mathews, 2010; Mathews and Chaffee, 2012). Three models for the connectivity of these frameworks are proposed (Fig. 21) (Van Niekerk and Mathews, 2010):

1. **Associative (noncovalent):** This model proposes that macromolecules are bonded together by non-bonding interactions that form a network of associated coal molecules. The macromolecules are bonded together by noncovalent bonds such as hydrogen bonds, $\boldsymbol{\pi - \pi}$ interactions of aromatic rings, van der Waals forces, and electrostatic interactions.
2. **Non-associative (covalent):** This model proposes that the macromolecular structures are bonded together by covalent bonds that trap a mobile phase within the structure. This allows for the structure to be relatively insoluble in organic solvents and also prevents the mobility of the trapped phase.
3. **Composite:** This model proposes that coal is made up of various sized molecules in an associative entangled structure.

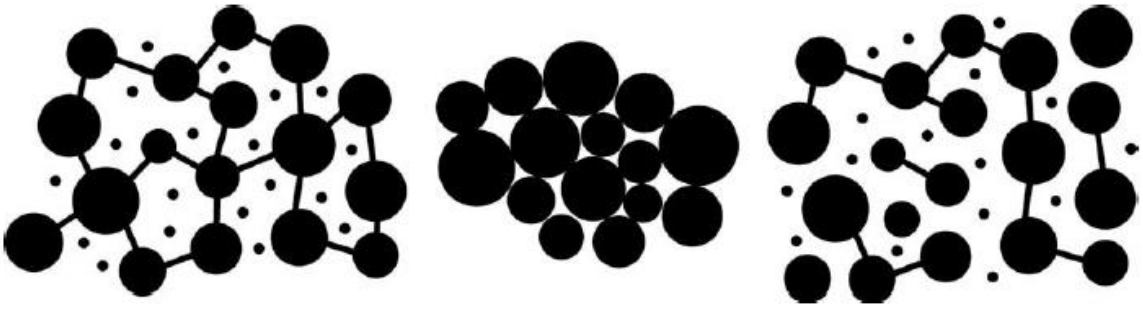

Figure 21: Left to right- Non-associative, Associative and Composite model (Nishioka (1992) in Van Niekerk and Mathews, 2010)

There are a vast array of models describing how these associative, non-associative, and composite models may build to form coal particles, many of which are described in Mathews and Chaffer (2012). The common feature is that the described structures are small in scale, containing between hundreds of atoms to >5000 atoms, with the most complex model containing 50789 atoms within a 728-cross-linked aromatic cluster, shown in Figure 22 (Mathews and Chaffer, 2012; Castro-Marcano *et al.,* 2012).

The production of such molecular frameworks allows for an increased understanding of the link between chemical structure and coal properties as well as the behaviour of coal chemical systems (Castro-Marcano *et al.,* 2012). However, even with these large advancements, there are still large gaps in our understanding of the mechanics of coal reactivity and structural alteration in the presence of thermal stresses and inorganic organic interaction (Castro-Marcano *et al.,* 2012).

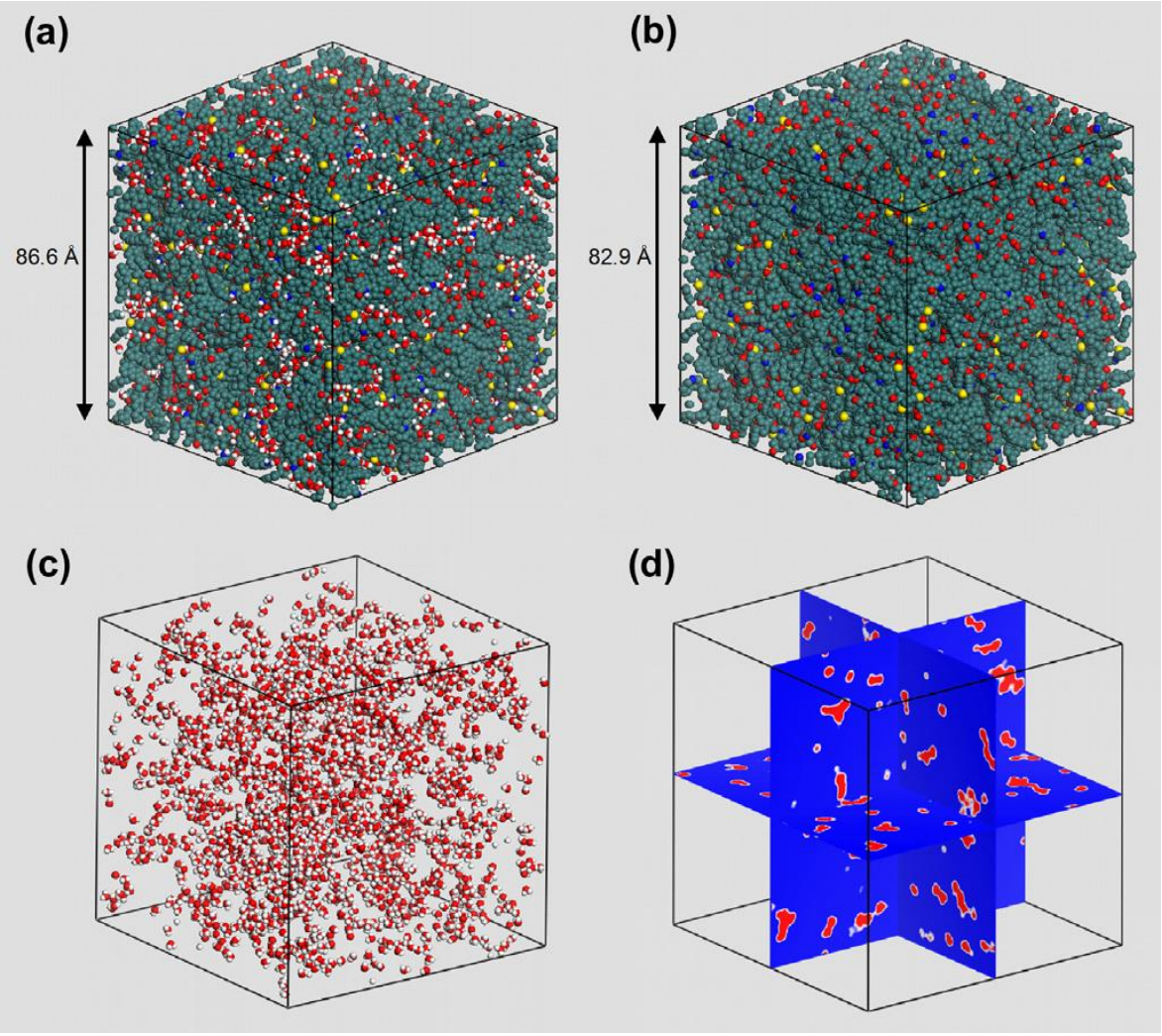

Figure 22: Molecular model for Illinois No. 6 coal: (a) including moisture component, (b) dry state, (c) showing the 2214 water molecules alone, and (d) 2D slices parallel to the x, y and z-axes. The occupied volume by the water molecules forming aggregates is shown in red. Atoms are represented by van der Waals spheres and colored as follows: carbon-green; hydrogen-white; oxygen-red; nitrogen-blue; sulfur-yellow. Hydrogens attached to the coal structure are not shown to aid visualisation. The length of the periodic cubic box is displayed for (a) and (b), with the same scale applied to (c) and (d) (Castro-Marcano *et al.,* 2012).

CHAPTER 5: SITE SELECTION AND SAMPLING

To investigate the physicochemical nature of metamorphosed coal, it was necessary to identify an intersection that had been freshly exposed to oxygen, in order to limit the oxidation effects. The Ithemba Lethu shaft at Sasol's Secunda mining operations situated in the Highveld Coalfield (Fig. 7) was selected for sampling, as a 3.5 m dolerite dyke had recently been mined through the C4 L coal seam. The seam is hosted within the Vryheid formation of the Karoo Supergroup at a depth of ~140 m below surface with the dolerite dyke identified as the locally defined DO8 (Fig. 23).

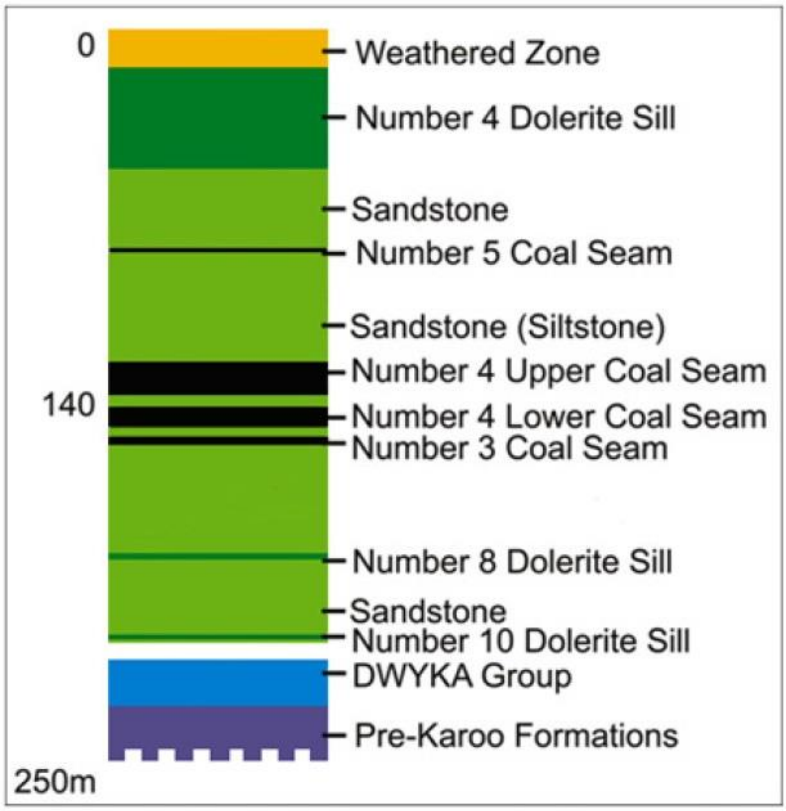

Figure 23: Generalised stratigraphy of the Ithemba Lethu mining operation, Sasol Secunda.

Coal from the sampled area hosted a large array of inorganic carbonaceous cleats with the intruding dolerite re-carbonated to a large degree. A sizeable component of the original magmatic material was replaced by carbonates such as siderite, calcite, and dolomite. Unfortunately, due to the underground mining safety regulations, no photographs were allowed. However, Figure 24 shows a similar situation at an open cast operation in close proximity to the sampled location.

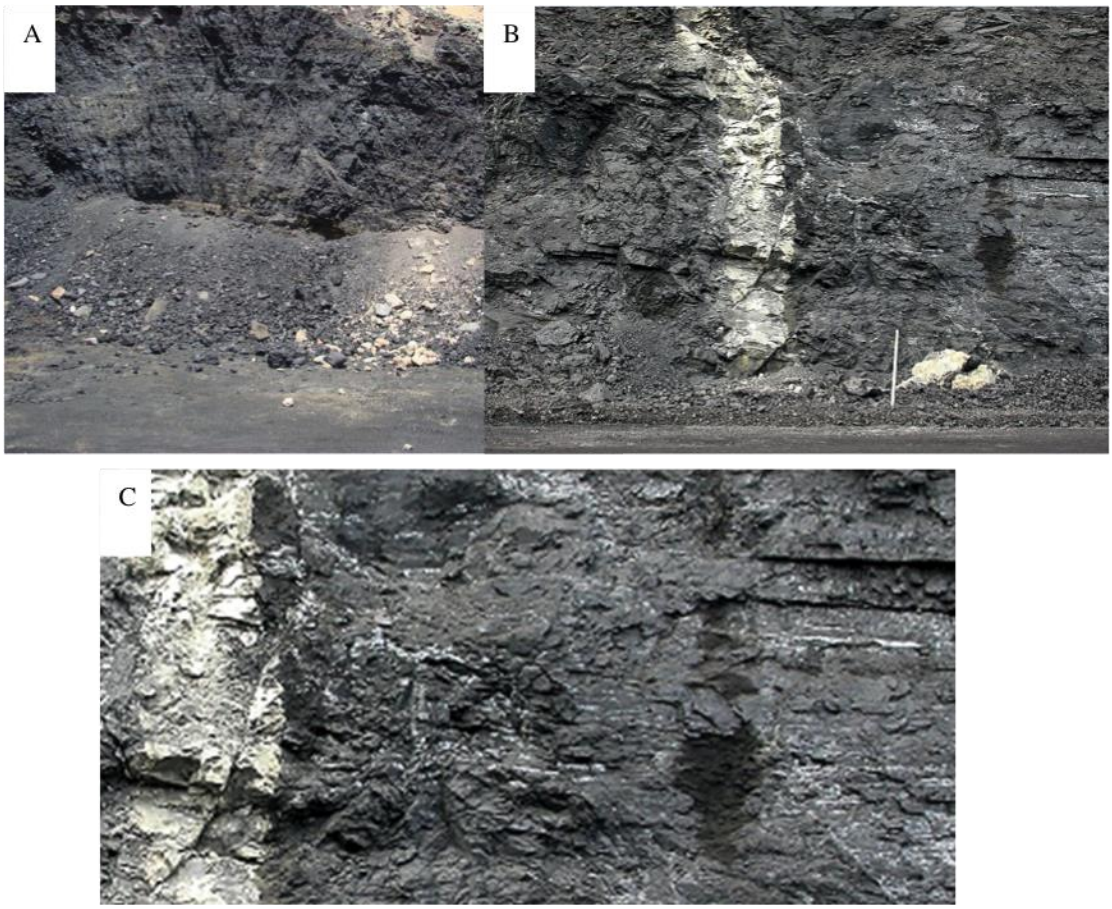

Figure 24: Photographs of re-carbonated dolerite intrusion through bituminous coal of the Highveld Coalfield. (A): Image of unaffected coal on the same exposed mining bench. (B): Image of perpendicular dolerite dyke intersecting the coal seam. (C): Zoomed in image of carbonaceous cleat infill's adjacent to the dolerite intrusion.

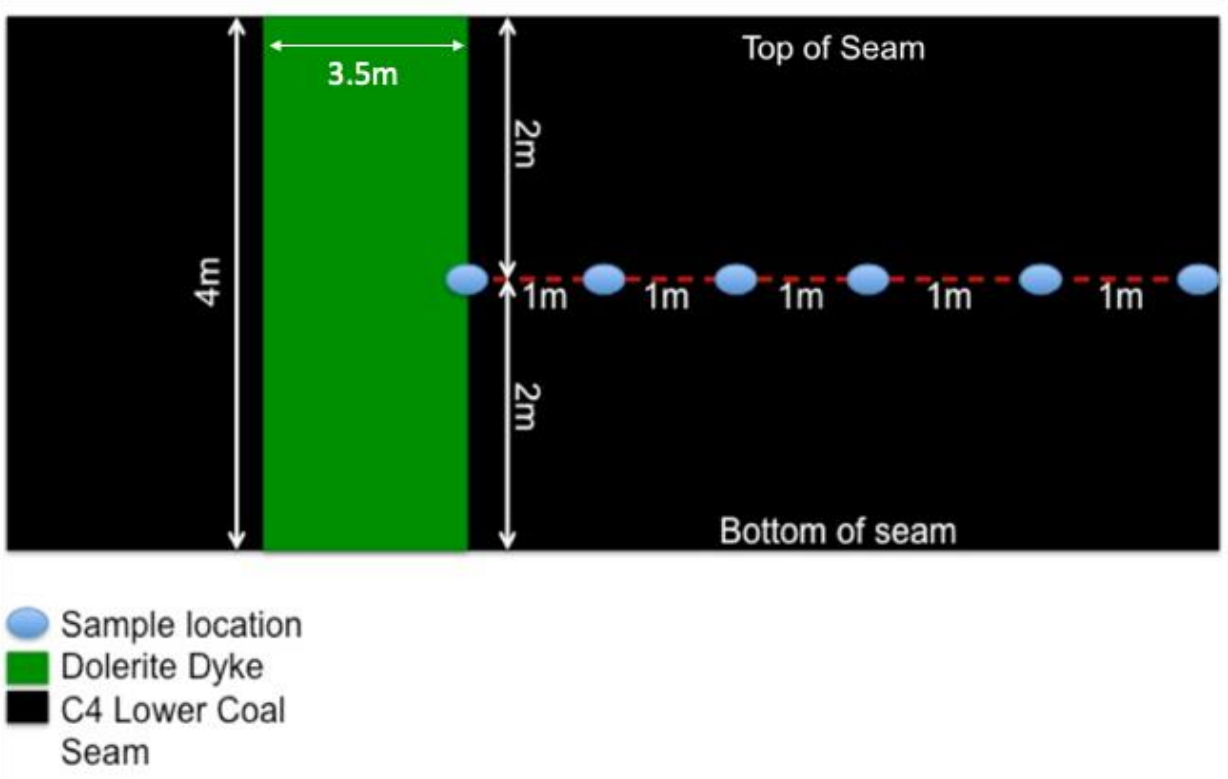

Figure 25: Schematic representation of sampling methodology.

Twenty samples were taken of the C4 lower coal seam at 1 m intervals moving away from the dyke at a consistent stratigraphic height (Fig. 25). The samples were split into two sets, with one set remaining whole and intact (sample set A), while the other was milled into a 15 μm powder (sample set B). In the following chapters, the specifics of each analytic technique that was applied is discussed, as well as any additional sample preparation to the sample set associated with them.

5.1. Summary Discussion

When exploring the sampling site, visible physical character changes were noticeable in not only the coal but also in the dolerite itself. Figure 24 displays a surface example of the re-carbonated dolerite intrusion cross cutting a bituminous coal seam of the Highveld Coalfield. This re-carbonation proves the potential for fluid mobilisation and precipitation. At hand specimen level, the coal in close proximity to the dolerite intrusion has been visibly becoming more friable and less lustrous texture (Fig. 24).

CHAPTER 6: COAL PETROGRAPHY AND REFLECTANCE ANALYSIS

Petrographic analysis of coal has been a fundamental qualitative and quantitative technique for over 90 years (Lowry, 1963). As the fundamental descriptive technique, petrography is essential in understanding the physical variations between coal types and the effects of *in situ* environments on these types. In a South African context, the application of petrography in identification of maceral types and concentrations has had a profound effect on the understanding of the combustibility of coal with respect to maceral group concentrations. In addition petrography allows identification and description of the variation in macerals during exposure to the effects of thermal intrusive bodies on the structural and textural properties of coal.

With a specific focus on the effect of these thermal intrusive environments, a direct comparison is available in the work of Gröcke *et al.* (2009), where the thermal influence of dolerites on the Secunda C4 lower coal seam are investigated. Although focused on thermogenic methane release, the research of Gröcke *et al.* (2009) provides a good comparison for the petrographic data below. A point noted by Gröcke *et al.* (2009) is the potential cooling through convection of material within 1.2 to 1.5-times the width of the dyke. Gröcke *et al.* (2009) suggested that convection cooling may have reduced temperatures from ~ 625 °C to between 100 to 200 °C within the contact aureole. In addition to cooling through convection, Gröcke *et al.* (2009) demonstrated petrographic evidence of direct thermal influence on the structural character of vitrinite macerals adjacent to the intrusion. The structural alteration is noted by the development of devolatilisation vacuoles that have altered the maceral into an isotropic coke.

The work of Golab *et al.* (2006) investigated the mineralogy of thermally altered Permian coals of Australia petrographically and geochemically. Golab *et al.* (2006) showed two generations of mineralogical material, specifically carbonaceous material. Golab *et al.* (2006) postulated that the first set of carbonaceous material was generated during the coalification process, while the second generation was the result of precipitation from fluid percolation. The heat produced from the doleritic intrusion adjacent to the seam drove this fluid percolation.

6.1. Methodology

The approach used in this study followed traditional petrographic analysis. Samples from the ground material of sample set B were used to create 4 cm diameter epoxy mounts. These mounts were then polished and analysed under reflected light, using oil immersion objectives at 32x magnification. Photomicrographs of the samples were taken to display representative examples of each sampled area, with specific focus on textural variations. Further investigations were done through vitrinite reflectance analysis, as this allowed for a more holistic understanding of maturation across the transact. A minimum of 100 unique vitrinite reflectance readings were taken per sample and the data then

statistically analysed. In addition to this, maceral group analysis was undertaken by ICCP-accredited Prof. NJ Wagner to understand the distribution of maceral types across the sample set.

6.2. Results

Below are the results of all petrographically related analyses from sample set B.

The data displayed in Table 6 shows the variable maceral compositions across the sampled transect; however, a distinctive trend appears when this is simplified down to the reactive and non-reactive maceral groups. Figure 26 allows for a clearer view on the maceral composition across the transect. The peaks in reactive maceral groups at ~ 2, 5, 10, 13, 16 and 19 m from the dolerite intrusion are remarkable.

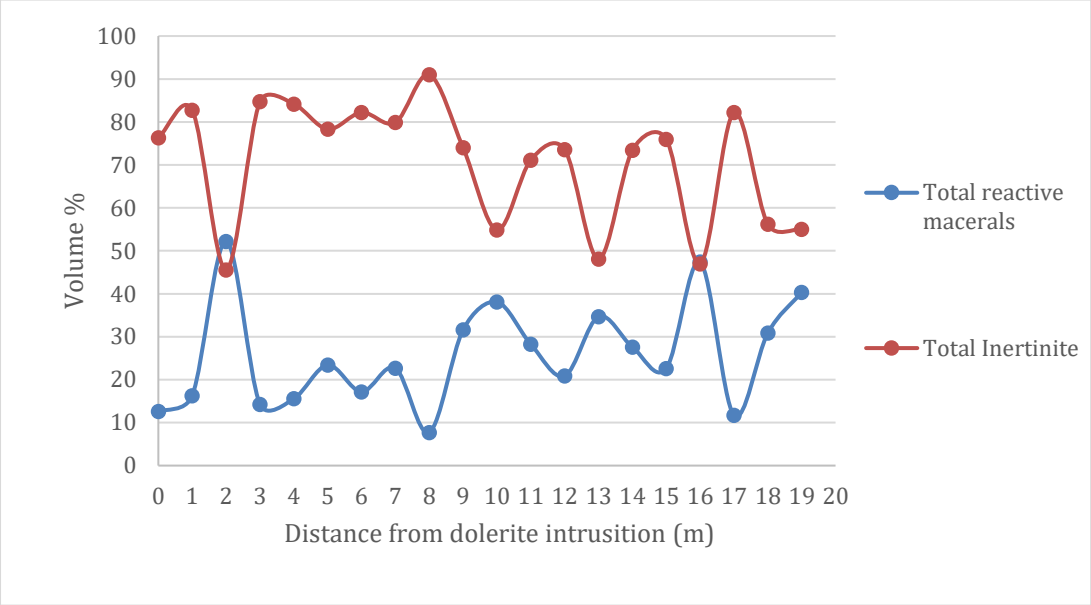

Figure 26: Graphic depicting the volume percentage reactive macerals and total inertinite moving away from the dolerite dyke.

From Table 6, the peaks in reactive macerals correlate well with increases in the collotelinite occurrence. When looking at the samples surrounding these collotelinite peaks at 2, 5, 10, 13, 16 and 18-19 m, there is a corresponding spike in inert semifusinite occurrence both before and after the collotelinite peak.

When looking at the mean reflectance's in Table 6 it can be seen that the greatest mean vitrinite reflectance values are seen within maximum distance of 5 m from the intrusion. This relationship is well displayed in Figure 27, where total vitrinite reflectance histograms for the transect are plotted, the primary data for these histograms can been found in Table 13 in Appendix B The elevated vitrinite reflectance mean values are good proxies for thermally influence on these coal samples..

Table 6: Maceral Group analysis of samples DK0-DK 19

Sample no:		DK0		DK1		DK2		DK3		DK4		DK5		DK6		DK7		DK8		DK9		DK10		DK11		DK12		DK13		DK14		DK15		DK16		DK17		DK18		DK19	
		inc. mm	mmf	inc. mm	mmf	inc. mm	mmf	inc. mm	mmf	inc. mm	mmf	inc. mm	mmf	inc. mm	mmf	inc. mm	mmf	inc. mm	mmf	inc. mm	mmf	inc. mm	mmf	inc. mm	mmf	inc. mm	mmf	inc. mm	mmf	inc. mm	mmf	inc. mm	mmf	inc. mm	mmf	inc. mm	mmf	inc. mm	mmf
MACERAL GROUP	MACERAL (vol%)	vol%	vol%	vol%	vol%	vol%	vol%	vol%	vol%	vol%	vol%	vol%	vol%	vol%	vol%	vol%	vol%	vol%	vol%	vol%	vol%	vol%	vol%	vol%	vol%	vol%	vol%	vol%	vol%	vol%	vol%	vol%	vol%	vol%	vol%	vol%	vol%	vol%	vol%	vol%
Vitrinite	telinite	0.5	0.6	0.0	0.0	0.0	0.0	0.2	0.2	0.0	0.0	0.5	0.5	0.0	0.0	0.2	0.2	0.0	0.0	0.0	0.0	0.0	0.0	0.4	0.4	0.0	0.0	0.2	0.3	0.0	0.0	0.0	0.0	0.5	0.5	0.0	0.0	0.2	0.2	1.0	1.1
	collotelinite	5.5	6.2	4.4	4.5	34.5	35.5	4.4	4.4	3.6	3.7	10.3	10.5	4.1	4.3	4.9	5.1	1.5	1.6	6.7	6.8	17.7	20.4	8.0	8.6	6.0	6.5	18.1	22.9	6.3	6.7	7.5	7.9	34.1	37.8	2.3	2.5	13.6	16.5	12.0	13.0
	vitrodetrinite	0.0	0.0	0.0	0.0	0.0	0.0	0.0	0.0	0.0	0.0	0.0	0.0	0.0	0.0	0.0	0.0	0.0	0.0	0.0	0.0	0.0	0.0	0.0	0.0	0.0	0.0	0.0	0.0	0.0	0.0	0.0	0.0	0.0	0.0	0.0	0.0	0.0	0.0	0.0	0.0
	collodetrinite	3.5	3.9	5.8	6.0	13.3	13.7	4.6	4.7	2.9	3.0	3.2	3.3	4.9	5.2	8.7	9.0	0.6	0.7	13.1	13.3	10.3	11.8	9.0	9.7	8.0	8.6	8.7	11.0	10.4	11.0	6.8	7.1	6.8	7.5	2.1	2.3	6.7	8.2	19.9	21.4
	corpogelinite	0.0	0.0	0.0	0.0	0.0	0.0	0.0	0.0	0.2	0.2	0.5	0.5	0.0	0.0	0.6	0.6	0.0	0.0	0.2	0.2	0.0	0.0	0.2	0.2	0.0	0.0	0.4	0.6	0.6	0.6	0.0	0.0	0.0	0.0	0.0	0.0	0.8	1.0	0.6	0.6
	gelinite	3.0	3.4	1.9	2.0	1.2	1.3	1.5	1.5	1.7	1.7	2.5	2.5	0.6	0.6	0.4	0.4	0.4	0.5	1.0	1.1	1.4	1.6	1.0	1.1	1.4	1.5	1.1	1.4	1.4	1.5	0.7	0.7	0.5	0.5	2.5	2.8	1.6	1.9	1.2	1.3
	pseudovitrinite	0.0	0.0	0.0	0.0	0.0	0.0	0.0	0.0	0.0	0.0	0.0	0.0	0.0	0.0	0.0	0.0	0.0	0.0	0.0	0.0	0.0	0.0	0.0	0.0	0.0	0.0	0.0	0.0	0.0	0.0	0.0	0.0	0.0	0.0	0.2	0.2	0.0	0.0	0.0	0.0
Inertinite	fusinite	8.3	9.3	7.1	7.2	9.1	9.4	10.9	11.1	15.1	15.4	12.6	12.8	10.4	10.9	15.8	16.3	2.1	2.3	12.9	13.1	6.9	7.9	6.0	6.5	7.0	7.5	5.6	7.1	5.5	5.8	6.3	6.6	10.2	11.3	3.3	3.7	10.2	12.5	7.6	8.2
	reactive semifusinite	0.0	0.0	1.2	1.2	1.0	1.0	1.0	1.0	1.7	1.7	1.7	1.8	2.3	2.5	4.3	4.5	0.0	0.0	5.2	5.3	2.8	3.2	5.0	5.4	0.4	0.4	2.5	3.1	3.3	3.5	2.3	2.5	4.3	4.8	0.6	0.7	3.5	4.3	1.4	1.5
	inert semifusinite	25.4	28.4	45.5	46.6	16.7	17.3	38.7	39.5	41.1	41.9	31.0	31.5	38.9	41.0	32.1	33.3	23.4	24.5	37.8	38.4	27.8	31.9	37.1	40.0	38.6	41.8	30.4	38.4	38.7	40.8	40.1	42.3	24.4	27.0	27.6	30.4	23.8	29.0	21.5	23.1
	micrinite	0.8	0.8	1.2	1.2	2.0	2.0	1.9	2.0	1.0	1.0	2.7	2.8	0.6	0.6	1.6	1.6	0.6	0.7	1.2	1.3	1.6	1.9	1.2	1.3	0.8	0.9	0.0	0.0	2.2	2.4	1.2	1.2	0.0	0.0	0.2	0.2	0.8	1.0	2.6	2.8
	macrinite	0.0	0.0	0.0	0.0	0.5	0.5	0.0	0.0	0.0	0.0	0.2	0.3	0.2	0.2	0.0	0.0	0.0	0.0	0.2	0.2	0.0	0.0	0.4	0.4	0.2	0.2	0.0	0.0	0.4	0.4	0.2	0.2	0.2	0.3	0.0	0.0	0.0	0.0	0.0	0.0
	secretinite	0.8	0.8	0.7	0.7	1.7	1.8	1.2	1.2	1.0	1.0	0.5	0.5	1.4	1.4	1.2	1.2	0.0	0.0	0.6	0.6	0.4	0.5	1.2	1.3	1.0	1.1	1.1	1.4	0.6	0.6	0.5	0.5	0.7	0.8	0.4	0.5	0.8	1.0	0.6	0.6
	funginite	0.0	0.0	0.0	0.0	0.0	0.0	0.0	0.0	0.0	0.0	0.0	0.0	0.0	0.0	0.0	0.0	0.0	0.0	0.0	0.0	0.0	0.0	0.0	0.0	0.0	0.0	0.0	0.0	0.0	0.0	0.0	0.0	0.0	0.0	0.0	0.0	0.2	0.2	0.0	0.0
	inertodetrinite R	0.0	0.0	1.0	1.0	0.5	0.5	0.7	0.7	0.7	0.7	2.2	2.3	2.9	3.1	2.2	2.2	4.1	4.3	2.5	2.5	3.6	4.2	2.2	2.4	2.4	2.6	1.8	2.3	3.7	3.9	2.1	2.2	0.5	0.5	3.1	3.5	2.2	2.6	1.6	1.7
	inertodetrinite I	41.1	45.8	26.0	26.7	14.0	14.5	30.3	30.9	23.6	24.1	27.3	27.8	25.6	27.0	22.7	23.5	60.7	63.7	13.5	13.7	11.7	13.4	18.0	19.4	23.3	25.2	6.7	8.5	19.0	20.1	23.3	24.6	6.8	7.5	46.9	51.6	14.7	18.0	19.7	21.2
Liptinite	sporinite	0.0	0.0	1.9	2.0	1.5	1.5	1.5	1.5	3.6	3.7	1.2	1.3	2.3	2.5	1.4	1.4	0.9	0.9	2.5	2.5	1.8	2.1	2.4	2.6	2.8	3.0	1.8	2.3	1.8	1.9	2.6	2.7	0.5	0.5	0.8	0.9	2.4	2.9	2.4	2.6
	cutinite	0.0	0.0	0.0	0.0	0.2	0.3	0.0	0.0	0.7	0.7	1.2	1.3	0.0	0.0	0.0	0.0	0.0	0.0	0.0	0.0	0.0	0.0	0.0	0.0	0.0	0.0	0.0	0.0	0.0	0.0	0.2	0.2	0.2	0.3	0.0	0.0	0.0	0.0	0.2	0.2
	resinite	0.0	0.0	0.0	0.0	0.0	0.0	0.0	0.0	0.0	0.0	0.0	0.0	0.0	0.0	0.0	0.0	0.0	0.0	0.4	0.4	0.4	0.5	0.0	0.0	0.0	0.0	0.0	0.0	0.0	0.0	0.0	0.0	0.0	0.0	0.0	0.0	0.0	0.0	0.0	0.0
	alginite	0.0	0.0	0.0	0.0	0.0	0.0	0.2	0.2	0.2	0.2	0.0	0.0	0.0	0.0	0.0	0.0	0.2	0.2	0.0	0.0	0.0	0.0	0.0	0.0	0.0	0.0	0.0	0.0	0.0	0.0	0.5	0.5	0.0	0.0	0.0	0.0	0.0	0.0	0.0	0.0
	liptodetrinite	0.0	0.0	0.0	0.0	0.0	0.0	0.2	0.2	0.0	0.0	0.0	0.0	0.0	0.0	0.0	0.0	0.0	0.0	0.0	0.0	0.0	0.0	0.0	0.0	0.0	0.0	0.0	0.0	0.0	0.0	0.0	0.0	0.0	0.0	0.0	0.0	0.0	0.0	0.0	0.0
	suberinite	0.0	0.0	0.0	0.0	0.0	0.0	0.0	0.0	0.0	0.0	0.0	0.0	0.0	0.0	0.0	0.0	0.0	0.0	0.0	0.0	0.0	0.0	0.0	0.0	0.0	0.0	0.0	0.0	0.0	0.0	0.0	0.0	0.0	0.0	0.0	0.0	0.0	0.0	0.0	0.0
	exsudatinite	0.0	0.0	0.0	0.0	0.0	0.0	0.0	0.0	0.0	0.0	0.0	0.0	0.0	0.0	0.0	0.0	0.0	0.0	0.0	0.0	0.0	0.0	0.0	0.0	0.0	0.0	0.0	0.0	0.0	0.0	0.0	0.0	0.2	0.3	0.0	0.0	0.0	0.0	0.0	0.0
Mineral matter	silicate (clay/qz)	2.5		0.7		0.5		0.5		0.5		0.0		2.0		1.2		2.1		0.4		1.4		1.8		0.8		1.3		2.5		1.4		3.2		3.3		4.1		2.6	
	sulfide	1.0		0.5		0.0		0.0		0.0		0.0		1.8		1.2		0.0		0.0		10.9		3.4		3.6		12.1		1.2		0.7		2.9		0.0		9.0		0.4	
	carbonate	6.8		1.2		2.5		1.5		1.5		1.5		1.6		0.8		2.6		1.0		0.6		2.0		3.4		7.4		1.6		3.0		3.4		5.9		4.9		4.0	
	other	0.0		0.0		0.0		0.0		0.0		0.0		0.0		0.2		0.0		0.0		0.0		0.0		0.0		0.0		0.0		0.0		0.2		0.0		0.0		0	
SUMMARY TABLE																																									
MACERAL GROUP	**VITRINITE**	**12.6**	**14.0**	**12.2**	**12.5**	**49.0**	**50.5**	**10.7**	**10.9**	**8.5**	**8.7**	**17.0**	**17.3**	**9.6**	**10.1**	**14.8**	**15.3**	**2.6**	**2.7**	**21.0**	**21.3**	**29.4**	**33.8**	**18.6**	**20.1**	**15.3**	**16.6**	**28.6**	**36.2**	**18.8**	**19.9**	**14.9**	**15.7**	**41.8**	**46.3**	**7.1**	**7.8**	**22.8**	**27.8**	**34.7**	**37.4**
TOTALS (vol%)	**INERTINITE**	**76.3**	**85.1**	**82.7**	**84.8**	**45.6**	**47.0**	**84.7**	**86.4**	**84.2**	**85.9**	**78.3**	**79.5**	**82.2**	**86.8**	**79.9**	**82.7**	**91.0**	**95.5**	**74.0**	**75.1**	**54.8**	**63.0**	**71.1**	**76.7**	**73.6**	**79.7**	**48.1**	**60.7**	**73.4**	**77.5**	**76.0**	**80.1**	**47.0**	**52.0**	**82.2**	**90.6**	**56.2**	**68.6**	**55.0**	**59.2**
	LIPTINITE	**0.0**	**0.0**	**1.9**	**2.0**	**1.7**	**1.8**	**1.9**	**2.0**	**4.6**	**4.7**	**2.5**	**2.5**	**2.3**	**2.5**	**1.4**	**1.4**	**1.1**	**1.1**	**2.9**	**3.0**	**2.2**	**2.5**	**2.4**	**2.6**	**2.8**	**3.0**	**1.8**	**2.3**	**1.8**	**1.9**	**3.3**	**3.4**	**0.9**	**1.0**	**0.8**	**0.9**	**2.4**	**2.9**	**2.6**	**2.8**
	MINERAL MATTER	**10.3**		**2.4**		**3.0**		**1.9**		**1.9**		**1.5**		**5.3**		**3.4**		**4.7**		**1.5**		**12.9**		**7.2**		**7.8**		**20.8**		**5.3**		**5.1**		**9.7**		**9.2**		**18.1**		**7.0**	
	TOTAL INERTINITE	**76.3**	**85.1**	**82.7**	**84.8**	**45.6**	**47.0**	**84.7**	**86.4**	**84.2**	**85.9**	**78.3**	**79.5**	**82.2**	**86.8**	**79.9**	**82.7**	**91.0**	**95.5**	**74.0**	**75.1**	**54.8**	**63.0**	**71.1**	**76.7**	**73.6**	**79.7**	**48.1**	**60.7**	**73.4**	**77.5**	**76.0**	**80.1**	**47.0**	**52.0**	**82.2**	**90.6**	**56.2**	**68.6**	**55.0**	**59.2**
	TOTAL REACTIVE MACERALS	**12.6**	**14.0**	**16.3**	**16.7**	**52.2**	**53.8**	**14.3**	**14.6**	**15.6**	**15.9**	**23.4**	**23.8**	**17.2**	**18.1**	**22.7**	**23.5**	**7.7**	**8.1**	**31.6**	**32.1**	**38.1**	**43.8**	**28.3**	**30.5**	**20.9**	**22.6**	**34.7**	**43.8**	**27.6**	**29.2**	**22.6**	**23.8**	**47.4**	**52.5**	**11.7**	**12.9**	**30.8**	**37.6**	**40.4**	**43.4**
VITRINITE REFLECTANCE ANALYSIS (RoV%)																																								
Vitrinite reflectance (RoV%)	Reflectance Mean	1.24		0.95		0.87		0.82		0.82		0.76		0.76		0.68		0.78		0.69		0.68		0.69		0.68		0.66		0.68		0.67		0.66		0.73		0.64		0.64	
	st. dev.	0.100		0.068		0.079		0.074		0.070		0.082		0.074		0.085		0.06		0.05		0.058		0.061		0.067		0.054		0.061		0.069		0.061		0.085		0.06		0.06	
	max	1.80		1.10		1.05		1.00		0.98		0.93		0.91		0.90		0.93		0.85		0.52		0.85		0.83		0.90		0.84		0.85		0.79		0.90		0.83		0.82	
	min	1.10		0.77		0.58		0.53		0.67		0.52		0.57		0.53		0.65		0.59		0.85		0.49		0.43		0.53		0.55		0.50		0.47		0.55		0.51		0.47	
	RANK CATEGORY	Med rank B		Med rank C		Med rank C		Med rank C		Med rank C		Med rank C		Med rank C		Med rank C		Med rank C		Med rank C		Med rank C		Med rank C		Med rank C		Med rank C		Med rank C		Med rank C		Med rank C		Med rank C		Med rank C		Med rank C	

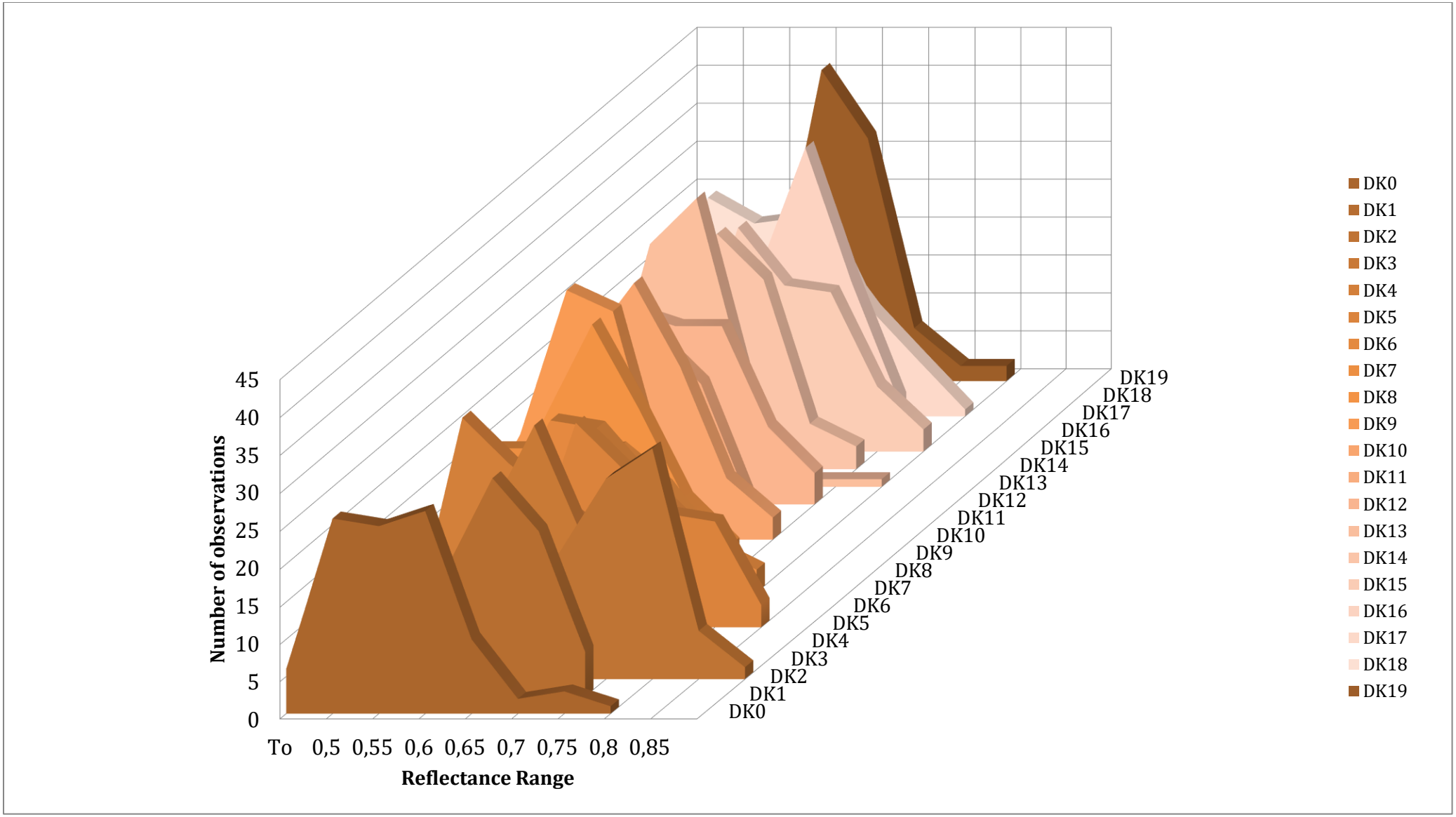

Figure 27: Histograms of reflectance ranges for all DK samples.

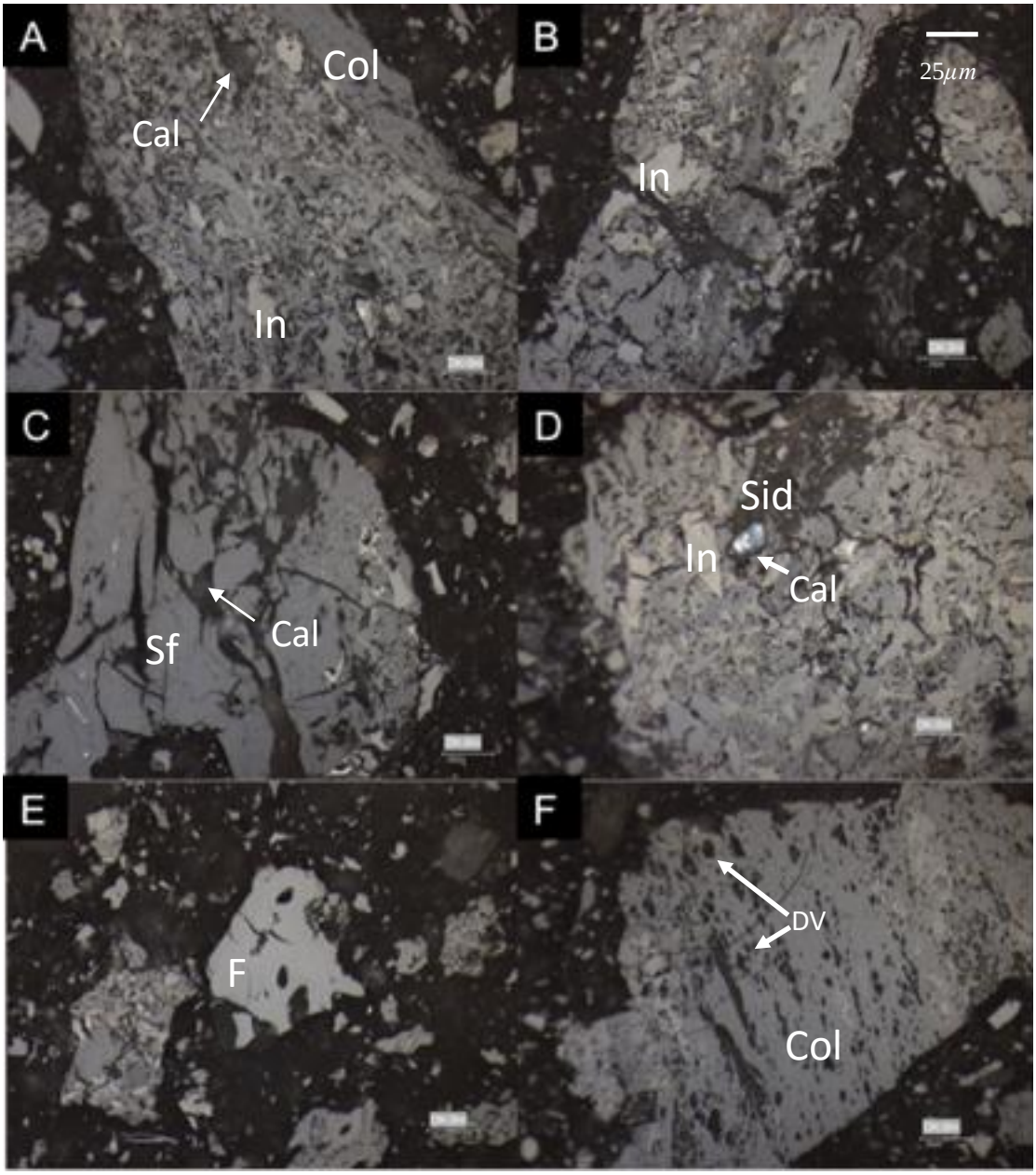

Figure 28: Representative photomicrographs of sample DK 0 at 0 m from the dolerite intrusion. Calcite (Cal), Collotelinite (Col), Inertodetrinite (In), Semifusinite (Sf), Siderite (Sid), Fusinite (F) and Devolatilization vacuoles (DV).

When looking at the vitrinite reflectance summary statistics of sample DK 0 in Table 6, a reflectance range of between 1.1 and 1.5 with a mean of 1.24 can be noted. This high reflectance mean is evidence of thermal influence on the vitrinite macerals in the sample. Figure 28A shows a representative inertodetrinite maceral assemblage. Collotelinite bordering the inertodetrinite features some minor pitting to its surface (possibly the early stages of devolatilization vacuoles), which provides evidence for the thermal effects of the adjacent dolerite dyke. The assemblage also hosts a small calcite inclusion. Figure 28B again displays a inertodetrinite assemblage featuring a fine-grained clay mineral groundmass. In Figure 28C, a fractured semifusinite maceral with calcite infill provides some evidence

for secondary precipitation of mineral matter within the sample, as the calcite has precipitated into the fractures of the maceral. The evidence for secondary precipitation of mineral matter is further seen in Figure 28D where the inertodetrinite maceral assemblage is host to pervasive siderite. The assemblage also hosts a well-rounded calcite inclusion. Figure 28E displays a large fragment of a fusinite maceral which is unaltered, in contrast the collotelinite within 28F which displays prominent devolatilization vacuoles, indicating the structural thermal effects on this sample.

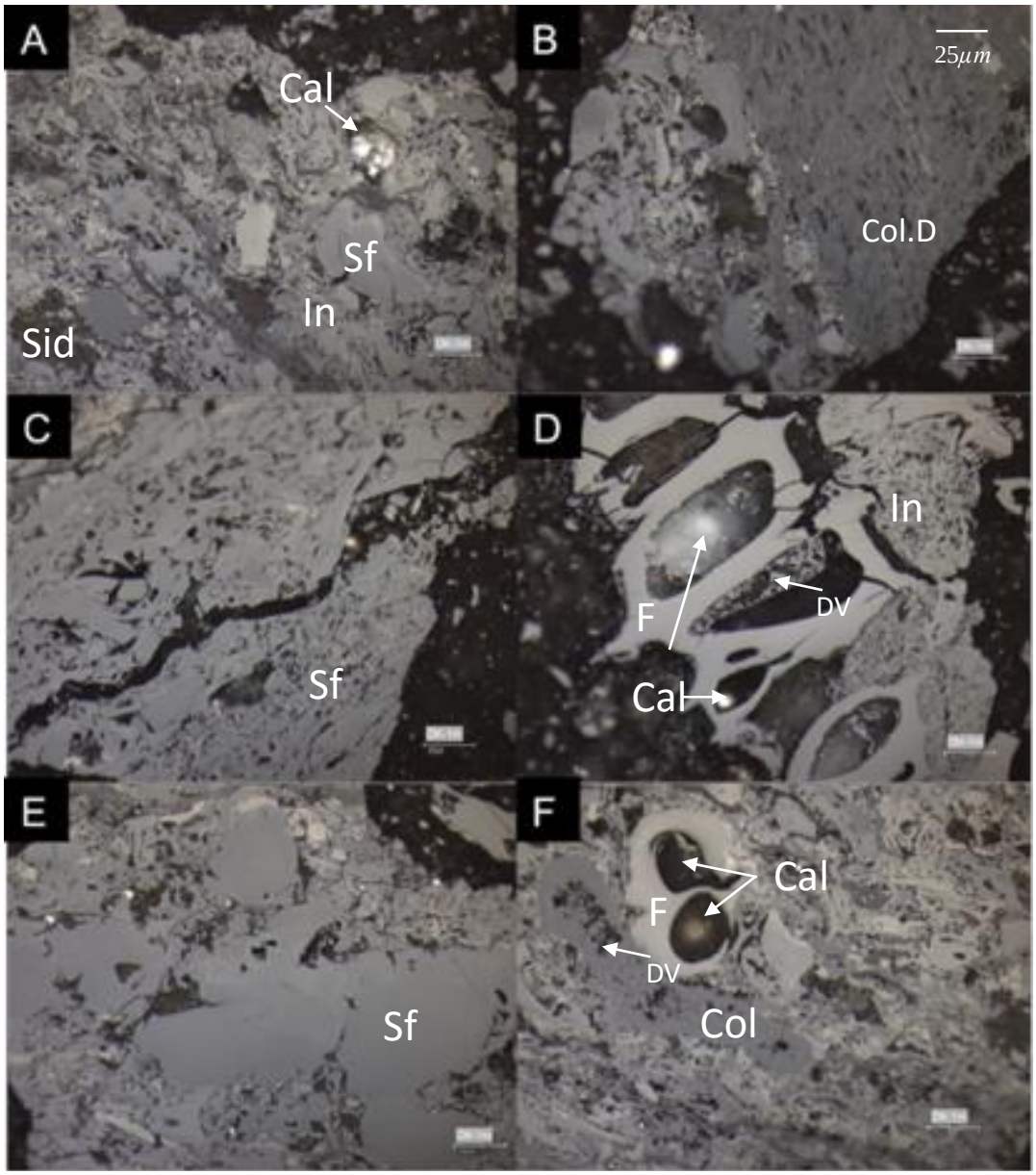

Figure 29: Representative photomicrographs of sample DK 1 at 1 m from the dolerite intrusion. Calcite (Cal), Collotelinite (Col), Inertodetrinite (In), Semifusinite (Sf), Siderite (Sid), Fusinite (F), Collodetrinite (Col.D) and Devolatilization vacuoles (DV).

At 1 m from the dyke coal contact, the vitrinite reflectance mean value is 0.95 with a range of 0.75 to 1.05 as noted in Table 6. When looking at the representative photomicrographs in Figure 29, image A displays a maceral assemblage of semifusinite and inertodetrinite with inclusions of both siderite and calcite, with no signs that the assemblage itself is altered to any large degree. Figure 29B displays a prominent collodetrinite maceral, which is more abundant in sample DK 1 than in Sample DK 0 (Table 6). The semifusinite maceral in 29C displays a significant fracture but is otherwise unaltered. In Figure 29D, a large infilled fusinite maceral flanked by inertodetrinite is noted, the infilling is primarily calcite and it also houses a collotelinite maceral with prominent devolatilization vacuoles, which provide evidence that the thermal influence of the adjacent dolerite is still pronounce in this sample. In contrast to D, Figure 29E shows an assemblage of unaltered inert semifusinite. Figure 29F displays a collotelinite maceral with pitting on the surface which could indicate the early stages of devolatilization vacuoles. In addition, the image shows a well formed fusinite maceral with calcite infill.

Advancing to 2 m from the intrusion (Fig. 30), a mean vitrinite reflectance (Table 6) is estimated at 0.87 within a range of 0.55 to 1.05. Figure 30A shows a central assemblage of fusinite with some minor surface alterations and is host to small fragments of semifusinite. The central maceral assemblage is flanked by a unaltered collotelinite maceral as well as a collodetrinite maceral with shows small surface cavities or pitting which have not fully developed into devolatilization vacuoles. Figure 30B shows a maceral assemblage of semifusinite, inertodetrinite and collotelinite. The collotelinite at the base of the assemblage displays minor surface cavities or pitting, which have once again not fully developed into devolitilzation vacuoles. The large unaltered fusinite maceral in 30C houses a well-rounded calcite inclusion, and 30D displays a more complex assemblage of fusinite and collotelinite, once again with a well-rounded calcite inclusion. The collotelinite in 30D has very subtle surface pits, which again have not developed into devolatilization vacuoles. The consistent lack of devolatilization vacuoles shows that the conductive thermal regime in this sample is not high enough to induce the development of vacuoles at distances greater than 3 meters. Figure 30E provides an example of the precipitation of siderite within the structure of both semifusinite and fusinite, and further displays an unaltered collotelinite maceral. The precipitation of siderite within semifusinite is shown in Figure 30F, with calcite also being housed within the fusinite maceral. Collotelinite in this image is unaltered.

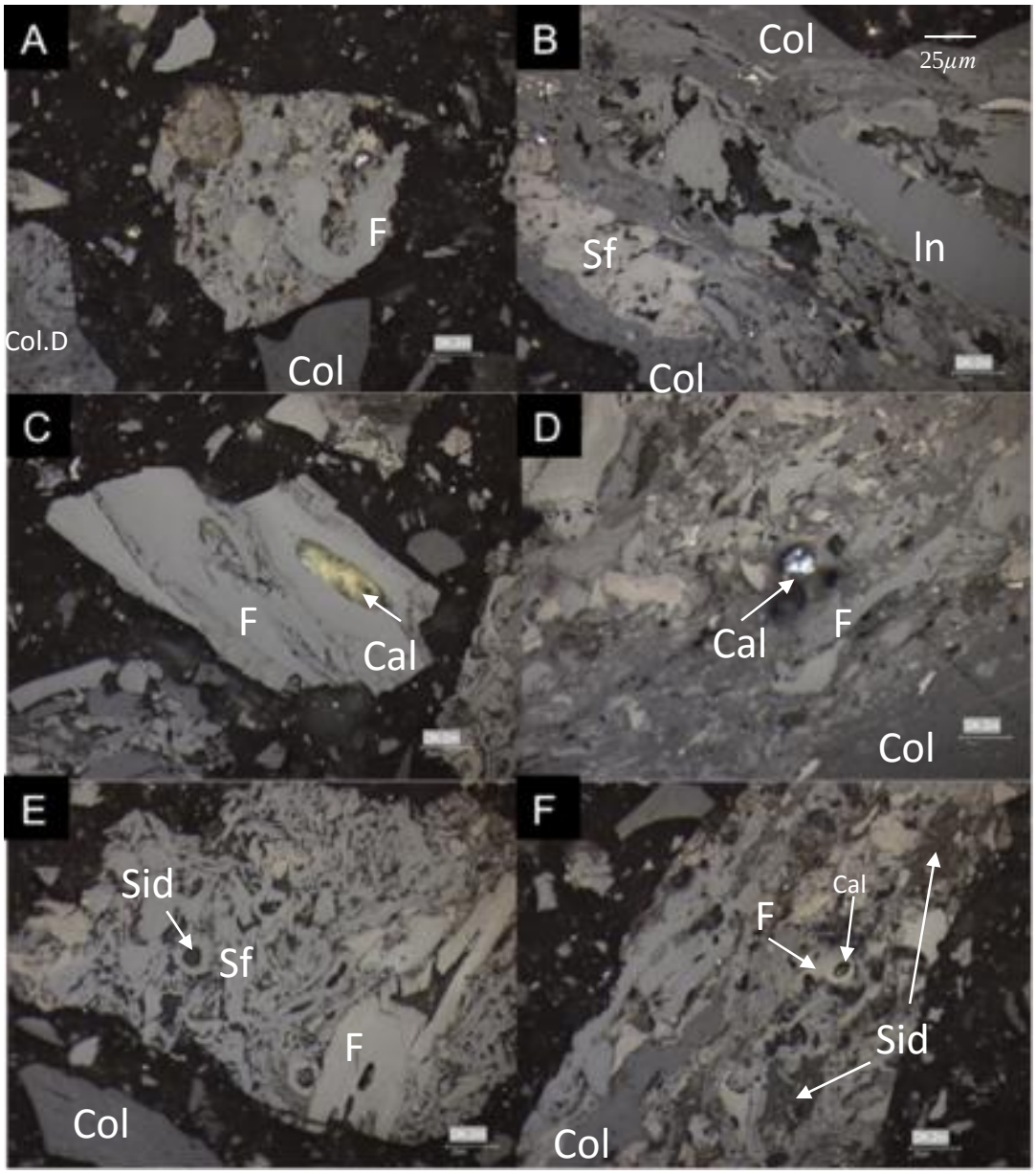

Figure 30: Photomicrographs of sample DK 2 at 2 m from the dolerite intrusion. Calcite (Cal), Collotelinite (Col), Inertodetrinite (In), Semifusinite (Sf), Siderite (Sid), Fusinite (F), Collodetrinite (Col.D).

The vitrinite reflectance analysis of the coal sample 3 m from the dyke intersection (Fig. 31) ranges between 0.6 and 1.05 with a mean value of 0.82 as noted in Table 6. In addition to this, the sample contains the highest levels of colltelinite in the transect at ~ 35%. In Figure 31A, a large collodetrinite maceral is host to ubiquitous siderite inclusions, and the areas hosting the inclusions are elongate pits. In Figure 31B, a semifusinite maceral plays host to both calcite and siderite inclusions; the siderite is present within the natural voids of the semifusinite maceral, whereas the angular calcite is present between a small inertodetrinite fragment and the main semifusinite maceral. The semifusinite and fusinite in Figure 31C are host to minor fractures, and the fusinite in 31C houses calcite within its structure. Figures 31D and E show the presence of pyrite within the sample, and it can be noted here

that the grains of pyrite are small rounded individual grains. Finally, Figure 31F displays a unaltered semifusinite maceral.

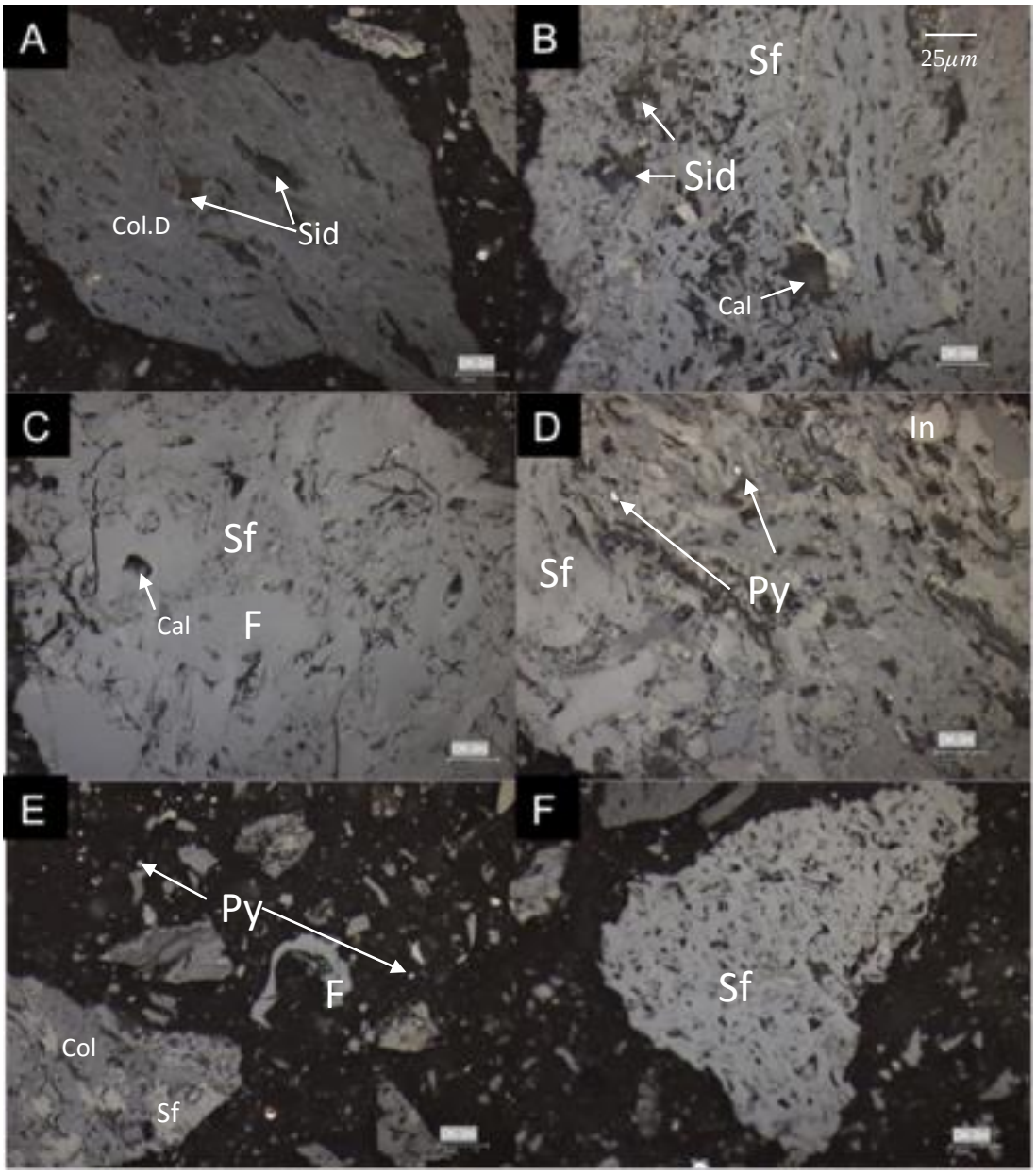

Figure 31: Photomicrographs of Sample DK 3 at 3 m from the dolerite intrusion. Calcite (Cal), Collotelinite (Col), Semifusinite (Sf), Siderite (Sid), Fusinite (F), Collodetrinite (Col.D) and (Py) Pyrite.

At a distance of 4 m from the intrusion (Figure 32), the mean vitrinite reflectance value remains elevated at 0.82 and ranges between 0.65 and 1 (Table 6). When examining the textural nature of the sample on micro scale, the representative photomicrographs in Figure 32 show mostly unaltered maceral amalgamations, such as seen in image 32A where both fusinite and semifusinite are unaltered. However, Figure 32B provides an example of elongate siderite infilling within the collodetrinite maceral, where the maceral also has small pits on its surface similar to that found in the collotelinite of

sample DK 2 (Figure 30). These pits have once again not developed into devolatilization vacuoles. Figure 32C shows siderite mineralization within the voids between the semifusinite and inertodetrinite maceral assemblages. The assemblage of semifusinite and collotelinite seen in Figure 32D is unaltered, with small rounded inclusions of calcite within the structure. The siderite in Figure 32E is amorphous with undefined edges within the semifusinite, and is accompanied by what appear to be fragments of fusinite. Figure 32F shows a collodetrinite maceral flanked by fusinite, where again the fusinite hosts a calcite inclusion.

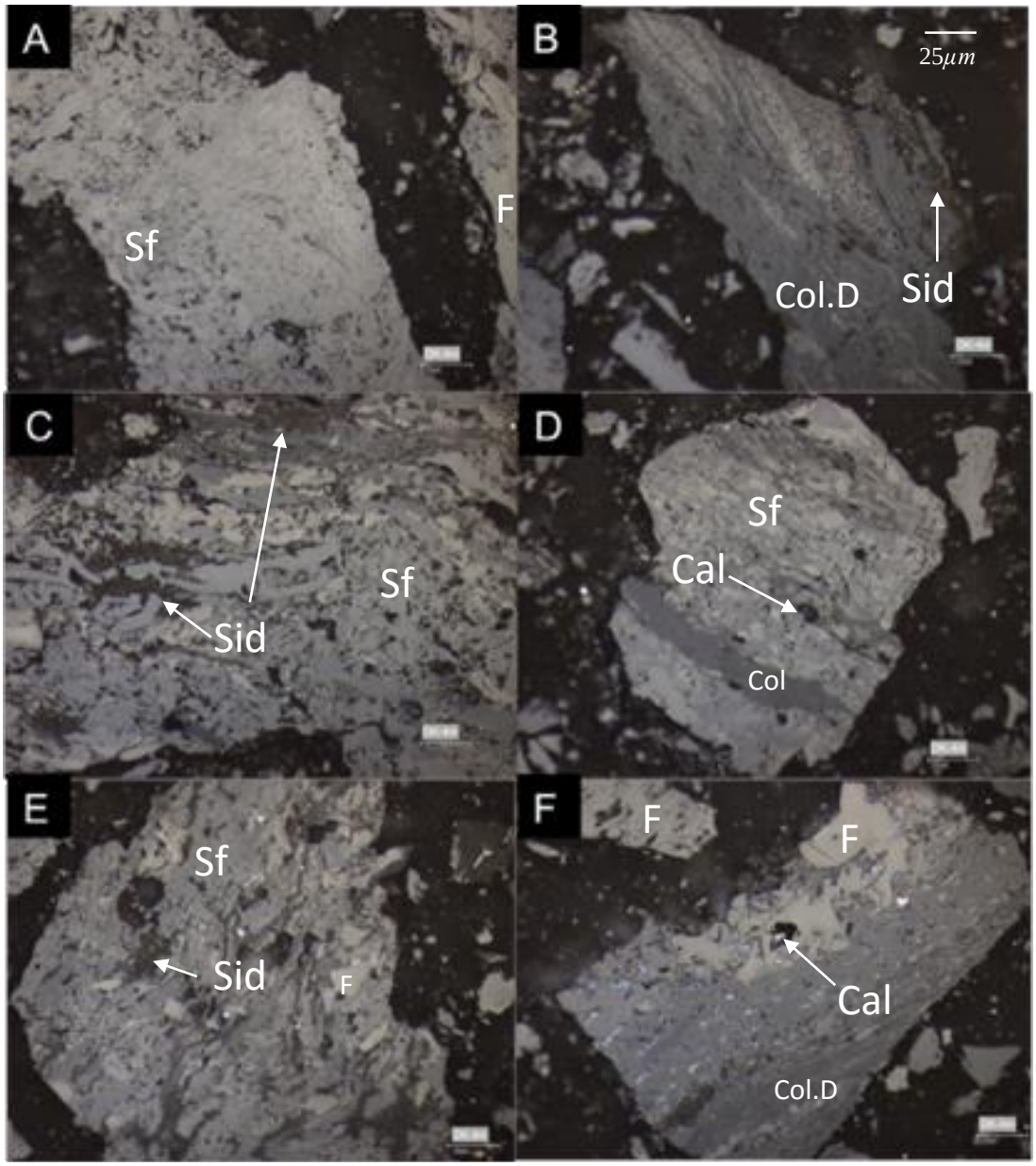

Figure 32: Photomicrographs of Sample DK 4 at 4 m from the dolerite intrusion. Calcite (Cal), Collotelinite (Col), Semifusinite (Sf), Siderite (Sid), Fusinite (F), Collodetrinite (Col.D)

Sample DK 5, as displayed in Figure 33, shows less evidence of thermal influence than the previous samples, and has a mean vitrinite reflectance value of 0.76 and a range of reflectance between 0.5 and 0.95 (Table 6). Looking at the textural nature of the particles at 5 m from the intrusion, Figure 33A shows a smooth surfaced collotelinite, with minor fracturing. Figure 33B, however, displays more altered collotelinite and collodetrinite macerals, both displaying pitted textures on their surface, with collodetrinite hosting fine-grained siderite inclusions. The semifusinite in Figure 33C is host to a large calcite inclusion as well as siderite which is amorphous in texture. The fusinite in Figure 33C hosts siderite within the gaps between maceral fragments, which is similarly displayed in Figure 33E. Figures 33D and F both show the presence of fine grains of pyrite. The collotelinite in 33D has some surface alteration similar to that noted in Figure 33A.

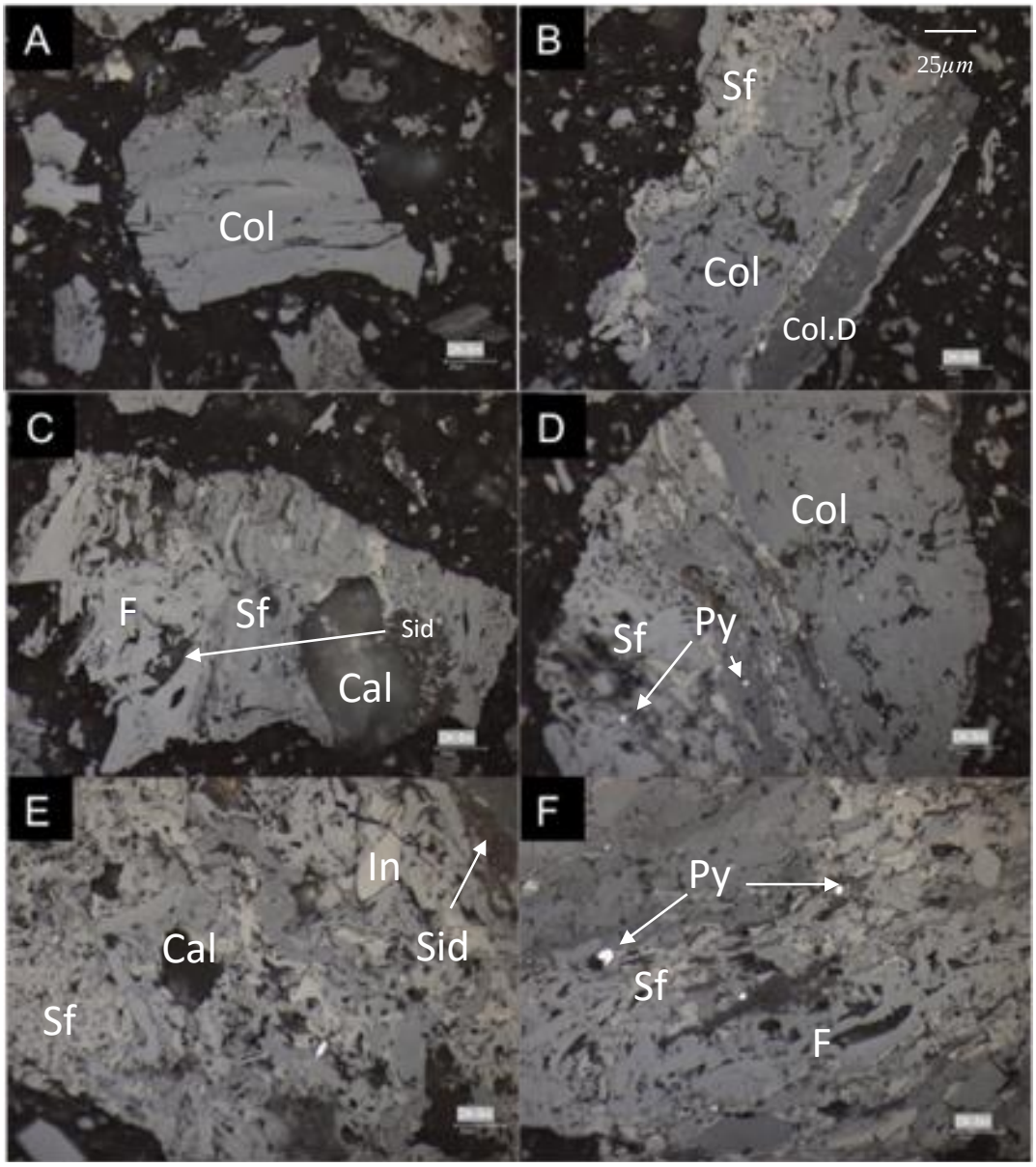

Figure 33: Photomicrographs of Sample DK 5 at 5 m from the dolerite intrusion. Calcite (Cal), Collotelinite (Col), Inertodetrinite (In), Semifusinite (Sf), Siderite (Sid), Fusinite (F), Collodetrinite (Col.D), (Py) Pyrite.

At 6 m from the intrusion (DK 6), the mean vitrinite reflectance has a value of 0.76 within a range of 0.55 and 0.95 (Table 6). Figure 34 shows a pitted texture in the collotelinite and collodetrinite macerals in images A, B, E and F. The collotelinite in Figure 34A hosts pyrite grains within the majority of the pits, and pyrite can be noted within the semifusinite bordering the collotelinite. Figure 34D displays well-formed semifusinite with amorphous siderite inclusions.

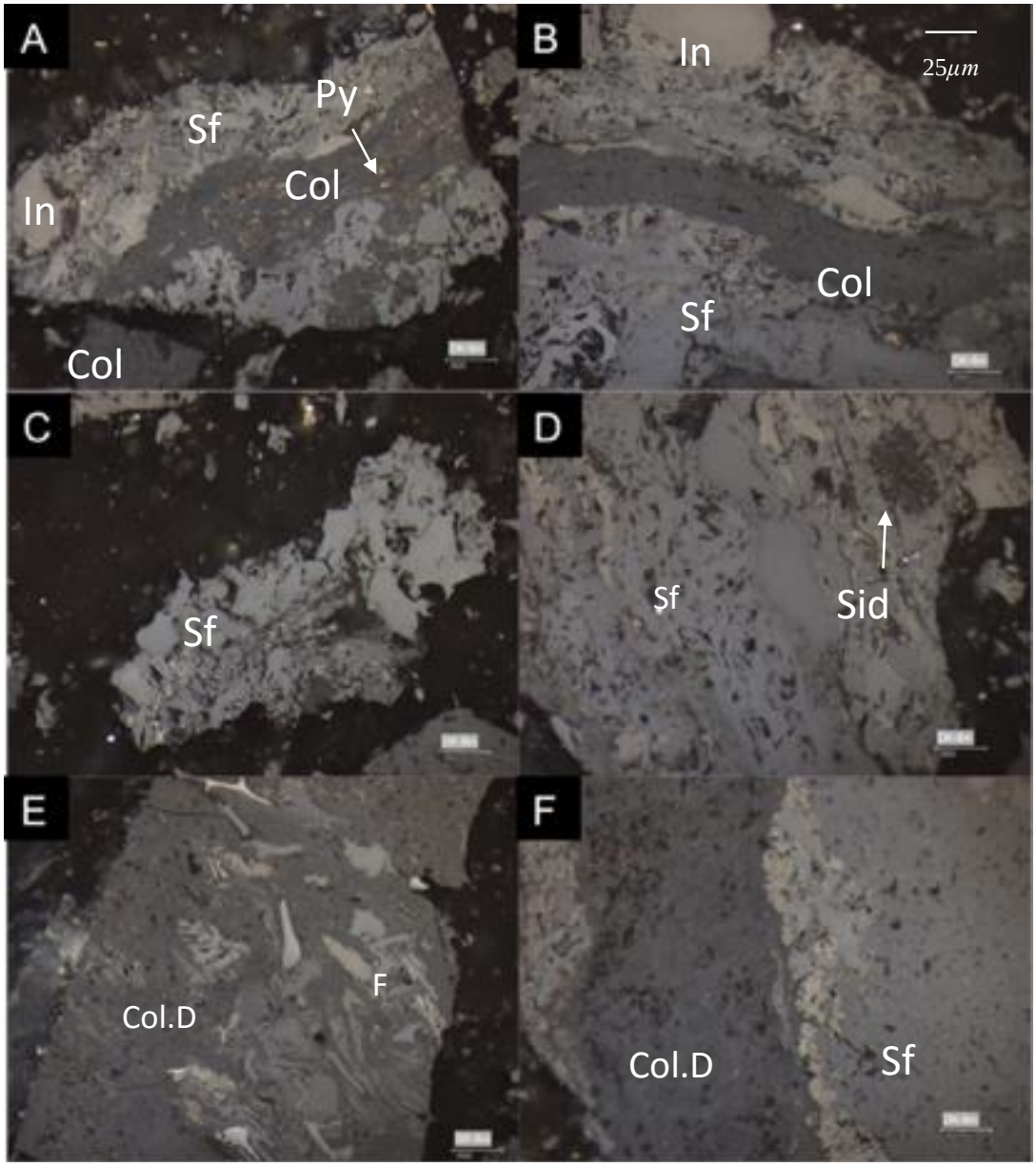

Figure 34: Photomicrographs of Sample DK 6 at 6 m from the dolerite intrusion. Pyrite (Py), Collotelinite (Col), Inertodetrinite (In), Semifusinite (Sf), Siderite (Sid), Fusinite (F), Collodetrinite (Col.D).

At 7 m from the intrusion (DK7), the mean vitrinite reflectance drops to 0.68 within a range of 0.5 and 0.9 (Table 6). The fusinite and semifusinite in Figures 35A, D and F are unaltered and well-formed, and Figures 35C and E show the inclusion of siderite within the structure of the semifusinite. There is visible siderite infill within the pitted texture of collodetrinite in Figure 35C, which contrasts to the

collotelinite of both Figures 35B and C, which show no surface alteration. Noteworthy is the large pyrite grain in the base of Figure 35F, the first instance in the transect that pyrite occurs in such large grains.

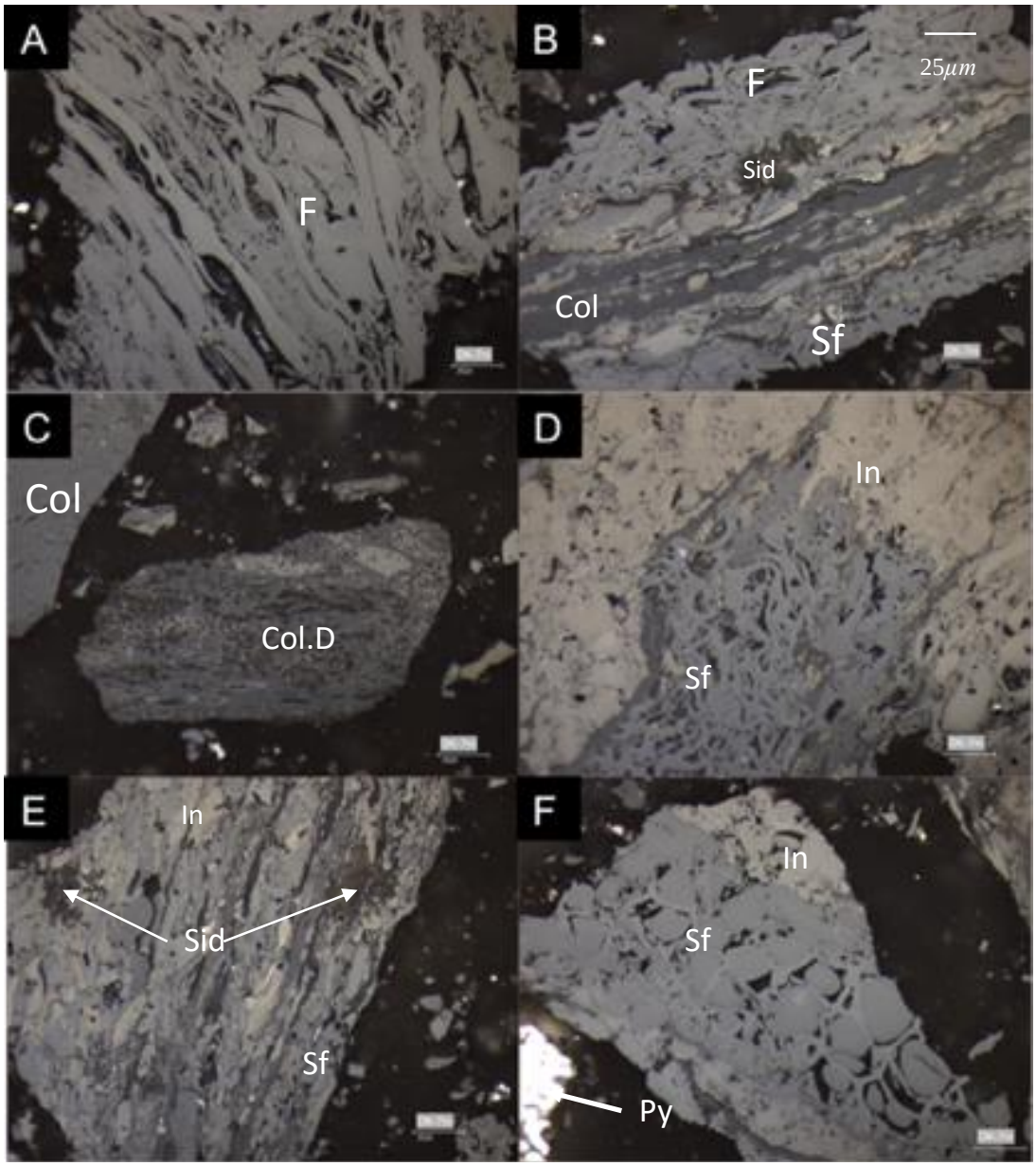

Figure 35: Photomicrographs of Sample DK 7 at 7 m from the dolerite intrusion. Collotelinite (Col), Inertodetrinite (In), Semifusinite (Sf), Siderite (Sid), Fusinite (F), Collodetrinite (Col.D).

At 8 m from the dolerite intrusion (DK 8), the mean vitrinite reflectance value is 0.78, within a range of 0.6 and 0.95, as seen in Table 6. Noteworthy from Table 6 is the large increase in inertodetrinite within the sample, making up ~60 % of the material. On a textural basis, Figure 36 displays inertodetrinite housing both calcite and pyrite inclusions, as seen in images A, B and D. The semifusinite in Figures 36C and F are unaltered, and the collodetrinite in 36E has ubiquitous siderite inclusions.

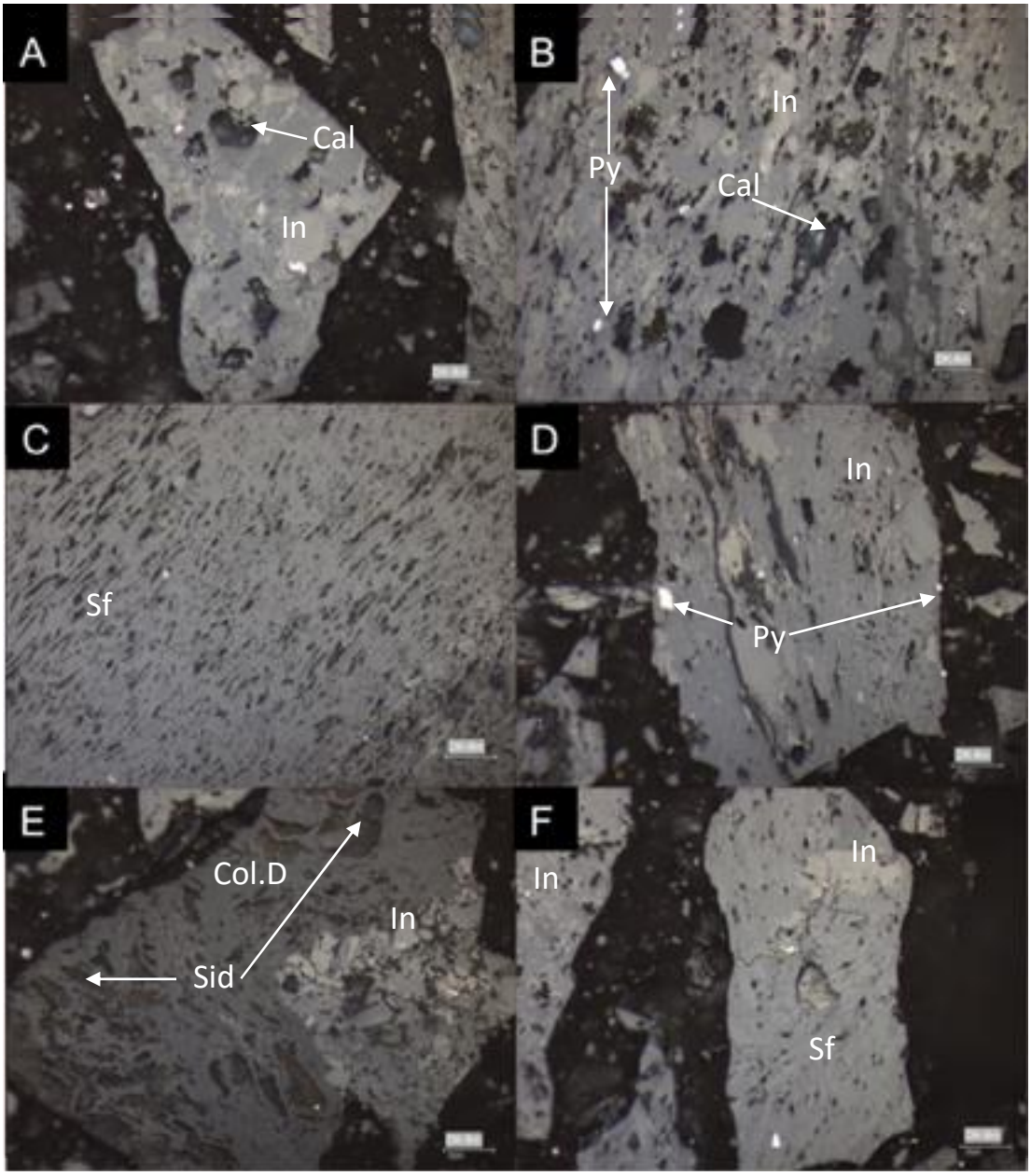

Figure 36: Photomicrographs of Sample DK 8 at 8 m from the dolerite intrusion. Calcite (Cal), Collotelinite (Col), Inertodetrinite (In), Semifusinite (Sf), Siderite (Sid), Collodetrinite (Col.D).

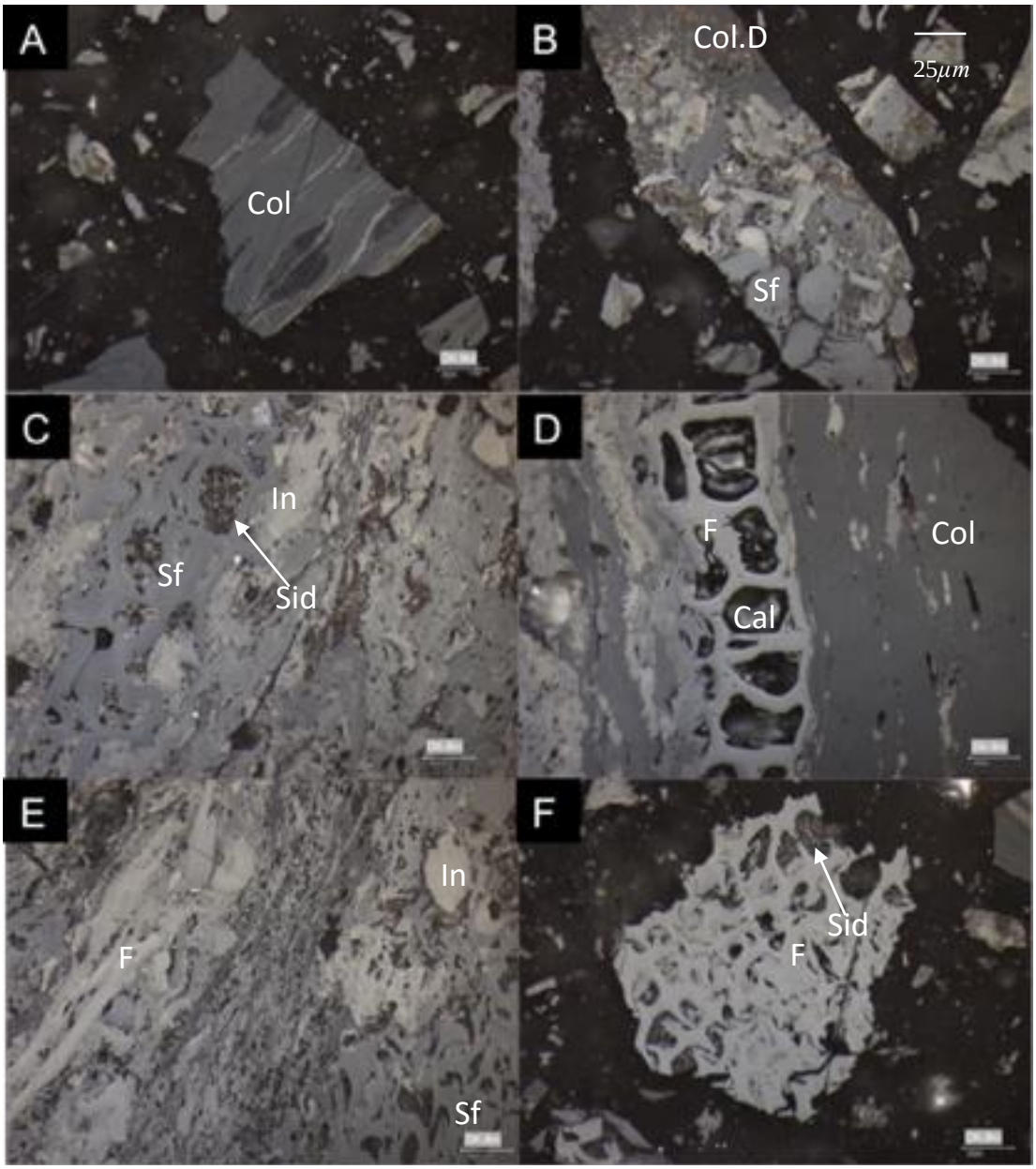

Figure 37: Photomicrographs of Sample DK 9 at 9 m from the dolerite intrusion. Calcite (Cal), Collotelinite (Col), Inertodetrinite (In), Semifusinite (Sf), Siderite (Sid), Fusinite (F).

The vitrinite reflectance analysis at 9 m (DK 9) has a range of 0.55 and 0.85, with a mean of 0.69 (Table 6). From a micro-textural perspective, Figure 37A displays an unaltered collotelinite maceral. The maceral assemblage in Figure 37B displays fine-grained inclusions of siderite in the collodetrinite, similar to that seen in sample DK 6. The complex assemblages in Figures 37C and E show semifusinite, fusinite and inertodetrinite with amorphous inclusions of siderite throughout. Prominent calcite grains can be seen in Figure 37D, housed within the fusinite maceral, and similarly, siderite is housed in the fusinite in Figure 37F.

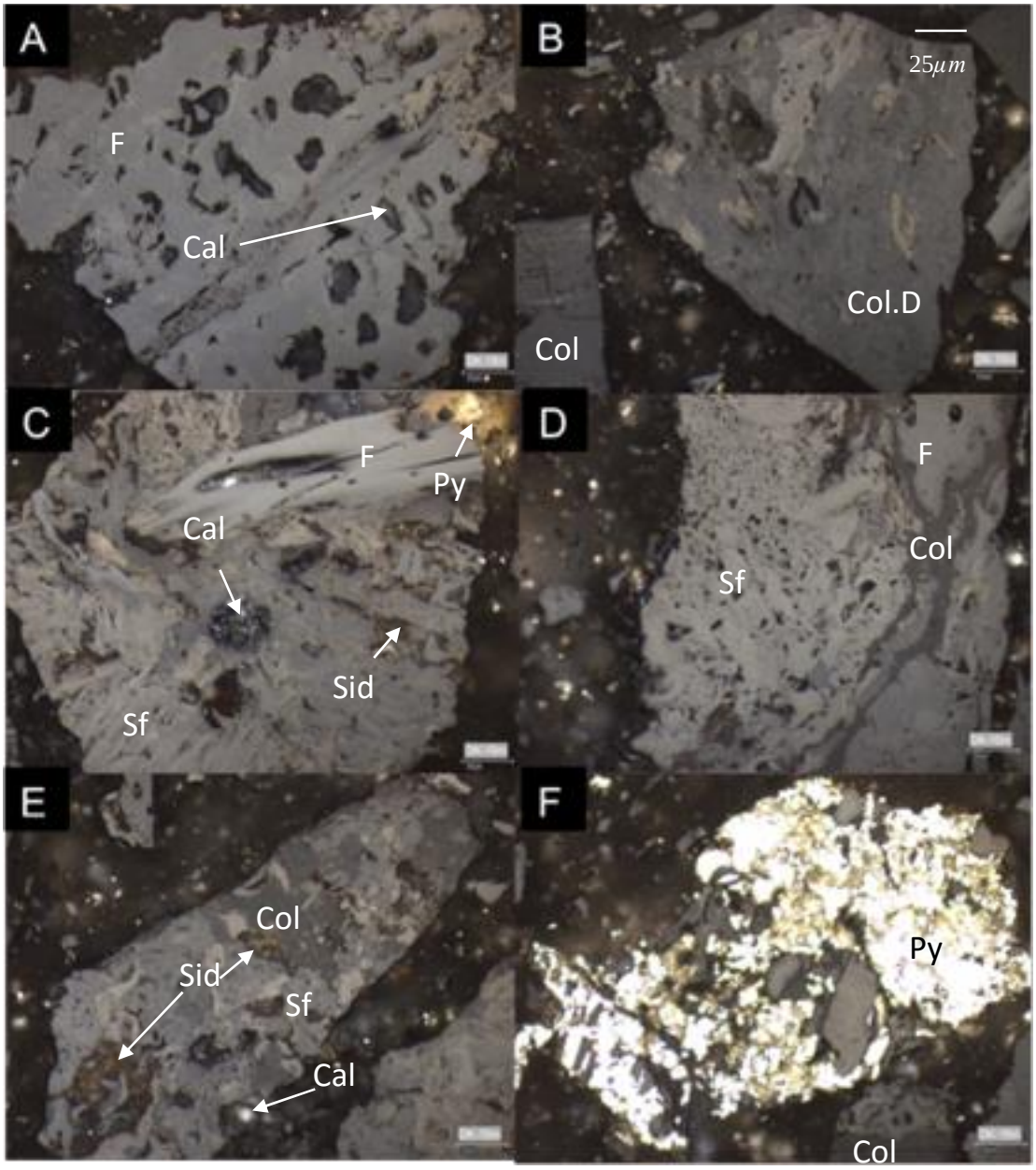

Figure 38: Photomicrographs of Sample DK 10 at 10 m from the dolerite intrusion. Calcite (Cal), Collotelinite (Col), Inertodetrinite (In), Semifusinite (Sf), Siderite (Sid), Fusinite (F), Collodetrinite (Col.D), (Py) Pyrite.

The vitrinite reflectance analysis at 10 m from the dolerite intersection (DK 10), has a mean value of 0.68 with a range of 0.5 and 0.85. Table 6 further indicates an elevated presence of collotelinite within the sample, as well as the second highest abundance of sulphides along the transect at ~ 11%. Looking at the sample on a micro-scale, Figure 38A displays a large fusinite maceral hosting calcite inclusions. Figure 38B displays both collodetrinite and collotelinite macerals, with the latter showing some fine-grained inclusions of siderite. The assemblage in Figure 38C displays semifusinite and fusinite hosting both calcite and siderite inclusions; in this instance both the siderite and calcite are amorphous in structure, similar siderite and calcite mineralization can be noted in Figure 38E. The pyrite grains in

Figures 38C and F display the duality of pyrite within the sample, appearing as both fine grains as well as large assemblages. Figure 38D is an unaltered assemblage of semifusinite, fusinite and collotelinite macerals.

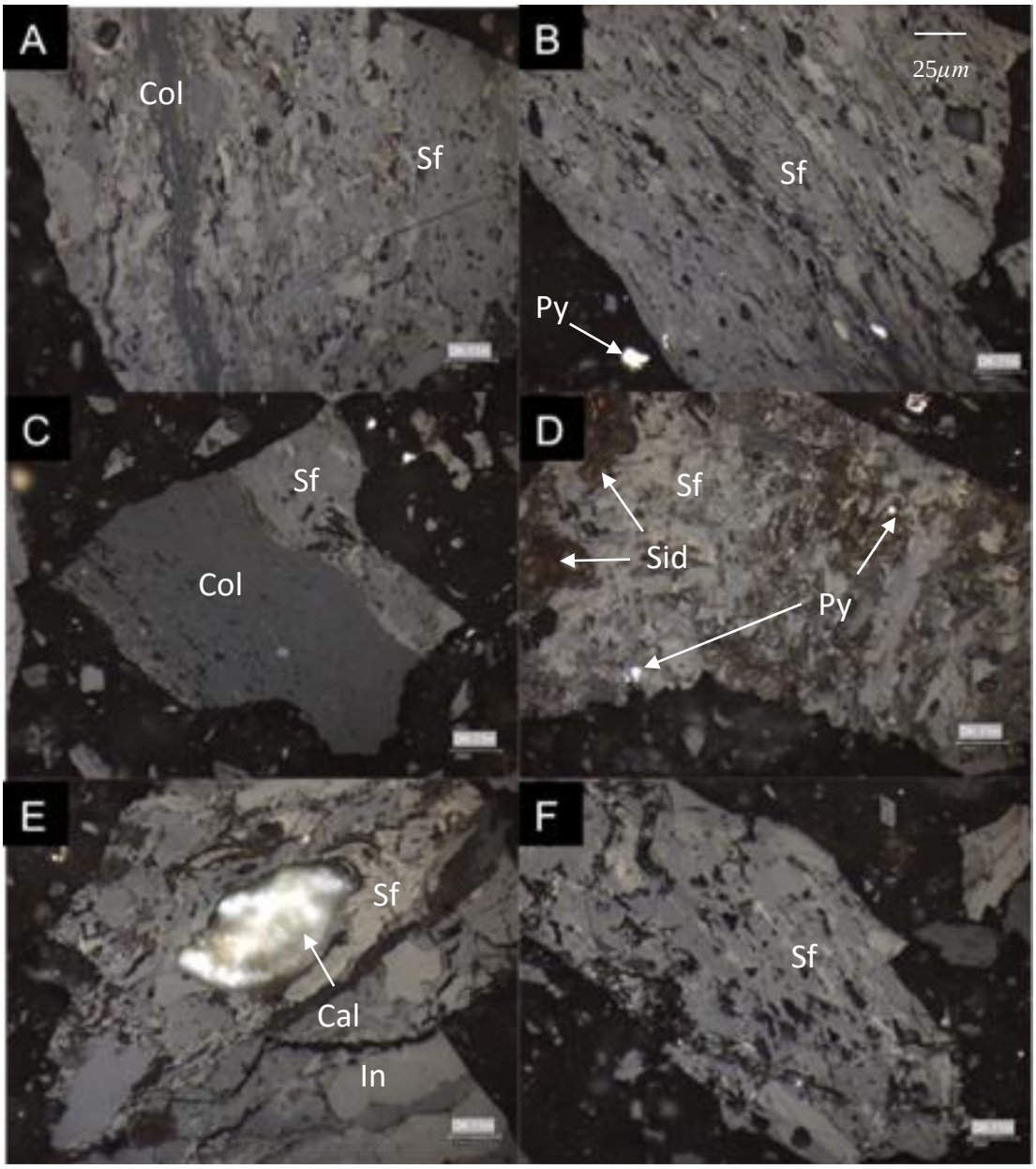

Figure 39: Photomicrographs of Sample DK 11 at 11 m from the dolerite intrusion. Calcite (Cal), Collotelinite (Col), Inertodetrinite (In), Semifusinite (Sf), Siderite (Sid), Fusinite (F), Pyrite(Py).

The vitrinite reflectance at 11 m from the dolerite intrusion (DK 11) has a mean of 0.69 within a range of 0.55 and 0.85 (Table 6). In Figures 39B, D and E, mineral matter hosted within semifusinite has 3 distinctive forms: large rounded grains, amorphous inclusions and small rounded grains. These forms represent calcite, siderite and pyrite respectively. The maceral content in the sample is mostly unaltered, with Figure 39C providing an example of a semifusinite and collotelinite assemblage which displays only minor pits within the collotelinite. Figure 39A provides more complex assemblages of

semifusinite and collotelinite, but again displays no major structural alteration, this is mirrored in image F with a large semifusinite grain.

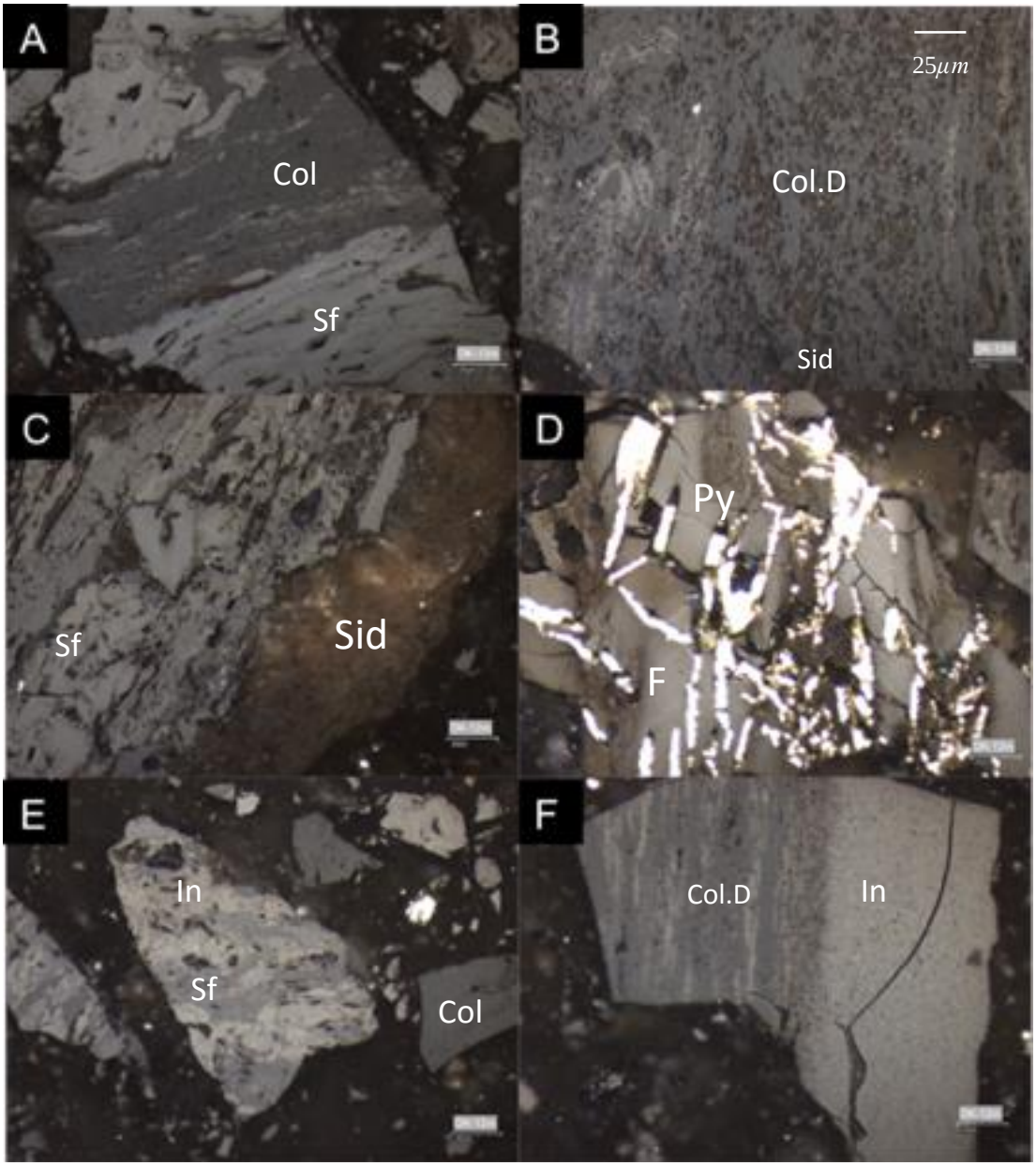

Figure 40: Photomicrographs of Sample DK 12 at 12 m from the dolerite intrusion. (Collotelinite (Col), Inertodetrinite (In), Semifusinite (Sf), Siderite (Sid), Fusinite (F), Collodetrinite (Col.D), Pyrite (Py).

The vitrinite reflectance data at 12 m from the intrusion (DK12) has a mean reflectance of 0.68 within a range of 0.5 and 0.85 (Table 6). The representative images within Figure 40 show the large concentration of sulphide and siderite mineral material within the sample, as seen in images C and D., while the siderite of image B is hosted as fine grains within the collodetrinite. Figure 40C shows a large siderite grain flanking the semifusinite. This is uncommon within the transact, as up until this point siderite mineralization has taken the form of fine amorphous grains akin to that seen in Figure 40B. Similarly the pyrite seen in Figure 40D has an elongate structure, forming along the boundaries of the

fusinite maceral. Figures 40A, E and F show well-formed macerals with little alteration, other than a fracture within the inertodetrinite of image F.

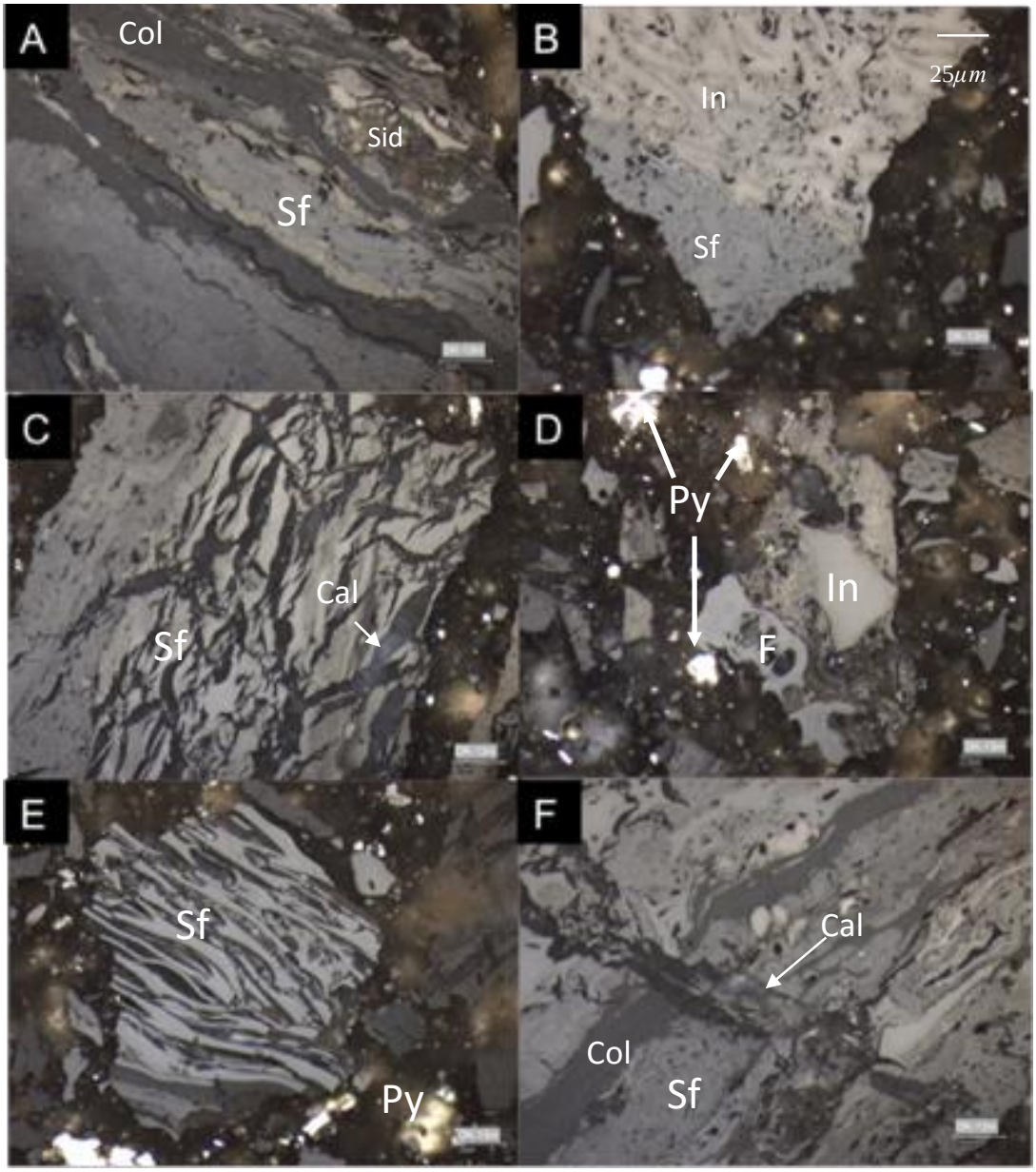

Figure 41: Photomicrographs of Sample DK 13 at 13 m from the dolerite intrusion. Collotelinite (Col), Inertodetrinite (In), Semifusinite (Sf), Fusinite (F), Pyrite (Py).

In Table 6 the vitrinite reflectance at 13 m (DK 13) from the dolerite intersection has a range of 0.5 to 0.9, with a mean value of 0.66. In addition, there is also an increased presence of collotelinite at a value of ~19% as well as the highest concentration of sulfides at ~12%. Of specific interest here are Figures 41C and F, in which calcite is present within angular fractures. Within image F, the calcite filled fracture runs perpendicular to the collotelinite and semifusinite assemblage, while in image C the fracturing is much more irregular in its orientation. Texturally the semifusinite, collotelinite and inertodetrinite of

Figures 41A, B, D and F are very regular, apart from a siderite inclusion in image A. Throughout the sample small pyrite grains are visible.

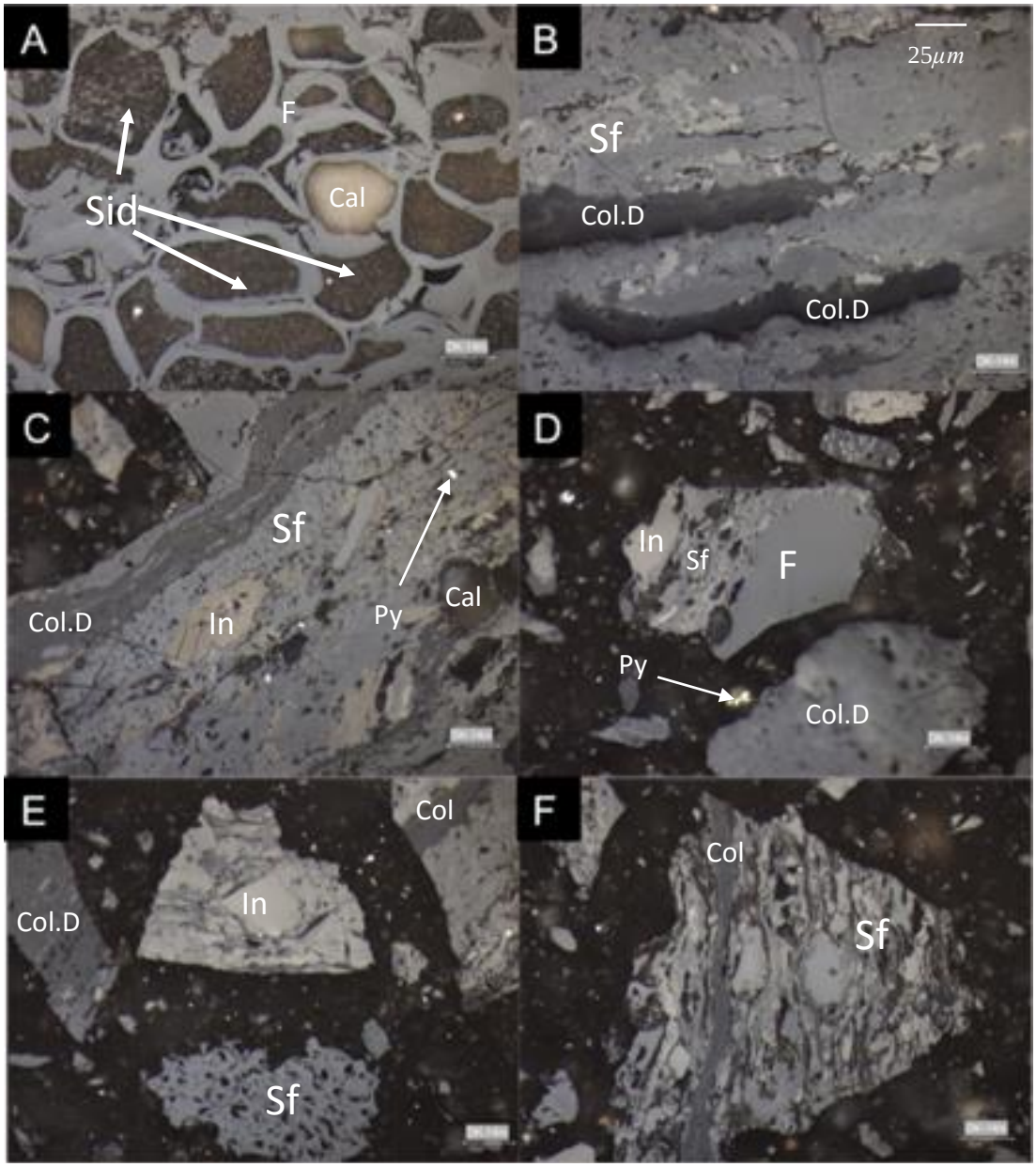

Figure 42: Photomicrographs of Sample DK 14 at 14 m from the dolerite intrusion. Collotelinite (Col), Inertodetrinite (In), Semifusinite (Sf), Siderite (Sid), Fusinite (F), Collodetrinite (Col.D).

The vitrinite reflectance at 14 m from the dolerite intrusion (DK 14) falls within a range of 0.5 to 0.85, with a mean of 0.68 as noted in Table 6. Figure 42A provides an example of large siderite and calcite inclusions within the fusinite. The assemblage in Figure 42B is of unaltered semifusinite and collodetrinite, which is texturally similar to macerals in Figures 42D and E. The collodetrinite, semifusinite and inertodetrinite assemblage in Figure 42C is host to fine grains of pyrite and a rounded calcite grain, and minor fracturing in the semifusinite is also noted. Figure 42F shows a maceral assemblage with alternating collotelinite and semifusinite, both without any signs of alteration.

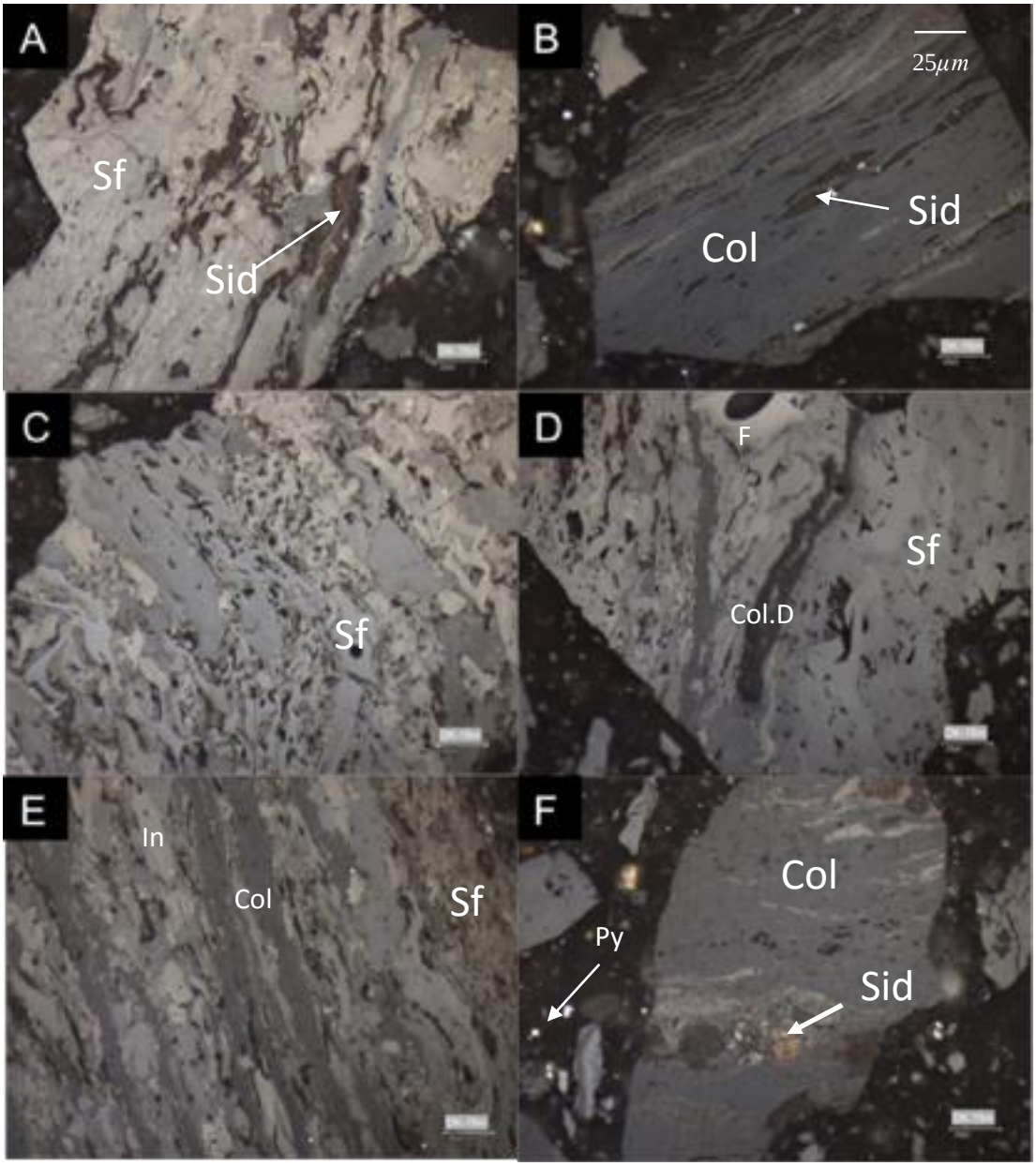

Figure 43: Photomicrographs of Sample DK 15 at 15 m from the dolerite intrusion. Collotelinite (Col), Inertodetrinite (In), Semifusinite (Sf), Siderite (Sid).

At a distance of 15 m from the intrusion (DK 15) the mean vitrinite reflectance value is 0.67, within a range of 0.45 and 0.85 (Table 6). Siderite presents itself as the prominent mineral inclusion of the sample, as can be noted in Figures 43A, B and F. The siderite in the sample is primarily amorphous and is present within the structural features of both semifusinite and collotelinite in Figures 43A and B respectively. However, in Figure 43F the siderite inclusion is more rounded and does not align with the structural features of the host collotelinite maceral. This could imply that the generation of the siderite in Figure 43F predates or is syn-genetic to the coalification of the collotelinite maceral, whereas the siderite in Figures 43A and B precipitated post formation of the host macerals. Figures 43C, D and E provide examples of the mostly unaltered nature of the sample.

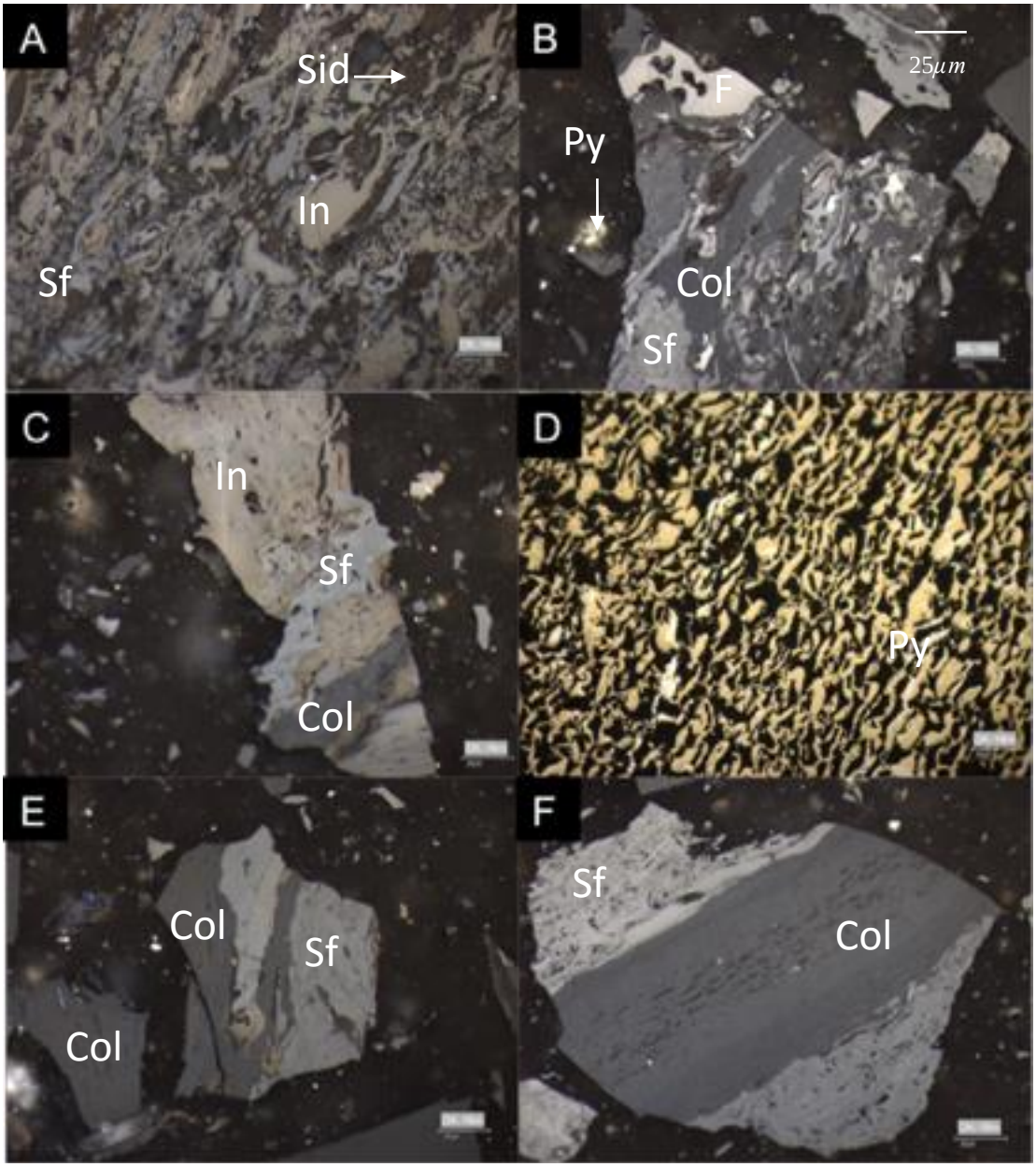

Figure 44: Photomicrographs of Sample DK 16 at 16 m from the dolerite intrusion. Pyrite (Py), Collotelinite (Col), Inertodetrinite (In), Semifusinite (Sf), (F) Fusinite

The vitrinite reflectance at 16 m from the dyke intersection (DK16) has a mean reflectance value of 0.66 within a range of 0.45 to 0.8 (Table 6). Figure 44A provides an example of a complex semifusinite, inertodetrinite and siderite assemblage, in which the semifusinite and inertodetrinite are fragmented, with the siderite included in the areas between fragments. This is in stark contrast to the well-formed collotelinite, semifusinite and inertodetrinite in Figures 44C, E and F. The large pyrite assemblage in Figure 44D display a greater concentration of pyrite mineralization than the previous example noted in sample DK 10 (Fig. 38) as well as a vastly different texture. Figure 44B provides an amalgamation of semifusinite, collotelinite and fusinite, with some fragments of fusinite interbedded with collotelinite.

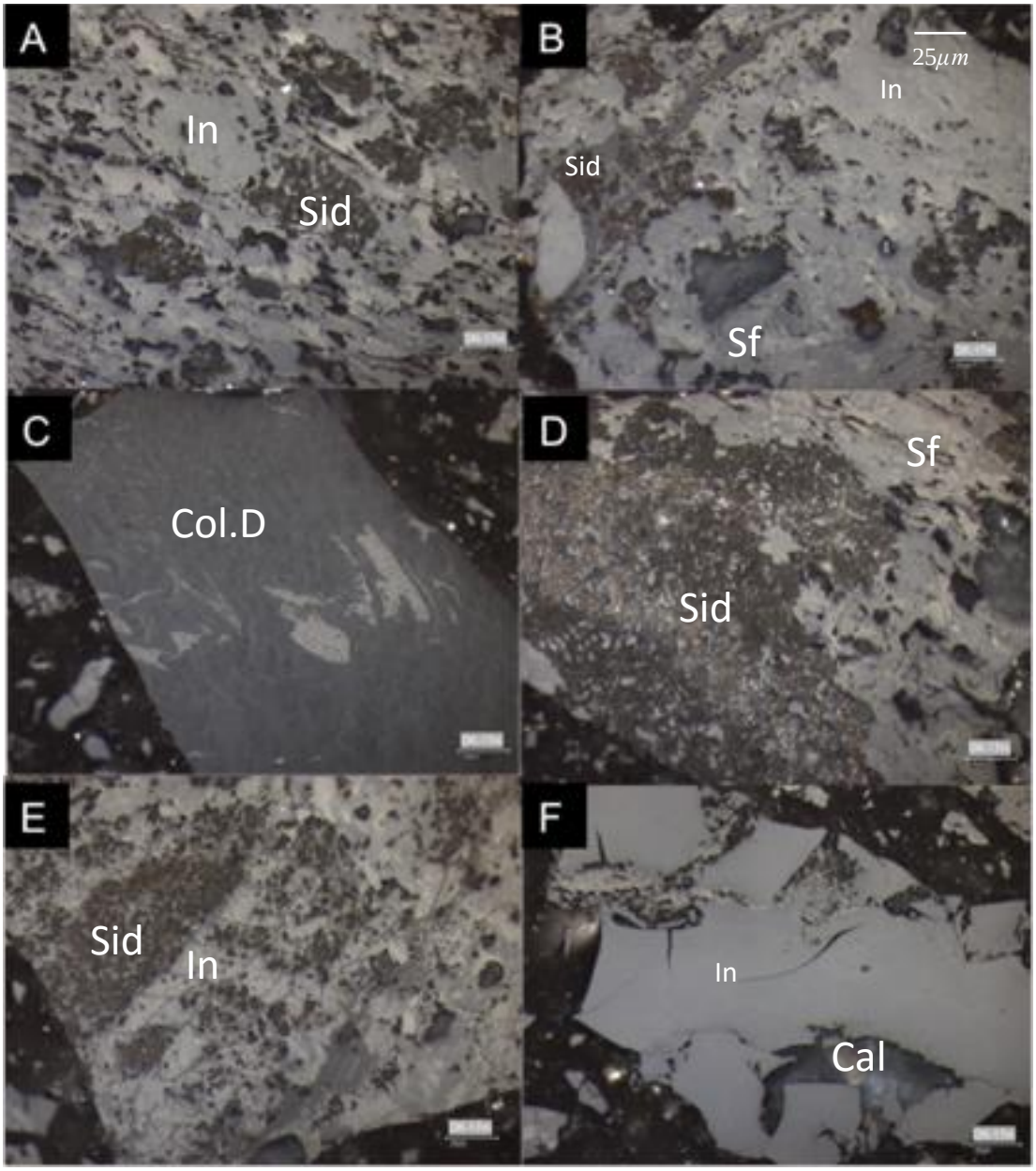

Figure 45: Photomicrographs of Sample DK 17 at 17 m from the dolerite intrusion. Calcite (Cal), Inertodetrinite (In), Semifusinite (Sf), Siderite (Sid), Collodetrinite (Col.D).

Advancing to 17 m from the intrusion (DK 17), the vitrinite reflectance data from Table 6 indicates a mean value of 0.73 in a range of 0.55 to 0.95. The representative photomicrographs of Figure 45, display siderite as a primary mineral inclusion in images A, B, D and E. Within Figures 45A and B, the siderite is included in the structure of the inertodetrinite and semifusinite, whereas in Figures 45D and E the siderite is more pervasive and occupies more of the semifusinite maceral's structure. A large calcite inclusion in Figure 45F is housed within an unaltered inertodetrinite. The collodetrinite in this sampe does not house any mineral inclusions in its uniform unaltered structure as seen in image C. It follows that the siderite mineralization of this sample has preference for the natural zone of weakness within the maceral hosts, implying that its formation is secondary to the maceral itself.

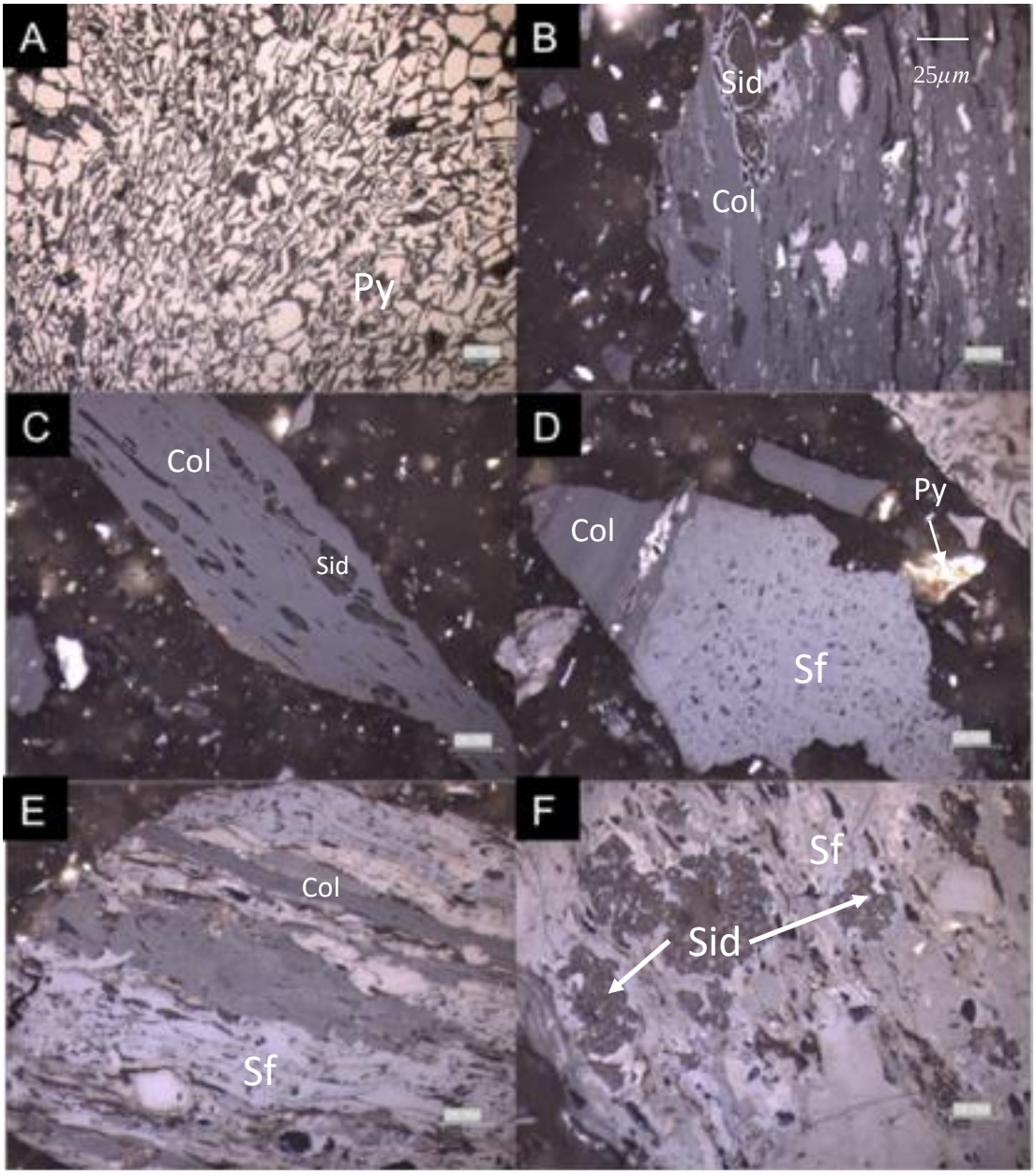

Figure 46: Photomicrographs of Sample DK 18 at 18 m from the dolerite intrusion. Collotelinite (Col), Semifusinite (Sf), Siderite (Sid).

At a distance of 18 m from the intrusion (DK 18), the mean vitrinite reflectance value is 0.64, with a range of values between 0.5 and 0.85 (Table 6). Figure 46A once again shows a large amalgamation of pyrite similar to that seen in samples DK10 and DK 16, but in this example the pyrite shows much less included maceral content than both DK 10 and 16. The collotelinite in Figures 46B and C is host to siderite inclusions within elongate pits within the maceral; in contrast the siderite inclusion in Figure 46F is structurally similar to that noted in Figures 45D and E. Figure 46D displays unaltered collotelinite and semifusinite with a small pyrite grain adjacent to this assemblage, and similarly the maceral assemblage in Figure 46E is well formed with no signs of alteration.

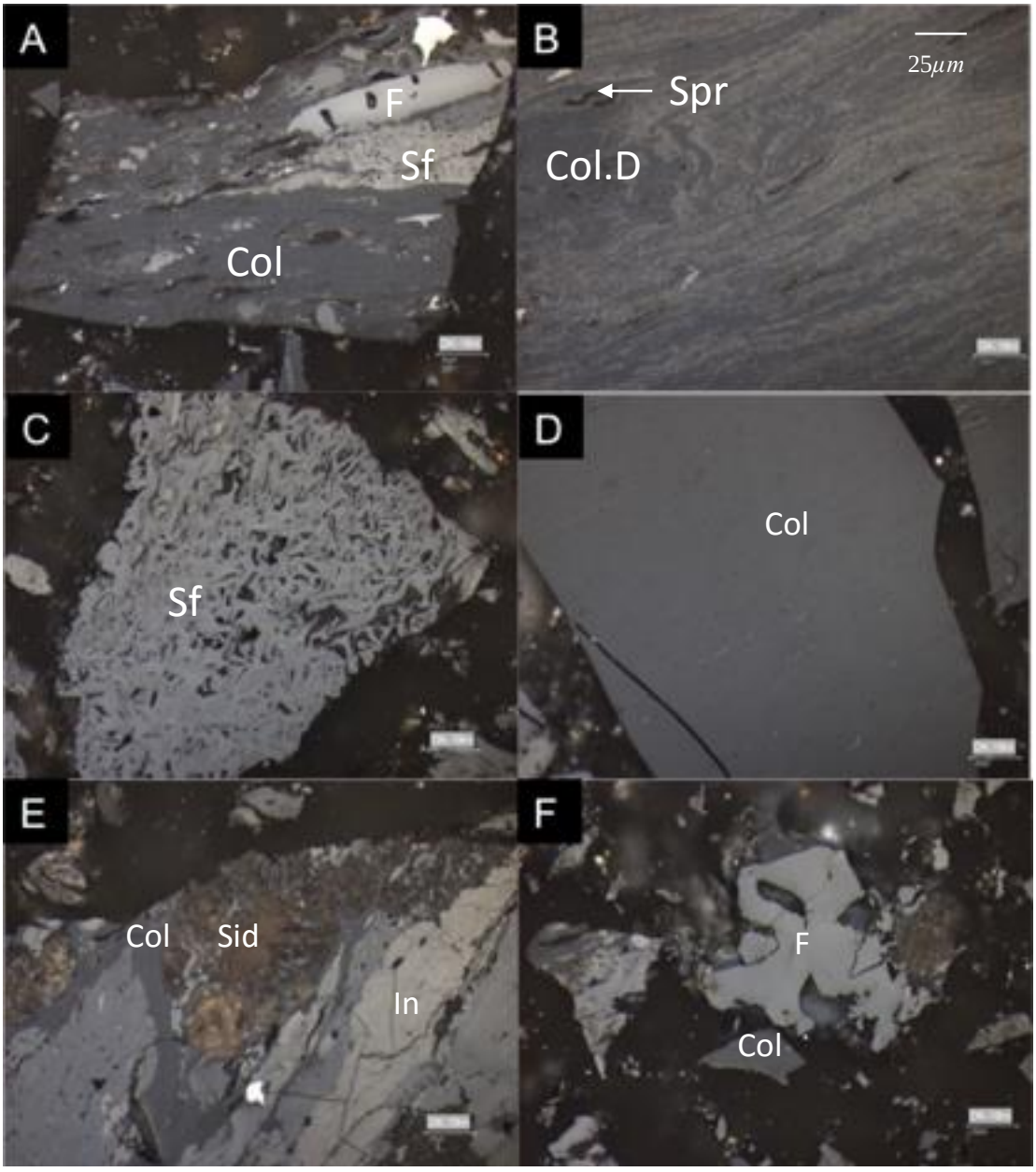

Figure 47: Photomicrographs of Sample DK 19 at 19 m from the dolerite intrusion. Collotelinite (Col), Inertodetrinite (In), Semifusinite (Sf), Siderite (Sid), Fusinite (F), Collodetrinite (Col.D), Sporinite (Spr).

At a distance of 19 m from the dolerite intrusion (DK 19), the vitrinite reflectance from Table 6 has a range of values between 0.45 and 0.85 with a mean value of 0.64. Figure 47 generally displays unaltered macerals, and Figures 47C and D specifically show collotelinite and semifusinite with no signs of alteration. The unaltered assemblages in Figures 47A and F consist of collotelinite with fragments of fusinite and semifusinite, whereas Figure 47E houses a large siderite inclusion with similar features to those identified in samples DK 17 and 18 (Figures 45 and 46). The collodetrinite in Figure 47B is well-formed and houses a small sporinite maceral. Overall the macerals in this sample were mostly unaltered with only minor carbonate inclusions.

6.3. Summary discussion

Petrographically, the sampled area shows only minor macro-scale evidence for thermal influence. When the reflectance and maceral group data is analysed (Table 6), more prominent evidence is identified. As noted from Figure 27 the mean vitrinite reflectance values are at their peak within 5 meters of the dolerite intrusion with a range of 0.82-1.24, but beyond 5 meters this value does not surpass 0.78.

The mean reflectance values are plotted in Figure 48, showing the peak values within 5 meters of the intrusion and clearly displaying the downward trend when moving further from the dolerite dyke. In addition, Figure 48 displays two spikes in mean vitrinite reflectance measured at 8 and 17 m; these values still do not exceed those noted within 5 meters of the intrusion. The samples DK 8 and 15 are unique in that they house the highest occurences of inertodetrinite anywhere in the transect, which may have influenced the reflectance analysis calibration as the standard deviation at these points is also elevated.

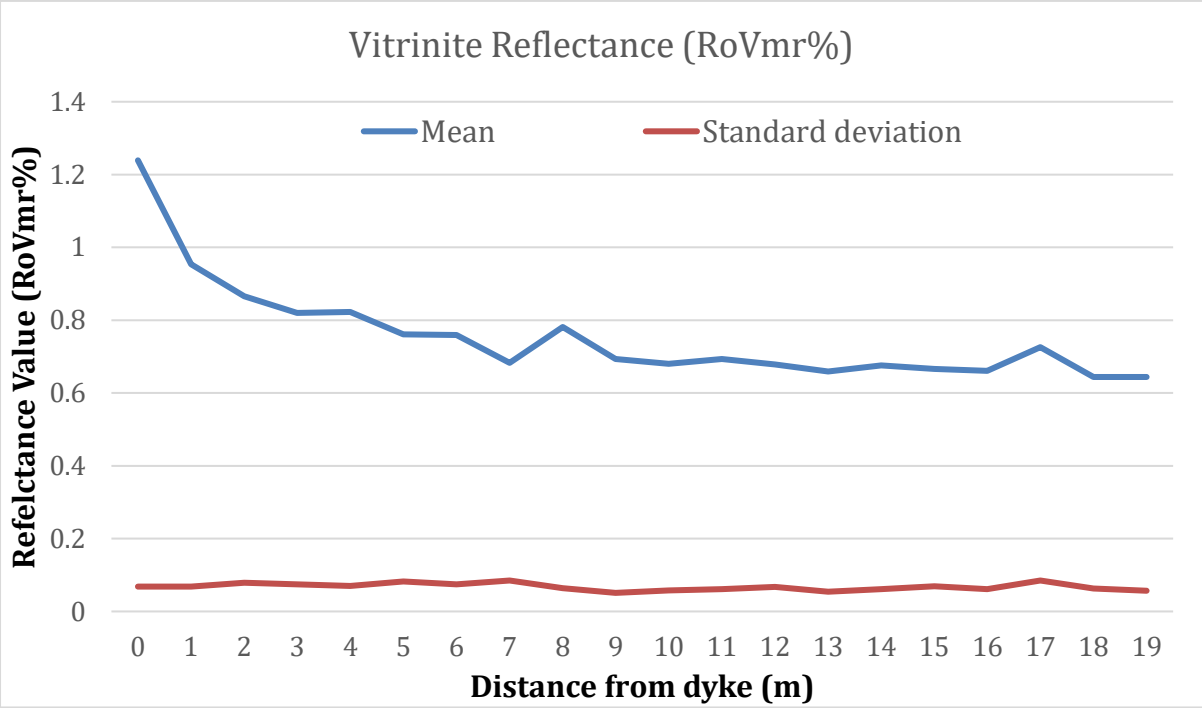

Figure 48: Total vitrinite reflectance central tendency values across sampled area.

Within the representative photomicrographs reviewed in this chapter, it is only in close proximity to the dolerite intrusion that devolitilzation vacuoles are clearly formed, with minor pitting being more prominent in the maceral assemblages. It must be noted that no coking of the vitrinite macerals has

taken place, and thus the temperatures are reduced within the conductive metamorphic aureole. If this is the case, drawing from Golab *et al. (*2007), it is reasonable to postulate that this reduction in temperature may be fluid-driven.

Petrographically, the samples show subtle variation when compared with directly adjacent samples, but there is a larger change over the full transect. The most prominent of these is the variability of texture, abundance and type of mineralization within the samples, specifically for the minerals siderite, calcite and pyrite:

- Siderite is noted throughout the transect, generally as a fine grained amorphous inclusion between maceral types or within textural features of macerals, such as pitting in collodetrinite macerals.
- The calcite mineralization is found in two main settings with the samples, firstly as a medium to large rounded inclusion, often associated with semifusinite, and secondly within the fibrous structure of fusinite (as shown in Figure 37D).
- Pyrite, is less common throughout the transect, but has three distinict morphologies within the sample area. The first of these is as small individual grains included within macerals, secondly it appears as large assemblages as seen in Figures 44 and 46. The third morphology is displayed in Figure 40, where the pyrite has formed within the fractures of a fusinite maceral.

The common feature of the mineralization is the association with secondary structural maceral features, namely fractures and pitting. These structural components can be derived from thermal influence and the mineralization can be directly ascribed to precipitation from fluids. This strengthens the case for fluid-driven convective temperature regulation.

When an overarching view of the microscopy across the 20 m transect is considered six groupings due to variations in texture, morphology and inorganic inclusions can be made:

1. From 0 to 2 m from the intrusion, high levels of fracturing of semifusinite macerals as well as devolatilization vacuoles are present within collotelinite macerals. It is plausible to assign these features to thermal effects of the igneous intrusion, due to the samples' proximity as well as the increased reflectance values noted in these samples.
2. From 3 to 5 m from the intrusion, the macerals show very little textural alteration or fracturing and much reduced vitrinite reflectance values. Siderite is more prevalent as a inclusion between maceral as well as within structural features, such as pitted texture within collodetrinite.
3. From 6 to 9 m from the intrusion, there is an increase in the pitted texture within collodetrinite macerals and a remarkable increase in visible siderite and calcite mineral inclusions.
4. At 10 m from the intrusion, the scale of the carbonate inclusions begins to increase as well as the first occurrence of large scale amalgamation of pyrite. The presence of pitted textures is all but gone; however fractures within macerals become more apparent, with these fractures being infilled by both calcite and pyrite. This persists up to 17 meters from the intrusion where the sample is devoid of sulphides.

5. At 18 m from the intrusion, sulphide are once again present in large amalgamations.
6. At 19 m from the intrusion, the macerals show no notable textural variations and is almost devoid of inorganic inclusions apart from occasional well formed siderite mineralization.

The six areas identified show a progression away from the dolerite of both mineral inclusions and textural variations. The fracturing and pitted textures near the dyke correlate with high vitrinite reflectance. As the mean vitrinite reflectance drops below 0.8, there is a shift to a more subtle pitted texture in vitrinite macerals. It is possible that this shows a decrease in the conductive effect of the dolerite intrusion on the coal. From 6 m onward, a noted influx of carbonate minerals and sulphides occurs with a lower degree of pitting of the vitrinite macerals. The reduction in pitting could again link to the reduction in conductive effect of the dyke due to the fluid driven convective temperature regulation.

CHAPTER 7: X-RAY TOMOGRAPHY OF COAL

Three-dimensional (3D) tomographic analysis was used to better understand the internal macro-structure of the coal samples. The technique allows for non-destructive analysis of the internal structure of the coal samples (Hoffman and De Beer, 2012). The application of 3D tomographic analysis to coal is not new and has been most frequently applied to the analysis of CO_2 sequestration and methane extraction potential of coal (Hoffman and De Beer, 2012). In addition, the ability of 3D tomography to detail the internal structure of coal and allow for accurate volumetric calculations has shown great potential in helping to understand *in situ* physical variations in coal (Hoffman and De Beer, 2012).

7.1. Methodology

The tomographic analysis of sample set A was performed at the South African Nuclear Energy Corporation (NECSA), where the samples were placed in the Nikon XTH 225 ST micro-focus X-ray tomography system. The system uses micro-focused X-rays to penetrate the sample; these X-rays are then detected and the data derived from the scan is then reconstructed into 3D images and processed using VG Studio Maxis software. The analysis was based on density differences between the organic, inorganic and pore spaces that then result in grey-scale variations in the processed tomographic imagery. From the imagery, volumetric and porosity calculations were done to identify the volumetric percentage of organic and inorganic constituents and pore spaces within the samples.

7.2. Results

The results of the tomographic volumetric analysis are displayed in Table 7, where the normative percentages of the measured values for mineral matter, pore space volume, and organic matter are displayed. Although 3D tomography is not yet able to distinguish between maceral types, it is very accurate at differentiating organic and inorganic material due to the large density variations. Directly comparing the mineral norm percentages of Table 7 to the petrographic point count analysis of Table 6 it can be immediately noted that the volume percentages vary dramatically, this is graphically displayed in Figure 50, with the most variable samples being DK 3, 4, 5, 13, 18, 19.

Due to the non-destructive nature of 3D tomography it is able to quantify *in situ* voids or pores within the structure of the sample. Looking to Table 7 there 4 outliers with distinctively high pore normative percentage of 5 %<, namely DK 0, 3, 8, and 15. When looking at the photomicrographs of these sample, none showed distinctive increases in voids or pores in their maceral structures. DK 0 was host to devolitilzation vacuoles, as was DK 1 and 2 which presented markedly lower normative pore percentages. DK 3 display slightly elevated pitting to the surface of collodetrinite, but again this is seen

in samples DK 6 and 7 which have lower normative pore percentages. The conclusion that can be drawn from this is that the pore identified by the 3D tomography are not readily identifiable through microscopy.

Volumetrically, the samples are very diverse in terms of the weightings of mineral matter, pore space and organic matter (Fig. 49). From Figure 49 it is worth noting that there is an inversely proportional relationship between the organic and mineral matter volumes. A specific noting of the samples DK 4, 13 and 18 which display distinctively higher mineral matter volume percentage, as well as low pore and organic matter volume percentages.

Table 7: Tomographic volume analysis data for C4 Lower coal samples moving away from the dolerite intrusion.

Distance from dyke (m)	*Mineral norm (%)*	*Pore norm (%)*	*Organic norm (%)*
0	4.73	5.92	89.35
1	6.17	2.03	91.8
2	5.6	1.56	92.84
3	28.39	5.62	65.99
4	41.84	0.44	57.72
5	18.61	0.76	80.63
6	13.86	1.63	84.51
7	10.43	2.47	87.1
8	10.98	6.49	82.52
9	6.47	2.23	91.3
10	20.97	1.31	77.72
11	17.24	3.92	78.84
12	5.86	1.03	93.11
13	59.55	0.3	40.15
14	11.29	0.44	88.27
15	8.98	17.17	73.85
16	9.3	1	89.7
17	12.77	1.98	85.25
18	43.53	1.06	55.41
19	38.79	1.8	59.42

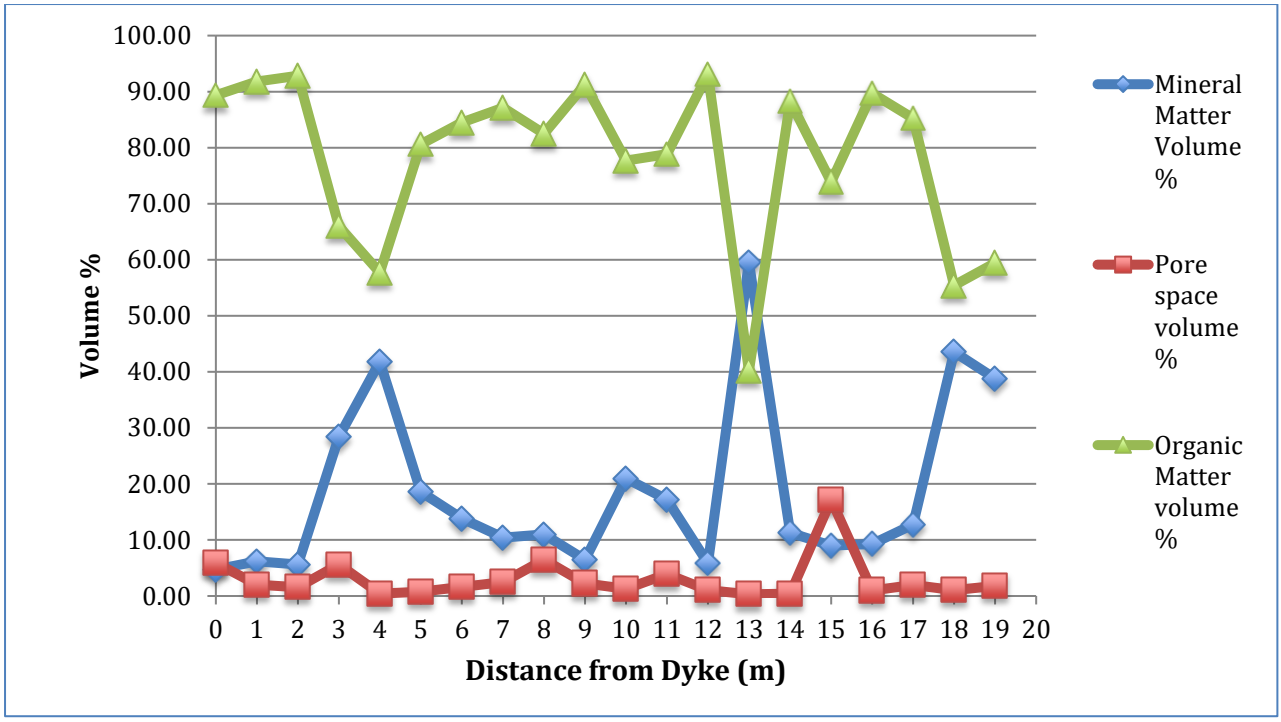

Figure 49: Comparative results of the mineral matter, pore space and organic matter volumes across the coal seam.

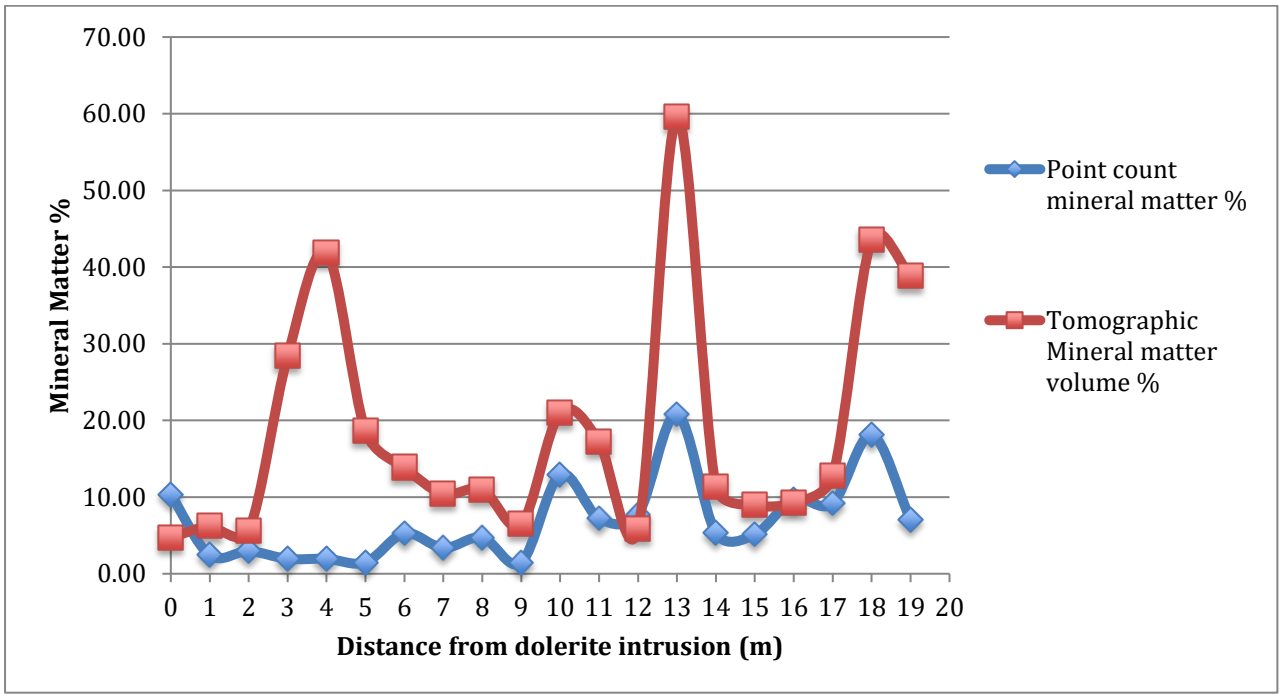

Figure 50: Comparison between petrographic mineral matter point-count percentage and tomographic mineral matter volume percentage.

Figure 50 shows the results of the petrographic mineral matter point-count analysis in relation to the tomographic mineral matter volume percentages. From this graphic, a strong correlation at distances greater than 5 m from the intrusion between the point count and tomographic data exists. Samples 3 and 4 show strong increases in mineral matter volume percentages that are not noted in the petrographic point-count data. It is possible that the tomographic volume percentages identify mineral

particles not visible in the standard point-count analysis. This is due to 3D tomographic analysis allowing for resolution down to the micron scale, and would explain the greater values within the tomographic data when compared to that of point-count analysis.

After investigation of the tomographic images three variations of inorganic mineralization where identified, sheet-like, large-grain, and fine-grained. Representative samples of these mineralization types were selected. The type examples are displayed and described below with the remaining images detailed in Appendix B.

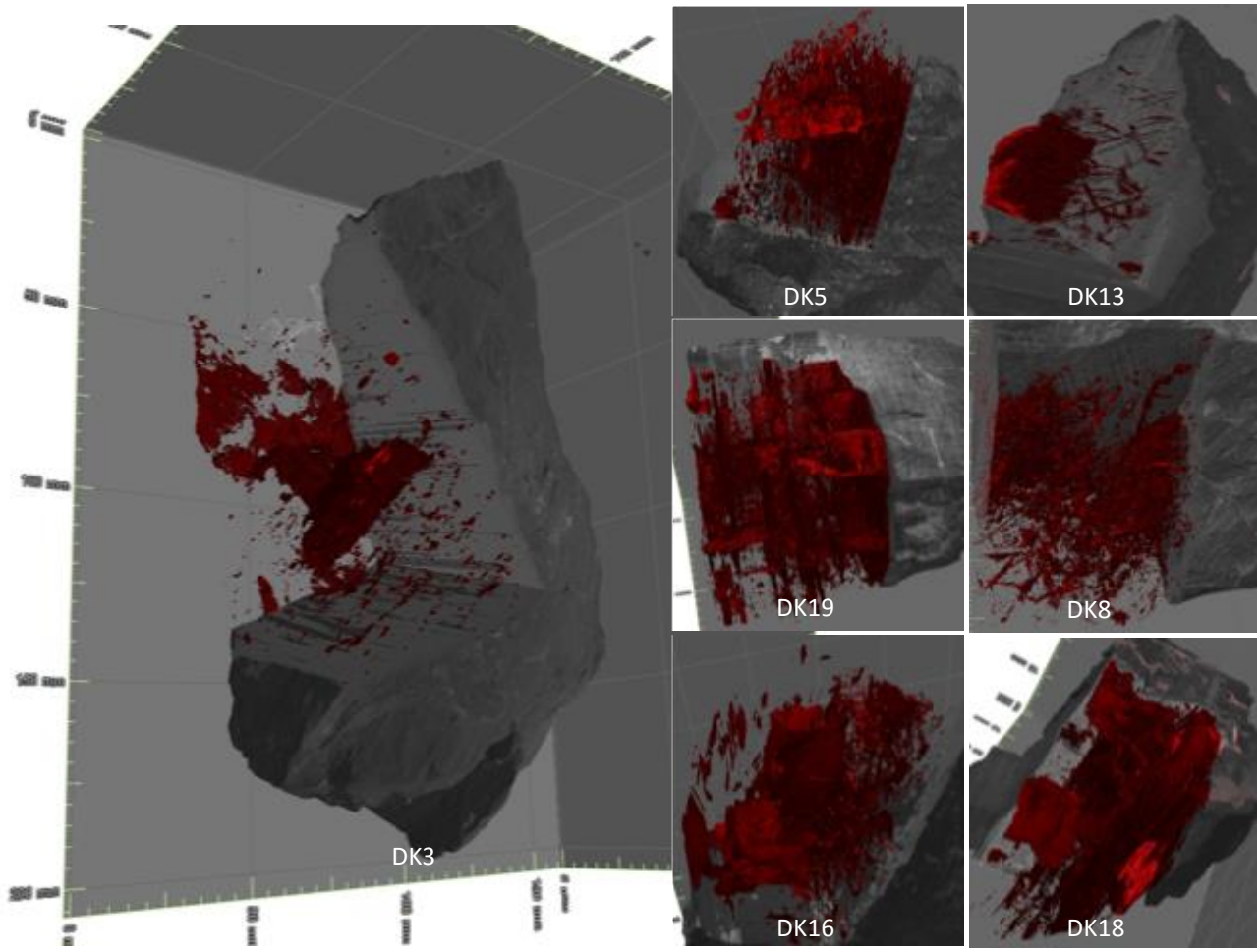

Figure 51: 3D tomographic image of sample DK 3 at 3 m from the dyke (Left) with the associated samples (Right) hosting sheet-like mineralization. Highlighted in red is the inorganic material's with the grey scale depicting the organic constituents.

Figure 51 is a type example of the sheet-like mineralization, this mineralization is also noted in the samples DK 3, 5, 8, 13, 16, 18, 19. Evident in these sample is a network of large inorganic sheets that frequently cross-cut the sedimentary layering of the coal. From the tomography it is not possible to identify the specific mineral type, however, when the petrography of these sample are consulted

siderite appears more prevalent in samples DK 3, 5, 8, 16,18 and 19 while calcite is more common in sample DK 13. From the often perpendicular orientation of the mineral sheets it is plausible to assume that these features are cleats. Coal cleats are fractures, generally occurring in perpendicular sets, which are often infilled with precipitate mineralization, however, due to the multitude of potential development mechanisms it is difficult to define the origin of the initial fracturing (Laubach *et al.,* 1998).

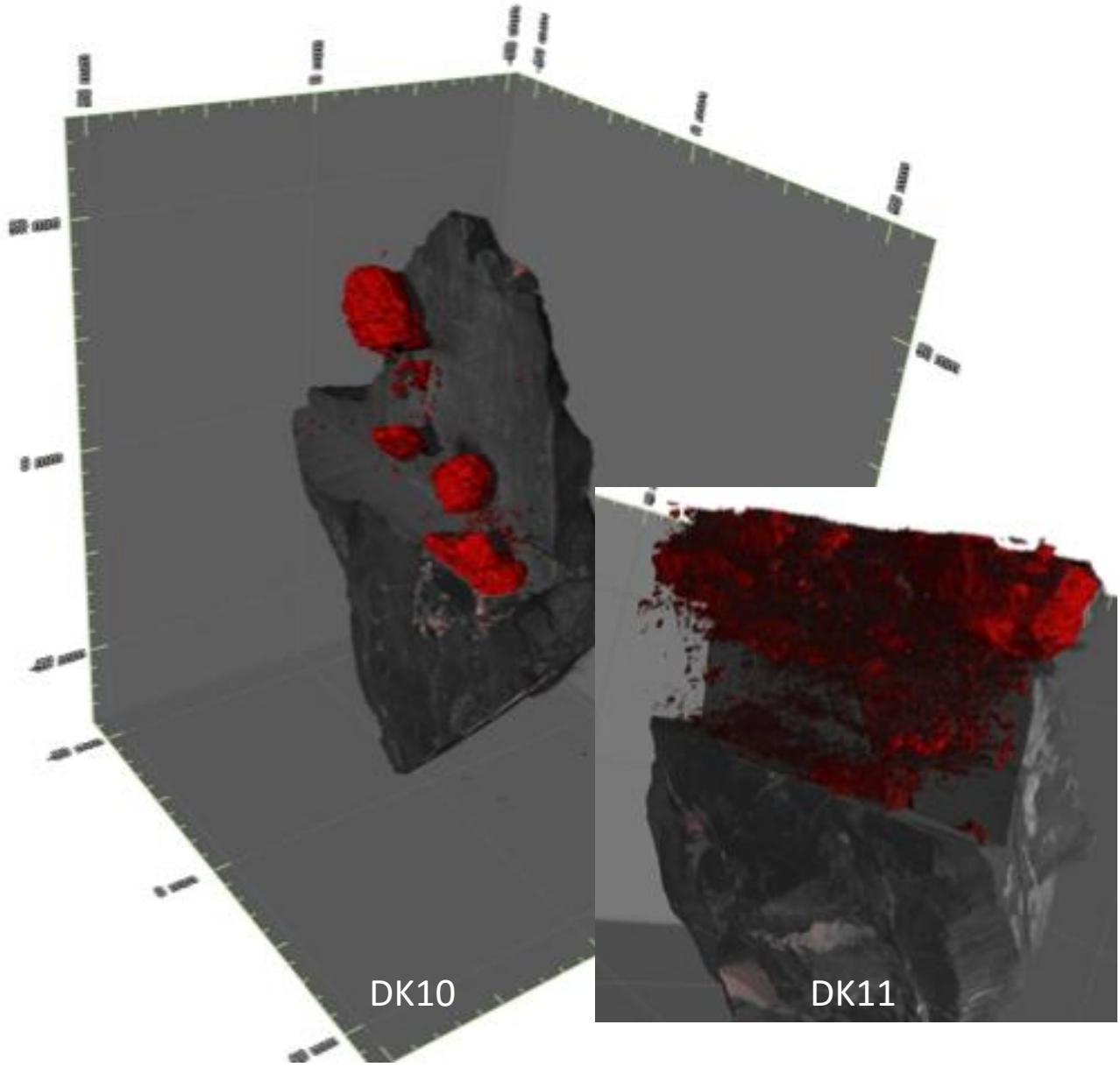

Figure 52: 3D tomographic image sample DK 10 and DK 11, these sample provide type examples for the large grain mineralization texture. Highlighted in red are the inorganic materials with the grey scale depicting the organic constituents.

The large-grain mineralization representative sample is at 10 m from the dolerite intrusion (Fig. 52). The mineralization occurs as large rounded concretions which cross-cut the sedimentary layering of the coal. The large concretions in sample DK 10 and 11 are unique in the transect, the scale of the

inclusions has however, not correlated to a significant increase in mineral matter within the samples with values from Table 7 of 20.97% and 17.24% for DK 10 and 11 respectively. However, when looking at the photomicrographs of these sample there is an increased presence of large grains, with sample DK 10 presenting with large pyrite amalgamations and DK 11 housing large calcite grains. The large grain are isolated, with no prevalent orientation noted in the 3D tomography, this is reiterated in the microscopy, where no distinctive inclusion pattern can be noted.

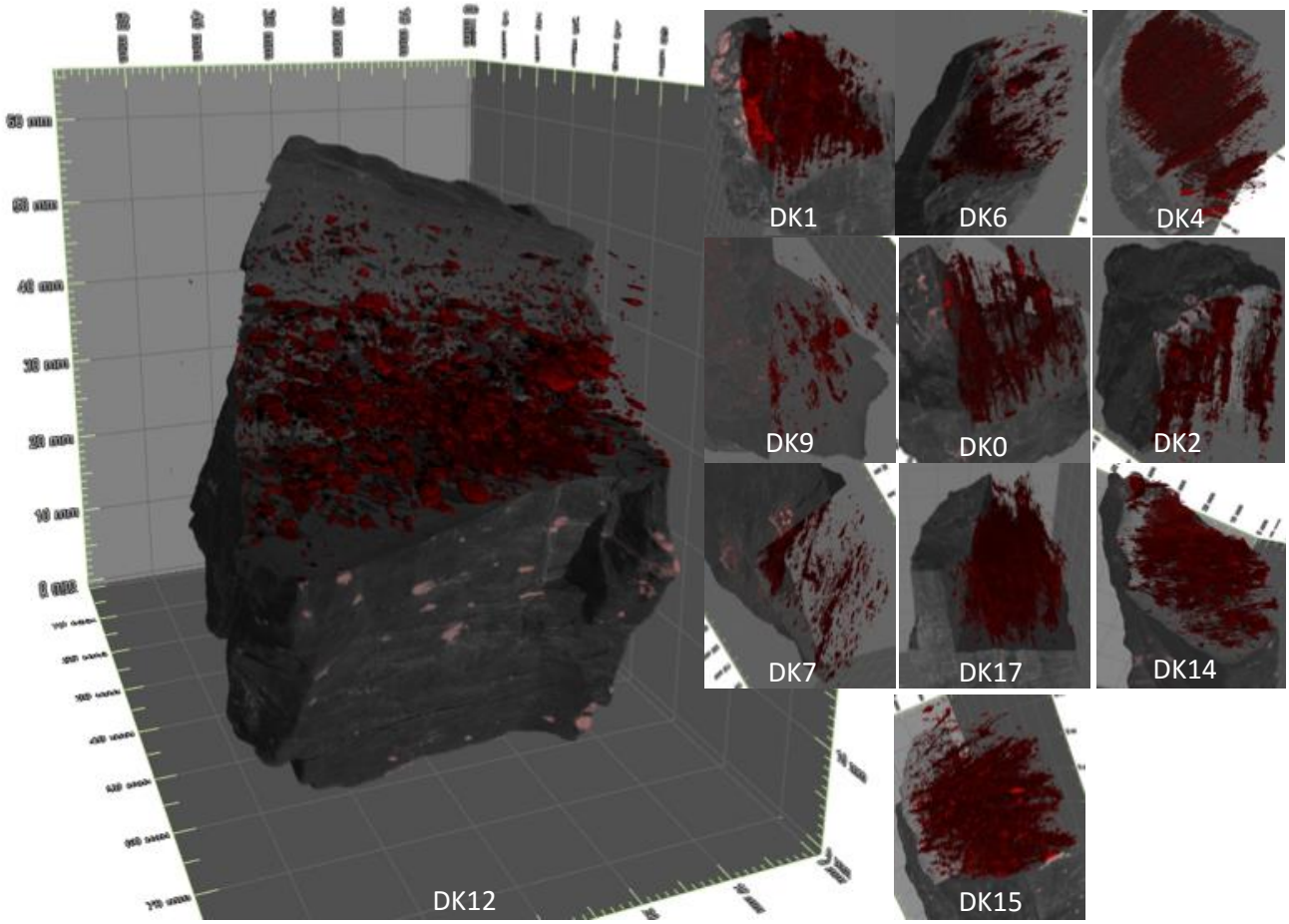

Figure 53: 3D tomographic image of sample DK 12 (left), the type example of the fine grained mineralization noted in the transect, to the right of the image are the associated samples with this type of mineralization. Highlighted in red is the inorganic materials with the grey scale depicting the organic constituents.

Fine grained mineralization is noted in the samples at 0, 1, 2, 4, 6, 7, 9, 12, 14, 15, and 17 m from the intrusion. The inorganic material maintains a relatively constant position along the bedding plains; there are, however, a few instances where the inorganic material cross-cuts the sedimentary boundaries. When looking at the petrography of these sample, a common feature of medium to fine grained siderite inclusion can be noted at sample distal to the dyke, while proximal samples are more fine grained and contain the addition of pyrite. All of the samples with fine grained mineralization appear to have an affinity for the mineralization to take place within collodetrinite macerals.

7.3. Summary discussion

Examining the tomographic results, it is evident that there is distinctive variability in the textural relationship between the inorganic and organic material in coal. Volumetrically, the samples show a consistent relationship between organic and inorganic material, while pore space has only minor influence. The samples are highly variable, with dramatic shifts in concentration of inorganic material. The most notable of these shifts occur at 3, 5, 9, 12, 14 and 17 m, where the samples vary sharply in terms of organic matter and inorganic material.

Further investigation into the inorganic volume percentages through comparison to the petrographic point-count analysis numbers showed strong correlation at distances greater than 5 m from the dolerite intrusion. The tomographic analysis shows consistently higher values for inorganic volume percentages when compared to the petrographic point-count analysis. It can be postulated that this disparity occurs for 2 reasons:

1. 3D tomography is able to more accurately identify much finer particulate matter than conventional point-count techniques.
2. 3D tomography allows for a more holistic view of the sample when compared to sample mounts utilised during point-count analysis.

The cross-cutting nature of the inorganics gives insight with regards to its origins. Cross-cutting of the sedimentary layers shows that at least some of the inorganic material is not syn-genetic to the coalification process, and thus must originate from a secondary source. The carbonate rich nature of the coal samples would allow for this inorganic material to be precipitated from saline fluid sources percolating through the coal material. Structurally, the two of the mineralizaiton textures further strengthen an argument for post-coalification mineralization.

Firstly, looking at the sheet-like mineralization, it is quite clear that these stuctures are cleats, due to their perpendicular relationship and positioning. With this, it can be inferred that the formation of the opening-mode fracture or cleats postdated coalification. With the regional tectonic setting stable it is thus reasonable to infer that the formation of these structures was induced through localised structural influences. The injection of the Karoo dolerites could provide the required pressures to form these fractures, with mineralzation taking place within these cleat through precipation.

Secondally, looking at the samples displaying fine-grained mineralization there is grain size variation within this texture. With samples proximal to the dolerite dyke having smaller grains to those in distal positions, this again provides causal correlation for the mineraliztion and the dolerite intursion. However when referring to the anomalous course grained mineraliztion of samples DK10 and 11 and based purely on the tomographic and petrographic there is not direct evidence linking the mineralization and the dolerite intursion.

CHAPTER 8: APPLICATION OF PRESSURISED LIQUID EXTRACTION AND TWO-DIMENSIONAL GAS CHROMATOGRAPHY TIME OF FLIGHT MASS SPECTROMETERY

The organic makeup of coal itself is a poorly understood field, due to the difficulty in obtaining a complete organic makeup of the material (Li *et al.,* 2001). Discussion of organic geochemistry of coal requires the identification and description of complex solid samples. The analysis of such samples has recently used techniques such as Fourier Transmission Infrared Spectroscopy (FTIR) and Gas Chromatography Mass Spectrometry (GC-MS) with great success (Kubát, 1982; Blazso *et al.,* 1985; Sobeih *et al.,* 2008). However, due to convolution effects in results produced by these analysis techniques, many of the complex components cannot be specifically identified. This convoluting effect is due to the subtle variation apparent in organic molecules, as single peaks may mask the identification of molecules with similar properties (Seeley *et al.,* 2007). The petroleum industry has made great strides in circumventing this problem when analysing refined petroleum products such as diesel and petrol through the use of Two-dimensional Gas Chromatography Mass Spectrometry (GC*GC-MS) (Seeley *et al.,* 2007). The GC*GC-MS method has allowed for greater separation of molecules in the spectra, thus improving the organic understanding of the refined petroleum products.

Gas chromatography relies on the sample, in its current phase (solid or liquid), being transformed into a gas. The gas produced from the sample is then passed through a column that separates the molecular components so that they reach the detector at varying rates. This separation is caused by the difference between the ionisation potential of the analyte component and the polar/non-polar nature of the column. The ionisation differential allows for different molecules to reach the detector at quantifiable intervals. This detection is performed by means of Time-of-Flight Mass Spectrometry (TOFMS). The analyser at the end of the column detects the time taken for molecules of the gasified analyte to move from the point of gasification to the end of the column (Panić and Górecki, 2006). The second dimention in GC*GC-MS is a secondary column added orthogonally to the first. This column is fed intermittent samples of the gasified analyte by the modulator, which periodically samples the gases of the first dimension (Panić and Górecki, 2006). A simplified example of the apparatus set up is displayed in Figure 54 below.

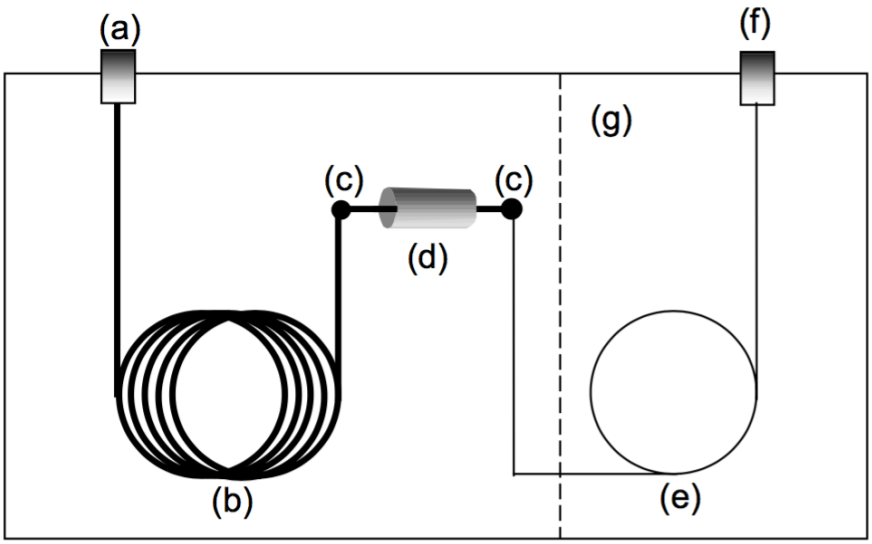

Figure 54: Schematic representation of GC*GC system- a) Injector; b) First-dimension column; c) Column connections; d) Modulator; e) Second dimension column; f) Detector g) Secondary column oven. (Adapted from Panić and Górecki, 2006).

The application of any form of gas chromatography on coal requires the material to be broken down into a state that can be readily gasified. GC-MS is often coupled with pyrolysis equipment, and the pyrolised gases are analysed with GC-MS (Sobeih *et al.,* 2008). Works such as Kubát (1982) and Blazso *et al.* (1985) applied GC-MS on pyrolised gasses to investigate the decomposition and recombination reactions occurring during the pyrolysis of brown coals. More recently, the technique has been coupled with lasers to perform micro-pyrolysis-GC. The technique shows promise, but the issue of pyrolysis reactions is that pyrolysis detracts from the *in situ* chemistry of the coal (Greenwood *et al.,* 2002). This hinderence has created the need for other forms of sample introduction such as solvent extraction.

The use of solvent extraction on the organic constituents of coal has been prevalent since the early 1920s, with the extraction of pyridine and residues from coking coal (Lowry, 1963). Work continued with extraction methods progressing to produce more complex extracts with current methods applying pressurisation and temperature variation to improve extraction yields (Li *et al.,* 2001; Assis *et al.,* 2000). Several techniques are available, each with its corresponding strengths, as detailed in Assis *et al.* (2000). The work of Assis *et al.*, (2000) showed that among Accelerated Solvent Extraction (ASE), Supercritical Fluid Extraction (SFE), Soxhlet, and ultrasonic extraction, ASE proved to be the least selective with regard to compounds extracted. However, the decreased selectivity also had decreased extraction yields compared to the other techniques (Assis *et al.,* 2000). Importantly, ASE has been shown to have no thermal influence on the organic molecules of the coal sample (Butala *et al.*, 2000).

The combination of ASE and GC on petroleum products and the investigation of the organic nature of soils have shown great potential (Hamilton *et al.,* 2007; Ong *et al.,* 2003; Seeley *et al.,* 2007; Liu and Phillips, 1991). The ASE-GC combination has been coupled with several detector types, in both single

dimension GC and two-dimensional GC (GC*GC) (Hamilton *et al.,* 2007; Ong *et al.,* 2003; Seeley *et al.,* 2007; Liu and Phillips, 1991). The advantage of ASE is that it extracts a broad spectrum of organic compounds at an acceptable yield. When the ASE method is coupled with GC*GC, it allows for a large degree of deconvolution and the detection of both aromatic and aliphatic compounds (Seeley *et al.,* 2007). Thus, to obtain a general or bulk organic geochemical analysis of coal, with none of the thermal decomposition and recombination reactions of pyrolysis-GC, ASE-GC*GC is an attractive solution but one that had not been attempted prior to this work.

8.1. Methodology

The approach adopted here for the geochemical investigation of sample set B, was to use GC*GC-TOF-MS. In order to perform the GC*GC-TOF-MS, samples from set B were first run through an ASE system to produce a concentrated solution that could then be processed by the GC*GC-TOF-MS.

The ASE system used was a Dionex 350 ASE hosted at the Pretoria office of the Council for Scientific and Industrial Research. To produce the extracts, ~15 g of the milled samples (sample set B milled to 15 μm) were mixed with diatomaceous earth and transferred into 34 ml ASE 350 cells. At the base of the cells, 30 mm glass fibre filters were placed prior to the sample introduction. Any remaining void space within the cells was filled with diatomaceous earth to reduce solvent usage during extraction.

The cells were then placed into the Dionex ASE 350. Once in place, the cells were heated to 100 °C at a pressure of 10342.14 kPa. The solvent, hexane, was then introduced into the cell at a rate of 1 ml/min to a total rinsing volume of 60 ml. The concentrated solute extracted ranged between 3-5 g per sample and was then sealed and stored in vials.

The extracts were analysed using the Leco Pegasus 4D GC*GC-TOF-MS, with the system parameters optimised using Leco's Chromatof software. The samples were run through a first-dimension Rxi-17 Sil MS (30m x 0.25mm x 0.25mm) column and second dimension Rxi-1 Sil MS (2m x 0.1mm x 0.1mm) column. Results from the analysis were transferred from the Chromatof software into Microsoft Excel for processing.

8.2. Results

A fundamental result of the GC*GC-TOF-MS analysis combine ASE is the first successful, extraction of organic geochemical information from solid coal material through the combination of these techniques. The results from the Leco Pegasus 4D GC*GC-TOF-MS provided an abundance of geochemical data, the vast amount of information has been distilled into critical representative imagery and data to avoid convolution through volume. The remaining geochemical data is displayed in Appendix A where the set of chromatograms and lists of exact extracted molecules are displayed for all samples.

.

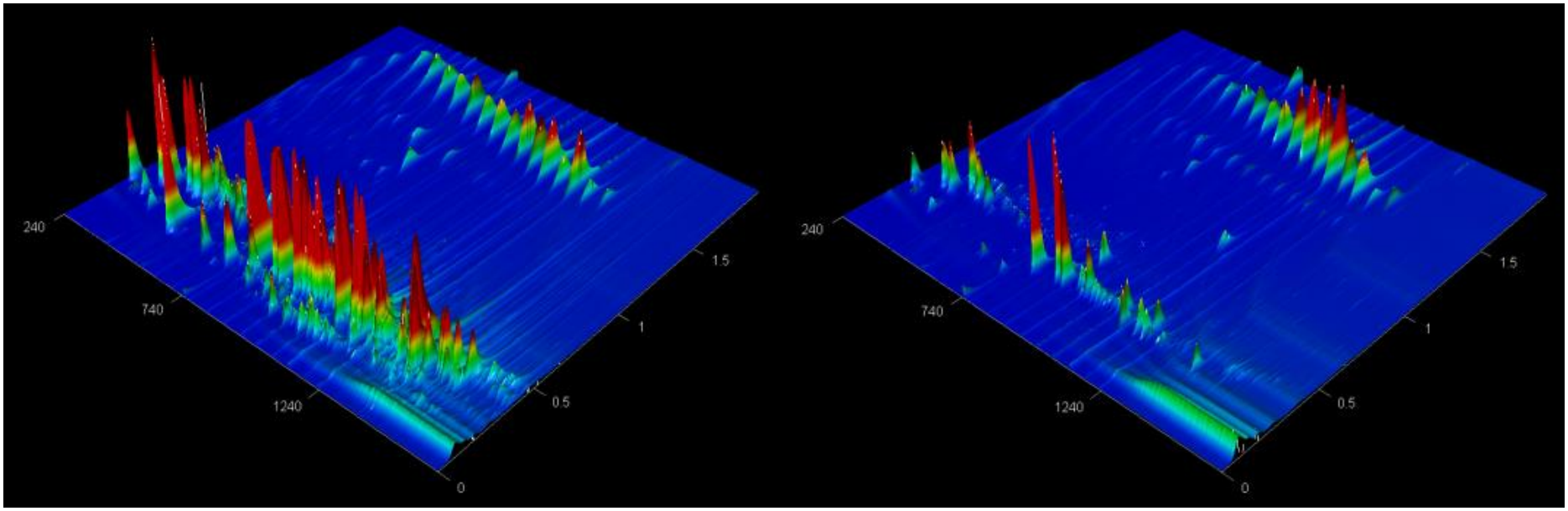

Figure 55: (Left) Chromatogram of sample at 0 m from the dolerite dyke, showing the time-of-flight distribution and peak intensities of the identified organic molecules. (Right) Chromatogram of sample at 19 m from the dolerite dyke. The most distal sample analysed was at 19 m, the chromatogram displays the 196 unique compounds identified. Once investigated, none of these compounds showed first-dimension residence times greater than 1620 s.

The chromatograms of Figure 55 provide visual representation of the identified organic components housed within the samples DK0 and DK19. These chromatograms where selected due to there position within the transect. The sample DK0, in direct contact with the dolerite intrusion, as well as sample DK19 (Fig. 55) show good separation of both aliphatic and aromatic compounds, with aromatic componds found within the second dimension retention times of between ~0-0.5 s, while the aliphatic componds are identifiable from ~0.5s upwards. The sample DK0 has a vastly more complicated chromatogram to that of sample DK19. This complexity disparity is further displayed in Figure 56, where the identified organic molecules are plotted on a scatter plot. The sample DK0 houses 838 unique organic compounds, while within sample DK19 only 196 unique organic compounds are identified. The complex nature of sample DK0 is not matched by any of the samples within in the transect. Further, within Figure 56 there is a noteable linear aliphatic trend of molecules between 1.5 and 2 seconds in the second dimension, similarly this is noted in sample at 19 m.

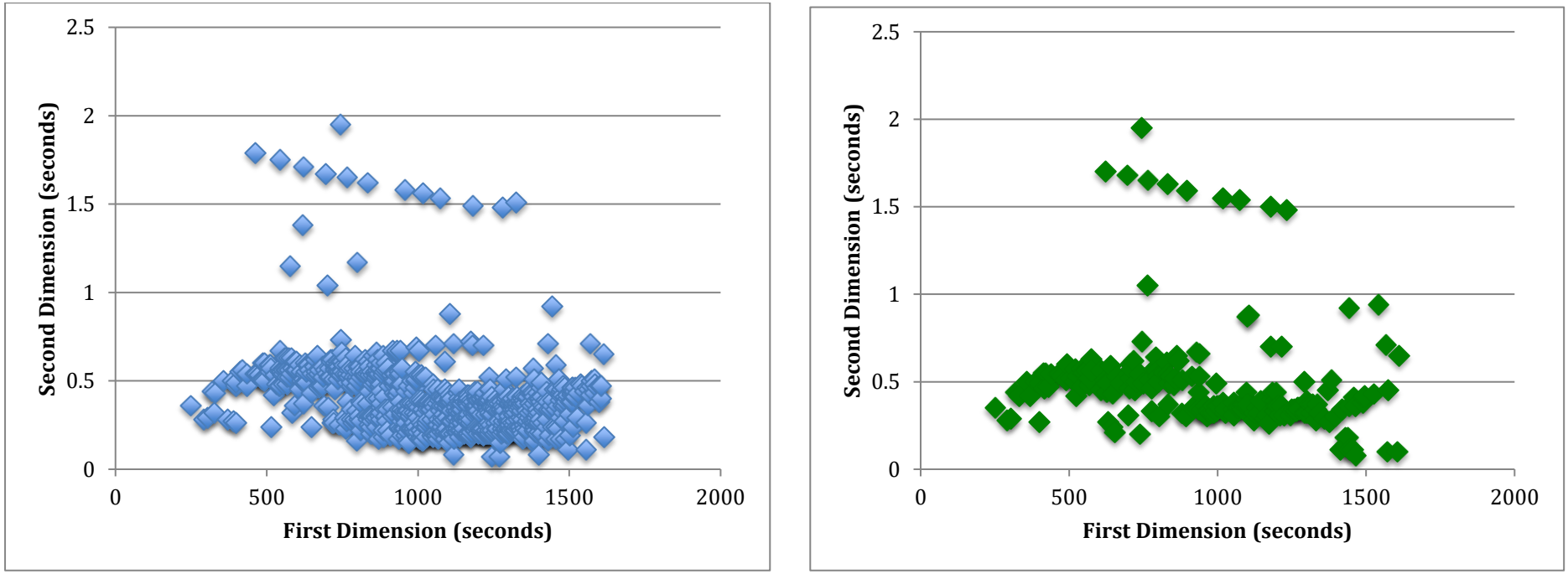

Figure 56: (Left) Chromatogram of sample at 0 m from the dolerite dyke. (Right) Chromatogram of sample at 19 m from the dolerite dyke.

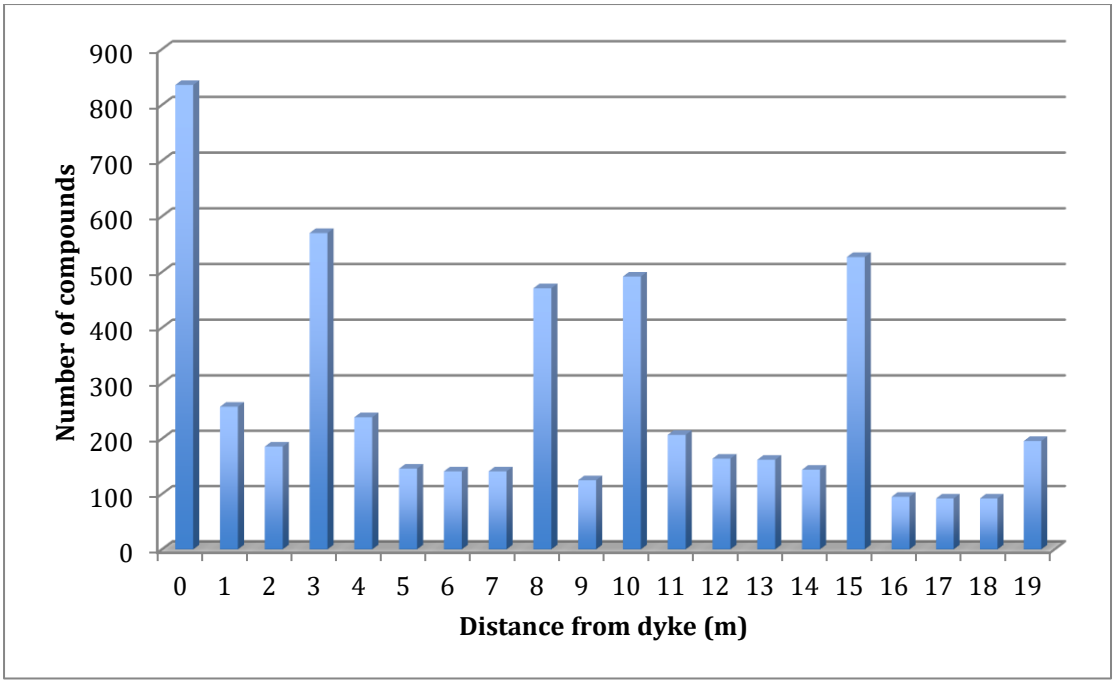

Figure 57:Number of unique organic compounds in samples away from the dolerite intrusion

Analysis of the number of unique organic compounds identified during chromatography is displayed in Figure 57. To note here are the peaks of samples at 0, 3, 8, 10, and 15 m away from the dolerite dyke. When examining the chromatograms of these samples in Figure 58, it is clear that the identified compounds in sample DK3, 8, 10 and 15 differ greatly to that of DK 0, similarly their chromatograms differ from the representative nature of DK 19 in Figure 55.

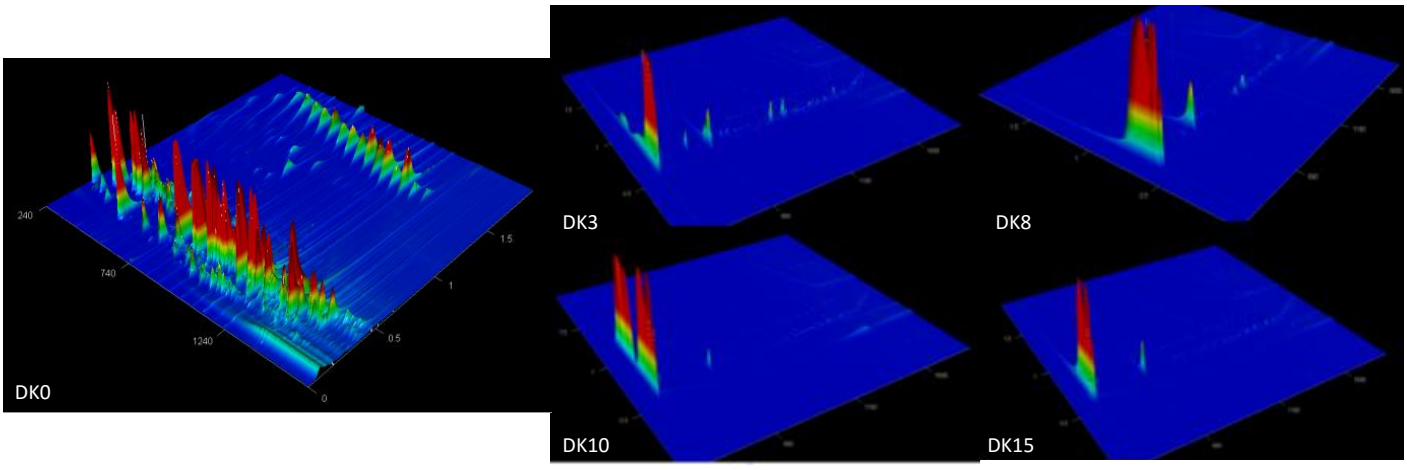

Figure 58: Comparison of chromatograms of samples DK0, 3, 8, 10 and 15

Further investigation of the hydrocarbon trends of the C4 lower coal seam is done through the chromatograms of Figures 59 and 60, displaying the identified molecules across all samples. The chromatogram in Figure 59 is complex with no distinctive trends clearly identifiable.

When the anomalous samples DK0, 3, 8, 10, and 15 are grouped together as seen in Figure 60 a distinctive feature is made clear. The variation in molecule numbers (Fig.57) of the anomalous samples is maintained in higher retention times in both the first and second dimensions. It should be noted that within the first dimension there appears to be limiting residence time of 1620 s, beyond which only samples DK 3, 8, 10 and 15 have organic molecules identified.

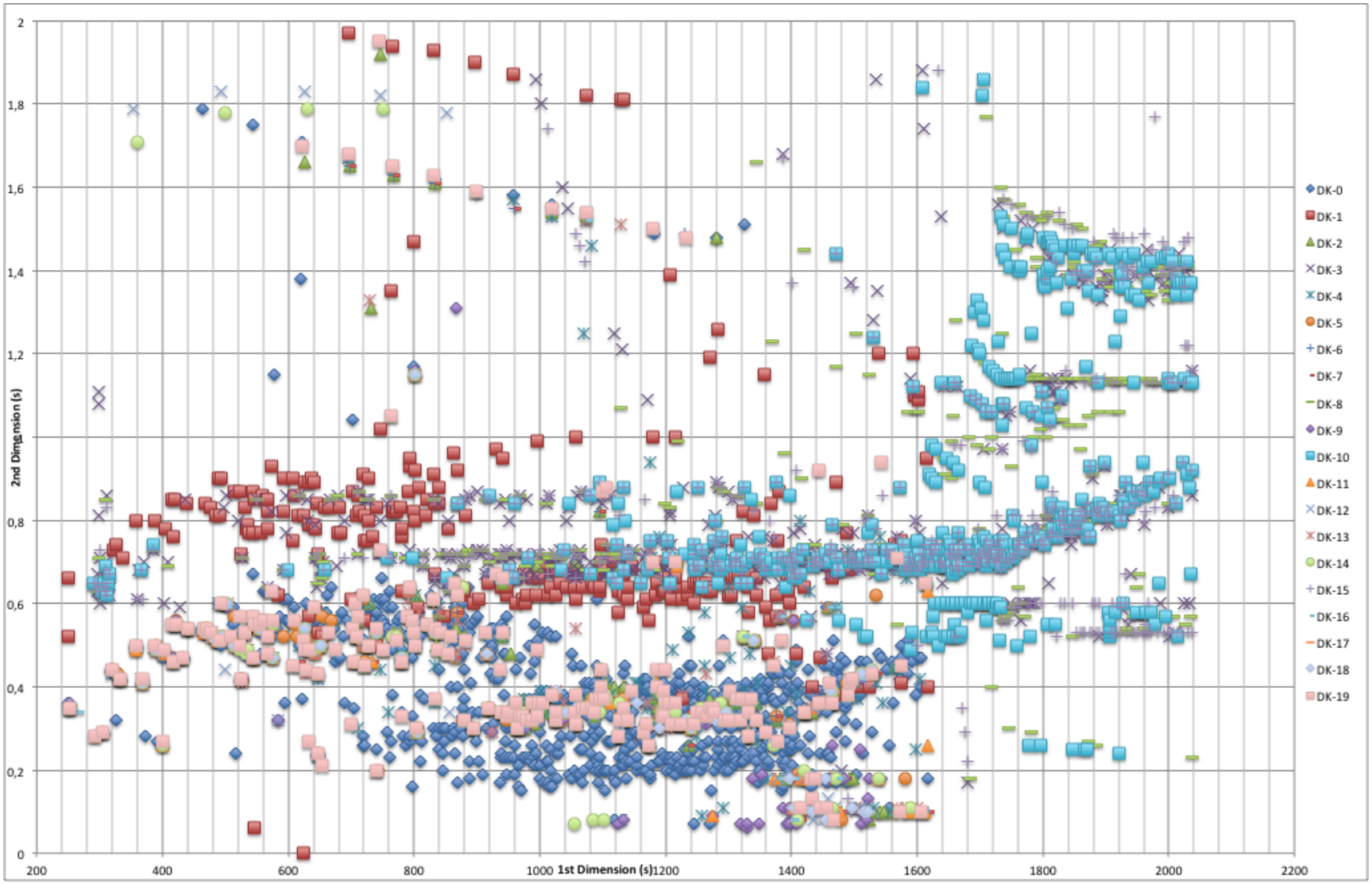

Figure 59: GC*GC chromatogram of all coal samples 0 – 19 m.

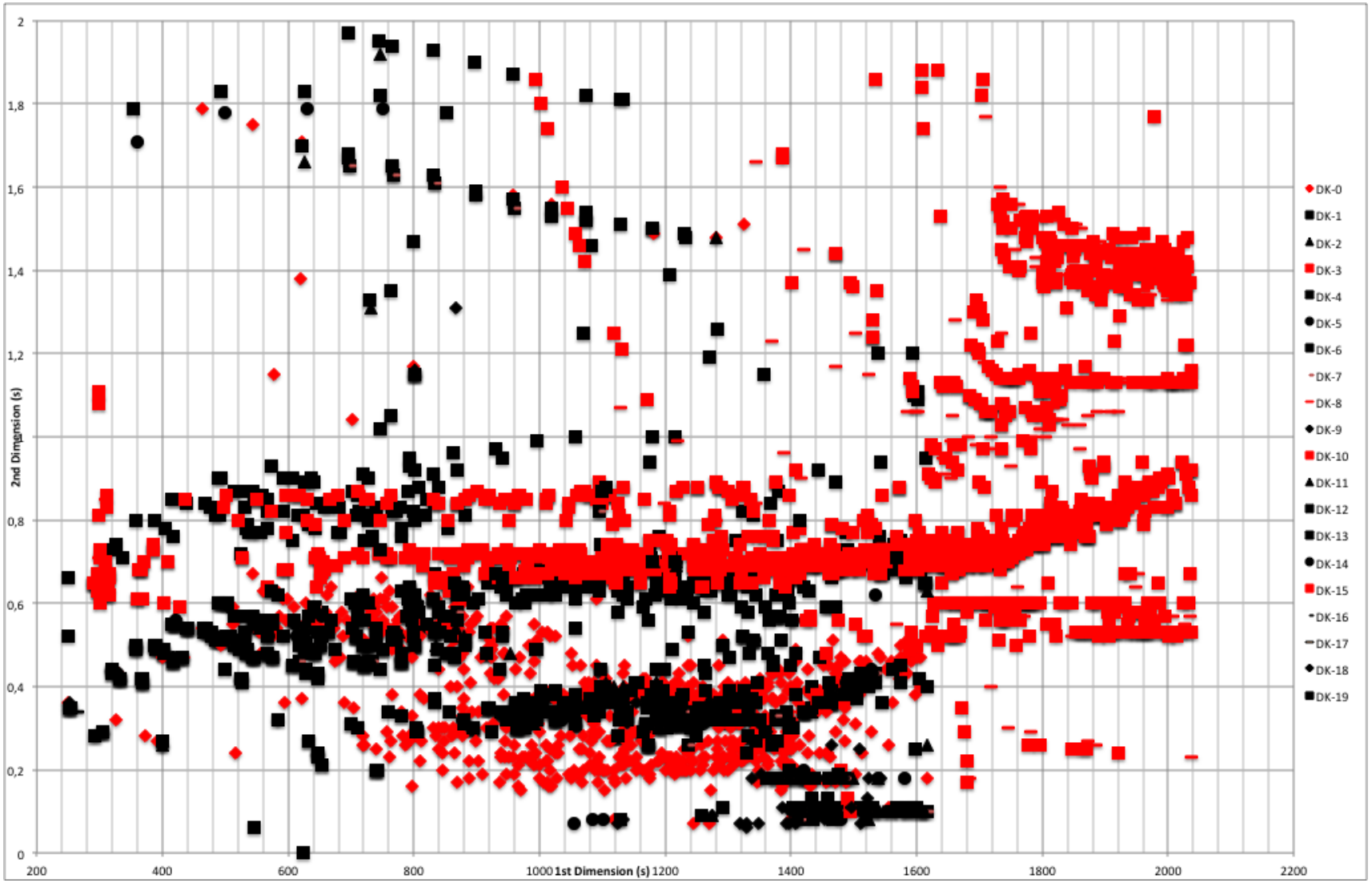

Figure 60:GC*GC chromatogram of all coal samples 0 – 19 m. Samples in red are those with anomalously high compound numbers: DK0, 3,8,10, and 15

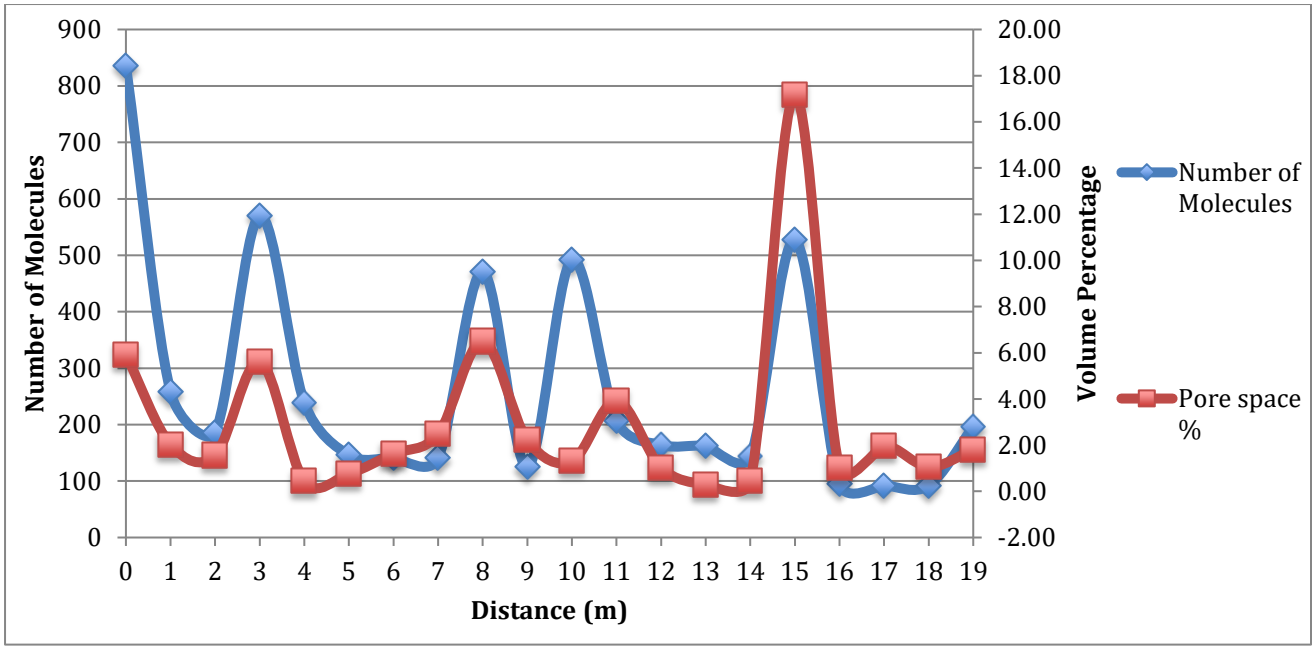

Figure 61: Graphic of identified organic molecules measured through GC*GCTOFMS and pore space volume percentage as measured through X-ray tomography

From Figure 61, it is worth noting the distinctive correlation between pore space volume percentage and the number of identified molecules per sample. This correlation is well defined with anomalies found only at 10 and 11m from the intursion, however these samples do display unique inorganic concretions as noted from the tomographic analysis.

Further, investigating the molecules within these samples to see how they differ from the surrounding samples (Appendix A) prominent compound types within samples 3, 8, 10, and 15 are Poly-Aromatic Hydrocarbons (PAHs). The works of Mastral and Callen (2000) showed the production of PAHs from combustion during power generation and Misz-Kennan and Fabiańska (2011) investigated PAH generation in self-heating coal dumps and showed that the development of PAHs in coal was directly related to thermal influence. Collins *et al.* (2014) directly linked the presence of PAH derivatives to the maturity of coal samples. In the context of this study, two primary properties of PAH molecules are of interest: their formation within thermally influenced coal and their solubility within fluids (Lorimer, 1984).

The samples with high molecule counts at 0, 3, 8, 10, and 15 m from the dolerite are shown in Figure 57. They are again identified in Figure 60 where they are separated from the full sample set and displayed in red. The notable differentiating feature of the samples at 3, 8, 10, and 15 m from the dolerite is that they contain molecules with first-dimension residence times greater than 1620 s. The residence correlates to the boiling point of the compound, with shorter residence times reflecting lower boiling points (Dettmer-Wilde and Engewald, 2014). With reference to Table 8, which list an extract from the data of Appendix A. The data displayed in Table 8 list the prominent abundance of PAHs and PAH

derivatives present in the samples. Misz-Kennan and Fabiańska (2011) and Collins *et al.* (2014) display the formation of PAH molecules from the heating of coals and their presence as an indication of increased maturation. In addition, the works of authors such and Volk *et al*. (2011) and Lorimer *et al.* (1984) note the high dissolution propensity of PAH and PAH derivatives in fluids. Correlating these PAH compounds and derivatives to all the analysed samples, it is identified that benzo (b) carbazole and benzo (c) carbazole appear only in samples DK 3, 8, 10, and 15. Benzocarbazole has been used within oil industry as a marker for migration (Clegg *et al.,* 1998).

Migration of crude oil refers to the movement of the crude oil form a source rock into a reservoir rock, generally a fine grained to a more coarse grained material host rock. This is termed primary migration (Amadei, 2005). Clegg *et al.* (1998) showed that the carbazole ratios may not be an accurate measure of distance of migration but were still indicative of transported hydrocarbons from source rock to the crude oil itself.

Applying this to the coal samples, the presences of benzocarbazoles in DK3, 8,10, and 15 displays that these compounds were transported form a source material. The correlation of porosity with compound peaks found in these samples, as noted in Figure 61, provides the likelihood that this transport was in a fluid phase.

Table 8: Identified PAH and PAH derivatives in samples at 3, 8, 10 and 15 m form the dolerite intrusion.

Molecule Name	*Formula*	*1st Dimension Time (s)*	*2nd Dimension Time (s)*	*Sample*
Anthracene, 1,2,3,4-tetrahydro-9-propyl-	C17H20	1644	0.72	DK-10
Anthracene, 2-ethyl-	C16H14	1706	0.72	DK-3
Anthracene, 2-ethyl-	C16H14	1706	0.72	DK-10
Anthracene, 9-(2-propenyl)-	C17H14	1922	0.82	DK-3
Anthracene, 9-(2-propenyl)-	C17H14	1686	0.71	DK-8
Anthracene, 9-(2-propenyl)-	C17H14	1762	0.74	DK-10
Anthracene, 9-(2-propenyl)-	C17H14	1700	0.72	DK-15
Anthracene, 9-ethenyl-	C16H12	1636	0.7	DK-8
Anthracene, 9-ethyl-9,10-dihydro-10-methyl-	C17H18	1702	0.73	DK-10
Anthracene, 9-ethyl-9,10-dihydro-10-methyl-	C17H18	1680	0.73	DK-15
Anthracene, 9-phenyl-	C20H14	1786	1.05	DK-3
Anthracene, 9,10-dihydro-	C14H12	1648	0.72	DK-15
Anthracene, 9,10-dihydro-9-(2-hydroxy-2-propyl)-9,10-dimethyl-	C19H22O	1714	0.73	DK-15
Anthracene, 9,10-dihydro-9,10-dimethyl-	C16H16	1646	0.72	DK-3
Anthracene, 9,10-dihydro-9,10-dimethyl-	C16H16	1646	0.72	DK-8
Anthracene, 9,10-dihydro-9,10-dimethyl-	C16H16	1662	0.73	DK-10
Benz(a)anthracene-7-carbonitrile	C19H11N	2036	1.16	DK-3
Benz(a)anthracene-7-carbonitrile	C19H11N	2036	1.16	DK-15
Benz(a)anthracene-7-carboxaldehyde	C19H12O	1748	1.06	DK-3
Benz(a)anthracene-7-carboxaldehyde	C19H12O	1772	1.07	DK-10
Benz(a)anthracene-7-carboxaldehyde	C19H12O	1748	1.06	DK-15
Benz[a]anthracene	C18H12	1682	1	DK-8
Benz[a]anthracene, 1-methyl-	C19H14	1664	1.12	DK-3

Benz[a]anthracene, 1-methyl-	C19H14	1658	1.13	DK-15
Benz[a]anthracene, 1,12-dimethyl-	C20H16	1718	1.06	DK-3
ffBenz[a]anthracene, 1,12-dimethyl-	C20H16	1718	1.06	DK-15
Benz[a]anthracene, 12-methyl-	C19H14	1664	1.12	DK-15
Benz[a]anthracene, 4-methyl-	C19H14	1888	1.06	DK-8
Benz[a]anthracene, 7-methyl-	C19H14	1796	1.02	DK-8
Benz[a]anthracene, 7-methyl-	C19H14	1704	1.08	DK-10
Benz[a]anthracene, 7-methyl-	C19H14	1692	1.09	DK-15
Benz[a]anthracene, 7,12-dimethyl-	C20H16	1872	1.05	DK-8
Benz[a]anthracene, 7,12-dimethyl-	C20H16	1718	1.06	DK-10
Benz[a]anthracene, 8-methyl-	C19H14	1658	1.13	DK-3
Benz[a]anthracene, 8-methyl-	C19H14	1824	1.04	DK-8
Benzo(b)carbazole	C16H11N	1734	0.97	DK-3
Benzo(b)carbazole	C16H11N	1734	0.97	DK-15
Benzo(c)carbazole	C16H11N	1860	0.97	DK-8
Benzo(c)carbazole	C16H11N	1782	0.98	DK-10
Benzo[c]phenanthrene, 1-methyl-	C19H14	1734	1.03	DK-3
Benzo[c]phenanthrene, 1,12-dimethyl-	C20H16	1840	1.03	DK-8
Benzo[c]phenanthrene, 6-methyl-	C19H14	1710	1.06	DK-3
Benzo[c]phenanthrene, 6-methyl-	C19H14	1804	1	DK-8
Benzo[c]phenanthrene, 6-methyl-	C19H14	1710	1.06	DK-10
Benzo[c]phenanthrene, 6-methyl-	C19H14	1710	1.06	DK-15
Carbazole	C12H9N	1668	0.68	DK-8
Carbazole	C12H9N	1666	0.68	DK-10
Carbazole	C12H9N	1666	0.68	DK-15
Carbazole, 1,6-dimethyl-	C14H13N	1778	0.74	DK-3
Carbazole, 1,6-dimethyl-	C14H13N	1790	0.74	DK-8
Carbazole, 2,3-dimethyl-	C14H13N	1786	0.74	DK-3

Carbazole, 2,5-dimethyl-		C14H13N	1750	0.72	DK-10
Carbazole, 3,5-dimethyl-		C14H13N	1708	0.72	DK-3
Carbazole, 4,5-dimethyl-		C14H13N	1708	0.71	DK-8
Chrysene, 1-methyl-		C19H14	1818	1.04	DK-8
Chrysene, 2-methyl-		C19H14	1684	1.1	DK-3
Chrysene, 2-methyl-		C19H14	1692	1.09	DK-10
Chrysene, 2-methyl-		C19H14	1702	1.08	DK-15
Chrysene, 4-methyl-		C19H14	1860	1.03	DK-8
Chrysene, 4-methyl-		C19H14	1734	1.03	DK-10
Chrysene, 4-methyl-		C19H14	1684	1.1	DK-15
Chrysene, 5-methyl-		C19H14	1832	1.04	DK-8
Chrysene, 5-methyl-		C19H14	1684	1.1	DK-10
Chrysene, 6-methyl-		C19H14	1658	1.13	DK-10
Dibenzothiophene, 3-methyl-		C13H10S	1680	0.7	DK-3
Dibenzothiophene, 3-methyl-		C13H10S	1654	0.7	DK-8
Dibenzothiophene, 4-methyl-		C13H10S	1638	0.7	DK-15
Fluoranthene		C16H10	1796	0.75	DK-3
Fluoranthene		C16H10	1796	0.75	DK-8
Fluoranthene		C16H10	1796	0.75	DK-10
Fluoranthene		C16H10	1796	0.75	DK-15
Fluoranthene, 2-methyl-		C17H12	1856	0.8	DK-3
Fluoranthene, 2-methyl-		C17H12	1856	0.8	DK-10
Fluoranthene, 2-methyl-		C17H12	1856	0.8	DK-15
Naphthalen-2-ol, morpholyl)(phenyl)methyl-	*1-(4-*	C21H21NO2	1878	0.82	DK-3
Naphthalen-2-ol, morpholyl)(phenyl)methyl-	*1-(4-*	C21H21NO2	1856	0.82	DK-8
Naphthalen-2-ol, morpholyl)(phenyl)methyl-	*1-(4-*	C21H21NO2	1892	0.83	DK-10
Naphthalen-2-ol, morpholyl)(phenyl)methyl-	*1-(4-*	C21H21NO2	1890	0.83	DK-15
Naphthalene, 1-(phenylmethyl)-		C17H14	1782	0.75	DK-3

Naphthalene, 1-(phenylmethyl)-	C17H14	1782	0.75	DK-10
Naphthalene, 1-phenyl-	C16H12	1834	0.77	DK-3
Naphthalene, 1-phenyl-	C16H12	1636	0.7	DK-10
Naphthalene, 1-phenyl-	C16H12	1636	0.7	DK-15
Naphthalene, 1,8-di-1-propynyl-	C16H12	1760	0.74	DK-3
Naphthalene, 1,8-di-1-propynyl-	C16H12	1760	0.74	DK-8
Naphthalene, 1,8-di-1-propynyl-	C16H12	1760	0.74	DK-10
Naphthalene, 1,8-di-1-propynyl-	C16H12	1760	0.74	DK-15
Naphthalene, 2-(1-methyl-2-phenylethenyl)-	C19H16	2036	0.92	DK-3
Naphthalene, 2-(1-methyl-2-phenylethenyl)-	C19H16	1946	0.86	DK-8
Naphthalene, 6,7-diethyl-1,2,3,4-tetrahydro-1,1,4,4-tetramethyl-	C18H28	1874	0.93	DK-15
Naphthalene, 7-butyl-1-hexyl-	C20H28	1666	0.77	DK-10
Naphthalene, 7-butyl-1-hexyl-	C20H28	1666	0.77	DK-15
Perylene	C20H12	1728	1.23	DK-10
Perylene, 3-methyl-	C21H14	1784	1.5	DK-3
Perylene, 3-methyl-	C21H14	1848	1.39	DK-15
Pyrene	C16H10	1850	0.77	DK-3
Pyrene	C16H10	1850	0.77	DK-8
Pyrene	C16H10	1850	0.78	DK-10
Pyrene	C16H10	1848	0.77	DK-15
Pyrene, 1-methyl-	C17H12	1888	0.81	DK-3
Pyrene, 1-methyl-	C17H12	1888	0.81	DK-8
Pyrene, 1-methyl-	C17H12	1888	0.81	DK-10
Pyrene, 1-methyl-	C17H12	1854	0.78	DK-15
Pyrene, 1,2,3,3a,4,5-hexahydro-	C16H16	1738	0.72	DK-3
Pyrene, 1,2,3,3a,4,5-hexahydro-	C16H16	1726	0.72	DK-8
Pyrene, 1,2,3,3a,4,5-hexahydro-	C16H16	1726	0.72	DK-10

Pyrene, 1,2,3,3a,4,5-hexahydro-	C16H16	1726	0.71	DK-15
Pyrene, 1,2,3,6,7,8-hexahydro-	C16H16	1656	0.72	DK-8
Pyrene, 1,2,3,6,7,8-hexahydro-	C16H16	1656	0.72	DK-15
Pyrene, 1,3-dimethyl-	C18H14	1956	0.87	DK-3
Pyrene, 1,3-dimethyl-	C18H14	1956	0.87	DK-10
Pyrene, 1,3-dimethyl-	C18H14	1956	0.87	DK-15
Pyrene, 2-methyl-	C17H12	1916	0.82	DK-3
Pyrene, 2-methyl-	C17H12	1856	0.8	DK-8
Pyrene, 2-methyl-	C17H12	1888	0.81	DK-15
Pyrene, 4,5,9,10-tetrahydro-	C16H14	1774	0.75	DK-3
Triphenylene, 1,2,3,4-tetrahydro-	C18H16	1878	0.82	DK-10
Triphenylene, 1,2,3,4-tetrahydro-	C18H16	1808	0.76	DK-15
Xanthene, 9,9-dimethyl-	C15H14O	1832	0.76	DK-15

8.3. Summary discussion

Investigation of the organic geochemical constituents of the samples done through GC*GC-TOF-MS showed a distinctive variation in chemical composition. The most prominent of these variations are identified in the chromatogram of Figure 60, showing more than 800 unique organic compounds identified within the sample at the contact between the dolerite and the coal. The identification of these compounds is not matched anywhere else in the transect; however, there are several instances of peaks in compound numbers. These influxes are identified in Figure 57, where samples DK3, 8, 10, and 15 all show dramatically larger compound numbers than the surrounding samples. It is apparent that the longer chain and higher carbon number compounds are present in samples DK3, 8, 10, and 15, and not in the remaining samples. This seems to be the differentiating factor between the high compound samples and the rest, as seen in Figure 60. In addition to the number of compounds identified, the presence of a multitude of PAH and PAH derivatives in these samples, alludes to thermal influence. A specific bio-marker, in the form of benzo (b) carbazole and benzo (c) carbazole, is present in sample DK 3, 8, 10, and 15.

The potential reasoning for the unique nature of sample DK0 is explained by contact with the dolerite dyke. This contact provides both increased conductive thermal influence as well as a conduit for fluid flow at the contact itself. The higher levels of conductive thermal influence provide a reason for the less complex nature of the compounds found in this sample, as the thermal impetus breaks down the organic compounds. Fluid flow along the boundary between dolerite and coal would provide a low

resistance channel for the precipitation of additional organic compounds entrained in the fluid. Evidence for fluid-based transportation of organic compounds is displayed through the combination of the GC*GC-TOF-MS results with the pore space analysis of the X-ray tomography. The correlation between increased pore space and the number of identified molecules is shown in Figure 60. The presence of highly soluble PAH and PAH derivatives in the samples DK 0, 3, 8, and 5, with both high pore space volume percentages and compound numbers, provides a setting where fluid transport and precipitation of soluble organic compounds is highly likely. This is further affirmed by the presence of the benzocarbazole bio-markers, which are known migration indicators.

A singular incidence of non-correlation of pore space and compound peaks, seen in Figure 61, is noted at 10 m from the dolerite intrusion. The samples DK 10 and DK 11 have unique inorganic textural nature, as seen in the X-ray tomography images. They show the presence of large inorganic concretions within the coal itself. These larger concretions may denote a propensity for larger pore spaces within the coal at this distance, which would more readily allow for the precipitation of inorganic and organic materials due to reduced pressure in these larger cavities. The result of this precipitation would be a reduction in overall remaining pore space, but also the potential for increase in organic complexity.

CHAPTER 9: APPLICATION OF THERMOGRAVIMETRIC PROXIMATE ANALYSIS

The natural heterogeneity of coal has created difficulties in its analysis, and the use of proximate analysis has been the staple geochemical test for coal since the early 1800s (Lowry, 1963). This technique applies specific heating ramps in confined gas controlled environments where mass loss is directly correlated to the loss of specific components within the coal material. The mass loss allows for a quantification of the bulk geochemical constituents. These constituents are termed as ash-, volatile matter-, fixed carbon-, and moisture percentages, with the sum of these ratios adding to 100 % (Speight, 2005).

The use of proximate analysis in the investigation of coal has been focused on producing standard values for the assessment of combustibility of coal (Warne, 1991). With the increasing use of poorer quality coals, the accurate assessment of coals has become more important (Warne, 1991). Making up part of these lower quality coals are coals found in regions affected by igneous intrusions.

Investigation of the thermal influence of igneous bodies on coal is extensively studied using proximate analysis. The works of Stewart *et al.* (2005); Rimmer *et al.* (2009) and Gröcke *et al.* (2009) are modern examples of how proximate analysis is applied to this problem. The approach of these investigations is to transect the coal progressively away from the magmatic intrusion. The proximate analysis results are then compared to identify any trends or associations. The general consensus is that these igneous bodies have a conductive thermal influence of approximately 1.2 – 1.5 times the thickness of the intrusion (Stewart *et al.,* 2005; Rimmer *et al.,* 2009; Gröcke *et al.,* 2009). This influence is most often denoted by variations in the fixed carbon-, volatile matter-, and ash content percentages. An inversion in the fixed carbon and volatile matter trends is seen once the edge of the conductive thermal zone is reached, often with a reduction in ash concentration (Stewart *et al.,* 2005; Rimmer *et al.,* 2009; Gröcke *et al.,* 2009).

9.1. Methodology

As a base measure of the bulk organic nature and reactivity of the samples, classical thermogravimetric proximate analysis was performed on sample set B. A three-stage proximate analysis procedure was used with a weight range of 10 – 15 mg of sample placed into a platinum crucible. The crucible was then inserted into the Perkin Elmer STA 6000 thermogravimetric analyser (TGA) housed at the University of Witwatersrand. The samples were exposed to a temperature ramping sequence from 30 °C to 110 °C at 50 °C/min in a nitrogen-rich environment at 40.0 ml/min. The samples were then held at 110°C for 3 min. During this ramping, it is assumed that all inherent moisture within the sample was driven off. The sample's temperature was then increased to 700 °C at 30 °C/min in the same nitrogen-rich environment. This stage was assumed to drive off the volatile material within the samples. The samples

were then heated to 900 °C at 30 °C/min in an oxygen rich environment at a flow rate of 40 ml/min, where the samples were then held for one min to ensure complete combustion of the organic material. The subsequent mass/time data was refined into the classical moisture-, volatile matter-, ash-, and fixed carbon percentages and then formatted into thermogravimetric curves to analyse the reactivity of the samples during the temperature ramping sequence

9.2. Proximate Analysis Results

The proximate analysis results are displayed in Table 9 and Figures 62 and 63 below.

Table 9: Proximate analysis results of C4 lower coals.

Distance from dyke (m)	*Moisture content (%)*	*Volatile matter (%)*	*Fixed carbon (%)*	*Ash (%)*
0	3.42	39.46	37.43	19.69
1	3.96	50.68	31.21	14.15
2	3.39	53.32	34.13	9.16
3	4.45	60.7	22.97	11.87
4	4.4	54.11	29.04	12.45
5	5.58	16.2	67.2	11.01
6	6.36	17.27	69.56	6.81
7	5.16	18.14	67.51	9.19
8	5.29	14.09	64.19	16.43
9	5.69	16.54	64.3	13.48
10	6.57	19.2	56.54	17.69
11	5.35	16.63	64.7	13.33
12	5.72	15.51	63.3	15.47
13	5.2	19.24	63.03	12.53
14	5.3	16.48	65.66	12.57
15	6.32	17.26	64.03	12.4
16	5.31	18.31	63.55	12.82
17	6.02	14.48	66.8	12.71
18	5.38	17.6	60.26	16.75
19	4.5	23.9	63.33	8.27

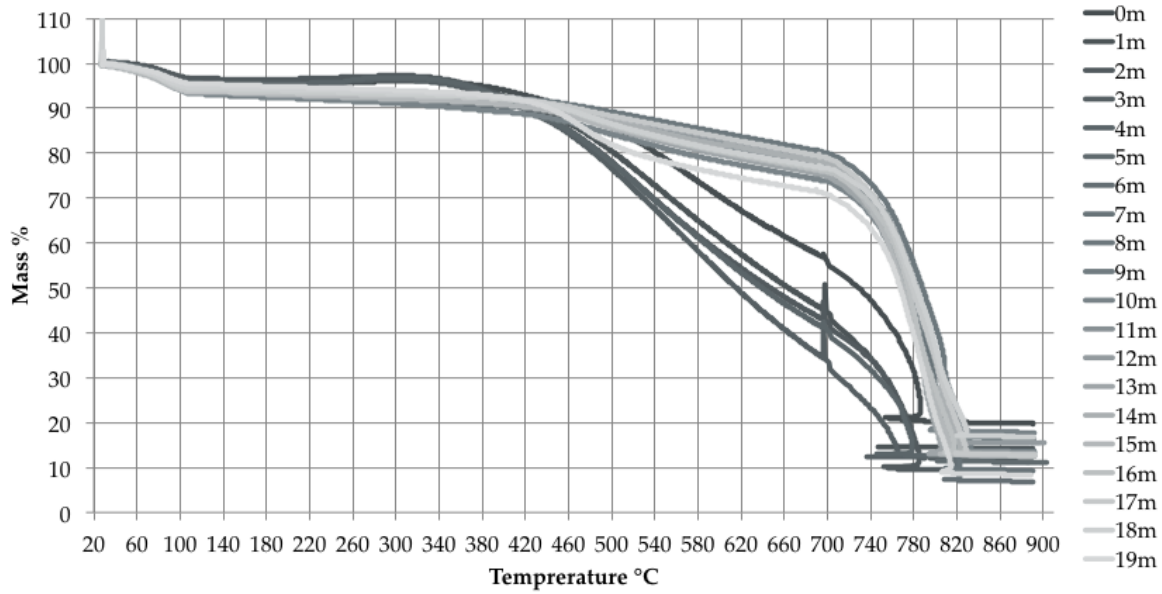

Figure 62: Thermogravimetric curves for all coal samples.

The thermogravimetric curves of Figure 62 depict the reactionary rates of the coal samples during proximate analysis. Notable mass influxes at ~ 690 °C are identified for samples within 5 m of the dolerite intrusion; beyond this the increase in mass is not identifiable.

The gradient of the curves between 460 – 820 °C are variable as all samples are undergoing identical temperature ramping sequences. The variation in gradients must be related to the rate of mass loss during rising temperatures in an anoxic environment. This shows a distinctly different reactive signature for samples closer to the dolerite intrusion (darker grey curves) when compared to those greater than 5 m from the dolerite intrusion.

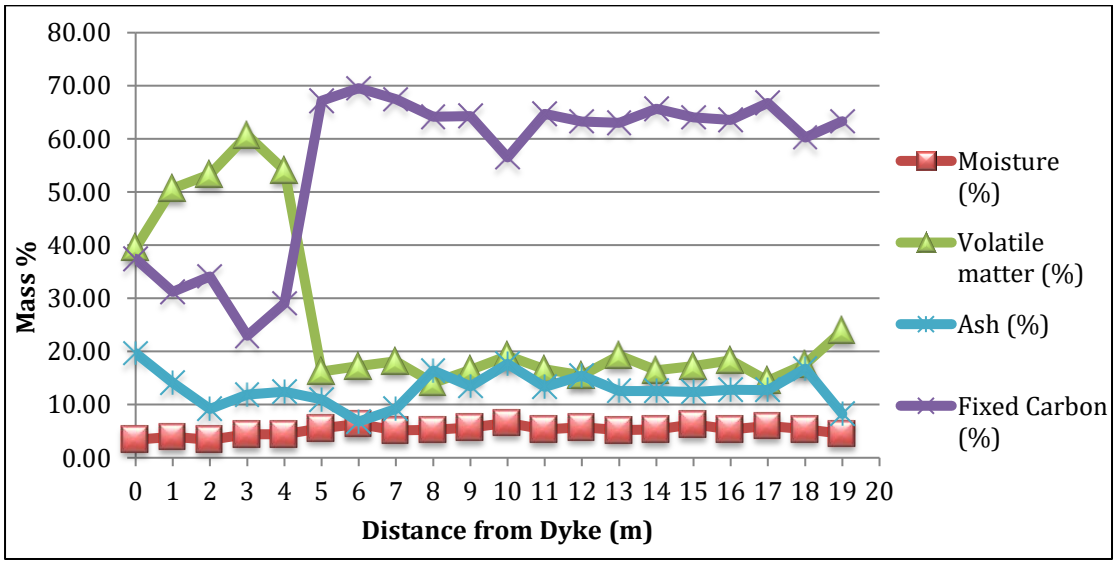

Figure 63: Proximate analysis results for all samples plotted against their position from the dolerite intrusion.

Figure 63 shows the systematic variations of the proximate analysis results from Table 9. Moving away from the dolerite intrusion, the moisture content and ash percentage remain relatively constant while a

significant change in the volatile matter percentage and fixed carbon percentage is noted. At a distance of 5 m from the intrusion, there is an inversion of the fixed carbon and volatile matter relationship. Of interest in Figure 63 are the high volatile matter percentage values which are greater the 50 % close to the intrusion, and the subsequent reduction and stabilisation of volatile matter percentage moving away from the intrusion.

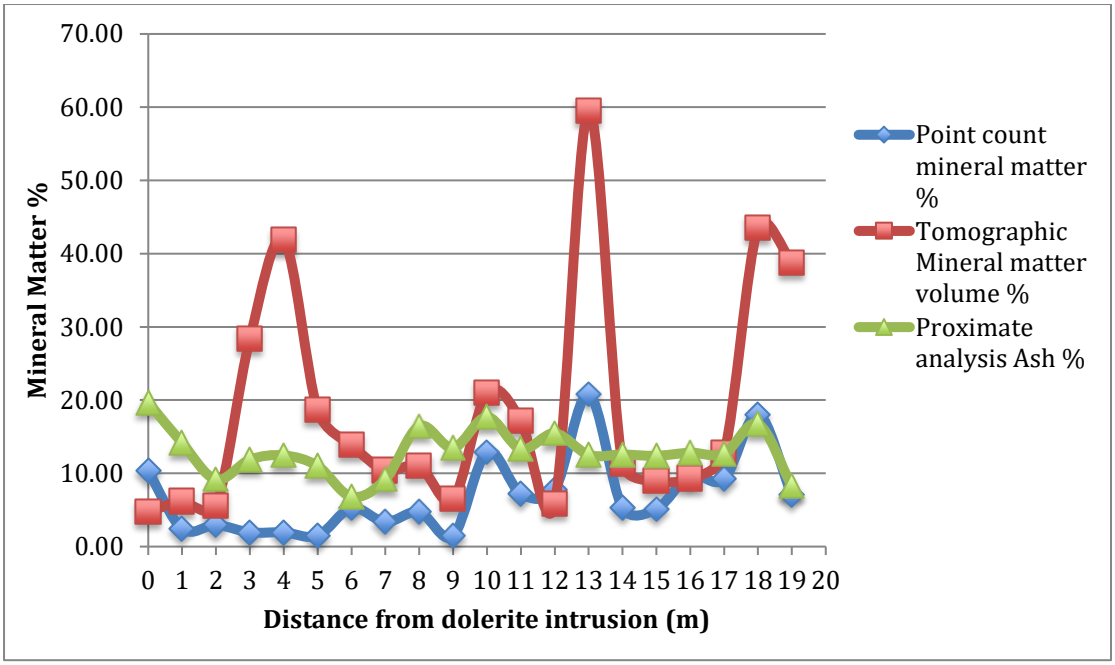

Figure 64: Comparison between petrographic mineral matter point-count percentage, tomographic mineral matter volume percentage and, proximate analysis ash percentage

Figure 64 is an expansion on the comparison seen in the X-ray tomography section. This figure adds proximate analysis ash content percentage to the comparison. Correlations between tomographic, petrographic, and proximate analyses are good. The volume percentages noted in the 3D tomography are, however, larger than those noted in either petrographic or proximate analyses. Of interest in Figure 63 are samples 3, 4, 5 and 13. The trends in tomographic mineral matter volume % in samples 3, 4 and 5 correlate to the proximate analysis ash % and not to the petrographic point-count analysis. Sample 13 shows a reduction in ash content while both petrographic point-count and 3D tomographic analyses show increases in inorganic material.

9.3. Summary discussion

Gröcke *et al.* (2009) investigated the C4 lower coal seam at the Sasol Secunda mining operation. The investigation was of a smaller dyke intersection than this study. During their petrographic investigation they noted devolatilisation vacuoles present within the volatile-rich vitrinite macerals within a distance from the dolerite contact that equated to 1.2 – 1.5x the cross-sectional width of the dolerite.

The zone of thermal effect is well described by Rimmer *et al.* (2009) and if this same theory is applied to the study area, the zone of thermal influence of the dolerite would be from ~ 4 – 5 m from the intrusion. This zone of thermal influence can be seen in Figure 62, where the reaction rates during the proximate analysis differ dramatically when comparing samples within 5 m of the dolerite to those beyond. This variation is most notable during the temperature ramping sequence designated for the measurement of volatiles. The rate of reaction, depicted by the gradient of the thermogravimetric curve, is dramatically steeper for the proximal samples within the first 5 m. This steeper gradient of the proximal samples is maintained until ~ 690 °C, at which point all the samples show a mass influx. The noted mass influx is postulated to be carbonation and sulphation reactions occuring in the Thermo Gravimetric Analysis (TGA). Several reactions described by Anthony *et al.* (2001) may be the cause of this influx:

$CaCO_3(s) \leftrightarrow CaO(s) + CO_2$ *equation 1*

$CaO(s) + CO_2\,(g) + 1/2O_2(g) \leftrightarrow CaCO_4(s)$ *equation 2*

$CaO(s) + CO_2\,(g) + 1/2O_2(g) \leftrightarrow CaCO_3(s)$ *equation 3*

$CaO(s) + H_2O\,(l, g) + 1/2O_2(g) \leftrightarrow Ca(OH)_2(s)$ *equation 4*

$Ca\,(OH)_2(s) + CO_2(g) \leftrightarrow CaCO_3(s) + H_2O(g)$ *equation 5*

These equations would allow for the formation of solid material from the gaseous molecules in the TGA. The temperature of reaction for these equations is 650 – 780 °C, which places the mass influx noted at ~690 °C perfectly in range (Anthony *et al.,* 2001). Once one or a combination of these reactions takes place, it is then followed by the breakdown of these solid particles due to the steady introduction of oxygen into the TGA system at 700 °C. Following the mass influxes, the distal samples' reactionary gradient is rapidly increased.

When assessing Figure 63, the noted inversion of volatile matter percentage and fixed carbon percentage falls in the 4 – 5 m range. This is in agreement with the TGA curves, where a difference is noted between the samples within 5 m of the dolerite and those beyond. The volatile-fixed carbon relationship and the reaction rates noted in the TGA curves both show the zone of thermal influence of the dolerite within 5 m of the dolerite-coal contact. The effect of the dolerite is consistent with the works of Rimmer *et al.* (2009). High volatile matter percentage proximal to the intrusion is, however, not a normal characteristic feature of heat affected coals.

Bussio and Roberts (2016) noted extensive variability in volatile matter percentages in proximity to dolerite in this area, with some volatile matter percentages in excess of 50 % for samples in direct contact with dolerite intrusions. A case can, therefore, be made that this increase in volatile matter percentage is plausible for the region, although not commonly seen in other areas. The mean vitrinite reflectance values are, however, not in agreement with the volatile matter percentages. The anomalous proximate analysis result is localised to the volatile matter percentage. When investigating the ash content values in Figure 64 there is a strong correlation between this and both the petrographic point-count and 3D tomography analysis. Further, the samples at 3, 4, and 5 m from the intrusion show

correlation to the 3D tomographic analysis only, which may be as a result of the particulate matter being too small to be recognised during petrographic point-counting. The sample at 13 m from the intrusion shows a drop in ash content but a noted increase in sulphides; the reaction of this with hosted carbonates during the pyrolysis could account for the lower ash content value when compared to the influxes in mineral matter as measured by both petrographic point-counting and 3D tomographic analysis.

CHAPTER 10: APPLICATION OF SCHMIDT HAMMER TESTING

Coherency and material strength for bulk samples are crucially important in the assessment and design of mining operations (Özkan and Bilim, 2008). The quantification of these values is often onerous, requiring time-consuming sample preparation (Özkan and Bilim, 2008). Authors such as Sheorey *et al*. (1984) and Poole and Farmer (1980) investigated the use of Schmidt hammer rebound data to evaluate coal strength as well as the consistency of its results and repeatability of the test. The benefit of this technique was the ease and simplicity of the actual analysis as well as its ability to be used *in situ* with no sample preparation (Sheorey *et al*., 1984). In both Sheorey *et al*. (1984) and Poole and Farmer (1980), the technique produce consistent, repeatable results if the data was derived from an average of multiple point tests.

The Schmidt hammer itself was developed in 1948 for non-destructive testing of concrete hardness and later used to estimate rock strength. The device itself is simple but reliable—consisting of a plunger released from a spring that then impacts a surface. The rebound of the plunger is measured and reading is taken directly form the device. There are two varieties of the device: an L-type and an N-type, each producing 0.735 and 2.207 Nm of impact energy, respectively (Torabi *et al*, 2010).

The works of Sheorey *et al*. (1984), Poole and Farmer (1980), and Özkan and Bilim (2008) investigated the use of Schmidt hammer analysis on coal as an *in situ* coalface test. The work showed that it was a reliable technique for strength estimations, provided that an optimal number of readings were taken as determined by the surface area of analysis (Özkan and Bilim, 2008).

10.1. Methodology

For the purpose of this study, an estimation of the approximate hardness of the coal was investigated to obtain a quantitative value for physical character. The approach described in Özkan and Bilim (2008) was adopted to garner the most representative results from the L-type Schmidt hammer readings. Readings were taken *in situ,* prior to sampling, at 1 m intervals systematically away from the contact of the intrusion at each of the sampling sites depicted in Figure 25. The areas of analysis were separated into blocks of 15 x 15 cm where a grid of 3 x 3 was set. Readings were taken at the centre of each grid point and the average of the 9 readings were taken as representative. The subsequent rebound values were then converted to Uniaxial Compressive Strength (UCS) values using the equation proposed by Haramy and DeMarco (1985):

$$UCS = 0.994N - 0.383 \quad \textit{equation 7}$$

10.2. Results

The Schmidt hammer results are presented below.

Table 10: Schmidt hammer *in situ* rebound results from the C4 lower coal seam Secunda.

Grid position	*1*	*2*	*3*	*4*	*5*	*6*	*7*	*8*	*9*	*Sum Ave = N*	*UCS = 0.994N-0.383*
Sample Number											
0	30	32	29	28	34	30	30	34	26	30.33	29.77
1	35	37	34	35	35	38	38	32	32	35.11	34.52
2	34	34	34	35	34	37	35	30	34	34.11	33.52
3	32	32	32	32	32	34	32	32	32	32.22	31.65
4	32	32	32	32	33	32	32	32	32	32.11	31.54
5	32	34	34	32	32	32	30	30	32	32	31.43
6	32	32	32	32	32	35	32	32	30	32.11	31.54
7	38	35	40	40	40	38	38	38	38	38.33	37.72
8	46	44	49	44	46	46	46	44	46	45.67	45.01
9	40	40	40	40	38	38	40	40	40	39.56	38.94
10	48	48	48	47	47	47	48	48	48	47.67	47
11	46	46	46	46	46	47	48	48	46	46.56	45.89
12	50	50	50	52	52	52	50	50	50	50.67	49.98
13	52	53	53	52	52	52	51	53	52	52.22	51.53
14	42	42	45	42	46	42	44	42	42	43	42.36
15	36	36	36	36	36	37	36	36	36	36.11	35.51
16	34	34	33	34	34	35	34	34	35	34.11	33.52
17	46	46	46	48	45	47	46	46	46	46.22	45.56
18	42	42	42	42	43	43	44	42	42	42.44	41.81
19	46	46	48	48	45	45	46	46	46	46.22	45.56

Table 10 displays the individual Schmidt hammer results with average N value shown in the column entitled “sum ave”. This value was then converted to the UCS value using the Haramy and DeMarco (1985) equation 7. The resultant UCS values are shown in Figure 65, where a noted increase in UCS variability can be seen for the samples beyond 6 m from the dolerite intrusion.

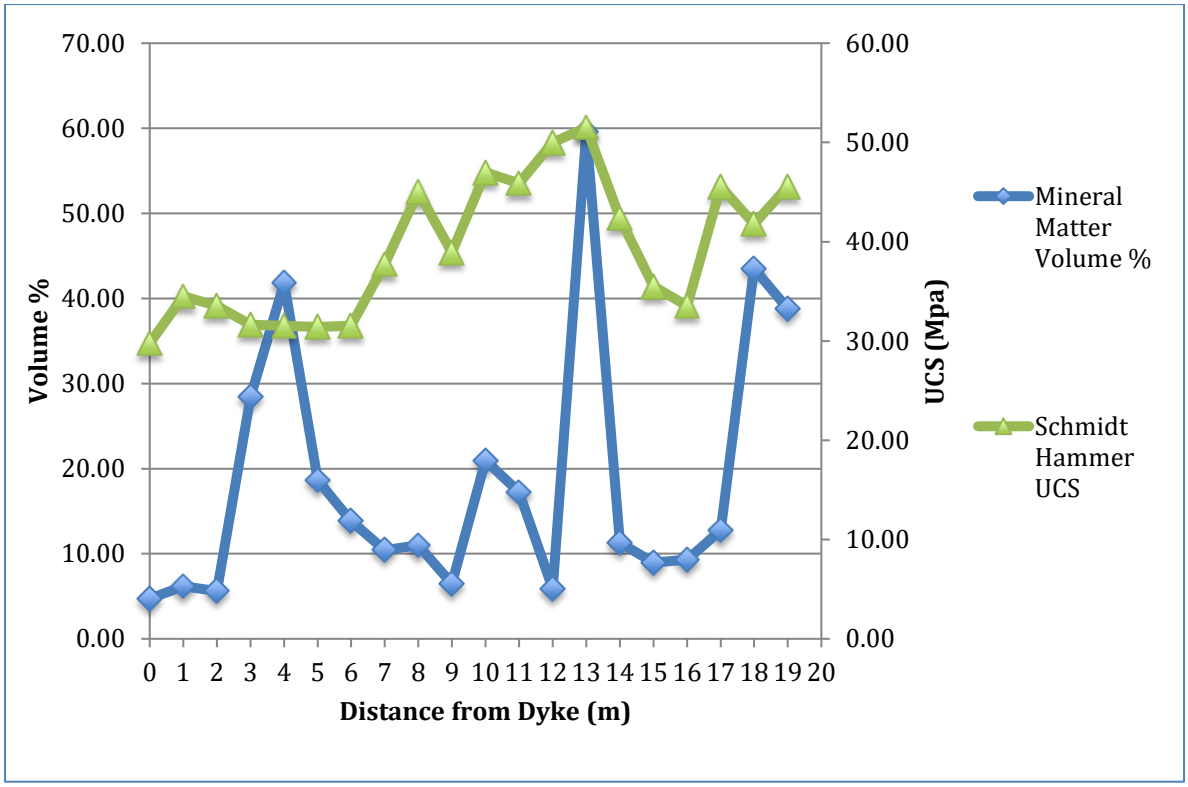

Figure 65: Comparative analysis of tomographic volumes of mineral matter and Schmidt hammer UCS results.

Within Figure 65, the variability of UCS increases with greater distance from the dolerite intrusion. Further investigation shows an increase in correlation to the mineral matter volume percentage with increasing distance from the dolerite intrusion (Fig. 65). Of specific importance is the stark drop in uniaxial compressive strength between 13 m and 14 m from the intrusion. This drop directly correlates to a large scale drop in mineral volume percentage within the sample; this correlation is also noted at 9 m.

Das (1972) investigated the variations in coal's Vickers microhardness, in relation to volatile matter concentration. The study focused on what Das termed abnormally metamorphosed coal and normal coal. By this he meant coal that had been affected by thermal alteration by magmatism and coal that hadn't, respectively. The findings are represented in Figure 66 and show the results of normal coal and abnormally metamorphosed coal.

The abnormally metamorphosed coal results display the position of the top and base of the seam. This was done as the sampled area was thermally affected by an igneous sill above the siltstone roof of the seam. Figure 66 shows the vastly differing micro-hardness values for coals of similar volatile matter content. Das (1972) concluded that this difference could be used as an indicator for the contact thermal metamorphism induced by the igneous sill.

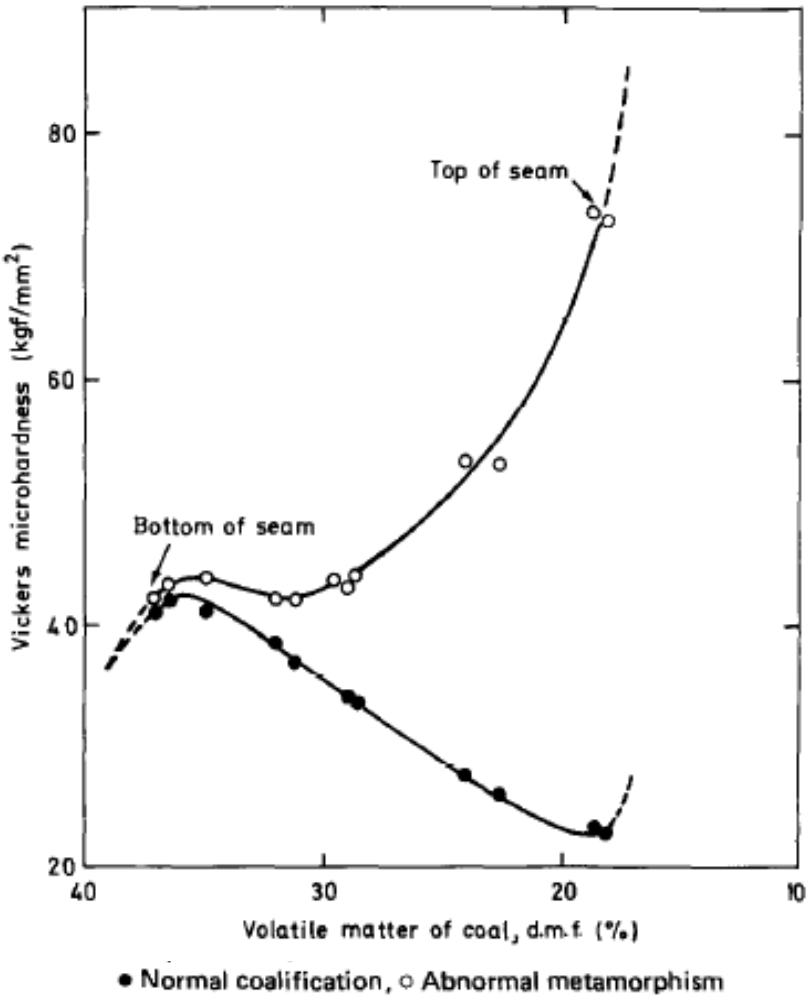

Figure 66: Vickers micro-hardness of normal coalification (normal coal) and abnormal metamorphism (abnormally metamorphosed coal) against volatile matter content (d.m.f % Dry mineral free percentage) (Das, 1972).

The almost linear decrease in micro-hardness with reduction in volatile matter under normal coalification is not observed for abnormally metamorphosed coal; rather, there is an increase in micro-hardness with a reduction in volatile matter. This increase in micro-hardness is most evident at volatile matter percentages below 25 %, as well as closer to the top of the coal seam. Das (1972) used point load testing and authors such as Tiryaki *et al*. (2001), Babatunde (2010), and Vachaparampil (2016) have shown that point load techniques, such as Vickers micro-hardness, can be accurately compared to rebound techniques, such as the Schmidt hammer.

Using the approach of Das (1972) on the data collected here, a comparison between Schmidt hammer UCS and proximate analysis volatile mass percentage is shown in Figure 67. The scatter plot shows UCS values with a variance of between ~ 29 – 35 MPa, until a volatile matter percentage of less than 25 is reached. From this point, there is a large variance in the UCS values from ~ 31 – 53 MPa. Note that the samples with greater than 25 % volatile matter are only found within a distance of 5 m from the dolerite intrusion.

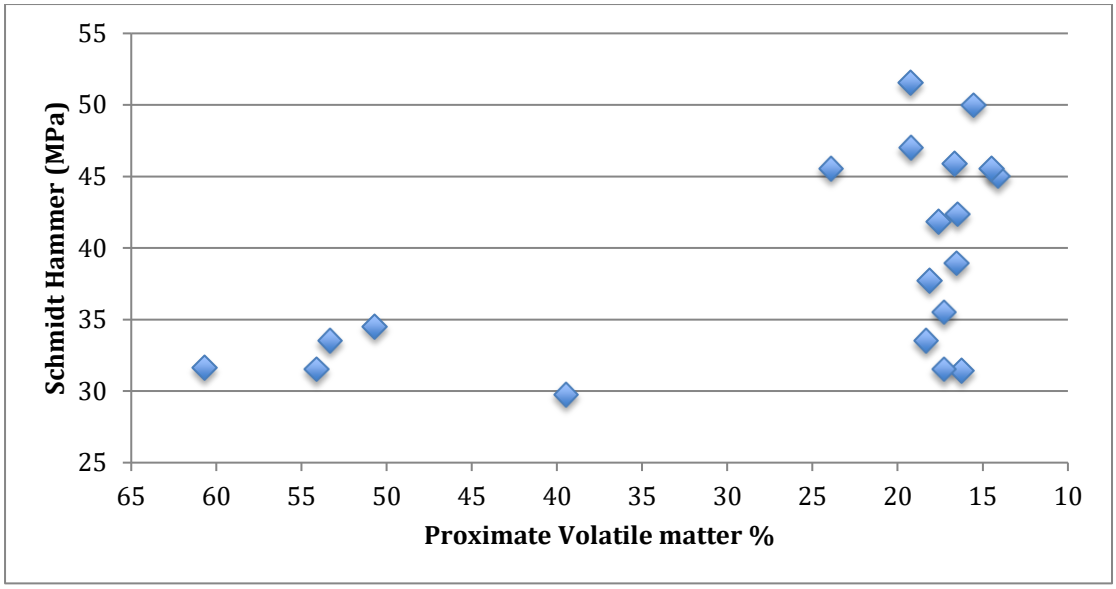

Figure 67: Graphical comparison of volatile matter percentage and Schmidt hammer USC for the C4 lower coal seam and dyke intersection.

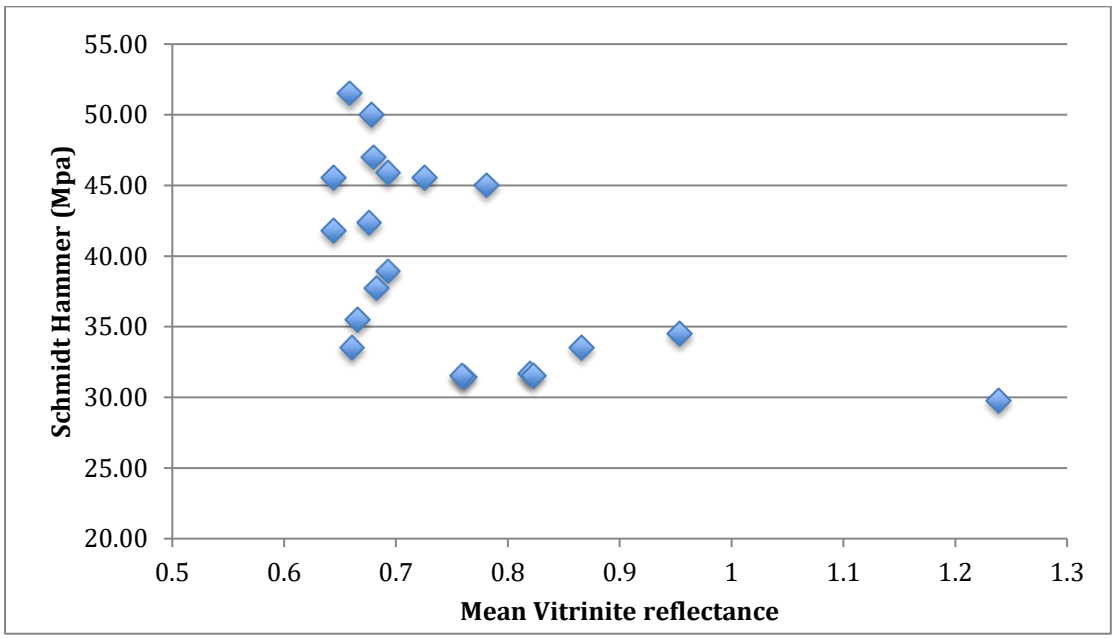

Figure 68: Comparative scatter plot of uniaxial compressive strength against mean vitrinite reflectance values.

Figure 68 displays a scatter plot of mean vitrinite reflectance against Schmidt hammer UCS. With increasing mean vitrinite reflectance there is an increase in consistency of UCS values. The consistency is most prevalent within samples with mean vitrinite reflectance values greater than 0.8. Of importance here is that only samples within 5 m of the dolerite intrusion host mean vitrinite reflectance values greater than 0.8.

Petrographic maceral group analysis allows for comparison between total reactive macerals, total inertinite and UCS as shown in Figure 69. Samples close to the dolerite intrusion show no correlation between maceral content and UCS; however, from 11 m and further there is a negative correlation with

the total reactive maceral content and UCS as well as a positive correlation with total inertinite. This depicts a general hardening effect with increasing inertinite.

Figure 70 from Hower *et al*. (2008) shows that there is a variation in maceral-type micro-hardness. From it, a note must be made that with varying maximum reflectance values pseudovitrinite has consistently higher micro-hardness values than that of vitrinite, showing that maceral types have unique micro-hardnesses. Figure 69 shows the relationship between UCS and maceral concentrations within the study area. Figure 69 displays that there is not a consistent correlation between maceral concentrations and hardness; however, at sample distances 0, 1, 7, 8, 9, 11, 12, 16, 17, 18, and 19 m, the concentrations of inertinite from point-count analysis correlate with the variations in the UCS.

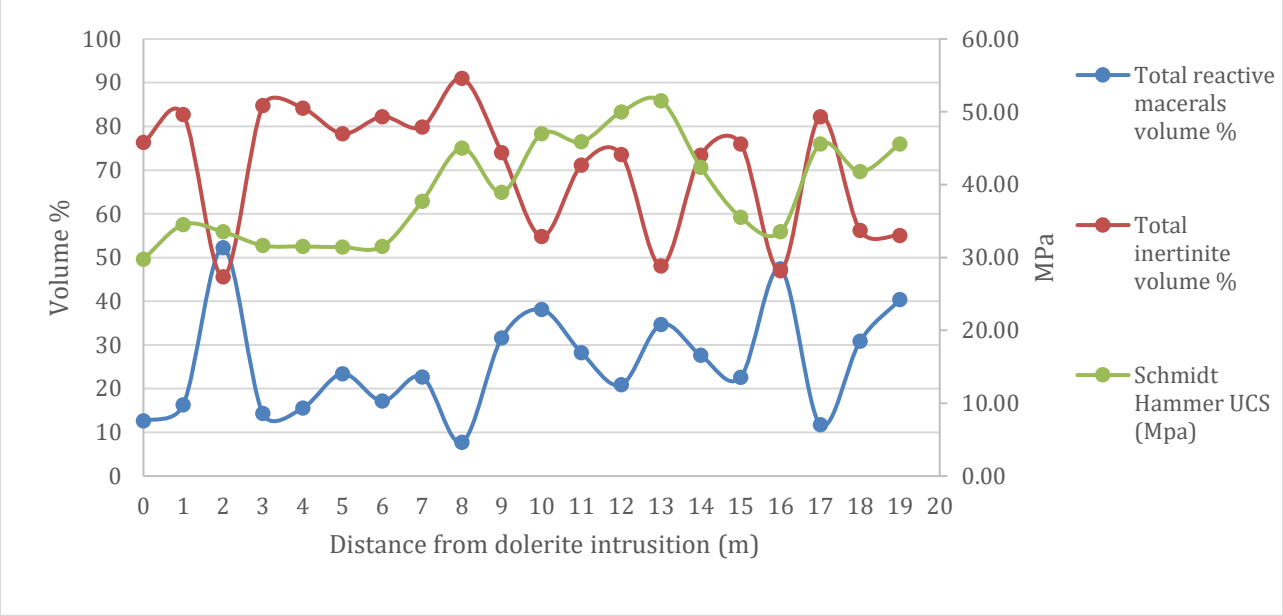

Figure 69: UCS compared to the petrographic maceral group analysis volume percentages of total reactive macerals and total inertinite.

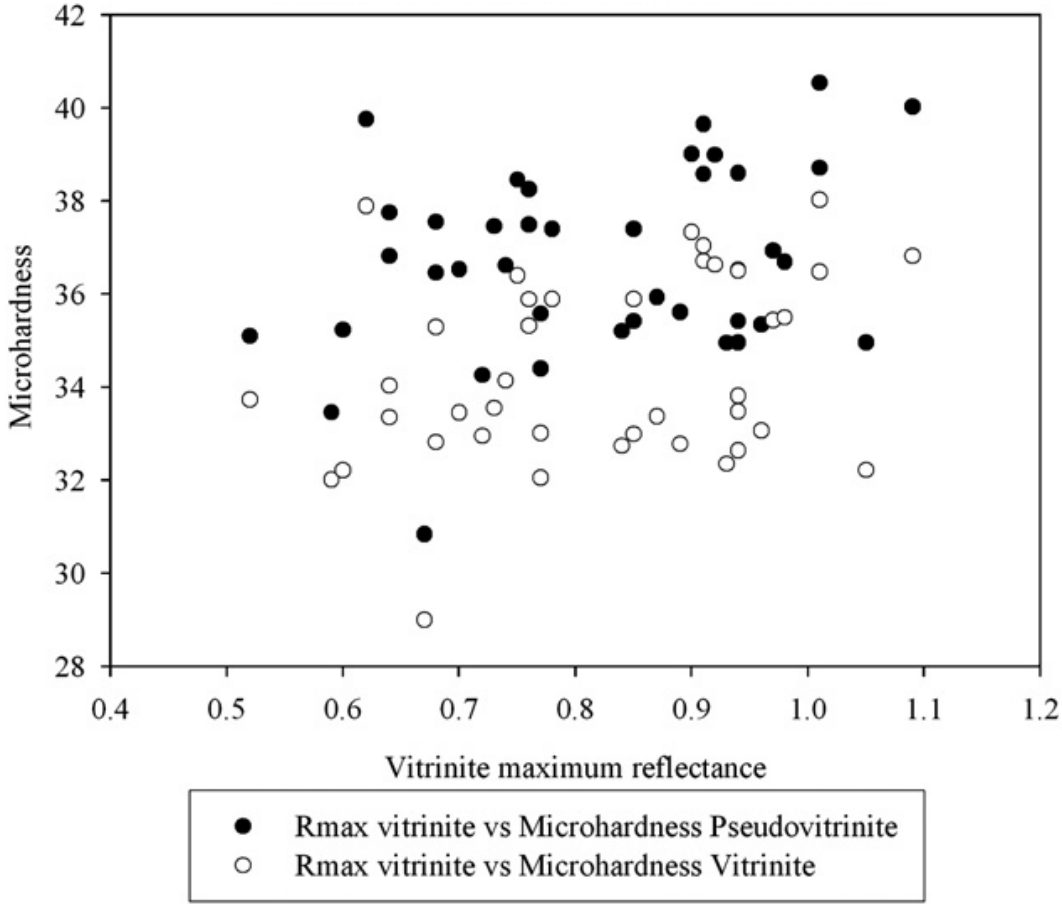

Figure 70: Telovitrinite and pseudovitrinite micro-hardness versus vitrinite (telovitrinite) maximum reflectance for Eastern Kentucky coals (Hower *et al.*, 2008)

10.3. Discussion

The results of the Schmidt hammer testing agrees with the results of Poole and Farmer (1980), Sheorey *et al.* (1984), and Özkan and Bilim (2008), reaffirming the potential use of the Schmidt hammer as an *in situ* testing tool. Further investigation of the results shows a consistent hardness of between 30 - 35 MPa up to a distance of 5 m from the dolerite intrusion. Beyond 5 m, the hardness values become erratic, with variability between 32 – 52 MPa but with a general hardening trend.

Looking at the relationship between mean vitrinite reflectance and UCS, there is a consistent hardness of 30 – 35 MPa for mean reflectance values of > 0.8. It is worth noting that samples with mean vitrinite reflectance of < 0.8 are only found within 5 m of the dolerite intrusion. The change in hardness values at 5 m falls in line with the zone of thermal influence as seen in the works by Stewart *et al.* (2005), Rimmer *et al.* (2009), and Gröcke *et al.* (2009). Of interest here is that the samples show a reduction in hardness closer to the intrusion—contrasting Stewart *et al.* (2005) and Das (1972), where the coals showed a hardening toward the igneous intrusion. From literature, the thermal influence zone noted in Rimmer *et al.* (2009) and Gröcke *et al.* (2009) shows a distinctive physical change in the maceral components. Within the Secunda study area physical change in maceral components seems to have a homogenising effect on the structural properties of the coal, allowing for a more consistent UCS value.

Hower *et al*. (2008) showed hardness variations between maceral types. These measurements were done on a maceral specific basis. When looking at Figure 69, there is no clear correlation with maceral concentrations and hardness. However, samples at 0, 1, 7, 8, 9, 11, 12, 16, 17, 18, and 19 m have a trend comparable to that of the Schmidt hammer analysis. In Figure 65 a correlation is noted between mineral matter content and UCS at sample locations 9, 14, 15, and 16 m, where the reduction in mineral matter correlates with a large drop in UCS. Throughout the sampled area, compositional variations of maceral concentrations and mineral matter volume percentage have a notable effect on the coal UCS, with increasing inertinite and mineral matter having a hardening effect on the coal samples.

CHAPTER 11: DISCUSSION

The primary aim of this project is to better understand the physicochemical nature of heat-affected coals. The link between physical and chemical properties requires that these results be compared and contrasted in order to understand the physicochemical properties of heat-affected coal and the mechanics of its metamorphism.

The approach used a variety of classical, modern, and new techniques to provide a broad view of the metamorphosed coal seam. In order to understand the interrelationship of each of these data sets, Table 11 displays the results of a correlation test of the data derived from each technique. Of importance within this table is the lack of strong linear correlations within the data. Understanding the reasons behind the lack of linear correlations is critical in defining the parameters of the metamorphic system as well as the applicability and the quality of the techniques and data produced by them.

To understand the metamorphic system, a review of the underground sampling that took place at the iThemba Lethu Shaft, in Sasol South Africa's Secunda mining operation is required. The sampling of the freshly-exposed coal face was performed to mitigate any oxidation effects on the coal. The site itself is intruded by an extensively re-carbonated locally defined DO8 dolerite. The re-carbonation of the dolerite provides the first of many indications of hydrothermal action and secondary carbonate mineralisation. The re-carbonation of the dolerite provides two mechanisms through which the coal could be altered: thermally and hydrothermally.

Table 11: Pearson's correlation matrix of results from all analysis techniques results and their corresponding r-values (sample correlation coefficient).

	Distance from dolerite intrusion	Schmidt Hammer UCS (Mpa)	3D Tomography Mineral Norm %	3D Tomography Pore Space Norm %	3D Tomography Organic Matteral Norm %	Proximate Analysis Moisture Content %	Proximate Analysis Volatile Matter %	Proximate Analysis Fixed carbon %	Proximate Analysis Ash Content%	Petrography Point count anaylsis: Vitrinite macerals	Petrography Point count anaylsis: Inertinite macerals	Petrography Point count anaylsis: Liptinite macerals	Petrography Point count anaylsis: Mineral Matter	Petrography Point count anaylsis: Total Inertinite	Petrography Point count anaylsis: Total reactive macerals	GC*GCTOFMS : Number of Compounds	Mean Vitrinite reflectance
Distance from dolerite intrusion	1.00																
Schmidt Hammer UCS (Mpa)	0.62	1.00															
3D Tomography Mineral Norm %	0.30	0.30	1.00														
3D Tomography Pore Space Norm %	0.01	-0.19	-0.27	1.00													
3D Tomography Organic Matteral Norm %	-0.31	-0.26	-0.97	0.03	1.00												
Proximate Analysis Moisture Content %	0.54	0.39	-0.02	0.12	-0.01	1.00											
Proximate Analysis Volatile Matter %	-0.67	-0.55	0.08	-0.01	-0.08	-0.77	1.00										
Proximate Analysis Fixed carbon %	0.67	0.50	-0.06	-0.02	0.07	0.74	-0.98	1.00									
Proximate Analysis Ash Content%	-0.04	0.22	-0.09	0.13	0.06	-0.03	-0.05	-0.16	1.00								
Petrography Point count anaylsis: Vitrinite macerals	0.24	0.09	0.12	-0.28	-0.05	-0.20	0.04	0.02	-0.21	1.00							
Petrography Point count anaylsis: Inertinite macerals	-0.40	-0.28	-0.33	0.30	0.26	0.08	0.09	-0.11	0.04	-0.94	1.00						
Petrography Point count anaylsis: Liptinite macerals	0.07	-0.01	0.34	0.03	-0.36	0.22	0.11	-0.07	-0.26	-0.07	0.09	1.00					
Petrography Point count anaylsis: Mineral Matter	0.51	0.55	0.54	-0.17	-0.52	0.20	-0.35	0.27	0.40	0.27	-0.59	-0.26	1.00				
Petrography Point count anaylsis: Total Inertinite	-0.40	-0.28	-0.33	0.30	0.26	0.08	0.09	-0.11	0.04	-0.94	1.00	0.09	-0.59	1.00			
Petrography Point count anaylsis: Total reactive macerals	0.33	0.15	0.14	-0.29	-0.07	-0.06	-0.08	0.13	-0.24	0.98	-0.92	0.05	0.26	-0.92	1.00		
GC*GCTOFMS : Number of Compounds	-0.43	-0.26	-0.16	0.61	0.01	-0.26	0.36	-0.46	0.51	-0.28	0.26	-0.25	-0.04	0.26	-0.37	1.00	
Mean Vitrinite reflectance	0.76	0.37	0.40	0.00	-0.41	0.04	-0.27	0.32	-0.22	0.39	-0.45	0.06	0.33	-0.45	0.40	-0.27	1.00

Looking at the results of the five techniques used, a consistent pattern emerges. This pattern shows six zones of results moving further away from the dolerite intrusion. Within the petrographic analysis, 6 zones were noted:

1. From 0 to 2 m from the intrusion, high levels of fracturing of semifusinite macerals as well as devolatilization vacuoles present within collotelinite macerals. It is plausible to assign these features to thermal effects of the igneous intrusion, due to the samples proximity as well as the increased reflectance values noted in these samples.
2. From 3 to 5 m from the intrusion, the macerals show very little textural alteration or fracturing and much reduced vitrinite reflectance values. Siderite is more prevalent as an inclusion between macerals as well as within structural features, such as pitted texture within collodetrinite.
3. From 6 to 9 m from the intrusion, there is an increase in the pitted texture within collodetrinite macerals and a remarkable increase in visible siderite and calcite mineral inclusions.
4. At 10 m from the intrusion, the scale of the carbonate inclusions begins to increase as well as the first occurrence of large scale amalgamation of pyrite. The presence of pitted textures is all but gone, however fractures within macerals become more apparent, with these fractures being infilled by both calcite and pyrite. These features persist towards 17 meters from the intrusion where the sample is devoid of sulphides.
5. At 18 m from the intrusion, sulphide are once again present in large amalgamations.
6. At 19 m from the intrusion, the macerals show no notable textural variations and is almost devoid of inorganic inclusions apart from occasional well formed siderite mineralization.

The zones noted in the petrographic analysis were defined through textural, point-count, and vitrinite reflectance variations. Looking at the vitrinite reflectance values in isolation, there is an increase approaching the dolerite, displaying the increasing thermal influence that the dolerite had on the coal. It is critical to note that no coking of the coal has occurred.

When viewing the textural and point-count data, two primary features are apparent. One is that there are no textural features relating to high-temperature metamorphism. Rather, there are subtle pitted textures within the vitrinite macerals. Secondly, the appearance and amount of inorganic material within samples is highly variable, with localised influxes between 6 and 17 m from the intrusion. Viewing these two features in conjunction with the reflectance figures, there are cells of common trends that become easily definable and are denoted by the six zones. Hence, it is prudent to look at each technique and the results thereof with the viewpoint of a polynomial rather than linear correlation.

The quantitative results derived from 3D X-ray tomography show large volumetric variations in organic material, inorganic material, and pore spaces. Of interest is the strong correlation between the tomographically measured inorganic content and the results from petrographic point-counting. This correlation is maintained beyond 5 m from the intrusion. Prior to this the measurements have little correlation. In addition to this, the X-ray tomography data shows inflexion points at 3, 5, 9, 12, 14, and 17 m from the intrusion. These data inflexion points mark a strong trend change in the volume of organic and inorganic material (Fig. 49). The inflexion points correlate strongly with the boundaries noted in the petrographic zones. Effectively, the tomographic results do not correlate to the

petrographic results directly until 5 m from the intrusion, which from the reflectance values, seems to be the boundary of thermal influence. Beyond 5 m, the petrographic and tomographic results can be grouped into 6 zones. The zones in the tomography are defined by textural features of the inorganic material found in them as well as the compositional inflexion points.

The correlation between results is further shown in the GC*GC-TOF-MS data, specifically when looking at the number of unique compounds identified against pore space volume data form tomographic analysis. Figure 61 shows a near perfect correlation between the two data sets, barring a deviation at a distance of 10 m and 11m from the intrusion. What this shows is that pore space may provide the deposition setting for organic molecules not housed within the maceral structures.

The samples at 10 m and 11m from the intrusion are the only instance where an increase in unique compounds is not matched with an increase in pore space. Samples DK10 and 11 have unique inorganic texture, displaying large grained mineralization, but which cross-cut the sedimentary layering of the coal. This cross-cutting proves that the mineralization must have formed after the coal deposition. The formation of these grains has had an impact on the organic geochemistry of the sample.

The GC*GC-TOF-MS results and correlation to the tomographic analysis once again show a multitude of unique peaks. These peaks do not, however, occur at the boundaries of the zones seen in the petrographic analysis, but are noted within the zones. These peaks are also linked to the appearance of PAHs within the samples – more specifically Benzo (b) carbazole and Benzo (c) carbazole – compounds closely tied to the increased maturation of coals. These are compounds that the oil and gas sector commonly uses as markers to note the secondary migration of organic compounds. Essentially, the presence of Benzo (b) carbazole and Benzo (c) carbazole provides evidence that some of the organic constituents of these samples were transported via hydrothermal fluid to their current location.

Thermogravimetric analysis of the sample set produced unexpected results for volatile matter percentages. This has been attributed to the regional variations noted by Bussio and Roberts (2016). The ash measurements, however, provide a confirmation of the tomographic inorganic volume percentage figures but vary from the point-count data produced during petrography. This provides insight into the size range of the inorganic material hosted within coal, as samples at 3, 4, and 5 m from the intrusion show a correlation to the 3D tomographic analysis only, which may be a result of the particulate matter being too small to be recognised during petrographic point-counting. The Gröcke *et al.* (2009) investigation of a dyke intersection noted thermal influence within a distance from the dolerite contact that equated to 1.2 – 1.5x the cross-sectional width of the dolerite. When looking at the proximate analysis, reflectance analysis, and tomography-petrography relationships, a similar range is applicable to the sampling locality as the dyke investigated here has a width of 3 meters and the zone of contact thermal influence not extending past 5 meters.

The boundary of thermal influence is well displayed within the Schmidt hammer results, where there is a consistent UCS until ~ 6 m from the dolerite intrusion. Beyond 6 m from the intrusion, there are large degrees of variability, but a correlation can be seen with the concentrations of reactive and unreactive macerals. Figure 68 displays that there is some correlation with increased inertinite concentration and elevated UCS within the transect.

11.1. A systematic model of the devolatilisation process

The zones identified within the data are theorised to represent transitionary boundaries or fronts in which chemical and reactive changes take place. To describe these zones a simplistic model of the metamorphism of the coal is discussed.

The sampled coal's depositional environment, along the edge of a mid-Permian glacial valley, was subject to gradual climatic warming throughout its deposition. The region was intruded by numerous mafic igneous dykes and sills, associated with the Karoo large igneous province, during the mid-Jurassic. The igneous province was associated with extensional regime during the separation of East-Antarctica from Southern Africa during this period.

The sample site is intruded by a dolerite locally named DO8. From the works of Gurba and Weber (2001), Golab and Carr (2004), and Gröcke *et al*. (2009), it would be expected that this intrusion would have a thermal metamorphic aureole of 1.2 – 1.5x the cross-sectional width of the dolerite. This is confirmed by the petrographic reflectance values and corroborated by the tomographic and thermogravimetric analysis.

At the time of intrusion, the effect of the conductive heat from the dyke would directly alter the morphology of the more reactive maceral groups, such as vitrinite, within this aureole (Stewart *et al*., 2005; Rimmer *et al*., 2009; Gröcke *et al*., 2009). From the low degree of structural changes in vitrinite macerals noted in the petrographic analysis, it is safe to assume that there was a low level of conductive heat produced from this specific dolerite. The petrography shows only minor textural alteration of the vitrinite macerals. A pertinent feature of this sample locality is the high degree of re-carbonation in the intrusion. The low degree of textural alteration of the coal and high degree of re-carbonation in the dolerite is the first indication of a more hydrothermal metamorphic regime.

Even though only minor textural variations are noted in the samples, the morphology change would weaken the structure of the maceral. This would allow any further thermal influences, such as reinjection through the dolerite conduit or hydrothermal influence, to rapidly change the macerals. In this specific location, the conductive heating of the dolerite has mobilised fluids, evidenced through the GC*GC-TOF-MS identification of Benzo (b) carbazole and Benzo (c) carbazole. In addition, the presence of secondary carbonate minerals cross-cutting the sedimentary layering of the coal, noted in the 3D tomography, strongly suggests that a carbonate-rich fluid has percolated through the coal subsequent

to its deposition. The origin of these fluids could potentially be from the hydrated surrounding sediments, the coal itself, and a small component from the mafic dyke.

The hydrothermal fluids produced by the conductive heating would percolate through the surrounding sediments and the coal, following paths of least resistance. This would allow more porous and permeable areas of the coal to be more greatly affected. The reactivity of the hydrothermal fluid with macerals would be two-fold. Firstly, the heat (approximated at ~ 300 °C by Hatcher and Clifford (1997)) would be capable of disrupting the structure of some weakly formed maceral groups, such as resinites. The morphological changes in these macerals would have similar influences on the reactivity of the organic compounds as those changes produced from conductive heating. Secondly, the salinity and organic nature of the percolating fluid itself would be able to not only react with the maceral but also entrain some of the organic compounds. The efficacy of this would be dependent on the nature of the organic compound and its reactive affinity to the temperature and composition of the percolating fluid.

As the dolerite cools, so the influence of the hydrothermal fluid will be reduced. With the reduction in temperature, the percolation of the hydrothermal through the coal will slow and the energy state of the fluid will be lower. At this lower energy state, the fluid will have a reduced ability to hold entrained compounds, so the entrained material will begin to precipitate out of the fluid. From the GC*GC-TOF-MS results display the presence of highly soluble PAH and PAH derivatives in the samples DK0, 3, 5, and 8, which have both high pore space volume percentages and compound numbers, providing a setting where fluid transport and precipitation of soluble compounds is highly likely. This precipitation will result in the formation of secondary carbonaceous cleats, and in some cases re-carbonation of the dolerite itself. Evidence for this in the increase in mineral matter volume percentages in samples 2 – 6, 9 – 12, 13, 18 and 19 m from the dolerite intrusion (Fig. 65). Noteworthy here is that the organic and inorganic material would be deposited at different hydrothermal energy states. Evidence for the is see with an increase in organic compounds at sample sites 3, 8, 10, 15, and 19 m form the intrusion, while inorganic influxes appear ~ 1 m later. Again, the organic influxes show a direct relation to the porosity of the samples, thus it can be concluded that these molecules are deposited within the pores of the samples while the inorganic material fills these pores.

Porosity increases are therefore the trigger for the precipitation of both organic and inorganic material in the coal. These precipitation fronts are gradational, spanning 2 – 4 m. They may be defined by both the thermal energy state of the fluid and the composition of the fluid with respect to its organic and inorganic components. To simplify the model, Figure 71 is a schematic representation where the precipitation fronts are noted in grey.

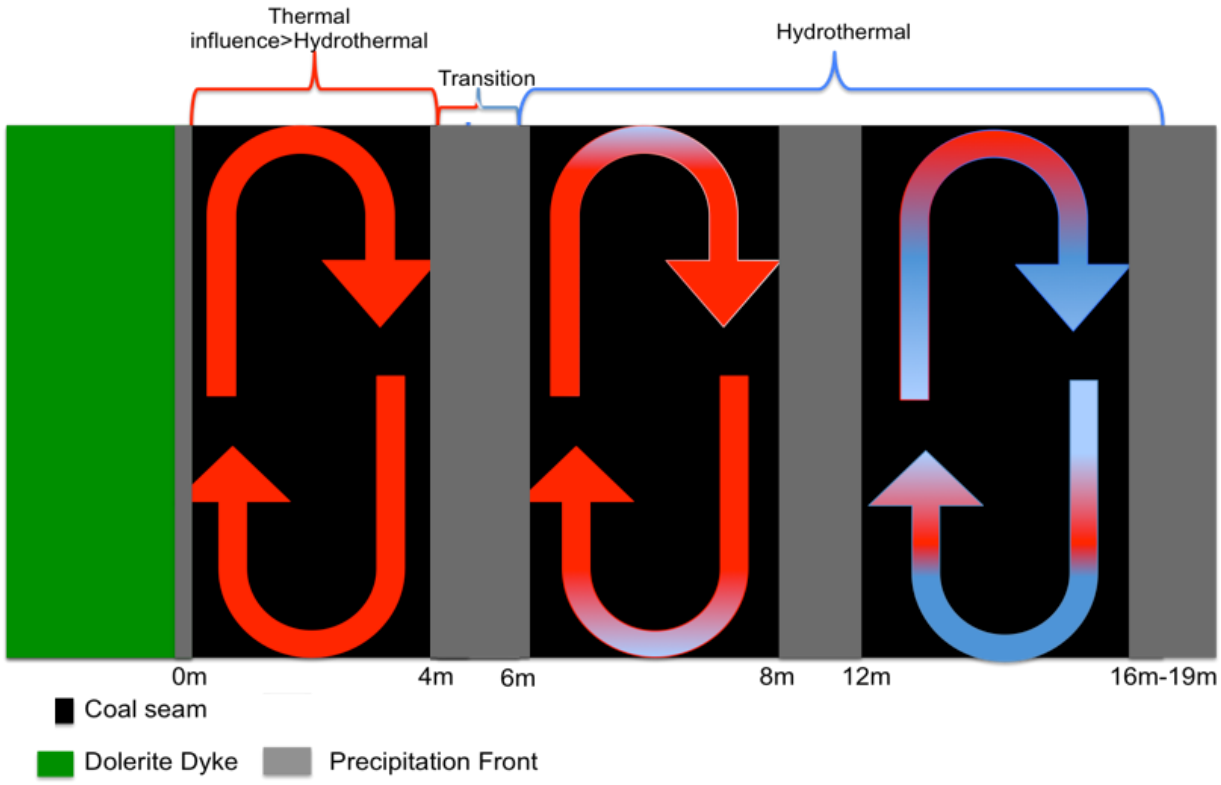

Figure 71: Schematic precipitation front model

CHAPTER 12: CONCLUSIONS AND RECOMENDATIONS

The economic significance of coal as a current and future energy source cannot be denied, and neither can the environmental impact of its by-products. The physicochemical properties of coal are complex, and attempts at defining its chemical structure by scholars such as Castro-Marcano *et al*. (2012) are only now beginning to describe the tens of thousands of molecules possibly found in the diverse organic chemical make-up of coal. This complexity is increased when coal is influenced by thermal intrusions such as dolerites. The effects of these magmatic bodies on coal are both chemical and physical in nature. Advancing this understanding of coal material is critically important in its future exploration and beneficiation.

The current viewpoint taken on coal that has been exposed to igneous bodies is that the changes in quality are governed by a simple linear process as a result of conductive heating of the coal material. This heating drives off volatile components within the coal, leaving a material that is unreactive with very little potential economic use. From the results presented in this research, it has become clear that the physical and chemical properties of the coal are intrinsically linked. Thus, to understand the mechanics of devolatilisation, or rather, the metamorphic processes acting on coal, analysis of both the physical and chemical features must be jointly undertaken.

The multiple techniques applied in this work allow for the cross-confirmation of physical and chemical trends within a complex system. The model produced shows the progressive non-linear metamorphic environment through which the sample site was altered, and the dramatic influence that hydrothermal fluids have on organic systems. The devolatilisation of coal to produce “burnt” coal is a process of both chemical and physical alteration and reaction. This alteration and reaction occurs on a micro-scale, with the ramifications of this presenting on the macro-scale. The link between the physical and the chemical can be noted in both reactivity and physical properties. Coals that have been exposed to igneous intrusions will react differently depending on the maceral compositions and how these compositions react to both thermal and hydrothermal regimes. The concept of unusable or devolatilised coal is one that should be used cautiously, as the mechanics of coal metamorphism are complex and the redistribution and placement of volatile components needs to be clearly understood.

Within the results, the link between unique organic complexity and porosity of metamorphosed coal shows that the number of compounds housed outside maceral structures with the general porosity of the coal is large. This has implications on the potential future use and extraction of valuable organic compounds from metamorphosed coal material. The identification of these compounds through a combination of ASE and GC*GC-TOF-MS shows the need for development of new techniques to investigate the complex nature of coal. The application of GC*GC-TOF-MS coupled with PLE in the environmental sector has large scope, due to the identification of potential carcinogenic materials.

3D tomographic analysis allowed for non-destructive quantification of organic and inorganic volume percentages, that showed that some of the inorganic material may be combusted during traditional proximate analysis. In addition, the tomographic analysis allowed for a quantification of porosity within whole samples. A more simplistic success is the correlation of UCS and the concentration of inertinite macerals, showing the direct link between compositional variation and physical character in coal.

Looking forward, the use of GC*GC-TOF-MS in the coal sector has massive potential when combined with PLE. Further investigation into the optimisation of this process is required in order to refine the extraction technique for various coal types. Additionally, by applying Direct Analysis in Real-time Mass Spectrometry (DART) to specific macerals, it would allow for the organic geochemical mapping of macerals. This information would allow for the direct link of specific organic components to individual maceral types and, if combined with micro-hardness testing, it would allow for a deeper understanding of macerals.

The application of Schmidt hammer testing in mining environments to provide an onsite measure of the thermal effect on coal is clear. Further investigation into coal seam and coal type variation on the technique is needed, however, in order to refine this technique for use in the mining sector. Specifically, a base line for UCS and inertinite concentration is required in order for this to be a viable *in situ* technique.

Tomographic analysis of coal has massive potential use within the coming years due to is ability to extract pore spaces digitally from samples and analyse their permeability. The implications for future gas exploration are clear. The classical proximate and petrographic analysis techniques provide vital information regarding the reactivity and structure of the coal. Of interest is a further combination of these techniques with the new techniques demonstrated in this work in order to aid in the better clarification of maceral chemistry.

An aim outlined in Chapter 1 was to provide a holistic view on the macroscopic physicochemical properties of coal. Specific focus is placed on areas affected by dolerite intrusions, and on producing a more comprehensive understanding of the mechanics and the effects of metamorphic processes acting on the coal. The use of classical and new techniques, supported by literature, accomplished this aim. The data produced here has effectively used modern and classical coal analysis techniques. The information generated from both modern and classical techniques need not be used in isolation and, critically, the cross-referencing of techniques provides fundamental insight into the complexity of the physicochemical nature of coal in a modern age.

REFERENCE

- Abu El-Enen M.M., Okrusch M., Will T.M., Contact Metamorphism and metasomatism at a dolerite-limestone contact in the Gebel Yelleq area, Northern Sinai, Egypt, *Mineralogy and Petrology,* 2004, 81, 135 -164.
- Anthony E.J., Iribarne A.P., Iribarne J.V., Talbot R., Jia L., Granatstein D.L., Fouling in a 160MWe FBC boiler firing coal and petroleum coke, *Fuel,* 2001, 80, 1009-1014.
- Assis L.M., Pinto J.S.S., Lancas F.M., Comparison among different extraction methods (PFE, SFE, Sonication, Soxhlet) for the isolation of organic compounds from coal, *Journal of Microcolumn Separations,* 2000, 12, 292-301.
- Aydin, A.; Basu A., The Schmidt hammer in rock material characterization, *Engineering Geology,* 2005, 81, 1-14.
- Alonso M.J.G., Borrego A.G., Alvarez D., Kalkreuth W., Menedez R., Physicochemical transformations of coal particles during pyrolysis and combustion, *Fuel,* 2001, 80, 1857-1870.
- Al-Otoom A.Y., Shawabkeh R.A., Al-Harahshesh A.M., Shawaqfeh A.T., the chemistry of minerals obtained from the combustion of Jordanian oil shale. *Energy,* 30, 5, 611 -619.
- Amadei C., Encyclopaedia of Hydrocarbons: Volume 1: Exploration, production and transport, Istituto Della Encicilopedia Italiana, Rome, 2005, 65-84.
- Babatunde A., Analysis of variability of rock properties influencing wear of bit, *Journal of Science and Technology,* 2010, 5,2, 1-7.
- Barsky V., Vlasow G., Rudnitsky A., Composition and structure of coal organic mass. Analytical Review, *Chemistry and Chemical Technology,* 2009, 3, 315-319.
- Bhutto A.W., Bazmi A.A., Zahedi G., Underground coal gasification: From Fundamentals to applications, *Progress in energy and combustion science*, 2013, 39, 189-214.
- Blazso M., Szekely T., Till F., Varhegyi G., Jakab E., Szabo P., Pyrolysis –gas chromatographic-mass spectrometric and thermogravimetric-mass spectrometric investigation of brown coals, *Journal of Analytical and Applied Pyrolysis,* 1985, 8, 255-269.
- Butala S.J.M, Medina J.C., Hulse R.J., Bartholomew C.H., Lee M.L., Pressurized fluid extraction of coal, *Fuel,* 2000, 79, 1657-1664.
- Bussio J.P., Effect of dolerite intrusions on coal quality in the Secunda coalfields of South Africa, MSc Thesis, University of Pretoria, 2012.
- Bussio J.P. and Roberts R.J., A large scale investigation into changes in coal quality caused by dolerite dykes in Secunda, South Africa-implications for the use of proximate analysis on a working mine, *Journal of African Earth Science,* 2016, 117, 401-409.
- Cadle A.B., Cairncross B., Christie A.D.M., Roberts D.L., The Karoo Basin of South Africa: type basin for the coal bearing deposits of southern Africa, *International Journal of Coal Geology,* 1993, 23, 117-157.
- Castro-Marcano F., Lobodin V.V., Rodgers R.P., McKenna A.M., Marshall A.G., Mathews J.P., A molecular model for Illinois No. 6 Argonne Permium coal: Moving toward capturing the continuum structure, *Fuel,* 2012, 95, 35-49.
- Chen W., Xu R., Clean coal technology development in China, *Energy Policy,* 2010, 38, 2123-2130.
- Clegg H., Wilkes H., Oldenburg T., Santamria-Orozco D., Horsfield B., Influence of maturity of carbazole and benzocarbazole distributions in crude oils and source rocks from the Sonda de Campeche, Gulf of Mexico, *Organic Geochemistry,* 1998, 29, 1-3, 183-194.

- Collins L., Tselev A., Jesse S., Okatan M.B., Proksch R., Mathews J.P., Mitchell G.D., Rodrigues B.J., Kalinin S.V., Ivanov I.N., Breaking the limits of structural and mechanical imaging of the heterogeneous structure of coal macerals, *Nanotechnology,* 2014, 25, 43, 1-24.
- Cormos C.C., Integrated assessment of IGCC power generation technology with carbon capture and storage (CCS), *Energy*, 2012, 42, 434-445.
- Daniels E.J., Altaner S.P., Marshak S., Eggleston J.R., Hydrothermal alteration in anthracite from eastern Pennsylvania: Implications for mechansisms of anthracite formation, *Geology*, 1990, 18, 247-250.
- De Olivera D.P.S., Cawthorn R.G., Dolerite intrusion morphology at Majuba Colliery northeast Karoo Basin, Republic of South Africa, *International Journal of Coal Geology,* 1999, 41, 333 -349.
- Dettmer-Wilde K., Engewald W., Theory of Gas Chromatography, *Practical Gas Chromatography*, 2014, 21-57.
- Das, B., Micro-hardness of abnormally metamorphosed coal. *Fuel*, 1972, 51, 52-53.
- Donahue C.J., Rais E.A., Proximate Analysis of coal *J. Chem. Educ.*, 2009, 86, 222-224.
- Duncan A.R., Erlank A.J., Marsh J.S., Regional Geochemistry of the Karoo Igneous Province, *Special Publication of the Geological Soceity of South Africa*, 1984, 13, 355-388.
- Eberhard A., The future of South African Coal: Market, Investment, and Policy Challenges, *Program on Energy and Sustainable Devleopment Standford University press,* 2011, 100, 1-48.
- Encarnación J., Fleming T.H., Elliot D.H., Eales H.V., Synchronous emplacement of Ferrar and Karoo dolerites and the early breakup of Gondwana, *Geology*, 1996, 24, 535-538.
- Engewald W., Dettmer-Wilde K., Practical Gas Chromatography, *Springer-Verlag, Berlin, Heidelberg,* 2014, Chapter 2.
- Fabiańska M.J., Ćmiel S.R., Misz-Kennan M., Biomarkers and the aromatic hydrocarbons in bituminous coals of upper Silesian coal basin: Example from 405 coal seam of the Zaleskie Beds (Poland), *International Journal of Coal Geology,* 2013, 107, 95-111.
- Falcke T.J., Hoadley F.A, Brennan D.J., Sinclair S.E., The sustainability of clean coal technology: IGCC with /without CCS, *Process safety and environmental protection*, 2010.
- Falcon R. and Ham A.J., The characteristics of Southern African coals, *Journal of the South African Institute of Mining and Metallurgy,* 1988, 88, 5, 145-161.
- Fedyaeva O.N., Vostrikov A.A., Hydrogenation of bitumen in situ supercritical water flow with and without addition of zinc and aluminium, *The Journal of Supercritical Fluids*, 2012, 72, 100-110.
- Finkelman R.B., Bostick N.H., Dulong F.T., Senftle F.E., Thorpe A.N., Influence of an igneous intrusion on the inorganic geochemistry of a bituminous coal from Pitkin County, Colorado, *International Journal of Coal Geology*, 1998, 36, 223-241.
- Franco A., Diaz A.R., The future challenges for 'clean coal technologies': Joining efficiency increase and pollutant emission control, *Energy*, 2009, 34, 348-354.
- Fredericks P.M., Warbrooke P., Wilson M.A., A study of the effect of igneous intrusions on the structure of an Australian high volatile bituminous coal, *Organic Geochemistry*, 1985, 8, 329-340.
- Gamson P.D., Beamish B.B., Johnson D.P., Coal microstructure and micro-permeability and their effects on natural gas recovery, *Fuel,* 1993, 72, 87-99.
- Greenwood P.F., Jasper D.H., van Heemst J.D.H., Guthrie E.A., Hatcher P.G., Laser micropyrolysis GC-MS of lignin, *Journal of Analytical and Applied Pyrolysis*, 2002, 62, 365-373.

- Gröcke D.R., S.M., Yoksoulian L.E., Cairncross B., Tsikos H., Van Hunen J., No evidence for thermogenic methane release in coal from the Karoo-Ferrar large igneous province, *Earth and Planetary Science Letters,* 2009, 277, 204-212.
- Golab A.N., Carr P.F., Changes in geochemistry and mineralogy of thermally altered coal, Upper Hunter Valley, Australia, *International Journal of Coal Geology,* 2004, 57, 197 -210.
- Golab A.N., Hutton A.C., French D., Petrography, carbonate mineralogy and geochemistry of thermally altered coal in Permian coal measures, Hunter Valley, Australia, *International Journal of Coal Geology*, 2006, 70, 150-165.
- Golab A.N., Hutton A.C., French D., Petrography, carbonate mineralogy and geochemistry of the thermally altered coal in Permian coal measures, Hunter Valley, Australia, *International Journal of Coal Geology,* 2007, 70, 150-165.
- Gruner E., Bousquet G., Atlas general des houilléres, *Comité Central des Houilléres de France*, Paris, 1911, Pt. 2, 5.
- Gurba L.W., Weber C.R., Effect of igneous intrusions on coalbed methane potential Gunnedah Basin, Australia, *International Journal of Coal Geology,* 2001 46, 113-131.
- Hamilton J.F., Lewis A.C., Millan M., Bartle K.D., Herod A.A., Kandiyoti R., Comprehensive Two-Dimensional Gas Chromatography Coupled to Time-of-Flight Mass Spectrometry of Coal Liquids Produced During a Coal Liquefaction Process, *Energy and Fuels,* 2007, 21, 286-294.
- Hancox P.J., Rubidge B.S., Breakthrough in the biodiversity, biogeography, biostratigraphy and basin analysis of the Beaufort Group *J. Afr. Earth Sci.* 2001 33. 563 -577.
- Hancox P.J., Gotz A.E., South Africa's coalfields-A 2014 perspective, *International Journal of Coal Geology,* 2014, 132, 170-254.
- Haramy, K.Y., DeMarco, M.J., Use of Schmidt hammer for rock and coal testing. Proceedings of 26th US symposium on rock mechanics, 26–28 June, Rapid City, 1985, 549–555.
- Hatcher P.G., Clifford D.J., The organic geochemistry of coal: from plant materials to coal, *Organic Geochemistry,* 1997, 27, 251-274.
- Heinberg R., Fridley D., The end of cheap coal, *Nature*, 2010, 468, 367-369.
- Hoffman J.W., De Beer F.C., Characteristics of the Micro-Focus X-ray Tomography Facility (MIXRAD) at Necsa in South Africa, *18th World Conference on Non-destructive Testing,* 2012
- Höök M., Zittel W., Schindler J., Aleklett K., Global coal production outlooks based on a logistic model, *Fuel*, 2010, 89, 3546-3558.
- Hower J.C.; Trinkle E.J.; Raione R.P., Vickers microhardness of telovitrinite and pseudovitrinite from high volatile bituminous Kentucky coals, *International Journal of Coal Geology,* 2008, 75, 76-80.
- IEA, 2008, Energy Technology Perspectives 2008 – Scenarios and Strategies to 2050, in support of the G8 Plan of Action, International Energy Agency, Paris, France
- Jeffrey L.S., Characterization of the coal resources of South Africa, *Journal of the South African Institute of Mining and Metallurgy,* 2005, 95-102.
- Jourdan F., Feraud G., Bertrandh., Watkeys M.K., From flood basalts to the inception of ocenization: Example from th $^{40}Ar/^{39}Ar$ high-resolution picture of the karoo large igneous province, *Geochemistty Geophisics Geosystems,* 2007, 8, 2.
- Journdan F., Féraud G., Bertrand H., Kampunzu A.B., Tshoso G., Le Gall B., Tiercelin J.J., Capiez P., The Karoo Triple Junction questioned: Evidence from Jurassic and Proterozoic $^{40}Ar/^{39}Ar$ ages and geochemistry of the Giant Okavango Dyke Swarm (Botswana), *Earth Planet. Sci. Lett.,* 2004, 222, 989-1006

- Kozusnikova A., Determination of microhardness and elastic modulus of coal components by using indentation method, *Geolines,* 2009, 22, 40-43.
- Kubát J., Dobal V., Šebesta P., The additivity principle in pyrolysis-gas chromatography of brown coal, *Journal of Analytical and Applied Pyrolysis,* 1982, 3, 263-269
- Laubach S.E., Marrett R.A., Olson J.E., Scott A.R.., Characteristics and origins of coal cleat: A review, *International Journal of Coal Geology,* 1998, 35, 175-207
- Le Gall B., Tshoso G., Jourdan F., Féraud G., Kenna T.C., Tiercelin J.J., Kampunzu A.B., Mondisi M.P., Dyment J., Maia M., 40Ar/39Ar geoghronology and structural data from the Giant Okavango and related mafic dyke swarms, Karoo Igneos Province, Northern Botswana, *Earth Planet. Sci. Lett*., 2002, 202, 595-606.
- Levine D.G., Scholsberg R.H., Silbernagel B.G., Understanding the chemistry and physics of coal structure (A Review), *Proc. Natl, Acad. Sci. USA,* 1982, 79, 3365-3370.
- Lorimer J.W., Saugier-Cohen Adad M.T., Young C.L., Solubility data series-Polycyclic Aromatic Hydrocarbons: Binanry Non-Aqueous systems Part I: Solutes A-E, *International Union of Pure and Applied Chemistry IUPAC Secretariat,* 1995, 58, 1-337.
- Lowry H.H., 1963: Volume 1 and 2 of Chemistry of Coal Utilization, National research council committee, John Wiley and Sons, Michigan.
- Li Y., Michels R., Mansuy L., Fleck S., Faure P., Comparison of pressurized liquid extraction with classical solvent extraction and microwave-assisted extraction-application to the investigation of the artificial maturation of Mahakam coal, *Fuel,* 2002, 81, 747-755.
- Liu Z., Phillips J.B., Comprehensive two-dimensional gas chromatography using an On-Column thermal modulator interface, *Journal of Chromatographic Science,* 1991, 29, 227-231.
- Marsh J.S., Eales H.V., The chemistry and petrogenesis of Igneous Rocks of the Karoo Central Area, 13, 1984, *Special Publication Geological Society of South Africa,* Sothern Africa pp. 27 -67.
- Marsh, J.S., Geochemistry of Karoo basalts and dolerites in the North-Western Orange Free State: recognition and origin of two new Karoo basalt magma types. *20th Geological congress of the Geological Society of South Africa*, Potchefstroom, 1984, 91-94.
- Marsh, J.S., Mndaweni, M.J., Geochemical variations in a long Karoo dyke, Eastern Cape. *South African Journal of Geology*, 1998, 101, 119-122.
- Mastral A.M., Callén M.S., A review on Polycyclic Aromatic Hydrocarbon (PAH) Emissions from Energy Generation, *Environmental Science & Technology*, 2000, 34, 3051-3057.
- Mastalerz M., Drobniak A., Schmmelmann A., Changes in optical properties, chemistry, and micropore and mesopore characteristics of bituminous coal at the contact with dikes in the Illinois Basin, *International Journal of Coal Geology,* 2009, 77, 310-319.
- Mastalerz, M., Glikson, M., In-situ analysis of solid bitumenin coal: examples from the Bowen Basin and the Illinois Basin, *International Journal of Coal Geology,* 2000 42, 207–220.
- Mathews J.P., Chaffee A.L., The molecular representation of coal-A review, *Fuel,* 2012, 96, 1-14.
- Misz-Kennan M., Fabiańska M., Thermal transformation of organic matter in coal waste from Rymer Cones (Upper Silesian Coal Basin, Poland) *International Journal of Coal Geology,* 2011, 81, 4, 343-358.
- Mukhopadhyay P.K. and Hatcher P.G., Hydrocarbons from coal Chapter 4: Composition of coal, 1993, 79-113.
- Murchison D.G., Petrographic aspects of coal structure: reactivity of macerals in laboratory and natural environments, *Fuel,* 1991, 70, 296-315.

- Ong R., Lundstedt S., Haglund P., Marriott P., Pressurised liquid extraction-comprehensive two-dimensional gas chromatography for fast-screening of polycyclic aromatic hydrocarbons in soil, *Journal of Chromatography A,* 2003, 1019, 221-232
- Özkan, İ.; Bilim, N., A new approach for applying the in-situ Schmidt hammer test on a coalface. *International Journal of Rock Mechanics & Mining Sciences,* 2008, 45, 888-898.
- Panić O., Górecki T., Comprehensive two-dimensional gas chromatography (GCxGC) in environmental analysis and monitoring, *Anal Bioanal Chem,* 2006, 386, 1013-1023.
- Poole, R.W.; Farmer, I.W., Consistency and Repeatability of Schmidt hammer Rebound Data During Field Testing, *Journal of Rock Mechanics, Mineral Science and Geomechanics,* 1980, 17, 167-171.
- Regnault V., Ann. Chim. Phys., 1837, 66, 337-365.
- Riley T.R., Curtis M.L., Leat P.T., Watkeys M.K., Duncan R.A., Millar I.L., Owens W.H., Overlap of the Karoo and Ferrar magma types in KwaZulu-Natal, South Africa, *Journal of Petrology,* 2006, 47, 3, 541-566.
- Rimmer S.M., Yoksoulian L.E., Hower J.C., Anatomy of an intruded coal, I: Effect of contact metamorphism on whole-coal geochemistry, Springfield (No. 5) (Pennsylvanian) coal, Illinois Basin, *International Journal of Coal Geology,* 2009, 79, 74-82.
- Saidur R., Atabani A.E., Mekhilef S., A review on electrical and thermal energy for industries, *Renewable and sustainable energy reviews*, 2011, 15, 2073-2086.
- Seeley S.K., Bandurski S.V., Brown R.G., McCurry D.J., Seeley J.V., A comprehensive two-dimensional gas chromatography method for analysing extractable petroleum hydrocarbons in water and soil, *Journal of Chromatographic Science,* 2007, 45, 657-663.
- Sheorey, P.R.; Baratm, D.; Dask, N.; Mukherjee P.; Singh, B., Schmidt hammer rebound data for estimation of large scale *in situ* coal strength, *Journal of Rock Mechanics, Mineral Science and Geomechanics,* 1984, 21, 39-42.
- Speight J.G., 2005: Handbook of coal analysis, John Wiley and Sons, New Jersey, Print.
- Snyman P., Barclay J., The coalification of South African coal, *International Journal of Coal Geology,* 1989, 13, 375-390.
- Sobeih K.L., Baron M., Gonzalez-Rodriguez J., Recent trends and developments in pyrolysis-gas chromatography, *Journal of Chromatography,* 2008, 1186, 51-66.
- Stewart A.K., Massey M., Padgett P.L., Rimmer S.M., Hower J.C., Influence of a basic intrusion on the vitrinite reflectance and chemistry of the Springfield (No. 5) coal, Harrisburg, Illinois, *International Journal of Coal Geology,* 2005, 63, 58-67.
- Teichmüller M, Stach's Textbook of coal petrology, 3rd ed. Gerbüder Borntraeger, Berlin.
- Thomas C.G., Gosnell M.E., Gawronski E., Phong-anant D., Shibaoka M., The behaviour of inertinite macerals under pulverised fuel (pf) combustion conditions, *Organic Geochemistry,* 1993, 20, 779-788.
- Tiryaki B., Atasoy K., Yasith N.E., Studies in the relationships between hardgrove grindability and some rock index tests on Cayirhan coals, *17th International Mining Congress and Exhibition of Turkey IMCET,* 2001.
- Torabi S.R., Ataei M., Javanshir M., Application of Schmidt rebound number for estimating rock strength under specific geological conditions, *Journal of Mining & Environment,* 2010, 1, 2, 1-8.
- Tsai C., Scaroni A.W., The structural changes of bituminous coal particles during the initial stages of pulverized-coal combustion, *Fuel,* 1987, 66, 200-206.
- Vachaparampil A.W., Non-destructive index testing for relative assessment of rock strength, MSc Thesis, University of Oklahoma, 2016.

- Van Bergen P.F., Collinson M.E., De Leeuw J.W., Chemical Composition and ultrastructure of fossil and extant salvinialean microspore massulae and megaspores, *Grana Supplement*, 1993, 32, 18-30.
- Van Niekerk J.L., 1995: Geochemistry of the dolerites and the intrusion mechanisms of two major sills in the Secunda coalfield, PhD thesis, University of Stellenbosch
- Van Niekerk D., Mathews J.P., Molecular representation of Permian-aged vitrinite-rich and inertinite-rich South African coals, *Fuel,* 2010, 89, 73-82.
- Van Niekerk D., Pugmire R.J., Solum M.S., Painter P.C., Mathews J.P., Structural characterization of vitrinite-rich and inertinite-rich Permian-aged South African bituminous coals, *International Journal of Coal Geology,* 2008, 76, 290-300.
- Volk H., Pinetown K., Johnston C., McLean W., A desktop study of the occurrence of total petroleum hydrocarbon (TPH) and partially water-soluble organic compounds in Permian coals and associated coal seam groundwater, *Petroleum & Geothermal Research Portfolio,* 2011, 1 – 73.
- Wall T.F., Tate A.G., Bailey J.G., Jenness L.G., Mitchell R.E., Hurt R.H., The temperature, burning rates and char character of pulverised coal particles prepared from maceral concentrates, *Symposium (International) on Combustion,* 1992, 24, 1207-1215.
- Wang H., Nakata T., Analysis of the market penetration of clean coal technologies and its impacts in China's electricity sector, *Energy Policy,* 2009, 37, 338-351.
- Warne S.S.J., Proximate analysis of coal, oil shale, low quality fossil fuels and related materials by thermogravimetry, *TrAC Trends Anal. Chem.* 10, 6, 195 -199.
- White R., McKenzie D., Magmatism at Rift Zones: The Generation of Volcanic Continental Margins and Flood Basalts, *Journal of Geophysical Research*, 1989, 94, 86, 7685-7729.

APPENDIX A

Appendix A contains the chromatogram images of all the coal samples analysed as well as the excel GC*GC-TOF-MS data from the analysis.

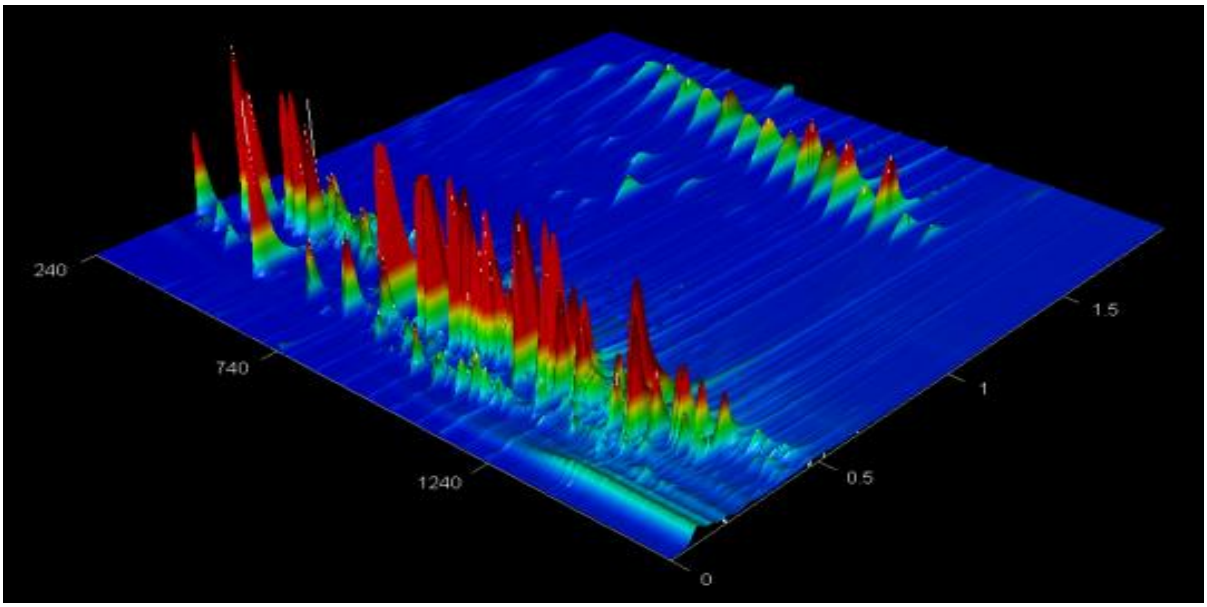

Figure 72: Chromatogram of sample at 0 m from the dolerite dyke, showing the time of flight distribution and peak intensities of the identified organic molecules.

The sample taken in direct contact with the dolerite intrusion (Fig. 72) shows good separation of both aliphatic and aromatic compounds; however, more intense peaks are noted in the aromatic compounds. This sample contains 838 compounds not found in other samples, over a large retention time spectrum.

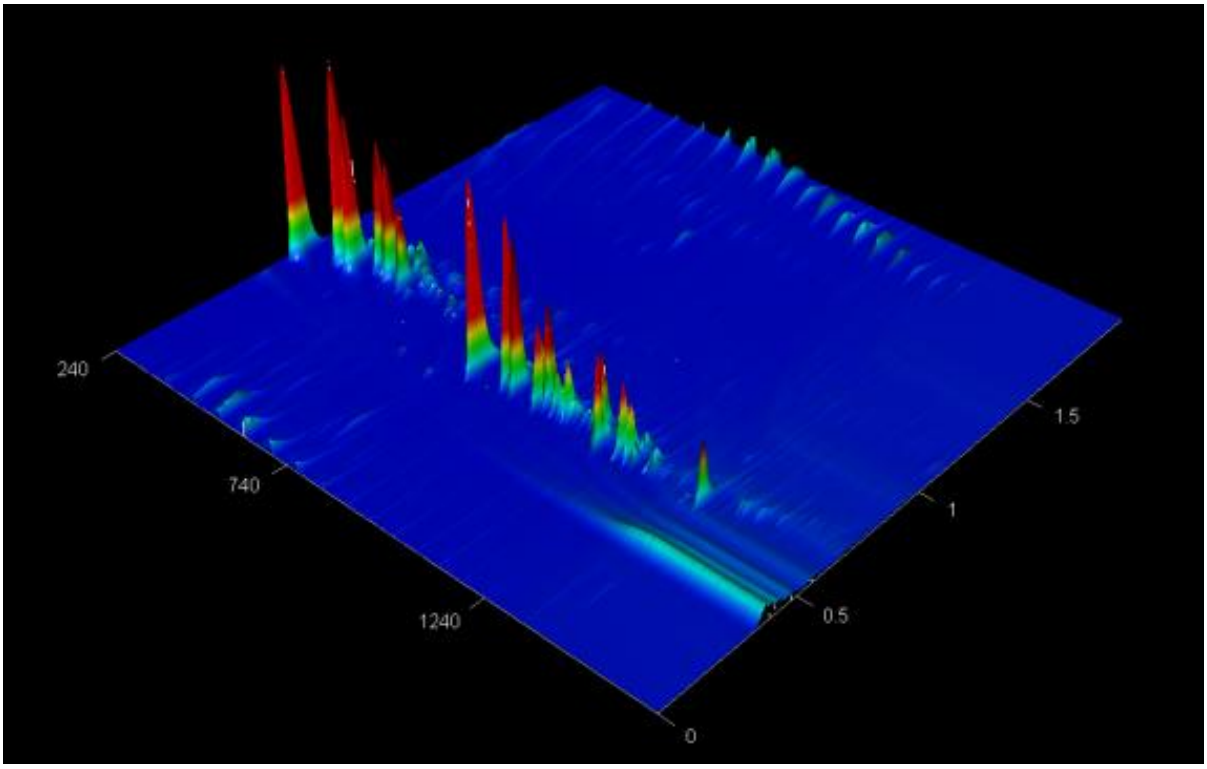

Figure 73: Chromatogram of sample at 1 m from the dolerite dyke.

At 1 m from the dolerite, the sample contains 258 unique organic compounds as seen in Figure 73. The separation due to the second dimension allows for clarity of both aliphatic and aromatic compounds with more intensive peaks in the aromatic compounds. Within this sample there no compounds beyond the 1620 s mark of the first dimension.

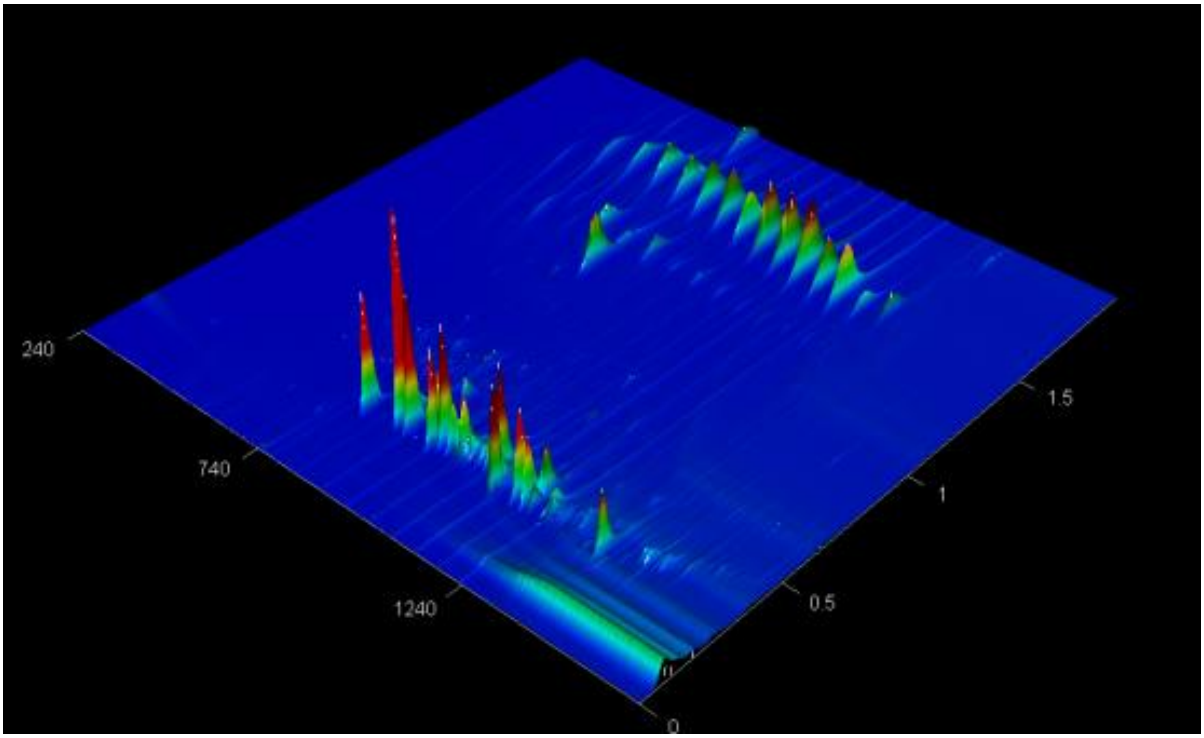

Figure 74: Chromatogram of sample at 2 m from the dolerite dyke.

At a distance of 2 m from the dolerite, only 186 unique organic compounds can be identified. The two-dimensional chromatogram in Figure 74 shows good separation of the compounds in both the aliphatic and aromatic groupings. Also to be noted is the similarity of the peak intensity of both the aliphatic and aromatic compounds. Within the first dimension no compounds are identified beyond 1620 s.

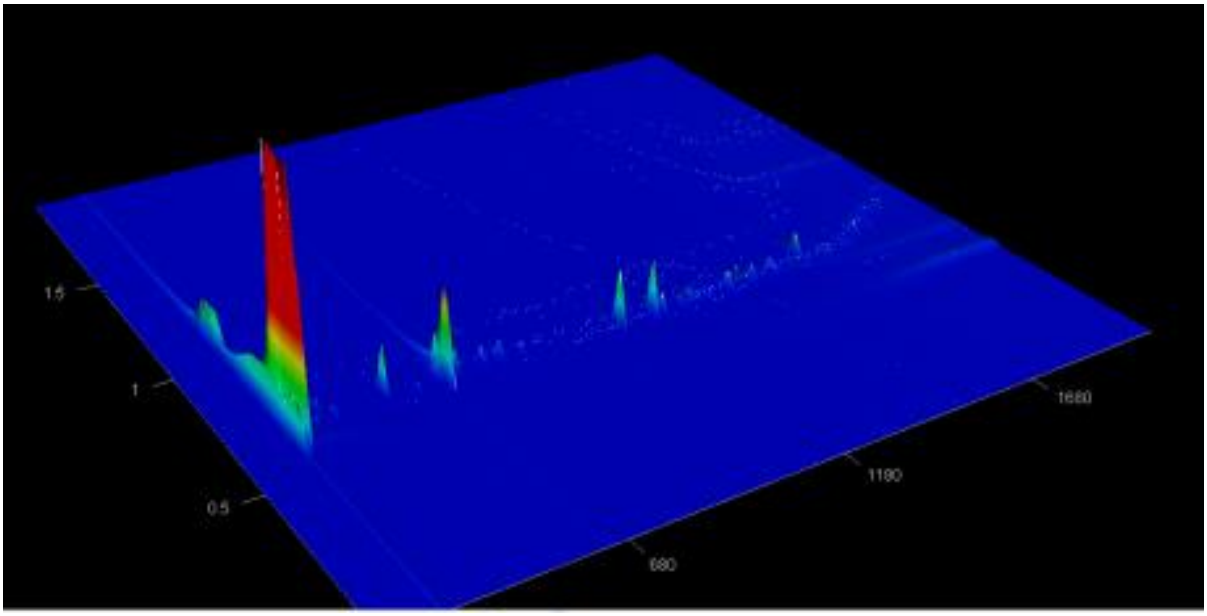

Figure 75: Chromatogram of sample at 3 m from the dolerite dyke.

The chromatogram of Figure 75, although not easily visible, contains 570 unique compounds identified. A set of 230 unique compounds have been identified that are present below 1620 s of the first dimension. The sample host both aliphatic and aromatic compounds, however peak intensities for the aliphatic compounds are low.

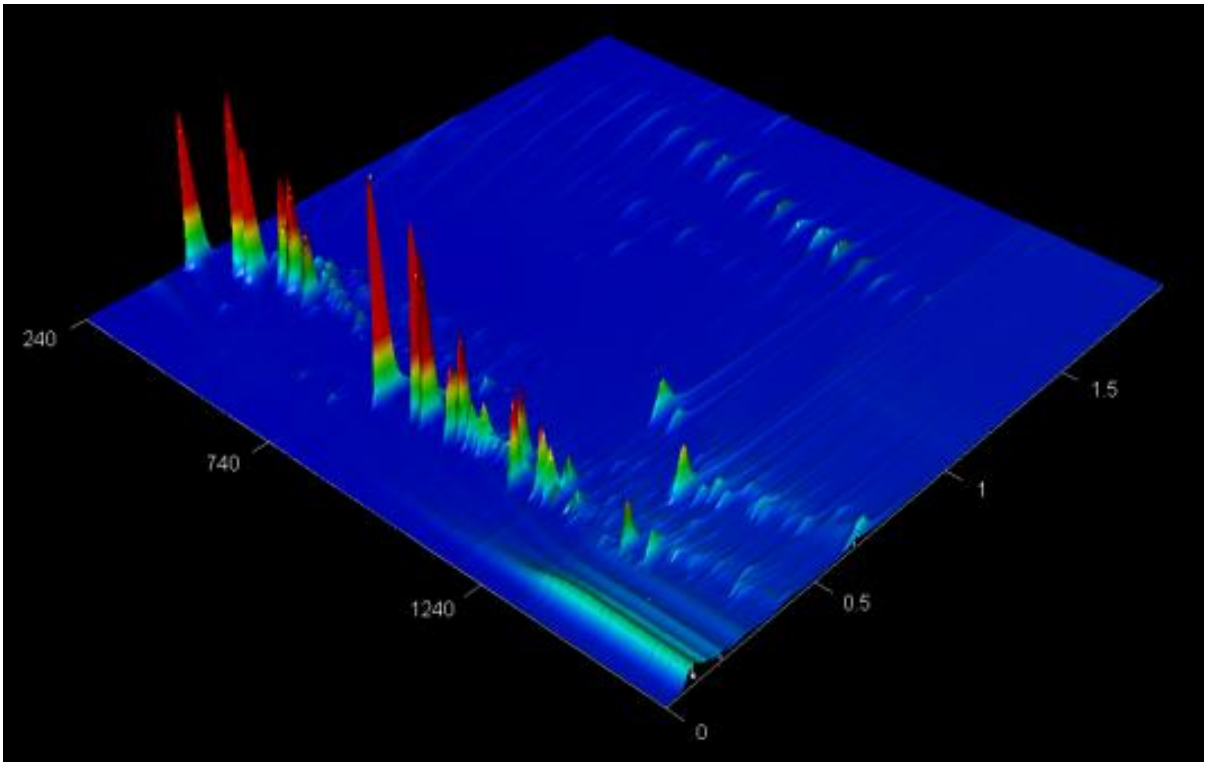

Figure 76: Chromatogram of sample at 4 m from the dolerite dyke.

At a distance of 4 m from the intrusion the chromatogram (Fig. 76) shows good separation of both aliphatic and aromatic compounds. 239 unique compounds are identified all of which are below 1620 s of the first dimension.

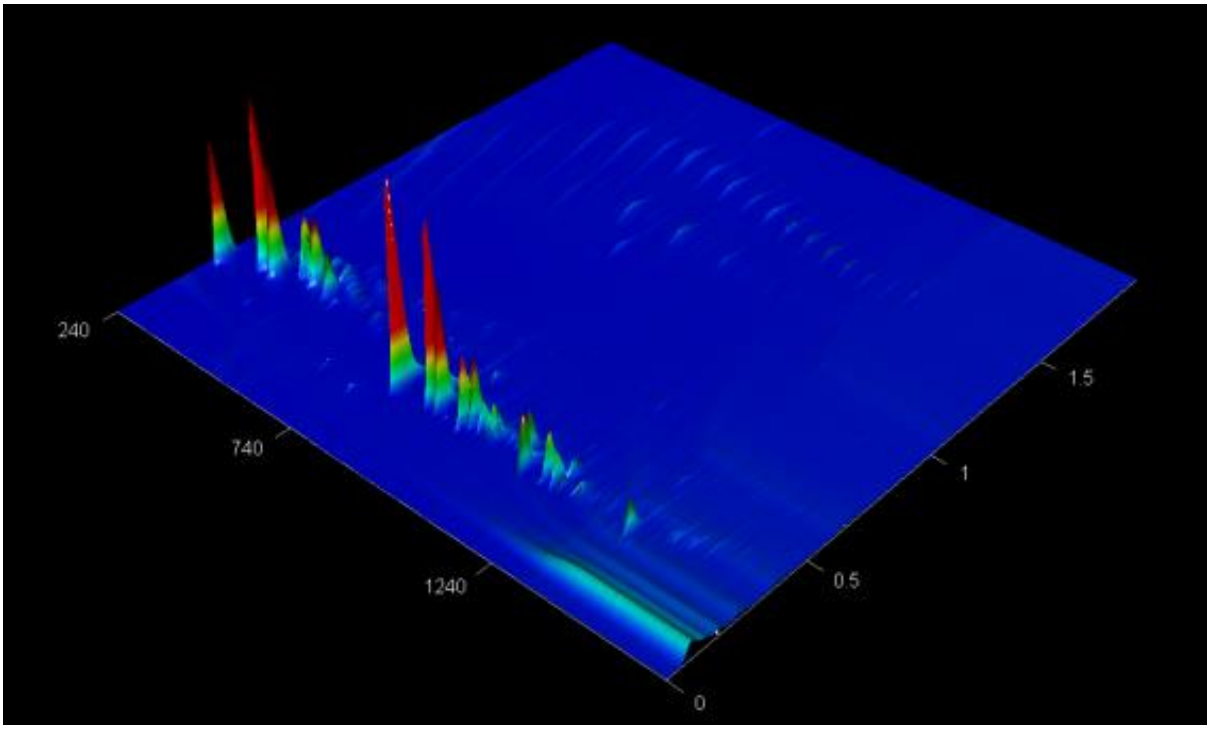

Figure 77: Chromatogram of sample at 5 m from the dolerite dyke.

The chromatogram in Figure 77 displays the 146 unique compounds of the sample 5 m from the dolerite intrusion. The residence time for all these compounds does not exceed 1620 s in the first dimension.

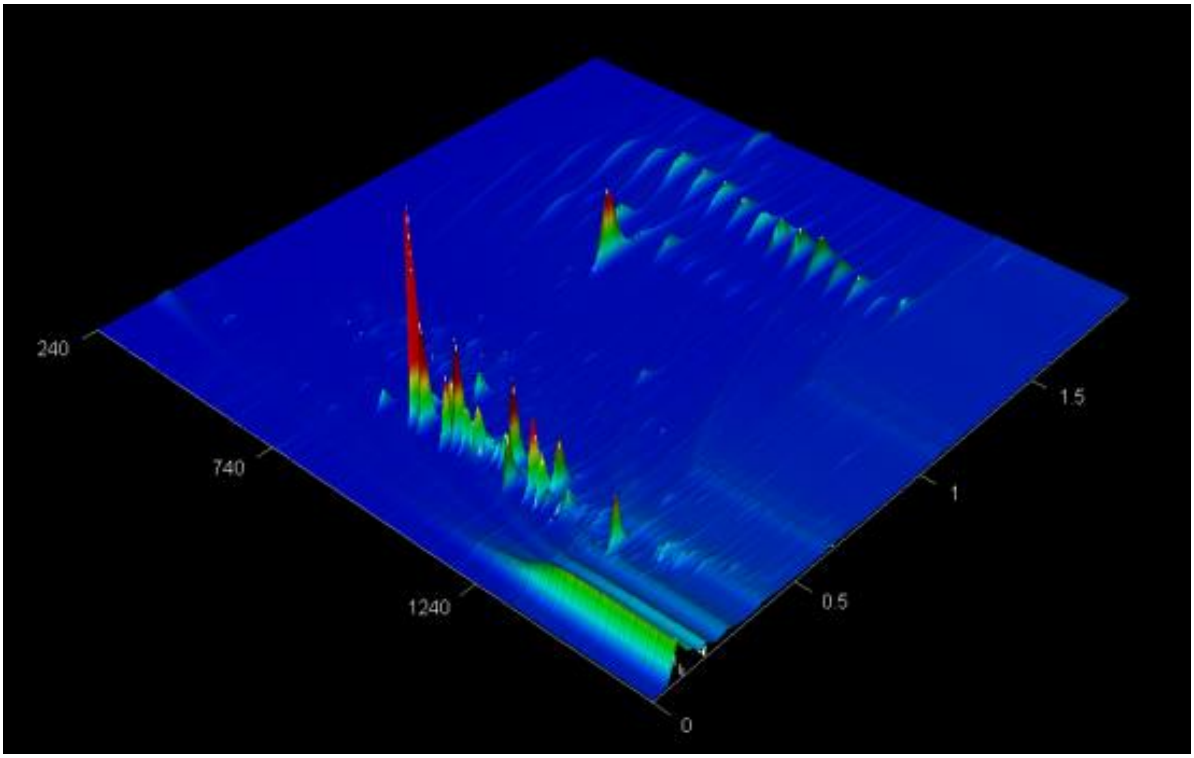

Figure 78: Chromatogram of sample at 6 m from the dolerite dyke.

Figure 78 displays the chromatogram for the coal sample 6 m from the dolerite intrusion. Noted in this sample are 140 unique compounds all with residence times below 1620 s. Good separation of the aliphatic and aromatic compounds can also be noted.

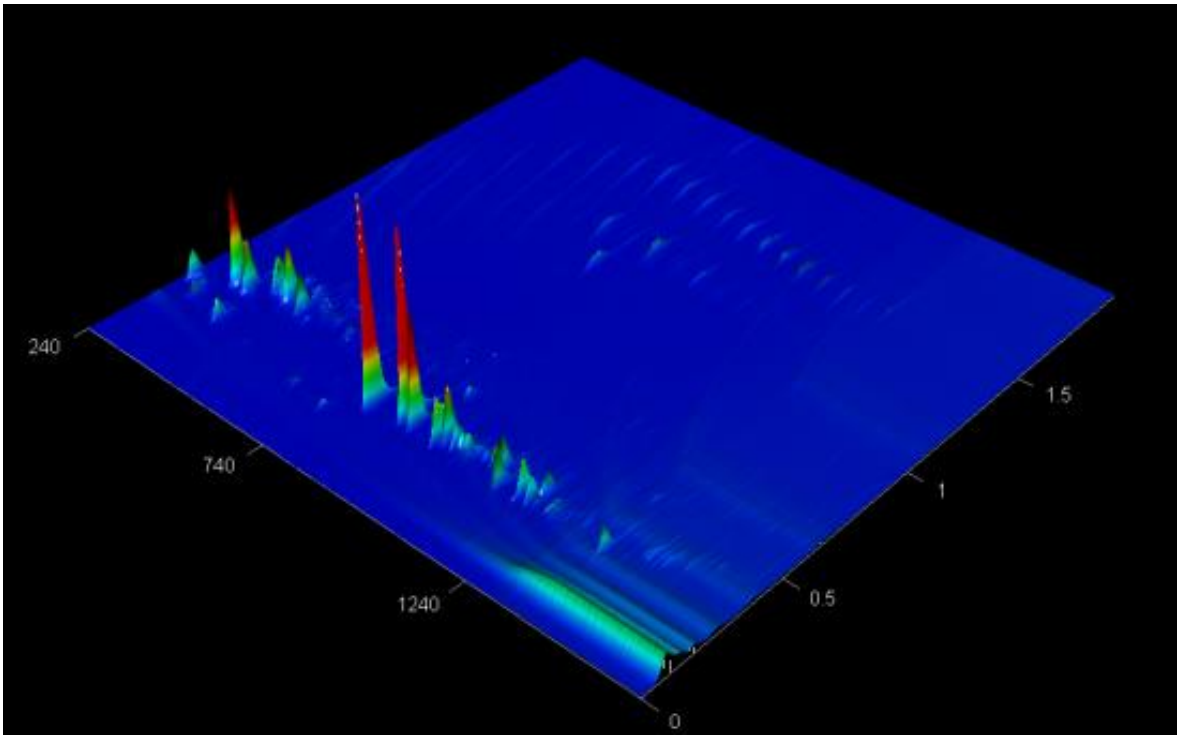

Figure 79: Chromatogram of sample at 7 m from the dolerite dyke.

At a distance of 7 m from the dolerite intrusion 140 unique compounds can be identified as seen in Figure 79. All of these 140 compounds have retention times of less than 1620 s in the first dimension and show good separation of the aliphatic and aromatic compounds.

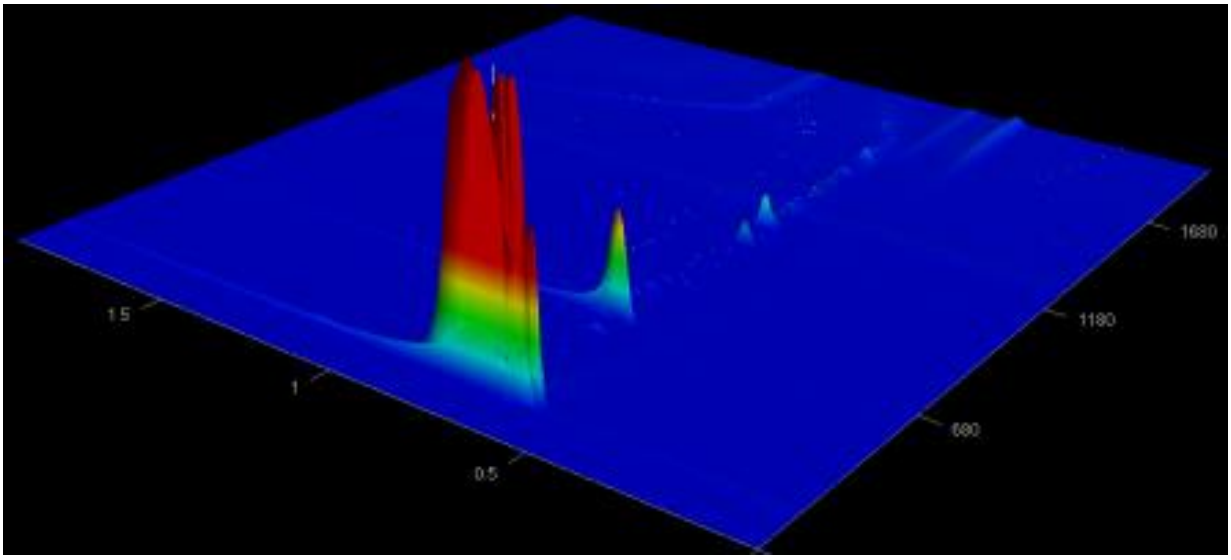

Figure 80: Chromatogram of sample at 8 m from the dolerite dyke.

The 471 unique compounds identified 8 m from the intrusion are shown in Figure 80; 268 of these compounds have residence times greater than 1620 s in the first dimension. The sample hosts both aliphatic and aromatic compounds; however, peak intensities for the aliphatic compounds are low.

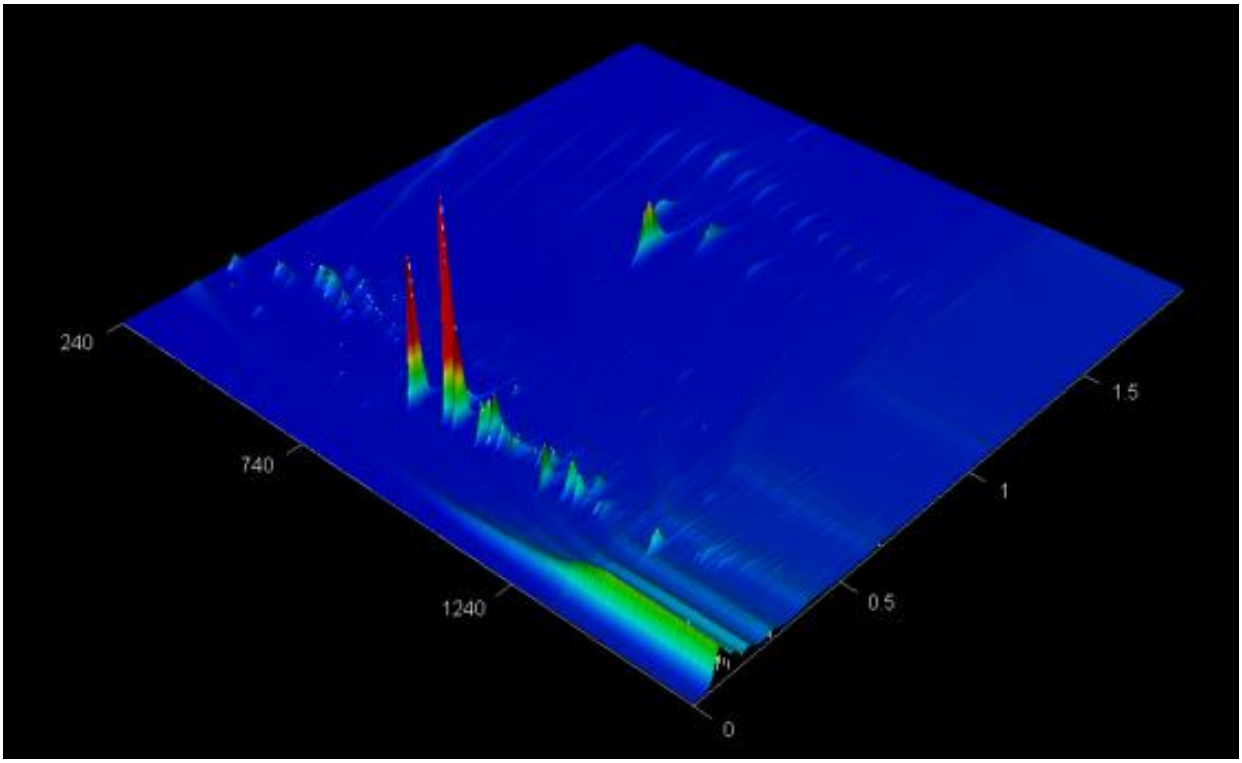

Figure 81: Chromatogram of sample at 9 m from the dolerite dyke.

At a distance of 9 m from the intrusion, 125 unique compounds can be identified, all of which have residence times of less than 1620 s in the first dimension (Fig 81). Clear distinction can be made between the aliphatic and aromatic compounds.

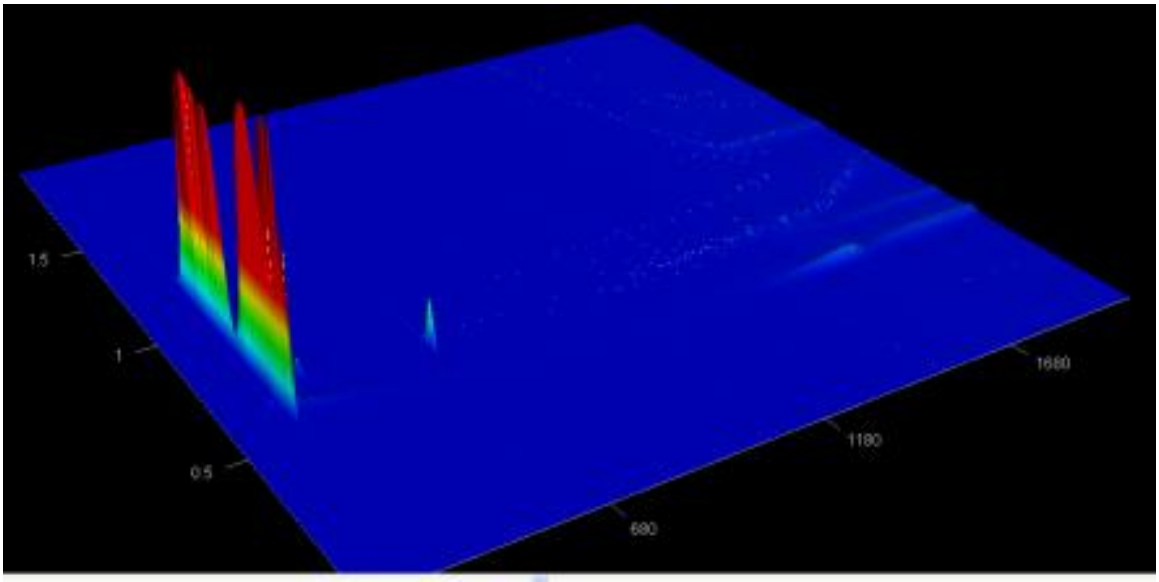

Figure 82: Chromatogram of sample at 10 m from the dolerite dyke.

The chromatogram in Figure 82 hosts 492 compounds. Due to the large peak intensity variations some compounds is less visible. However, the data in appendix A confirms that 330 of the detected compounds have retention times greater than 1620 s in the first dimension.

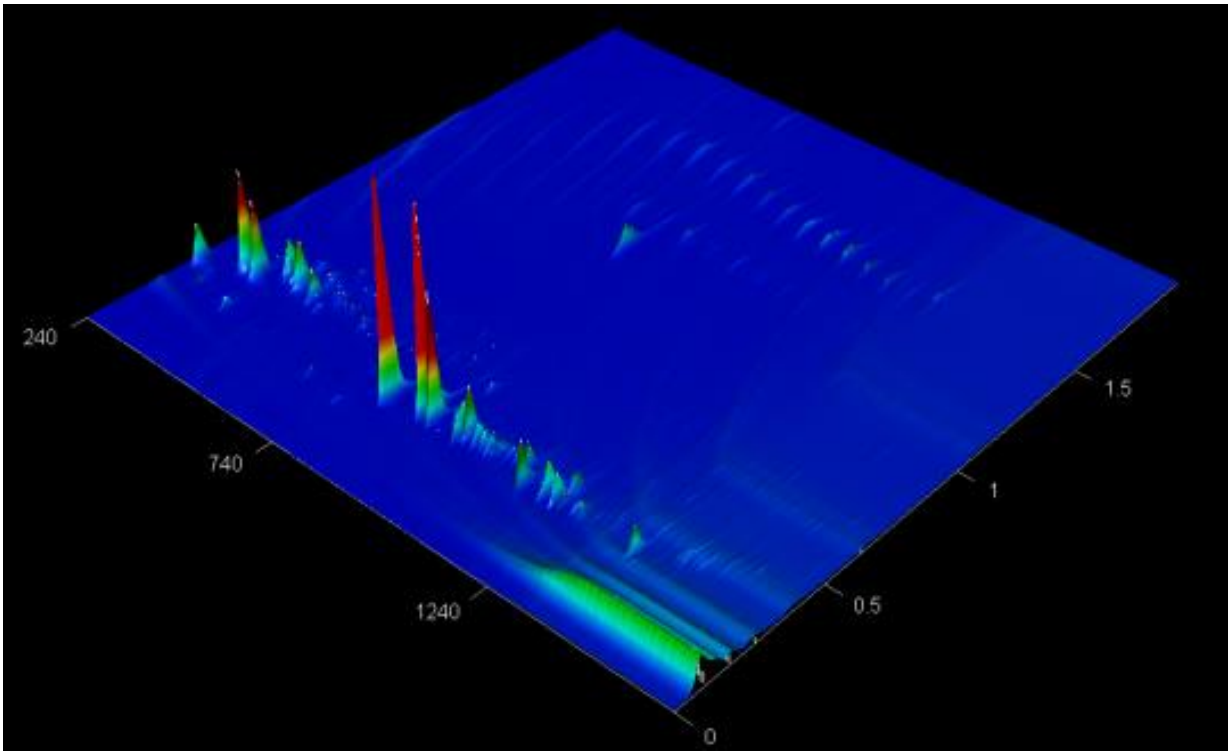

Figure 83: Chromatogram of sample at 11 m from the dolerite dyke.

At 11 m from the dolerite intrusion 207 unique organic molecules are identified (Fig. 83). The sample hosts no molecules with residence times greater than 1620 s in the first dimension.

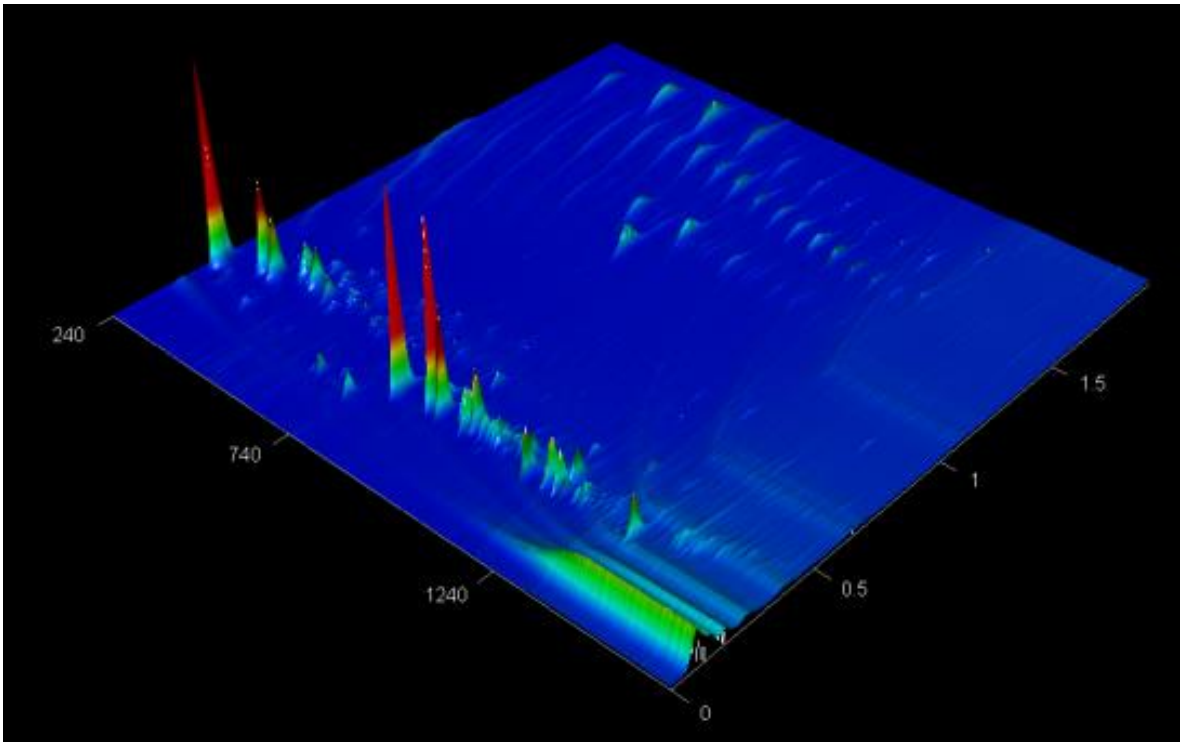

Figure 84:Chromatogram of sample at 12 m from the dolerite dyke.

The chromatogram in Figure 84 displays the organic signature of the sample taken 12 m from the dolerite intrusion; 164 unique molecules were identified with residence times below 1620 s in the first dimension. Good separation was achieved in both the aliphatic and aromatic compounds.

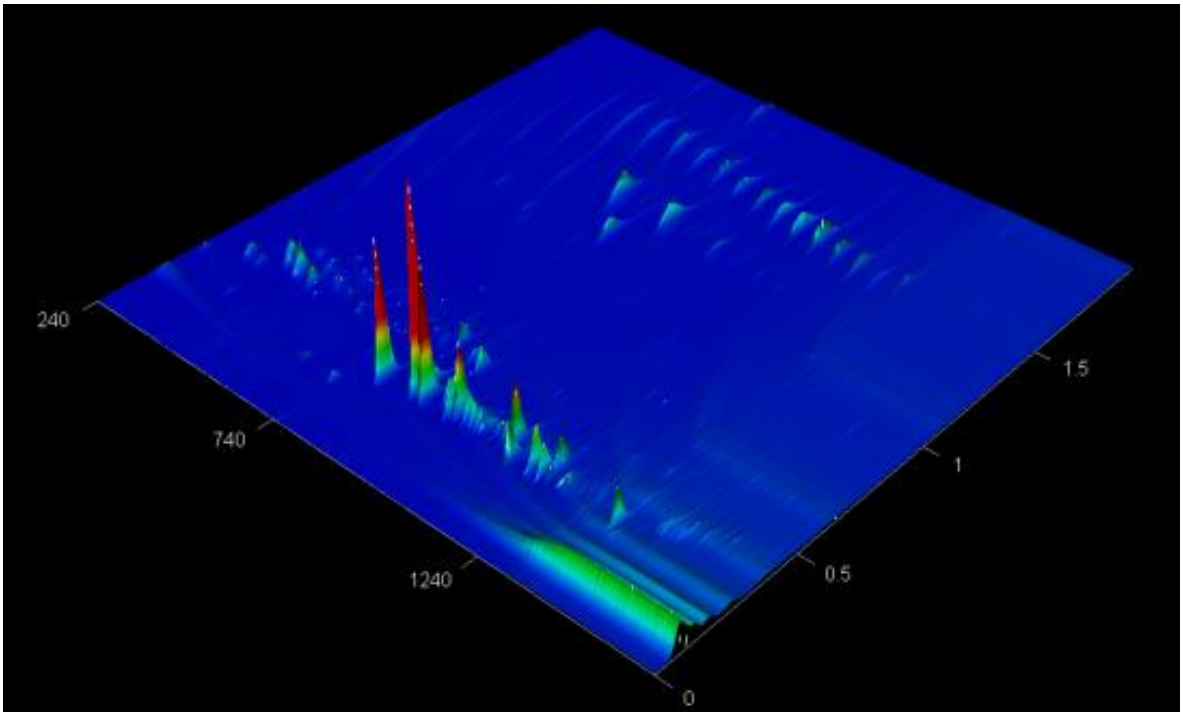

Figure 85: Chromatogram of sample at 13 m from the dolerite dyke.

One hundred and sixty two unique compounds were identified at a distance of 13 m from the dolerite intrusion (Fig. 85). None of the identified aromatic of aliphatic compounds have residence times exceeding 1620 s in the first dimension.

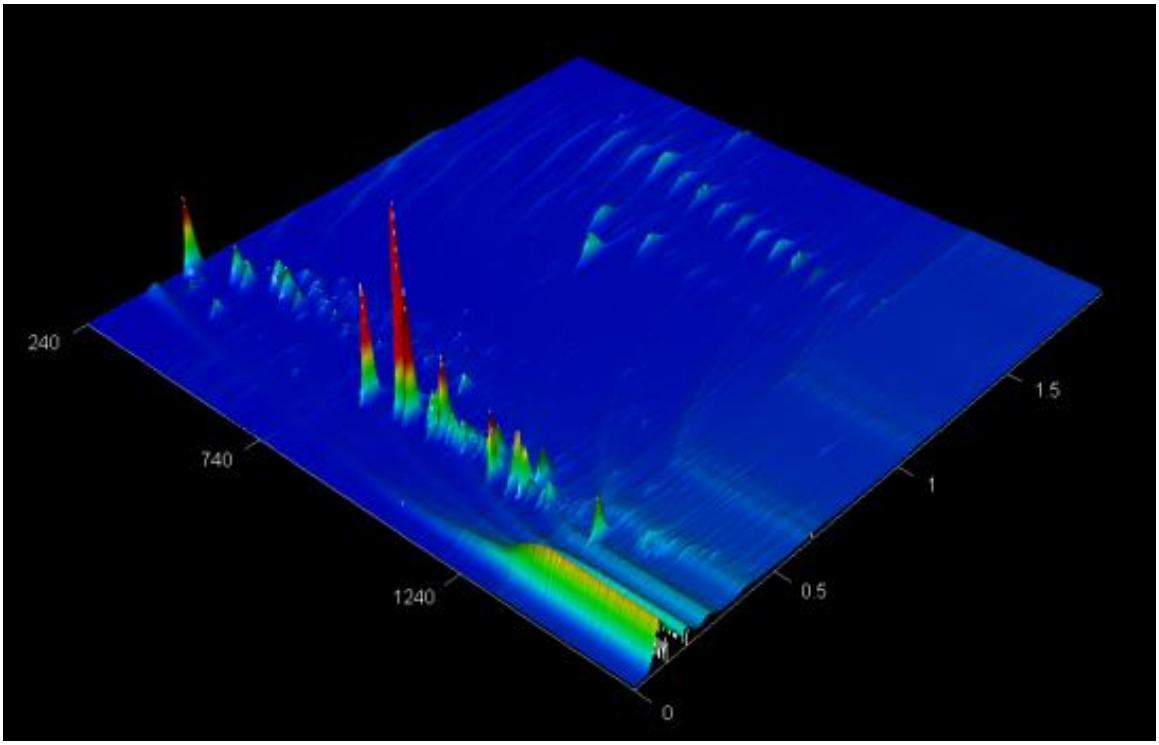

Figure 86: Chromatogram of sample at 14 m from the dolerite dyke.

Of the 144 unique compounds identified at 14 m from the dolerite seen in Figure 86, none exceed a first-dimension residence time of 1620s. The sample shows good separation of both aliphatic and aromatic compound in both the first and second dimension.

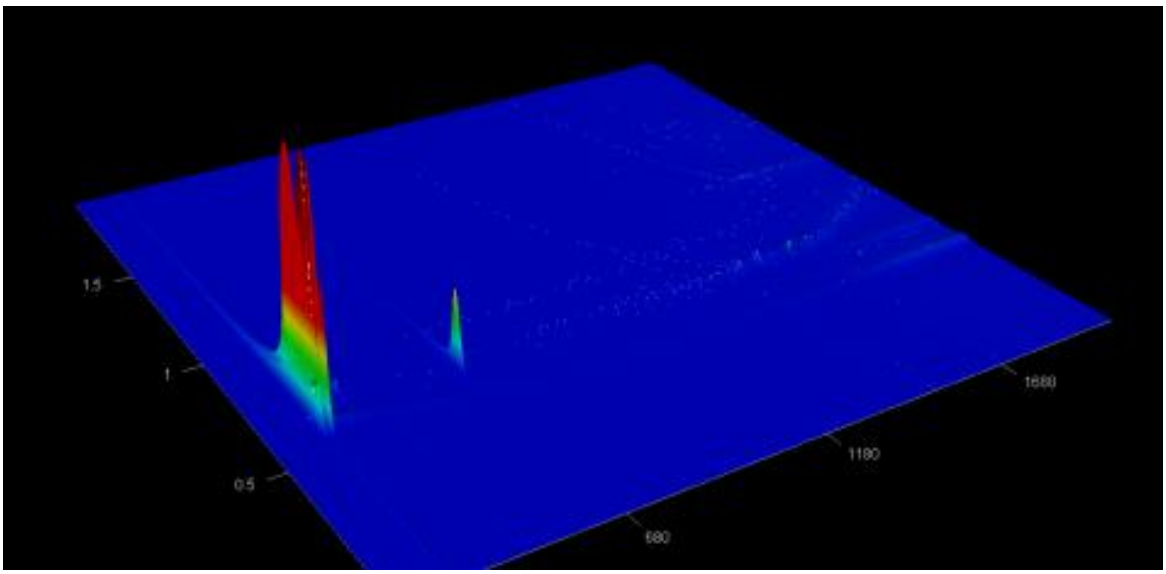

Figure 87: Chromatogram of sample at 15 m from the dolerite dyke.

Figure 87 displays the chromatogram of the sample at 15 m from the dolerite intrusion; 527 unique organic compounds were identified, with 284 of these compounds having first-dimension residence times greater than 1620 s.

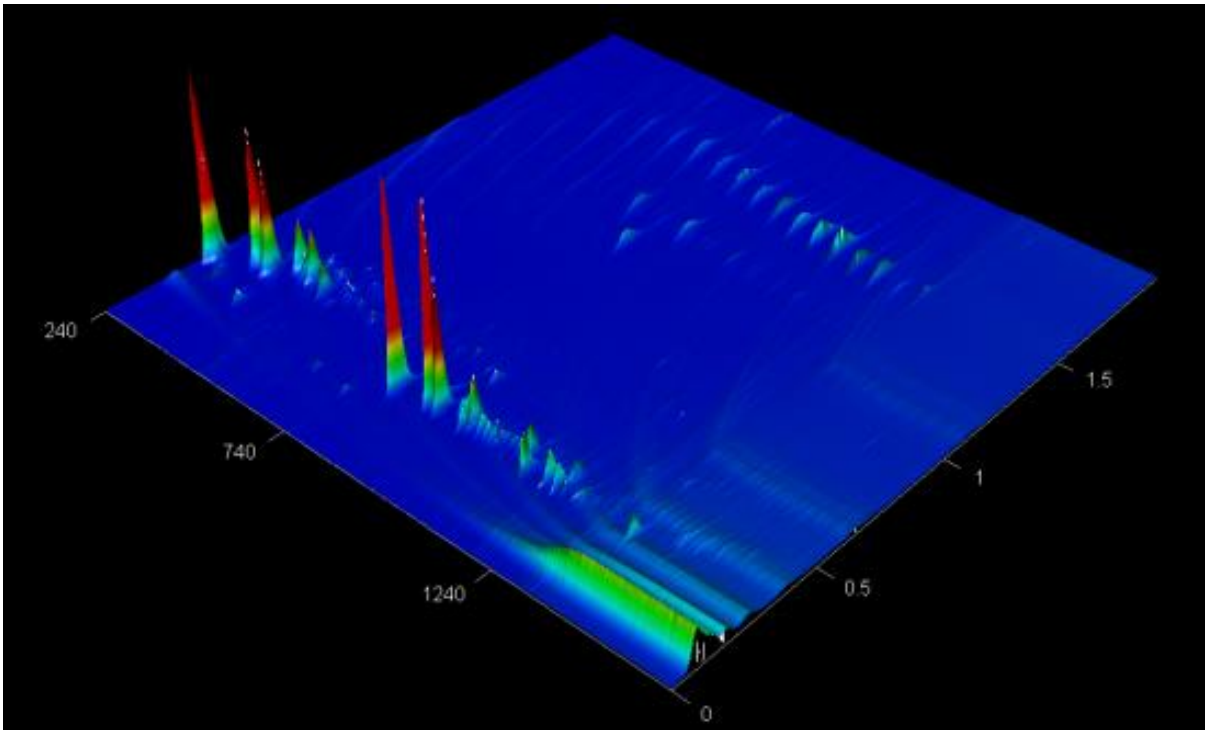

Figure 88: Chromatogram of sample at 16 m from the dolerite dyke.

At a distance of 16m from the dolerite intrusion 95 unique organic compounds were identified as seen in Figure 88. None of the identified compounds had first-dimension residence times greater than 1620 s.

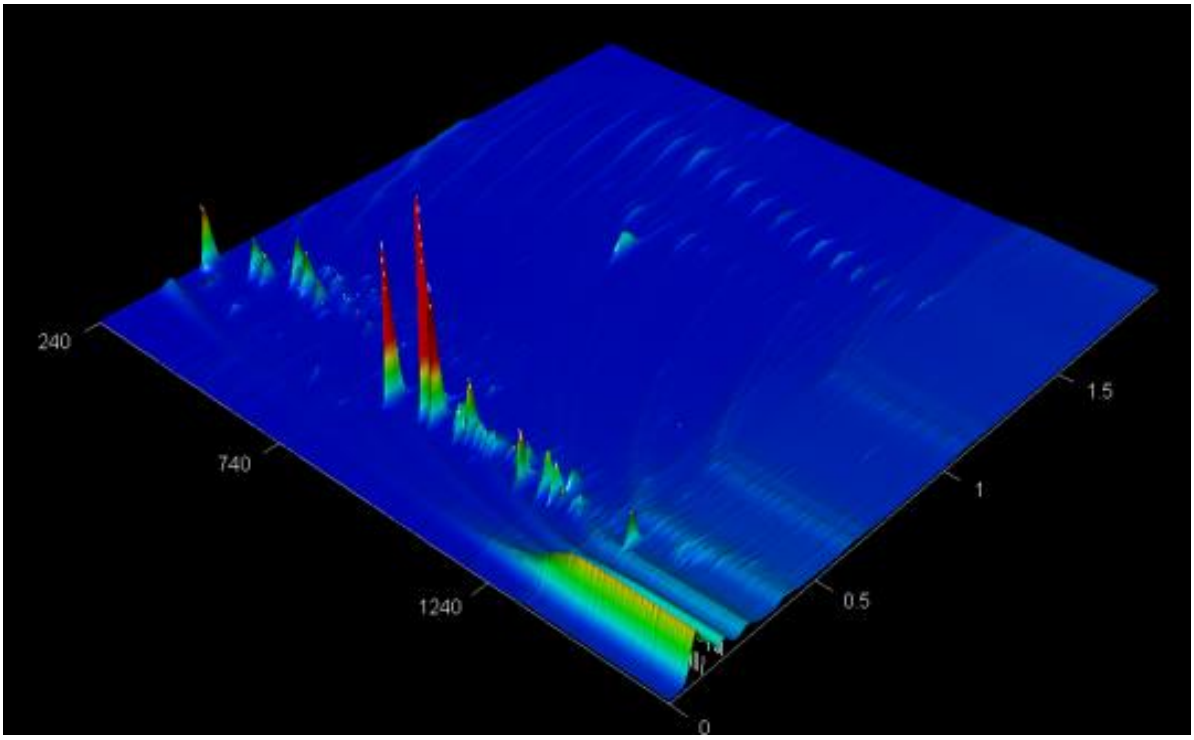

Figure 89: Chromatogram of sample at 17 m from the dolerite dyke.

Figure 89 displays the chromatogram of the sample taken 17m from the dolerite intrusion; these samples host 93 unique organic compounds. Good separation is achieved in both the first and second dimensions, with no compounds having residence times greater than 1620s in the first dimension.

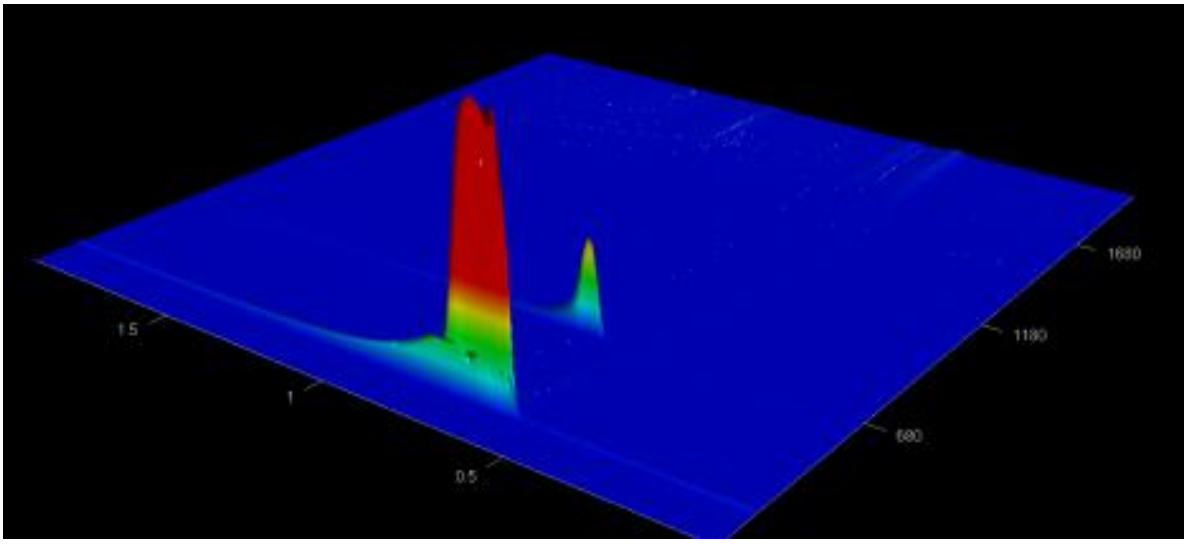

Figure 90: Chromatogram of sample at 18 m from the dolerite dyke.

The chromatogram in Figure 90 displays the organic signature at a distance of 18 m from the dolerite intrusion. At this distance 92 unique organic compounds were identified. None of these compounds had first-dimension residence times greater than 1620 s.

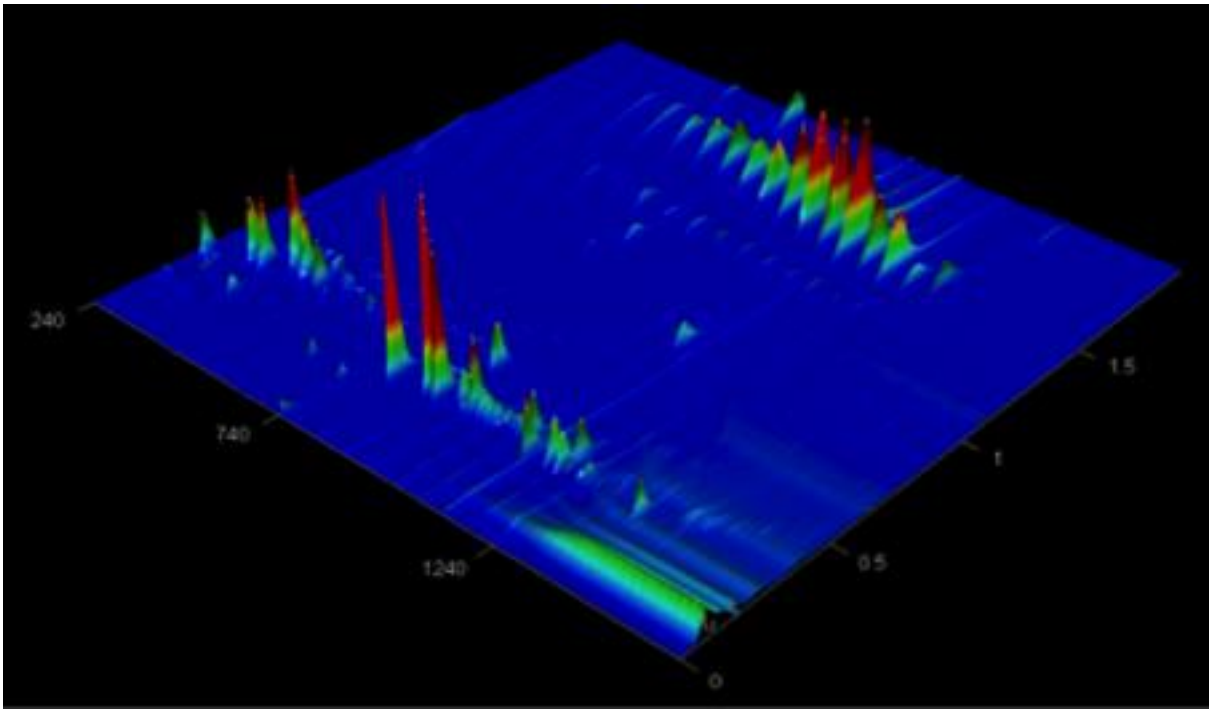

Figure 91: Chromatogram of sample at 19 m from the dolerite dyke.

The most distal sample analysed was at 19 m; the chromatogram in Figure 91 displays the 196 unique compounds identified. Once investigated, none of these compounds showed first dimension residence times greater than 1620 s.

Table 12: Complete table of unique organic compounds identified through GC*GCTOFMS analysis.

Molecule Name	*Formula*	*Molecular Weight*	*1st Dimension Time (s)*	*2nd Dimension Time (s)*	*Sample*
(2-Methyl[1,3]dithian-2-yl)methanol	C6H12OS2	164	1736	0.56	DK-15
[1,1'-Biphenyl]-4-carboxaldehyde	C13H10O	182	1682	0.69	DK-10
[1,1'-Biphenyl]-4,4'-diamine, 3,3'-dimethyl-	C14H16N2	212	1770	0.73	DK-15
[1,1':3',1''-Terphenyl]-2'-ol	C18H14O	246	1970	0.89	DK-3
[1,1':4',1''-Terphenyl]-2,2''-diamine	C18H16N2	260	2022	0.94	DK-3
[14]Annulene, 1,6:7,12-bis(methano)-, anti-	C16H14	206	1762	0.73	DK-10
[14]Annulene, 1,6:8,13-bis(methano)-, syn	C16H14	206	1788	0.76	DK-3
[2](1,4)Naphthaleno[2](2,6)pyrazinophane-1,11-diene	C18H12N2	256	1738	1.08	DK-15
1-(10-Methylanthracen-9-yl)ethanone	C17H14O	234	1832	0.81	DK-15
1-(2-Vinylphenyl)-1H-isochromene	C17H14O	234	1768	0.76	DK-8
1-Allyldimethylsilyloxy-3,5-dimethylbenzene	C13H20OSi	220	1714	0.6	DK-8
1-Buten-3-yne	C4H4	52	1846	0.52	DK-8
1-Butyl(dimethyl)silyloxy-2-phenylethane	C14H24OSi	236	1890	0.6	DK-15
1-Cyclohexyldimethylsilyloxy-2-phenylethane	C16H26OSi	262	1716	0.6	DK-3
1-Di(tert-butyl)silyloxy-2-phenylethane	C16H28OSi	264	1746	0.59	DK-8

1-Dimethyl(isopropyl)silyloxy-2-phenylethane	C13H22OSi	222	1752	0.59	DK-3
1-Dimethyl(octyl)silyloxy-2-phenylethane	C18H32OSi	292	1706	0.6	DK-10
1-Ethyl-2-methylphenanthrene	C17H16	220	1796	0.78	DK-3
1-Hydroxypyrene	C16H10O	218	1706	0.97	DK-3
1-Iodo-2-methylundecane	C12H25I	296	1924	1.29	DK-10
1-Methoxymethylfluorene	C15H14O	210	1644	0.73	DK-10
1-Methyl-acridone	C14H11NO	209	1660	0.98	DK-15
1-Phenanthrenecarboxylic acid, 1,2,3,4,4a,9,10,10a-octahydro-1,4a-dimethyl-7-(1-methylethyl)-, methyl ester, [1R-(1à,4aá,10aà)]-	C21H30O2	314	1862	0.85	DK-10
1-Phenyl-1H-inden-4-ol	C15H12O	208	1922	0.8	DK-3
1-Phenyldibenzofuran	C18H12O	244	1694	0.98	DK-8
1-Pyrenemethanol	C17H12O	232	1884	0.82	DK-3
1,1'-Binaphthalene, 3,3',4,4'-tetrahydro-	C20H18	258	1718	1	DK-8
1,11,11-Trimethyl-1,2,3,4-tetrahydro-1,4-methanophenazine	C16H18N2	238	1676	0.74	DK-15
1,2-Benzenedicarboxylic acid, diisooctyl ester	C24H38O4	390	1898	0.93	DK-8
1,2-Benzenedicarboxylic acid, mono(2-ethylhexyl) ester	C16H22O4	278	1898	0.93	DK-3
1,2-Butadiene, 1,1,4-triphenyl-3-trimethylsilyl-4-trimethylsilyloxy-	C28H34OSi2	442	1712	0.6	DK-3
1,2-Dicarboxy-3-(4-chlorophenyl)-2,3(1H)-dihydropyrido(1,2-a)benzimidazole	C19H15ClN2O4	370	1630	0.97	DK-10
1,2,3,4-Tetrahydro-1-phenyl-1,2,3-methanonaphthalene	C17H14	218	1782	0.75	DK-8

1,2,3,4-Tetrahydro-1,3-methanophenanthrene, 2,2-dimethyl-	C17H18	222	1668	0.73	DK-8
1,2,3,4-Tetrahydrophenanthren-9-ol	C14H14O	198	1728	0.7	DK-3
1,3-Pentadiene, 1,1-diphenyl-, (Z)-	C17H16	220	1816	0.79	DK-3
1,4-Benzenediol, 2,6-bis(1,1-dimethylethyl)-	C14H22O2	222	1762	0.75	DK-15
1,4-Bis(nitratomethyl)anthracene	C16H12N2O6	328	1770	0.77	DK-10
1,4-Bis(trimethylsilyl)-1,3-butadiyne	C10H18Si2	194	1662	0.6	DK-3
1,4-Bis[à-methoxyethyl]benzene	C12H18O2	194	1670	0.6	DK-10
1,4,7-Trimethyl-2-azafluorene	C15H15N	209	1800	0.75	DK-3
1,5-Diphenyl-2H-1,2,4-triazoline-3-thione	C14H11N3S	253	1660	0.93	DK-8
1,5,6,7-Tetramethyl-3-phenylbicyclo[3.2.0]hepta-2,6-diene	C17H20	224	1648	0.73	DK-10
1,7-Dimethyldibenzothiophene	C14H12S	212	1736	0.72	DK-10
1,9-Dihydropyrene	C16H12	204	1832	0.79	DK-15
11H-Benzo[a]carbazole	C16H11N	217	1750	0.93	DK-8
11H-Benzo[a]fluoren-11-one	C17H10O	230	2032	0.88	DK-3
11H-Benzo[a]fluorene	C17H12	216	1910	0.82	DK-3
11H-Benzo[b]fluorene	C17H12	216	1892	0.81	DK-3
11H-Indeno[1,2-b]quinoxaline, 2-methyl-	C16H12N2	232	1936	0.85	DK-8
11H-Indeno[2,1-a]phenanthrene	C21H14	266	1802	1.37	DK-3
13-Bromo-15-(2-methoxyphenyl)tricyclo[8.2.2.2(4,7)]hexadeca-1(13),4(16),5,7(15),10(14),11-hexaene	C23H21BrO	392	1700	0.74	DK-10

13H-Dibenzo[a,h]fluorene	C21H14	266	1934	1.4	DK-15
1H-1,3-Benzimidazol-5-ol, 2-phenyl-	C13H10N2O	210	1720	0.71	DK-3
1H-Inden-1-one, 2-(2,3-dihydro-1H-inden-1-ylidene)-2,3-dihydro-	C18H14O	246	1942	0.87	DK-3
1H-Indole-3-carboxaldehyde, 5-fluoro-1-(phenylmethyl)-	C16H12FNO	253	1646	0.95	DK-10
1H-Pyrazole, 3,5-diphenyl-	C15H12N2	220	1998	0.83	DK-3
1H-Thiopyrano[3,4-c]pyridine-5-carbonitrile, 6-isobutylsulfanyl-3,3-dimethyl-8-morpholin-4-yl-3,4-dihydro-	C19H27N3OS2	377	1846	0.25	DK-10
2-(4-Methylphenyl)benzoic acid	C14H12O2	212	1736	0.72	DK-8
2-[4-(2-Hydroxy-phenyl)-thiazol-2-yl]-5-phenyl-penta-2,4-dienenitrile	C20H14N2OS	330	1700	0.89	DK-10
2-Amino-1-phenylethanol, trimethylsilyl ether	C11H19NOSi	209	1770	0.6	DK-3
2-Benzyl-[1,4]benzoquinone	C13H10O2	198	1712	0.7	DK-15
2-Biphenylcarboxylic acid	C13H10O2	198	1710	0.69	DK-3
2-Butyne-1,4-diol, 4-(5-methyl-2-furanyl)-1,1-diphenyl-	C21H18O3	318	1870	0.82	DK-3
2-Chloro-4,6-dimethoxy-1,5-naphthyridine	C10H9ClN2O2	224	1662	0.74	DK-3
2-Cyclopenten-1-one, 3-(1-hepten-1-yl)-2-(trimethylsilyl)-	C15H26OSi	250	1744	0.59	DK-3
2-Dibenzofuranol	C12H8O2	184	1660	0.68	DK-3
2-Dimethylsilyloxytetradecane	C16H36OSi	272	1670	0.53	DK-10
2-Ethylphenol, tert-butyldimethylsilyl ether	C14H24OSi	236	2032	0.6	DK-3
2-Fluorenamine	C13H11N	181	1724	0.7	DK-8
2-Fluorenecarboxaldehyde	C14H10O	194	1648	0.7	DK-10

2-Heptanone, 6-(3-acetyl-2-methyl-1-cyclopropen-1-yl)-6-methyl-	C14H22O2	222	1986	0.6	DK-3
2-Hydroxyfluorene	C13H10O	182	1682	0.69	DK-3
2-Hydroxymethyl-10-methylanthracene	C16H14O	222	1738	0.75	DK-10
2-Phenanthrenol	C14H10O	194	1874	0.76	DK-15
2-Phenyl-2H-1,2,3-benzotriazole	C12H9N3	195	1962	0.8	DK-15
2-Phenylnaphthalene	C16H12	204	1710	0.71	DK-3
2,2'-Binaphthalene	C20H14	254	1828	1.09	DK-3
2,2'-Biquinoline	C18H12N2	256	1738	1.08	DK-10
2,4-Dihydroxybenzoic acid, bis(tert-butyldimethylsilyl) ether, tert-butyldimethylsilyl ester	C25H48O4Si3	496	1998	1.33	DK-8
2,4-Hexadiyne	C6H6	78	1730	0.51	DK-10
2,4,6-Trimethyl-7-oxo-4,7-dihydro-triazolo(3,2-c)triazine	C7H9N5O	179	1684	0.6	DK-10
2,5-Dimethyl-4-(4-aminophenyl)pyridine	C13H14N2	198	1642	0.7	DK-10
2,6-Dihydroxybenzoic acid, bis(tert-butyldimethylsilyl) ether, tert-butyldimethylsilyl ester	C25H48O4Si3	496	1762	1.4	DK-10
2,6-Diphenylpyridine	C17H13N	231	1812	1.04	DK-3
2',4'-Dimethoxy-3'-methylpropiophenone	C12H16O3	208	1766	0.6	DK-3
2(1H)-Quinolinone, 3-methyl-	C10H9NO	159	1640	0.65	DK-3
2H-Isoquinolin-1-one, 3-amino-2-benzyl-7-nitro-4-thiophen-2-yl-	C20H15N3O3S	377	1872	0.27	DK-8
2H-Phenanthro[9,10-b]pyran	C17H12O	232	1892	0.83	DK-3

3-({1-[5-Benzyl-1-(4-fluorophenyl)-6-oxo-1,4,5,6-tetrahydro-[1,2,4]triazin-3-yl]ethylidene}hydrazono)-1,3-dihydroindol-2-one	C26H21FN6O2	468	1884	0.26	DK-8
3-(2,2-Diphenylvinyl)-3-isobutyl-2-methylperhydropyrrolo[1,2-a]pyrazin-1,4-dion	C26H30N2O2	402	1768	0.76	DK-3
3-Ethylphenol, tert-butyldimethylsilyl ether	C14H24OSi	236	2024	0.6	DK-3
3-Methylcarbazole	C13H11N	181	1722	0.7	DK-3
3-Phenanthrol	C14H10O	194	1870	0.76	DK-8
3,5-Dimethylphenol tbdms	C14H24OSi	236	1786	0.6	DK-3
3,6-Dioxa-2,7-disilaoctane, 2,2,7,7-tetramethyl-4,5-diphenyl-	C20H30O2Si2	358	1782	0.6	DK-3
3,7-Dimethyl-2,3,3a,4,5,6-hexahydro-1-benzofuran #	C10H16O	152	1906	0.56	DK-10
3H-1,4-Benzodiazepin-2-amine, 7-chloro-N-methyl-5-phenyl-N-(phenylmethyl)-, 4-oxide	C23H20ClN3O	389	1812	1.14	DK-8
3H-Pyrazole, 3,3-dimethyl-5-phenyl-4-phenylethynyl-	C19H16N2	272	2036	0.92	DK-10
3H-Pyrrolo[3,2-H]quinoline, 2,3,3-trimethyl-	C14H14N2	210	1620	0.73	DK-15
4-[(N,N-Dimethylcarbamoyl)diphenylmethyl]diphenylacetic acid	C30H27NO3	449	1746	0.3	DK-8
4-[2-(4-Methylphenyl)ethenyl]pyridin	C14H13N	195	1768	0.73	DK-10
4-Amino-9-fluorenone	C13H9NO	195	1962	0.79	DK-3
4-Ethylbenzoic acid, 2-butyl ester	C13H18O2	206	1994	0.57	DK-10
4-Ethylbenzoic acid, benzyl ester	C16H16O2	240	1972	0.57	DK-8

4-Ethylsulfanyl-3-nitro-N-(2-p-tolyloxy-ethyl)-benzamide	C18H20N2O4S	360	1708	0.88	DK-10
4-Fluoro-2-nitroaniline, 5-[4-(pyrrolidin-1-yl)carbonylmethylpiperazin-1-yl]-	C16H22FN5O3	351	2036	0.86	DK-3
4-Hydroxy-9-fluorenone	C13H8O2	196	1742	0.7	DK-3
4-Isopropylthiophenol	C9H12S	152	1806	0.55	DK-10
4-Methoxy-2,2'-dimethyl-4'-nitrobiphenyl	C15H15NO3	257	1874	0.81	DK-8
4-Methyl-acridone	C14H11NO	209	1670	0.98	DK-15
4-Methylcarbazole	C13H11N	181	1696	0.7	DK-3
4-Phenanthrenol	C14H10O	194	1874	0.76	DK-3
4-Phenoxybenzaldehyde	C13H10O2	198	1712	0.7	DK-10
4-Stilbene carboxaldehyde	C15H12O	208	1926	0.8	DK-15
4,5,6,7-Tetrahydroxy-1,8,8,9-tetramethyl-8,9-dihydrophenaleno[1,2-b]furan-3-one	C19H18O6	342	1952	0.67	DK-8
4H-Cyclopenta[def]phenanthrene	C15H10	190	1698	0.71	DK-3
5-Methoxy-2,3-dimethyl-7,9-diphenyl-1H-pyrrolo[2,3-f]quinoline	C26H22N2O	378	1718	0.4	DK-8
5-Methoxy(5H)dibenzo[a,d]cycloheptene	C16H14O	222	1770	0.76	DK-15
5-Naphthalen-1-yl-2H-pyrazol-3-ol	C13H10N2O	210	1732	0.71	DK-3
5-tert-Butyl-4-hydroxymethyl-2-methyl-furan-3-carboxylic acid	C11H16O4	212	1834	0.6	DK-15
5,12-Naphthacenedione	C18H10O2	258	1656	1.05	DK-8
5,6-Dihydrochrysene	C18H14	230	1962	0.86	DK-8
5,7,8,9,10,11-Hexahydro-4H-cyclopenta[a]pyrene	C19H18	246	1992	0.9	DK-3

5,8,11,14-Eicosatetraynoic acid, methyl ester	C21H26O2	310	1682	0.74	DK-10
5Alpha-cyano-3-methoxymethylenecholestane, (E)-	C30H49NO	439	1860	1.39	DK-15
5H-Dibenzo[a,d]cyclohepten-5-one, 10,11-dihydro-	C15H12O	208	1726	0.72	DK-3
5H-Dibenzo[a,d]cycloheptene, 5-chloro-10,11-dihydro-	C15H13Cl	228	1644	0.71	DK-10
5H-Dibenzo[a,d]cycloheptene, 5-methylene-	C16H12	204	1636	0.7	DK-3
6-Chrysenol	C18H12O	244	1946	0.85	DK-10
6,6-Diphenylfulvene	C18H14	230	1960	0.86	DK-10
6,6'-Biquinoline	C18H12N2	256	1738	1.08	DK-3
6,7,8,9-Benzo[b]fluorene	C17H16	220	1758	0.74	DK-15
6H-Dibenzo[b,d]-pyran	C13H10O	182	1702	0.69	DK-3
7-(4-Methoxy-phenyl)-cyclohepta-1,3,5-triene	C14H14O	198	1652	0.7	DK-3
7-Methyl-7-(1-methylethenyl)-2-phenylbicyclo[4.2.0]oct-1-ene	C18H22	238	1656	0.74	DK-15
7H-Benzo[c]carbazole	C16H11N	217	1782	0.97	DK-15
7H-Pyrrolo[2,3-h]quinoline, 2,4,8,9-tetramethyl-	C15H16N2	224	1792	0.76	DK-3
8-Chloro-1-methoxyphenazine 5-oxide	C13H9ClN2O2	260	1930	0.83	DK-8
8-Isopropyl-1,3-dimethylphenanthrene	C19H20	248	1932	0.89	DK-10
8,9-Benzodispiro[2.0.2.4]decane, 7-(3-methoxy-2-oxa-1-oxocyclopent-5-yl)-10-phenyl-	C25H26O3	374	1950	0.87	DK-15
9-Anthracenecarbonitrile	C15H9N	203	1844	0.77	DK-8
9-Anthracenecarboxaldehyde	C15H10O	206	1870	0.78	DK-10

9-Anthracenemethanol	C15H12O	208	1656	0.72	DK-3
9-Cyanophenanthrene	C15H9N	203	1844	0.76	DK-3
9-Ethyl-10-methylanthracene	C17H16	220	1842	0.8	DK-3
9-Ethyl-7H-benzo[de]anthracene	C19H16	244	1930	0.83	DK-3
9-Fluorenone, 2.4-dimethyl-	C15H12O	208	1716	0.71	DK-3
9-Hydroxy-4-fluorenylethylene oxide	C15H12O2	224	1830	0.77	DK-3
9-Methyl-10-phenylanthracene	C21H16	268	1936	0.83	DK-10
9-Methyl-9H-carbazole	C13H11N	181	1746	0.7	DK-8
9-Octadecenamide, (Z)-	C18H35NO	281	1818	0.83	DK-3
9-Phenanthrenol	C14H10O	194	1622	0.7	DK-8
9-Phenyl-5H-benzocycloheptene	C17H14	218	1762	0.74	DK-3
9,10-Anthracenedicarboxaldehyde	C16H10O2	234	1654	0.99	DK-8
9,10-Anthracenedione	C14H8O2	208	1752	0.71	DK-3
9,10-Anthracenedione, 1,4,4a,9a-tetrahydro-	C14H12O2	212	1708	0.71	DK-10
9,10-Anthracenedione, 1,4,5-trihydroxy-2-methyl-	C15H10O5	270	1634	1.88	DK-15
9,10-Anthracenedione, 1,4,5,8-tetraamino-	C14H12N4O2	268	1946	1.34	DK-10
9,10-Anthracenedione, 2-methyl-	C15H10O2	222	1824	0.76	DK-3
9,10-Dimethylanthracene	C16H14	206	1740	0.73	DK-3
9,10-Phenanthrenedione	C14H8O2	208	1752	0.71	DK-15
9,9-Dimethyl-9-sila-9,10-dihydrophenanthrene	C15H16Si	224	1630	0.73	DK-10
9,9'-Biphenanthrene, octacosahydro-	C28H46	382	1816	1.45	DK-3

9(10H)-Acridinone	C13H9NO	195	1654	0.9	DK-8
9(10H)-Phenanthrenone, 10-diazo-	C14H8N2O	220	2012	0.84	DK-3
9H-Carbazole-3,6-diamine	C12H11N3	197	1666	0.77	DK-3
9H-Carbazole, 9-methyl-	C13H11N	181	1746	0.71	DK-10
9H-Carbazole, 9-nitroso-	C12H8N2O	196	1668	0.68	DK-3
9H-Cyclopenta[a]pyrene	C19H12	240	1794	1.06	DK-3
9H-Fluoren-9-one, 1-hydroxy-	C13H8O2	196	1844	0.74	DK-3
9H-Fluoren-9-one, 2,3-dimethyl-	C15H12O	208	1694	0.73	DK-3
à-N-Normethadol	C20H27NO	297	1790	0.79	DK-15
à-Phenyldihydrothebaine	C25H27NO3	389	1836	1.16	DK-15
Acenaphtho(1,2-B)pyridine	C15H9N	203	1844	0.76	DK-15
Acetamide, 2-[6-cyclopropyl-3-cyano-4-(2-furyl)-2-pyridylthio]-	C15H13N3O2S	299	1866	1.13	DK-15
Acetic acid, [2-[(2-propenylamino)carbonyl]phenoxy]-	C12H13NO4	235	1712	0.6	DK-10
Acetic acid, à-(1-naphthyl)benzyl ester	C19H16O2	276	1984	0.88	DK-3
Acridine, 9-methyl-	C14H11N	193	1644	0.7	DK-3
Anthracene, 1,2,3,4-tetrahydro-9-propyl-	C17H20	224	1644	0.72	DK-10
Anthracene, 2-ethyl-	C16H14	206	1706	0.72	DK-3
Anthracene, 9-(2-propenyl)-	C17H14	218	1922	0.82	DK-3
Anthracene, 9-ethenyl-	C16H12	204	1636	0.7	DK-8
Anthracene, 9-ethyl-9,10-dihydro-10-methyl-	C17H18	222	1702	0.73	DK-10
Anthracene, 9-phenyl-	C20H14	254	1786	1.05	DK-3

Anthracene, 9,10-dihydro-	C14H12	180	1648	0.72	DK-15
Anthracene, 9,10-dihydro-9-(2-hydroxy-2-propyl)-9,10-dimethyl-	C19H22O	266	1714	0.73	DK-15
Anthracene, 9,10-dihydro-9,10-dimethyl-	C16H16	208	1646	0.72	DK-3
Anthrone	C14H10O	194	1622	0.7	DK-3
As-Indacen-1(2H)-one, 3,6,7,8-tetrahydro-3,3,6,6-tetramethyl-	C16H20O	228	1958	0.94	DK-10
Azulene, 4,8-dimethyl-6-phenyl-	C18H16	232	1904	0.83	DK-3
Benz(a)anthracene-7-carbonitrile	C19H11N	253	2036	1.16	DK-3
Benz(a)anthracene-7-carboxaldehyde	C19H12O	256	1748	1.06	DK-3
Benz[3,4]anthra[1,2-b]oxirene, 1a,11b-dihydro-6,11-dimethyl-	C20H16O	272	2036	0.92	DK-8
Benz[a]anthracene	C18H12	228	1682	1	DK-8
Benz[a]anthracene, 1-methyl-	C19H14	242	1664	1.12	DK-3
Benz[a]anthracene, 1,12-dimethyl-	C20H16	256	1718	1.06	DK-3
Benz[a]anthracene, 12-methyl-	C19H14	242	1664	1.12	DK-15
Benz[a]anthracene, 4-methyl-	C19H14	242	1888	1.06	DK-8
Benz[a]anthracene, 7-methyl-	C19H14	242	1796	1.02	DK-8
Benz[a]anthracene, 7,12-dimethyl-	C20H16	256	1872	1.05	DK-8
Benz[a]anthracene, 8-methyl-	C19H14	242	1658	1.13	DK-3
Benz[j]aceanthrylene, 3-methyl-	C21H14	266	1968	1.4	DK-3
Benzaldehyde, 4-(phenylethynyl)-	C15H10O	206	1870	0.77	DK-3
Benzazepin-1-one, 1,2,3,4-tetrahydro-7,8,9-trimethoxy-	C13H17NO4	251	1832	0.82	DK-15
Benzenamide, 2-(4-nitrophenyl)-, N-9-(9H-xanthenyl)-	C26H18N2O4	422	1756	0.72	DK-10

Benzenamine, 3,4-dimethyl-6-(2,4-dimethylphenylthio)-	C16H19NS	257	1844	0.81	DK-3
Benzene	C6H6	78	1906	0.52	DK-10
Benzene, [bis(methylthio)methyl]-	C9H12S2	184	2026	0.55	DK-8
Benzene, 1-methoxy-4-(phenylmethyl)-	C14H14O	198	1642	0.7	DK-8
Benzene, 1,1'-(1,2-ethenediyl)bis[2-methyl-	C16H16	208	1666	0.73	DK-3
Benzene, 1,1'-(2,2-dichloroethylidene)bis[4-ethyl-	C18H20Cl2	306	1724	0.74	DK-15
Benzene, 1,1'-ethylidenebis[3,4-dimethyl-	C18H22	238	1730	0.75	DK-10
Benzene, 1,1'-ethylidenebis[4-ethyl-	C18H22	238	1696	0.74	DK-3
Benzene, 2-chloro-1,3,5-tris(1-methylethyl)-	C15H23Cl	238	1650	0.75	DK-10
Benzeneacetic acid, à-[(trimethylsilyl)oxy]-, trimethylsilyl ester	C14H24O3Si2	296	1878	0.6	DK-15
Benzeneacetic acid, à-methyl-à,4-bis[(trimethylsilyl)oxy]-, methyl ester	C16H28O4Si2	340	1732	0.59	DK-3
Benzeneethanamine, 2-fluoro-á,3,4-trihydroxy-N-isopropyl-	C11H16FNO3	229	1710	0.75	DK-3
Benzeneethanamine, N-[(pentafluorophenyl)methylene]-4-[(trimethylsilyl)oxy]-	C18H18F5NOSi	387	1638	0.6	DK-10
Benzenethiol, o-isopropyl-,	C9H12S	152	1820	0.55	DK-10
Benzimidazol-5-amine, 1-(4-ethoxyphenyl)-	C15H15N3O	253	1936	0.86	DK-8
Benzo(a)pyren-7-ol	C20H12O	268	1638	1.53	DK-3
Benzo(b)carbazole	C16H11N	217	1734	0.97	DK-3

Benzo(c)carbazole	C16H11N	217	1860	0.97	DK-8
Benzo[b]benzofuran-2-carboxaldehyde	C13H8O2	196	1652	0.69	DK-15
Benzo[b]dihydropyran, 6-hydroxy-4,4,5,7,8-pentamethyl-	C14H20O2	220	1782	0.77	DK-8
Benzo[b]naphtho[2,3-d]furan	C16H10O	218	1836	0.78	DK-3
Benzo[c]cinnoline, 4-methoxy-	C13H10N2O	210	1720	0.71	DK-10
Benzo[c]cinnoline, 4-methyl-	C13H10N2	194	1870	0.76	DK-3
Benzo[c]cinnoline, 4,7-dimethyl-	C14H12N2	208	1922	0.8	DK-10
Benzo[c]phenanthrene, 1-methyl-	C19H14	242	1734	1.03	DK-3
Benzo[c]phenanthrene, 1,12-dimethyl-	C20H16	256	1840	1.03	DK-8
Benzo[c]phenanthrene, 6-methyl-	C19H14	242	1710	1.06	DK-3
Benzo[c]thiophene, 1,3-dihydro-	C8H8S	136	1626	0.57	DK-10
Benzo[gh]perimidine 1-oxide	C14H8N2O	220	2012	0.84	DK-15
Benzo[ghi]perylene	C22H12	276	1978	1.77	DK-15
Benzo[j]fluoranthene	C20H12	252	1706	1.28	DK-10
Benzo[k]fluoranthene	C20H12	252	1690	1.3	DK-10
Benzo[kl]xanthene	C16H10O	218	1870	0.8	DK-8
Benzocyclopentene, 4,5,6,7-tetraethyl-1-methyl-	C18H28	244	1874	0.93	DK-10
Benzofuran-2-one, 2,3-dihydro-4-nitro-	C8H5NO4	179	1724	0.59	DK-10
Benzoic acid, 2-acetyl-3-methoxy-	C10H10O4	194	1748	0.6	DK-3
Benzoic acid, 2-methoxy-, trimethylsilyl ester	C11H16O3Si	224	2002	0.52	DK-3
Benzoic acid, 3,5-dimethyl-, (3,5-dimethylphenyl)methyl ester	C18H20O2	268	1770	0.57	DK-8

Benzoic acid, tridecyl ester	C20H32O2	304	1700	0.78	DK-8
Benzophenone, 5-isopropyl-2-methyl-	C17H18O	238	1850	0.8	DK-3
Benzothiazole, 6-methyl-2-[4-(1-naphthylmethylen)aminophenyl]-	C25H18N2S	378	1782	0.29	DK-8
Bis-1,6-(4-cyclohepta-1,3,6-trienyl-phenoxy)-hexane	C32H34O2	450	1706	0.76	DK-10
Boron, diethyl(4-methyl-3,5-heptanediiminato-N,N')-, (t-4)-	C12H25BN2	208	1662	0.6	DK-10
Bumethanide tetra-methyl derivative	C21H28N2O5S	420	2036	0.23	DK-8
Carbamic acid, acetylthio-, O-methyl ester	C4H7NO2S	133	1938	0.57	DK-3
Carbamic acid, N-[5-(4-pyridyl)-1,3,4-oxadiazol-2-ylthiomethyl]-, 1-methylethyl ester	C12H14N4O3S	294	1730	0.59	DK-10
Carbazole	C12H9N	167	1668	0.68	DK-8
Carbazole, 1,6-dimethyl-	C14H13N	195	1778	0.74	DK-3
Carbazole, 2,3-dimethyl-	C14H13N	195	1786	0.74	DK-3
Carbazole, 2,5-dimethyl-	C14H13N	195	1750	0.72	DK-10
Carbazole, 3,5-dimethyl-	C14H13N	195	1708	0.72	DK-3
Carbazole, 4,5-dimethyl-	C14H13N	195	1708	0.71	DK-8
Chrysene, 1-methyl-	C19H14	242	1818	1.04	DK-8
Chrysene, 2-methyl-	C19H14	242	1684	1.1	DK-3
Chrysene, 4-methyl-	C19H14	242	1860	1.03	DK-8
Chrysene, 5-methyl-	C19H14	242	1832	1.04	DK-8
Chrysene, 6-methyl-	C19H14	242	1658	1.13	DK-10
cis-1,2-Diacetoxy-1,2-dihydrochrysene	C22H18O4	346	2034	0.92	DK-15

Colchiceine, N-desacetyl-N-TFA-	C21H20F3NO6	439	1736	1.46	DK-8
Cyclohepta[b]naphthalene-1-one	C15H14O	210	1776	0.73	DK-15
Cyclohexane, hexaethylidene-	C18H24	240	1620	0.74	DK-10
Cyclohexanone, 2-(2-nitro-2-propenyl)-	C9H13NO3	183	1936	0.55	DK-3
Cyclohexanone, 2,4-diacetyl-5-hydroxy-3-(4-methoxyphenyl)-5-methyl-	C18H22O5	318	1908	0.81	DK-3
Cyclopenta(def)phenanthrenone	C15H8O	204	1802	0.74	DK-3
Cyclopentanecarbonitrile, 2-ethoxy-4-(diphenylmethylene)-, trans--	C21H21NO	303	1848	0.81	DK-10
Cyclotrisiloxane, hexamethyl-	C6H18O3Si3	222	2010	0.53	DK-3
D-Homo-24-nor-17-oxachola-20,22-diene-3,16-dione, 7-(acetyloxy)-1,2:14,15:21,23-triepoxy-4,4,8-trimethyl-, (5à,7à,13à,14á,15á,17aà)-	C28H34O8	498	1944	1.13	DK-8
Desmethyldoxepin	C18H19NO	265	1758	0.74	DK-3
Dibenz[b,e]oxepin-11(6H)-one	C14H10O2	210	1740	0.72	DK-8
Dibenzo[a,c]cyclooctene, 5,6,7,8-tetrahydro-	C16H16	208	1652	0.72	DK-3
Dibenzothiophene, 3-methyl-	C13H10S	198	1680	0.7	DK-3
Dibenzothiophene, 4-methyl-	C13H10S	198	1638	0.7	DK-15
Dibutyl phthalate	C16H22O4	278	1624	0.71	DK-3
Dinaphtho[1,2-b:1',2'-d]furan	C20H12O	268	1702	1.31	DK-10
Dinaphtho[2,1-b:1',2'-d]furan	C20H12O	268	1694	1.33	DK-10
Diphenyl sulfone	C12H10O2S	218	1732	0.69	DK-3
Diphenylacetic acid, 4-((pyrrolidinocarbonyl)diphenylmethyl)-	C32H29NO3	475	1796	0.26	DK-10

Dodecanamide	C12H25NO	199	1814	0.83	DK-3
Ellipticine	C17H14N2	246	1922	0.86	DK-3
Ergoline-8-methanol, 8,9-didehydro-6-methyl-	C16H18N2O	254	2008	0.86	DK-15
Ethane, 1-(2,3-xylyl)-1-(3,4-xylyl)-	C18H22	238	1718	0.74	DK-15
Ethanesulfonyl chloride	C2H5ClO2S	128	1758	0.5	DK-10
Ethanol, 2-(octadecyloxy)-	C20H42O2	314	1830	1.1	DK-10
Ethanone, 1,2-diphenyl-2-[(trimethylsilyl)oxy]-	C17H20O2Si	284	1762	0.6	DK-8
Ethyl phosphoric acid, di-TMS derivative	C8H23O4PSi2	270	1950	0.57	DK-8
Fluoranthene	C16H10	202	1796	0.75	DK-3
Fluoranthene, 2-methyl-	C17H12	216	1856	0.8	DK-3
Fluorene, 4-[1,2-dihydroxyethyl]-	C15H14O2	226	1628	0.73	DK-3
Formamide, N-(9H-xanthen-9-yl)-	C14H11NO2	225	1754	0.72	DK-15
Gentisic acid, O,O'-bis(tert-butyldimethylsilyl)-, tert-butyldimethylsilyl ester	C25H48O4Si3	496	1822	1.37	DK-3
Hexacosanol, trimethylsilyl ether	C29H62OSi	454	1906	1.36	DK-8
Hexadecanoic acid, (2,2-dimethyl-1,3-dioxolan-4-yl)methyl ester	C22H42O4	370	1798	0.89	DK-10
Hexadecanoic acid, 2-hydroxy-1-(hydroxymethyl)ethyl ester	C19H38O4	330	1878	0.9	DK-3
Indeno(1,2,3-ij)isoquinoline	C15H9N	203	1902	0.79	DK-3
Indeno[1,2-b]pyridin-5-ol, 7-amino-	C12H10N2O	198	1740	0.7	DK-8
Indeno[2,1-b]chromene,	C16H10O	218	1816	0.77	DK-3
Indeno[2,1-c]pyridin-9-one, 3,5,7-trimetyl-	C15H13NO	223	1798	0.74	DK-15

Indeno[2,1-c]pyridine, 1,4,6-trimethyl-	C15H15N	209	1858	0.78	DK-15
Leucinylglycine hydrazine, N-[2,4-dinitrophnyl]-	C14H20N6O6	368	1816	0.87	DK-15
Morphinan-4,5-diol-6-one, 1-bromo-	C16H18BrNO3	351	1862	0.8	DK-3
N-Benzylisatoic anhydride	C15H11NO3	253	1666	0.93	DK-8
Naphthacene, 5,12-dihydro-	C18H14	230	1960	0.86	DK-15
Naphthalen-2-ol, 1-(4-morpholyl)(phenyl)methyl-	C21H21NO2	319	1878	0.82	DK-3
Naphthalene, 1-(phenylmethyl)-	C17H14	218	1782	0.75	DK-3
Naphthalene, 1-phenyl-	C16H12	204	1834	0.77	DK-3
Naphthalene, 1,8-di-1-propynyl-	C16H12	204	1760	0.74	DK-3
Naphthalene, 2-(1-methyl-2-phenylethenyl)-	C19H16	244	2036	0.92	DK-3
Naphthalene, 6,7-diethyl-1,2,3,4-tetrahydro-1,1,4,4-tetramethyl-	C18H28	244	1874	0.93	DK-15
Naphthalene, 7-butyl-1-hexyl-	C20H28	268	1666	0.77	DK-10
Naphtho[2,1,8,7-klmn]xanthene	C18H10O	242	1642	1.12	DK-3
Naphtho[3,4:2,3]bornene	C18H20	236	1678	0.73	DK-3
Nonadecane, 2-methyl-	C20H42	282	1868	1.17	DK-3
Nonadecane, 2,3-dimethyl-	C21H44	296	1642	0.95	DK-8
Nortriptyline	C19H21N	263	1686	0.71	DK-3
o-Terphenyl	C18H14	230	1948	0.87	DK-3
Octacosane	C28H58	394	1818	1.07	DK-8
Octadecanamide	C18H37NO	283	1710	0.75	DK-15
Octadecane, 6-methyl-	C19H40	268	1796	1.05	DK-10

Octadecanoic acid, 2-oxo-, methyl ester	C19H36O3	312	1646	0.95	DK-8
p-Xylenolphthalein	C24H22O4	374	1662	1.28	DK-8
Perylene	C20H12	252	1728	1.23	DK-10
Perylene, 3-methyl-	C21H14	266	1784	1.5	DK-3
Phenanthrene, 1-methyl-	C15H12	192	1662	0.71	DK-3
Phenanthrene, 1-methyl-7-(1-methylethyl)-	C18H18	234	1826	0.8	DK-3
Phenanthrene, 1,7-dimethyl-	C16H14	206	1734	0.73	DK-3
Phenanthrene, 2-phenyl-	C20H14	254	1742	1.05	DK-3
Phenanthrene, 2,3,5-trimethyl-	C17H16	220	1780	0.78	DK-3
Phenanthrene, 2,5-dimethyl-	C16H14	206	1754	0.74	DK-10
Phenanthrene, 3,6-dimethyl-	C16H14	206	1734	0.73	DK-8
Phenanthrene, 4,5-dimethyl-	C16H14	206	1722	0.72	DK-3
Phenanthrene, 5,6-dihydro-5-azido-6-hydroxy-	C14H11N3O	237	1724	0.7	DK-15
Phenanthrene, 9-ethyl-	C16H14	206	1726	0.73	DK-3
Phosphoric acid, 2-isothiocyanatoethyl bis(trimethylsilyl) ester	C9H22NO4PSSi2	327	1962	0.57	DK-8
Propanedinitrile	C3H2N2	66	1634	0.5	DK-10
Pyrene	C16H10	202	1850	0.77	DK-3
Pyrene, 1-methyl-	C17H12	216	1888	0.81	DK-3
Pyrene, 1,2,3,3a,4,5-hexahydro-	C16H16	208	1738	0.72	DK-3
Pyrene, 1,2,3,6,7,8-hexahydro-	C16H16	208	1656	0.72	DK-8
Pyrene, 1,3-dimethyl-	C18H14	230	1956	0.87	DK-3

Pyrene, 2-methyl-	C17H12	216	1916	0.82	DK-3
Pyrene, 4,5,9,10-tetrahydro-	C16H14	206	1774	0.75	DK-3
Pyridine-3-carbonitrile, 2-[2-(3,4-dihydroxyphenyl)-2-oxoethylthio]-4-methoxymethyl-6-methyl-	C17H16N2O4S	344	1978	0.55	DK-10
Pyridine-3,5-dicarbonitrile, 1,2-dihydro-6-amino-4-cyclohexyl-2-thione-	C13H14N4S	258	1930	0.81	DK-3
Quassin	C22H28O6	388	1700	1.2	DK-8
Retinoic acid, 5,6-epoxy-5,6-dihydro-, trimethylsilyl ester	C23H36O3Si	388	1756	1.14	DK-3
Silane, (hexacosyloxy)trimethyl-	C29H62OSi	454	1710	1.77	DK-8
Silane, diethoxymethyl-	C5H14O2Si	134	2034	0.57	DK-8
Silane, dimethyl(pentafluorobenzyloxy)tridecyloxy-	C22H35F5O2Si	454	1680	0.17	DK-3
Silane, dimethyl[(methylsilyl)methyl]-	C4H14Si2	118	1624	0.53	DK-10
Silane, dimethylbis(tetramethylcyclopentadienyl)- (mixed isomers)	C20H32Si	300	1778	0.6	DK-3
Silane, dodecyldiethoxymethyl-	C17H38O2Si	302	1958	0.57	DK-8
Silane, triethoxymethoxy-	C7H18O4Si	194	1882	0.6	DK-15
Spiro[2.3]hexane-5-carboxylic acid, 1,1-diphenyl-, methyl ester	C20H20O2	292	1776	0.75	DK-3
Tetradecanamide	C14H29NO	227	1814	0.84	DK-10
Tetrazepam	C16H17ClN2O	288	1950	0.87	DK-10
Thioxanthene	C13H10S	198	1702	0.71	DK-10

Tricyclo[7.4.1.1(2,7)]pentadeca-2,4,6,9,11,13-hexaene-8-ol	C15H14O	210	1820	0.76	DK-3
Tricyclo[8.4.1.1(3,8)]hexadeca-3,5,7,10,12,14-hexaen-2-one, anti-	C16H14O	222	1732	0.75	DK-3
Tricyclo[9.2.2.2(4,7)]heptadeca-1(14),2,4(17),5,7(16),11(15),12-heptaene	C17H16	220	1852	0.8	DK-3
Triethylene glycol monododecyl ether	C18H38O4	318	1736	0.78	DK-3
Triphenylene, 1,2,3,4-tetrahydro-	C18H16	232	1878	0.82	DK-10
Tris(2,6-dimethylphenyl)borane	C24H27B	326	1844	0.79	DK-15
Tyrosine, O-trimethylsilyl-, trimethylsilyl ester	C15H27NO3Si2	325	1760	0.6	DK-15
Unknown 10	C30H42O2	434	1738	1.5	DK-3
Unknown 100	C16H12O4	268	1984	0.57	DK-8
Unknown 101	C22H28O6	388	1988	1.13	DK-8
Unknown 102	C24H26N4O5	450	1988	1.39	DK-8
Unknown 103	C26H30N2O2S	434	1990	1.41	DK-8
Unknown 104	C19H11BrN4O4	438	1994	1.35	DK-8
Unknown 105	C30H42O2	434	1994	1.44	DK-8
Unknown 106	C23H36O3Si	388	2002	1.13	DK-8
Unknown 107	C19H14O2	274	2004	1.37	DK-8
Unknown 108	C30H42O2	434	2004	1.43	DK-8
Unknown 109	C25H27NO3	389	2006	1.14	DK-8
Unknown 11	C3H8O2	76	1764	0.56	DK-3
Unknown 110	C17H38O2Si	302	2008	0.57	DK-8

Unknown 111	C25H34B2OS2	436	2008	1.42	DK-8
Unknown 112	C19H19ClN2O2S	374	2010	1.13	DK-8
Unknown 113	C13H14N2	198	2010	1.35	DK-8
Unknown 114	C23H24N4O2	388	2024	1.13	DK-8
Unknown 115	C19H12Cl3NO3	407	2026	1.13	DK-8
Unknown 116	C22H19N3O3	373	2028	1.13	DK-8
Unknown 117	C28H28N2O2	424	2028	1.14	DK-8
Unknown 118	C19H16O2	276	2030	0.91	DK-8
Unknown 119	C30H42O2	434	2030	1.41	DK-8
Unknown 12	C17H19NO	253	1764	1.41	DK-3
Unknown 120	C20H23NO6	373	2032	1.13	DK-8
Unknown 121	C27H35NO	389	2032	1.14	DK-8
Unknown 122	C16H12N4O10	420	2034	1.13	DK-8
Unknown 123	C24H22O4	374	2036	1.13	DK-8
Unknown 124	C14H11N3S	253	1974	0.87	DK-10
Unknown 125	C21H21NO2	319	1976	0.87	DK-10
Unknown 126	C21H30O4	346	1984	0.65	DK-10
Unknown 127	C17H14O	234	1984	0.89	DK-10
Unknown 128	C36H32Si	492	1988	1.43	DK-10
Unknown 129	C30H42O2	434	1994	1.43	DK-10
Unknown 13	C26H30N2O2S	434	1764	1.52	DK-3
Unknown 130	C30H42O2	434	1998	1.44	DK-10

Unknown 131	C28H24O4	424	2000	1.13	DK-10
Unknown 132	C15H10N2	218	2000	1.14	DK-10
Unknown 133	C17H13N	231	2002	0.9	DK-10
Unknown 134	C22H28O6	388	2004	1.13	DK-10
Unknown 135	C30H42O2	434	2006	1.42	DK-10
Unknown 136	C22H28O6	388	2008	1.13	DK-10
Unknown 137	C22H35F5O2Si	454	2012	1.34	DK-10
Unknown 138	C16H18Si	238	2012	1.38	DK-10
Unknown 139	C8H9NO	135	2014	0.52	DK-10
Unknown 14	C30H42O2	434	1776	1.47	DK-3
Unknown 140	C13H10S	198	2016	1.37	DK-10
Unknown 141	C28H44OSi	424	2020	1.37	DK-10
Unknown 142	C16H24N2O	260	2022	0.94	DK-10
Unknown 143	C23H32O5	388	2024	1.14	DK-10
Unknown 144	C20H28	268	2026	1.37	DK-10
Unknown 145	C20H28	268	2028	1.34	DK-10
Unknown 146	C30H42O2	434	2028	1.42	DK-10
Unknown 147	C12H9F3N4	266	2030	1.37	DK-10
Unknown 148	C19H18O6	342	2034	0.67	DK-10
Unknown 149	C21H14	266	2034	1.37	DK-10
Unknown 15	C20H12N2O2	312	1780	1.16	DK-3
Unknown 150	C30H30	390	2036	1.13	DK-10

Unknown 16	C25H27NO3	389	1794	1.14	DK-3
Unknown 17	C20H16	256	1796	1.11	DK-3
Unknown 18	C22H28O6	388	1804	1.13	DK-3
Unknown 19	C30H42O2	434	1804	1.47	DK-3
Unknown 20	C14H15N	197	1806	1.42	DK-3
Unknown 21	C26H30O8	470	1808	0.65	DK-3
Unknown 22	C30H42O2	434	1808	1.47	DK-3
Unknown 23	C27H38O8	490	1810	1.13	DK-3
Unknown 24	C12H11ClN2	218	1810	1.43	DK-3
Unknown 25	C10H15NO	165	1816	1.11	DK-3
Unknown 26	C23H36O3Si	388	1816	1.14	DK-3
Unknown 27	C9H13N	135	1820	1.11	DK-3
Unknown 28	C19H14O2	274	1822	1.38	DK-3
Unknown 29	C19H14	242	1824	1.09	DK-3
Unknown 3	C22H35F5O2Si	454	1644	0.91	DK-8
Unknown 30	C23H20ClN3O	389	1824	1.14	DK-3
Unknown 31	C25H34B2OS2	436	1834	1.46	DK-3
Unknown 32	C23H36O3Si	388	1836	1.14	DK-3
Unknown 33	C20H30O4	334	1844	1.13	DK-3
Unknown 34	C21H14	266	1850	1.37	DK-3
Unknown 35	C14H15N	197	1850	1.39	DK-3
Unknown 36	C30H42O2	434	1852	1.45	DK-3

Unknown 37	C15H16N2	224	1858	0.78	DK-3
Unknown 38	C13H11NO	197	1864	1.37	DK-3
Unknown 39	C16H16O	224	1866	0.8	DK-3
Unknown 4	C8H5Cl3O	222	1648	0.73	DK-8
Unknown 40	C36H32Si	492	1884	1.44	DK-3
Unknown 41	C26H26V2	440	1886	1.34	DK-3
Unknown 42	C25H48O4Si3	496	1886	1.36	DK-3
Unknown 43	C11H14O3	194	1890	0.52	DK-3
Unknown 44	C25H45ClO2Si	440	1894	1.33	DK-3
Unknown 45	C21H20F3NO6	439	1894	1.35	DK-3
Unknown 46	C14H12N4O2	268	1896	1.36	DK-3
Unknown 47	C16H18Si	238	1898	1.39	DK-3
Unknown 48	C26H26V2	440	1906	1.37	DK-3
Unknown 49	C23H22BrN3O	435	1906	1.45	DK-3
Unknown 5	C19H15ClN2O4	370	1656	0.94	DK-8
Unknown 50	C27H40	364	1912	1.38	DK-3
Unknown 51	C30H42O2	434	1912	1.44	DK-3
Unknown 52	C16H19NS	257	1918	0.81	DK-3
Unknown 53	C19H14O2	274	1922	1.4	DK-3
Unknown 54	C18H14O	246	1926	0.86	DK-3
Unknown 55	C36H32Si	492	1926	1.44	DK-3
Unknown 56	C13H11NO	197	1928	1.37	DK-3

Unknown 57	C24H32O6	416	1930	1.44	DK-3
Unknown 58	C17H19N	237	1934	1.36	DK-3
Unknown 59	C19H18O6	342	1940	0.67	DK-3
Unknown 6	C20H15N3O3S	377	1694	0.59	DK-8
Unknown 60	C30H42O2	434	1944	1.44	DK-3
Unknown 61	C11H18O2Si	210	1946	1.39	DK-3
Unknown 62	C12H10N2O2S	246	1948	0.88	DK-3
Unknown 63	C18H14	230	1952	0.87	DK-3
Unknown 64	C16H13N	219	1966	1.45	DK-3
Unknown 65	C22H35F5O2Si	454	1968	1.33	DK-3
Unknown 66	C28H28N2O2	424	1972	1.42	DK-3
Unknown 67	C14H30FeOP2	332	1980	1.38	DK-3
Unknown 68	C24H51N3O2Si3	497	1992	1.37	DK-3
Unknown 69	C26H30N2O2S	434	1994	1.43	DK-3
Unknown 7	C22H35F5O2Si	454	1654	0.67	DK-3
Unknown 70	C26H22N2	362	1998	1.35	DK-3
Unknown 71	C22H28O6	388	2016	1.13	DK-3
Unknown 72	C30H42O2	434	2016	1.44	DK-3
Unknown 73	C13H11N	181	2020	1.34	DK-3
Unknown 74	C19H23N	265	2026	1.4	DK-3
Unknown 75	C30H42O2	434	2030	1.41	DK-3
Unknown 76	C24H27NO3	377	1920	1.38	DK-8

Unknown 77	C19H14O2	274	1922	1.38	DK-8
Unknown 78	C23H32O2Si	368	1924	1.13	DK-8
Unknown 79	C30H42O2	434	1928	1.45	DK-8
Unknown 8	C16H18N2	238	1656	0.73	DK-3
Unknown 80	C20H23NO6	373	1930	1.14	DK-8
Unknown 81	C20H13IN2O2	440	1930	1.37	DK-8
Unknown 82	C27H30O2	386	1934	0.54	DK-8
Unknown 83	C11H7N3O	197	1934	1.36	DK-8
Unknown 84	C22H28O6	388	1936	1.13	DK-8
Unknown 85	C8H23O4PSi2	270	1944	0.57	DK-8
Unknown 86	C17H13ClIN3O	437	1946	1.35	DK-8
Unknown 87	C21H19N5O2	373	1948	0.64	DK-8
Unknown 88	C19H23F3O3S	388	1954	1.14	DK-8
Unknown 89	C8H8	104	1960	0.54	DK-8
Unknown 9	C26H30N2O2S	434	1728	1.56	DK-3
Unknown 90	C22H27NO	321	1960	1.35	DK-8
Unknown 91	C30H42O2	434	1960	1.43	DK-8
Unknown 92	C16H14S2	270	1964	1.38	DK-8
Unknown 93	C30H42O2	434	1964	1.42	DK-8
Unknown 94	C19H14O2	274	1966	1.34	DK-8
Unknown 95	C22H20N2S2	376	1972	1.13	DK-8
Unknown 96	C18H12F2N2O3S	374	1972	1.14	DK-8

Unknown 97	C19H14O2	274	1972	1.34	DK-8
Unknown 98	C25H27NO3	389	1974	1.13	DK-8
Unknown 99	C21H24O3Si3	408	1982	1.13	DK-8
Xanthene, 9,9-dimethyl-	C15H14O	210	1832	0.76	DK-15
Xanthone	C13H8O2	196	1666	0.7	DK-3

APPENDIX B

Appendix B contains the tomographic images of all the coal samples analysed.

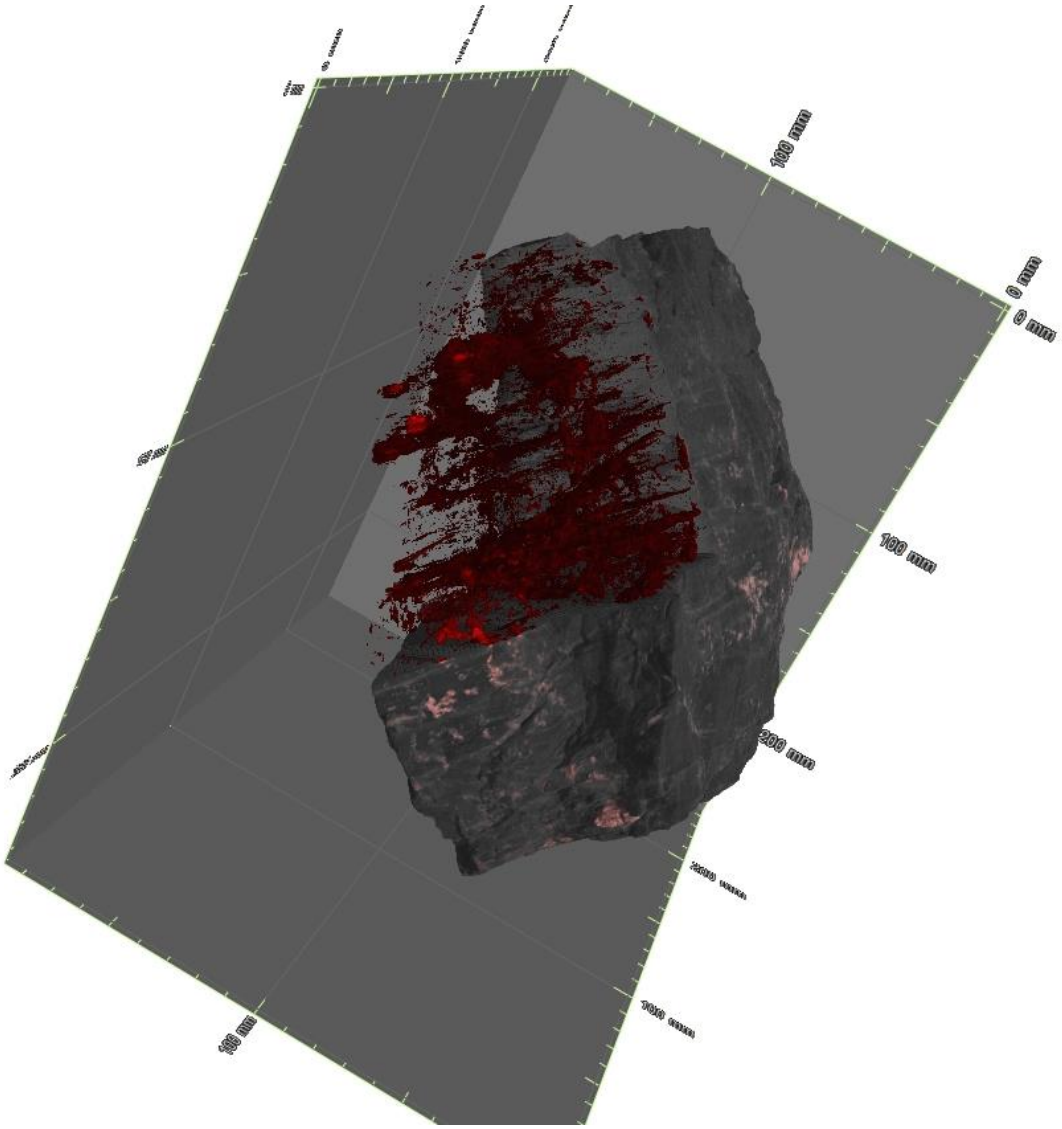

Figure 92: Three-dimensional tomographic image of coal at 0 m from the dyke. Highlighted in red is the inorganic material with the grey scale depicting the organic constituents.

The sample at 0 m displayed in Figure 92 shows a complex network of inorganic material within the coal. The inorganics are not constrained to the sedimentary boundaries, but also cross-cut these layers. In terms of the volumetric data, this samples hosts 4,37% inorganic material, 89,35% organic material and 5,92% pore space.

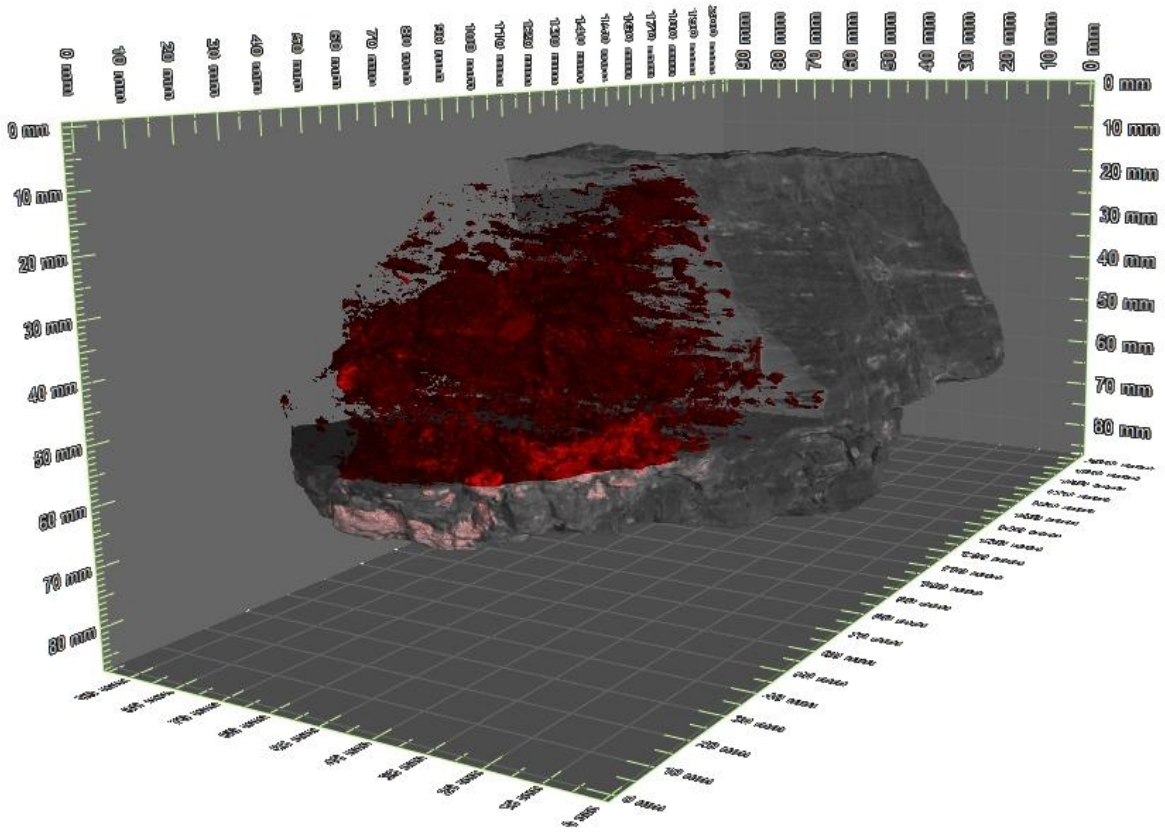

Figure 93: Three-dimensional tomographic image of coal at 1m from the dyke. Highlighted in red is the inorganic material with the grey scale depicting the organic constituents.

The tomographic image of the sample at 1m from the dolerite seen in Figure 93 shows cross cutting inorganic material interconnected throughout the organic sedimentary layers. Volumetrically the sample host 91,80% organic material, 6,17% inorganic material and 2,03% vacant pore spaces.

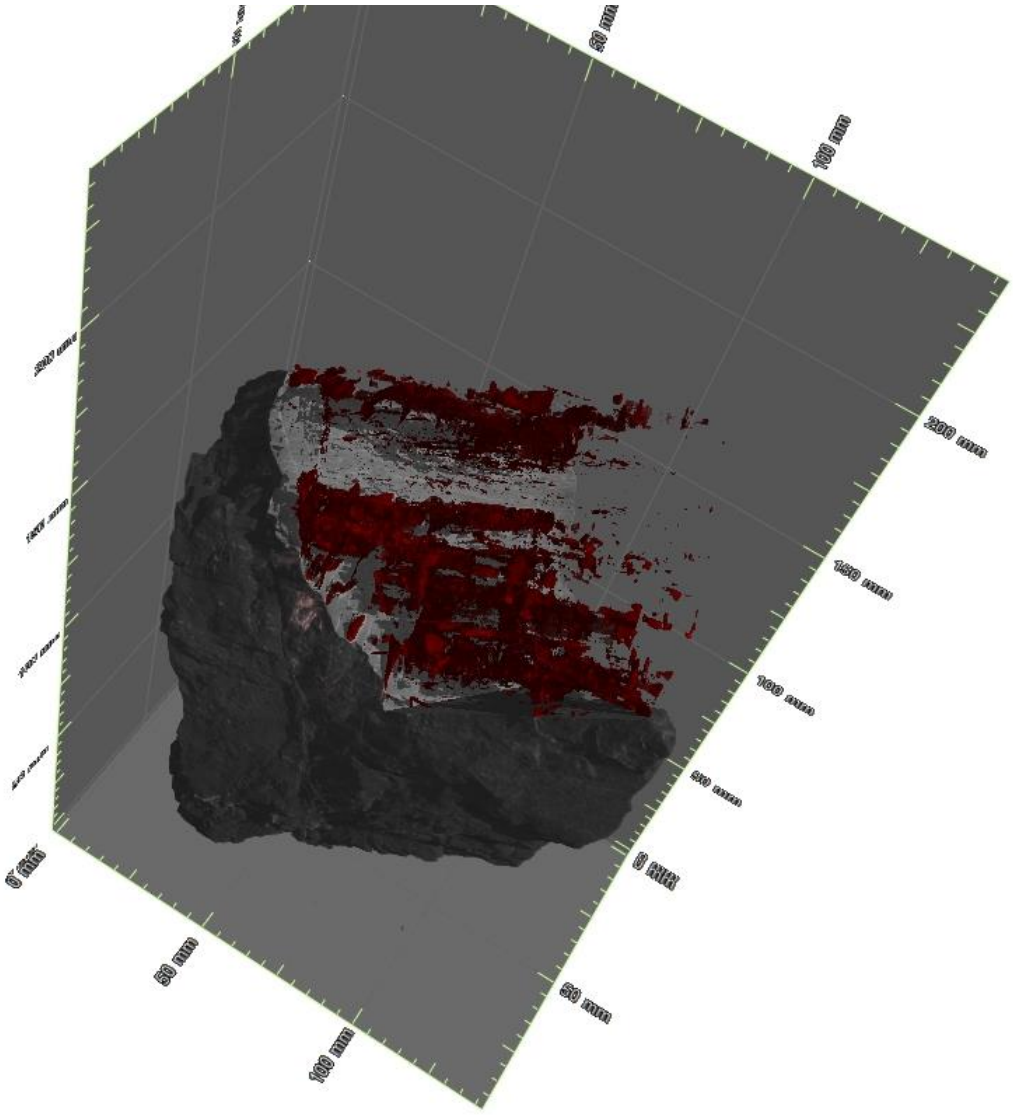

Figure 94: Three-dimensional tomographic image of coal at 2m from the dyke. Highlighted in red is the inorganic material with the grey scale depicting the organic constituents.

At a 2 m distance from the dolerite as seen in Figure 94 the inorganic constituents are hosted primarily within the sedimentary layering and only minor occurrences of cross-cutting relationships are visable. Volumetrically the sample hosts 5,60% mineral matter, 92,84% organic matter and 1,56% pore spaces.

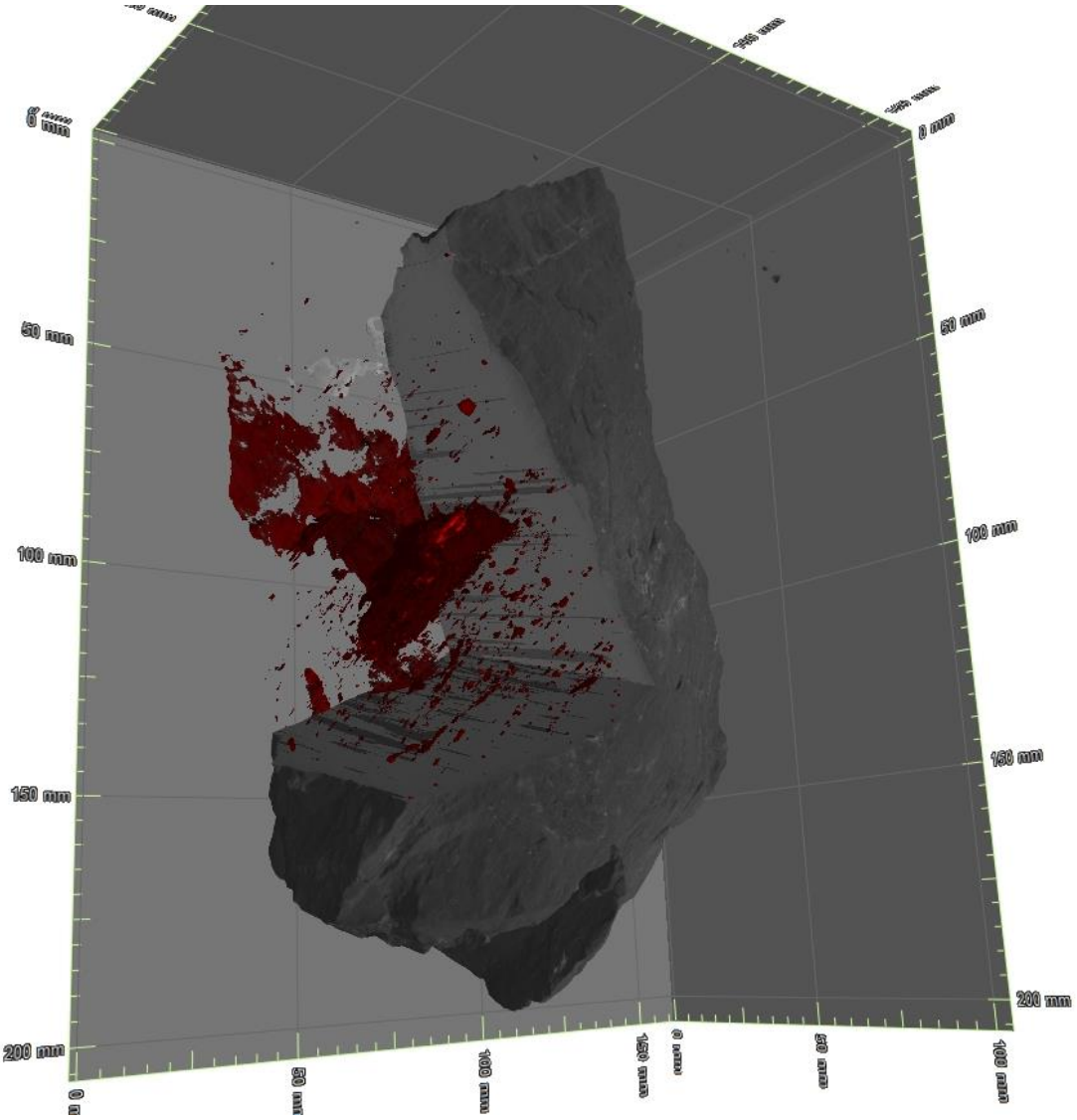

Figure 95: 3D tomographic image of sample DK 3 at 3 m from the dyke hosting sheet-like mineralization. Highlighted in red is the inorganic material's with the grey scale depicting the organic constituents.

Figure 95 is a type example of the sheet-like inorganic structures noted in the samples. The sample at 3 m from the dolerite intrusion displays a network of large inorganic sheets that frequently cross-cut the sedimentary layering of the coal; these cross-cutting feature is also prevalent in the samples at 5 and 8m.

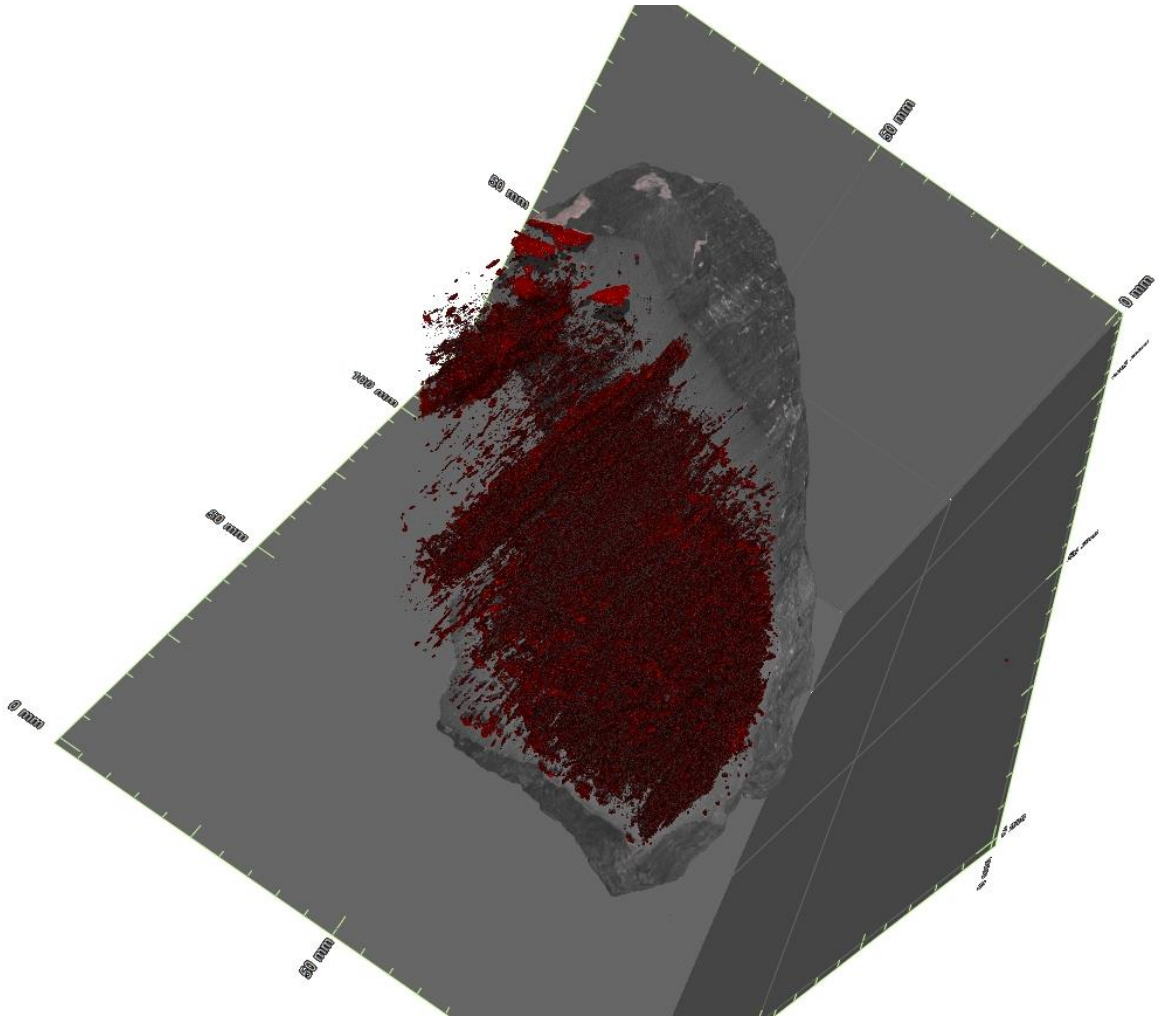

Figure 96: Three-dimensional tomographic image of coal at 4 m from the dyke. Highlighted in red is the inorganic material with the grey scale depicting the organic constituents.

The tomographic image of coal at a distance of 4m for the dolerite dyke seen in Figure 96, displays a fine-grained, complex network of inorganics. This network constitutes 41,84 % volumetrically, while organic matter and pore space volume percentages are 57,72 % and 0.44 % respectively.

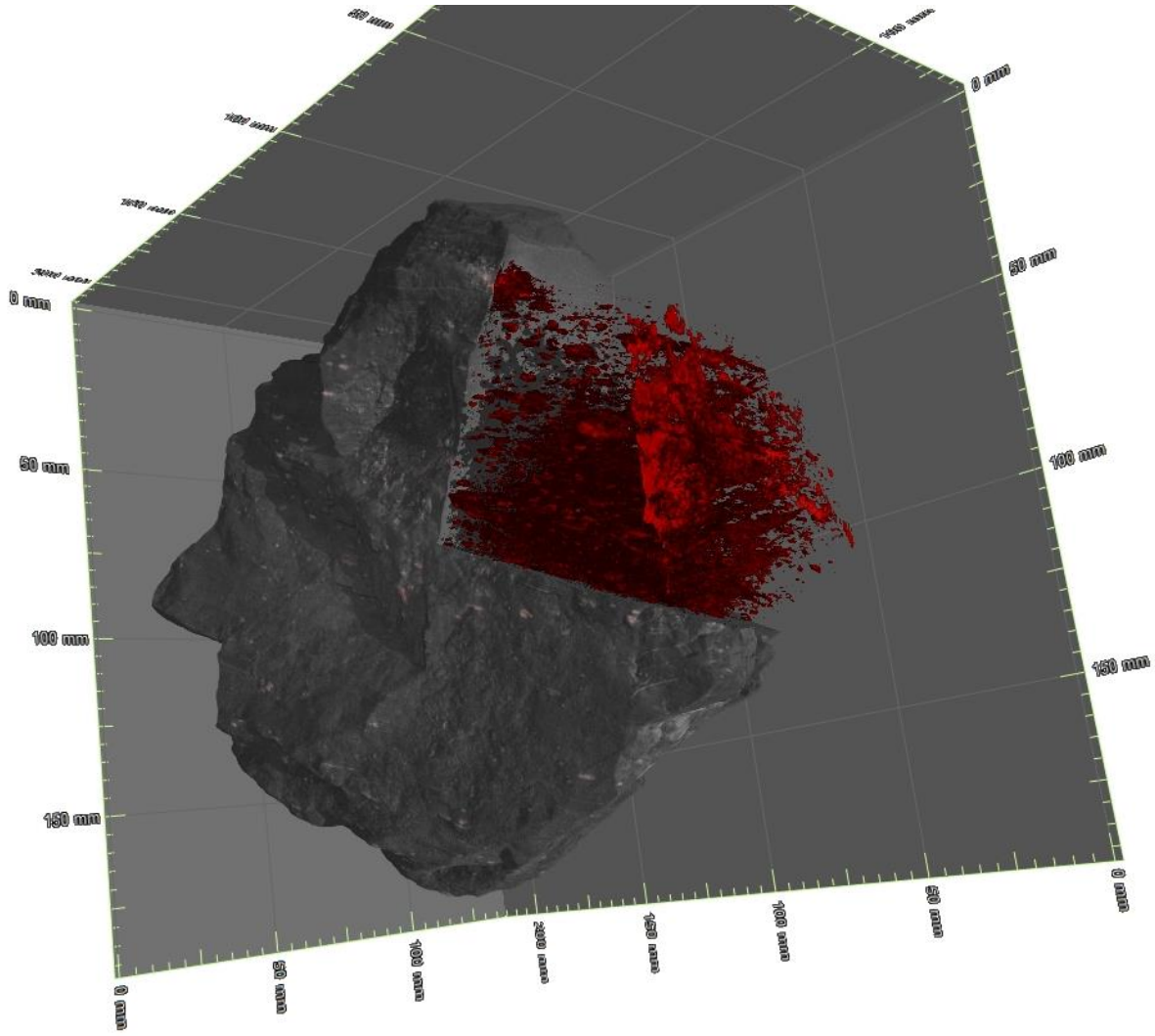

Figure 97: 3D tomographic image of sample DK 5 at 5 m from the dyke hosting sheet-like mineralization. Highlighted in red is the inorganic material's with the grey scale depicting the organic constituents.

Figure 97 of the sample 5m from the dyke displays large sheets of cross-cutting inorganics throughout the coal, with inorganics constituting only 18,61% of the volume, while organic matter and pore space volume percentages are 80,63 % and 0.76 % respectively.

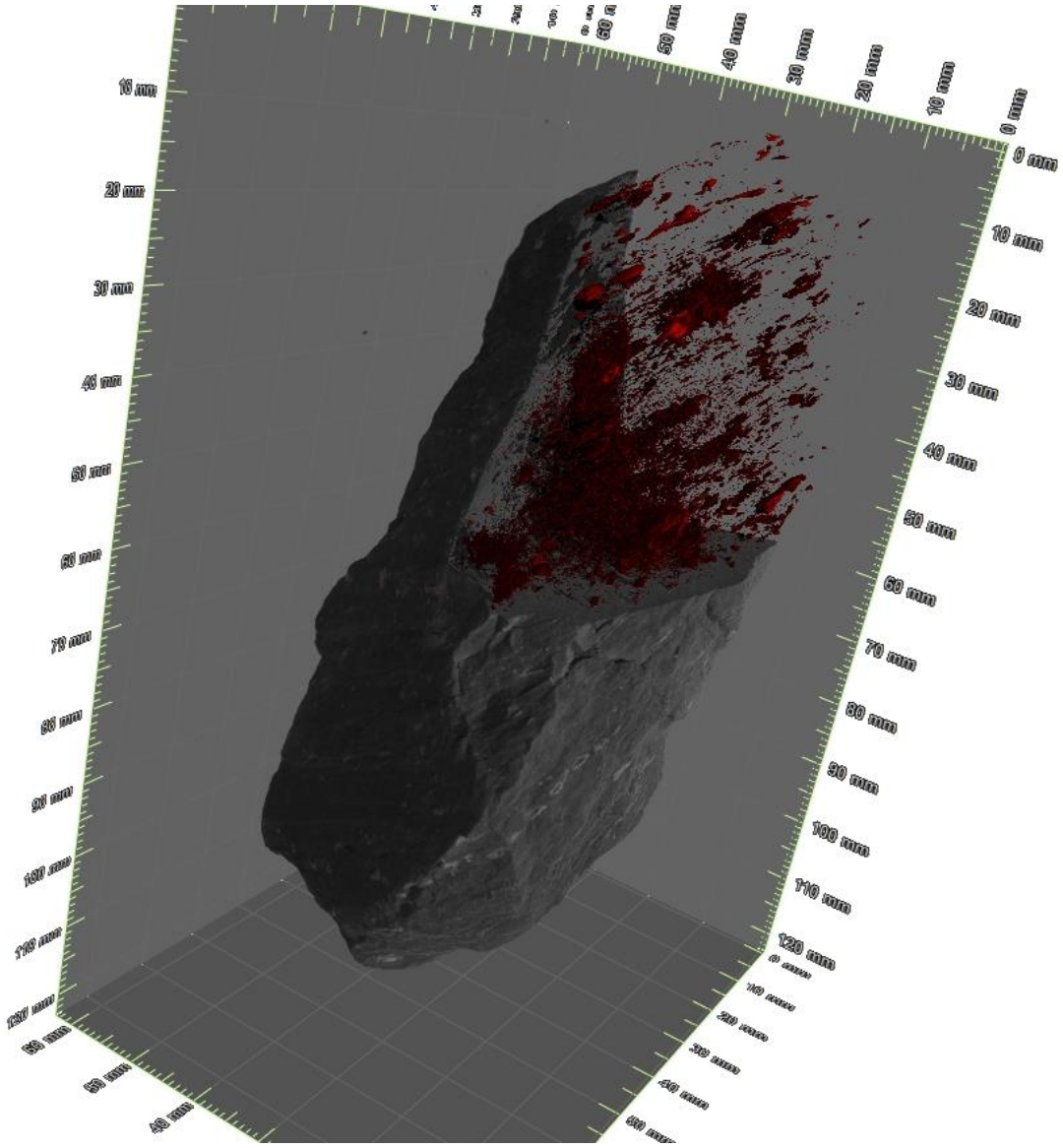

Figure 98: Three-dimensional tomographic image of coal at 6m from the dyke. Highlighted in red is the inorganic material with the grey scale depicting the organic constituents.

At a distance of 6m from the dolerite intrusion a mixture of both fine-grained and cross cutting sheet like structures of mineral matter can be seen within the coal sample (Fig. 98). These structures correspond to 13,83 % of the volume of the sample, while organic matter and pore spaces represent 84,51 % and 1,63 % of the volume.

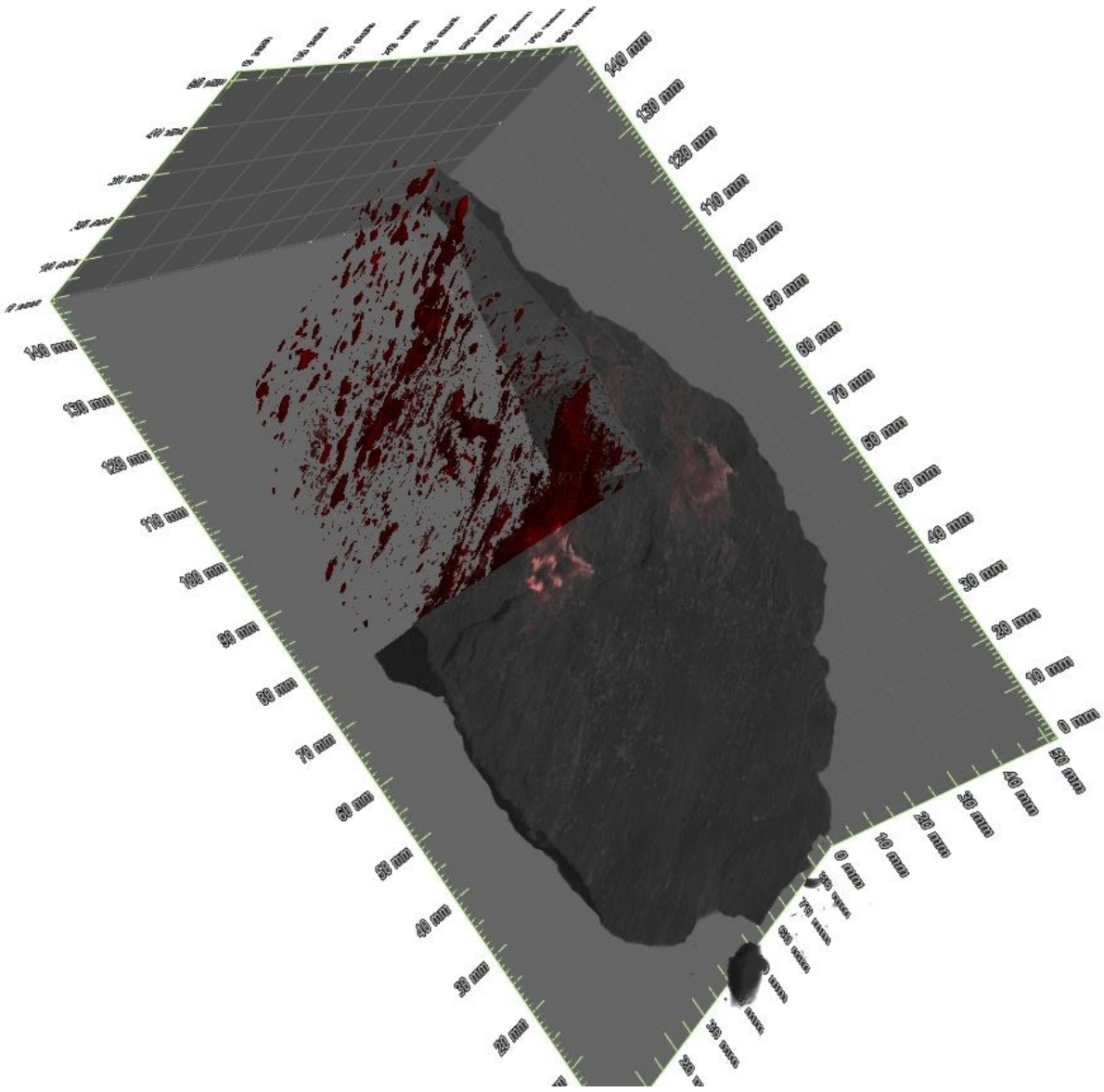

Figure 99: Three-dimensional tomographic image of coal at 7 m from the dyke. Highlighted in red is the inorganic material with the grey scale depicting the organic constituents.

Figure 99 displays tomographic image of a sample 7m from the intrusion. In this image the inorganic material is hosted as granular and sheet structures that cross-cut the sedimentary layering. In terms of volume the sample host 87,10 %; 10,43 % and 2,47 % organic matter, mineral matter and pore spaces respectively.

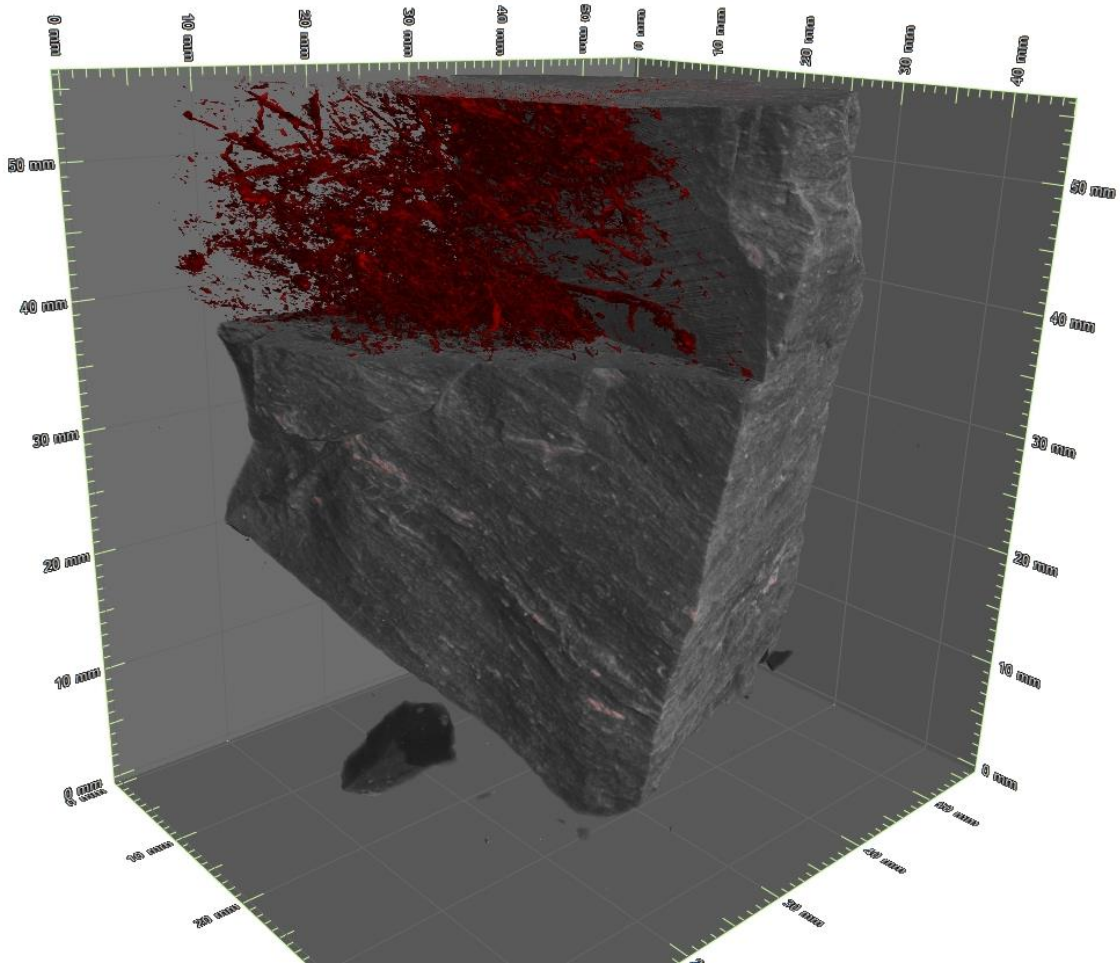

Figure 100: 3D tomographic image of sample DK 8 at 8 m from the dyke hosting sheet-like mineralization. Highlighted in red is the inorganic material's with the grey scale depicting the organic constituents.

The granular network of inorganics noted in Figure 100 at 8 m from the intrusion regularly cross-cut the sedimentary boundaries of the coal sample. Volumetrically the inorganics within the sample correspond to 10,98 % with the portions of organic matter and pore spaces being 82,52 % and 6,49 % respectively.

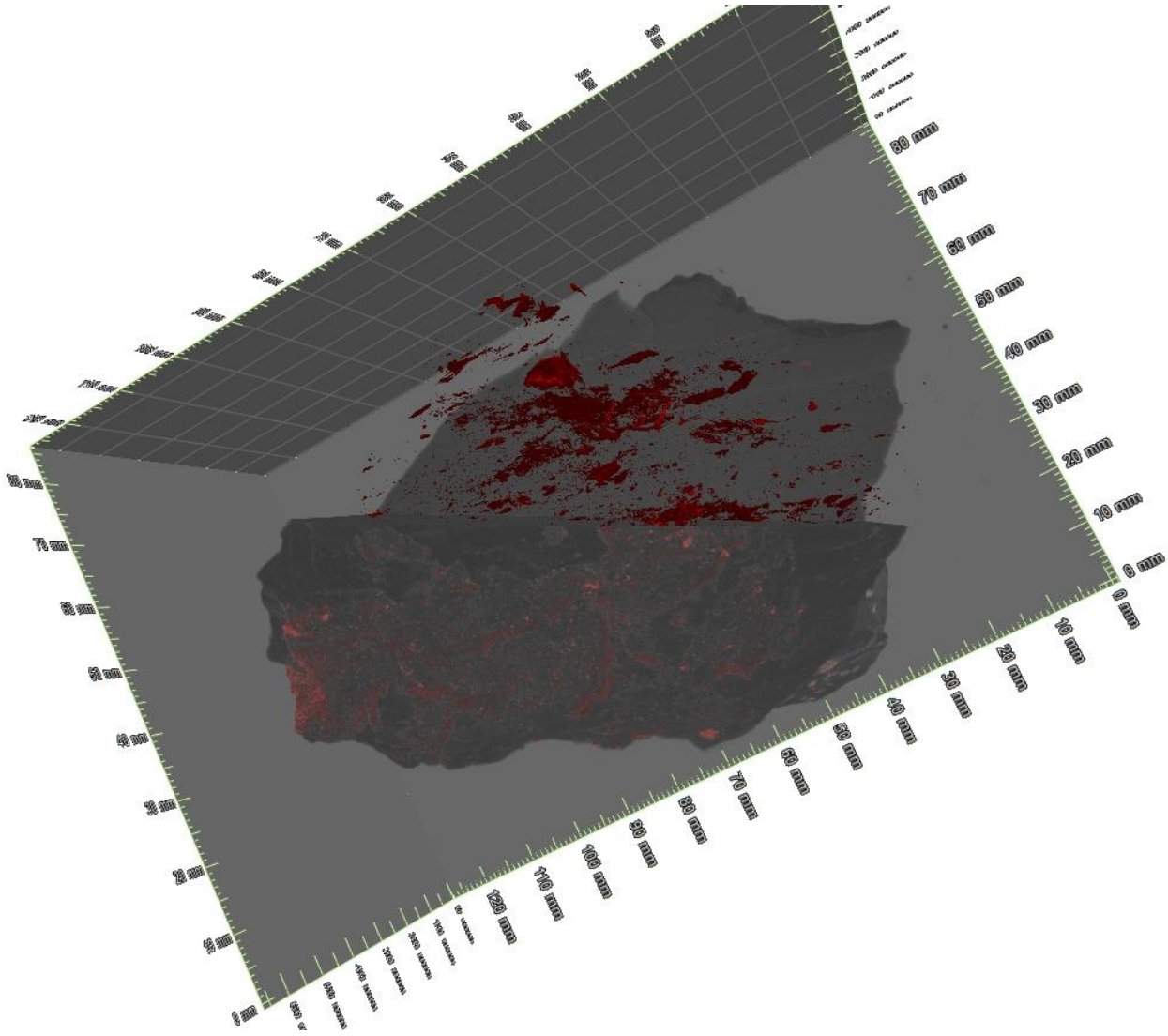

Figure 101: Three-dimensional tomographic image of coal at 9m from the dyke. Highlighted in red is the inorganic material with the grey scale depicting the organic constituents.

At a distance of 9m from the intrusion the percentage by volume of inorganic matter is 6,47 % with mineral matter and pore spaces occupying the remaining 91,30 % and 2,23 % respectively. In Figure 101 it can be noted that the mineral matter hosted in this sample are large concretions as well as fine-grained material. There are instances where the inorganics cross-cut the sedimentary boundaries, but for the majority of the sample the inorganics are hosted along the sedimentary layering.

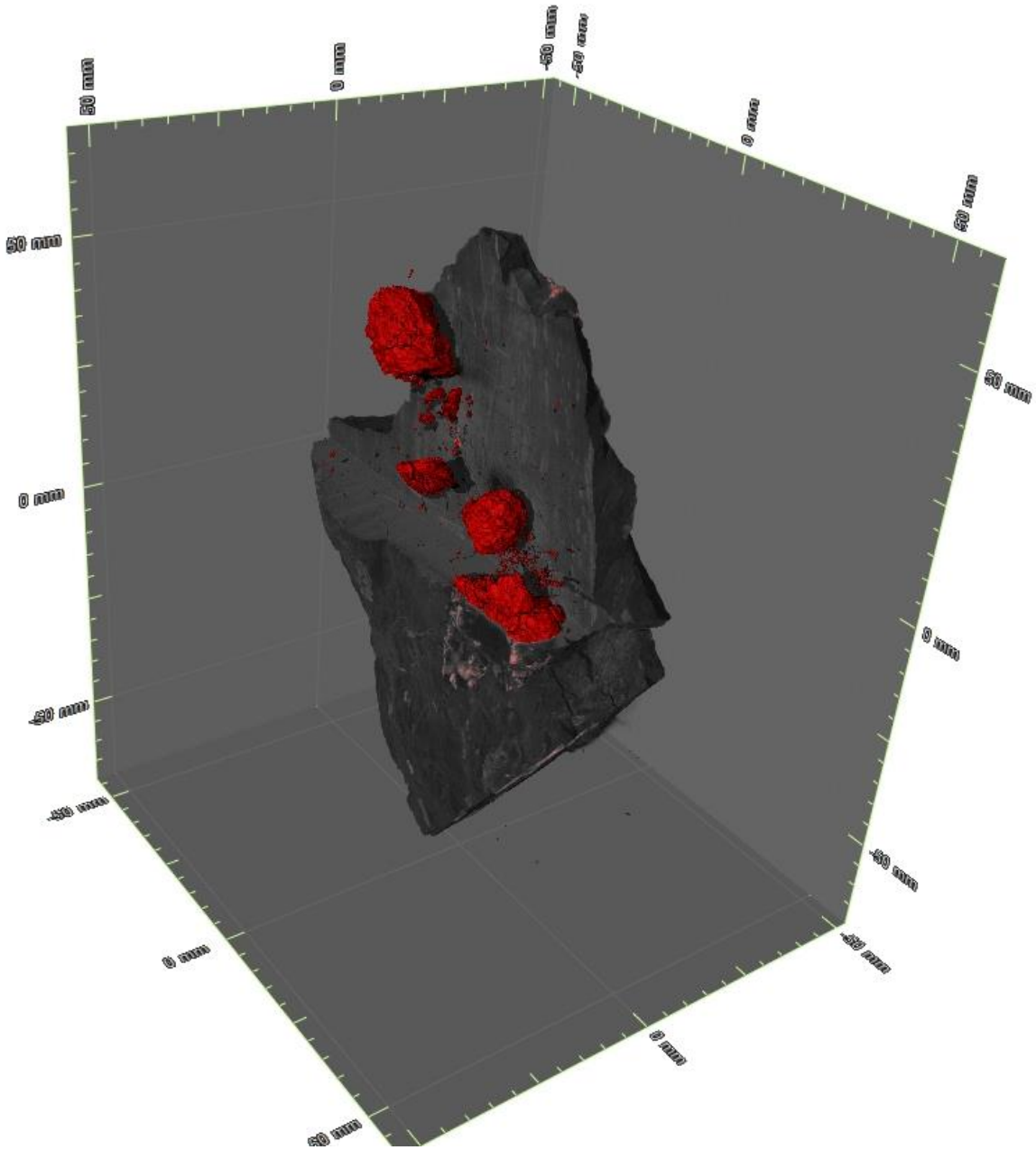

Figure 102: Three-dimensional tomographic image of coal at 10m from the dyke. Highlighted in red are the inorganic material, with the grey scale depicting the organic constituents.

The large-grain representative sample displayed in Figure 102 is at 10 m from the dolerite intrusion. The large inorganic concretions in the sample 10m from the dolerite intrusion clearly cross-cut the sedimentary layering of the coal; this cross cutting relationship is mirrored in samples at 11, 13, 16, 18, and 19 m. The sample at 10 m from the intursion is unique in the lack of interconnectivity of the inorganic concretions.

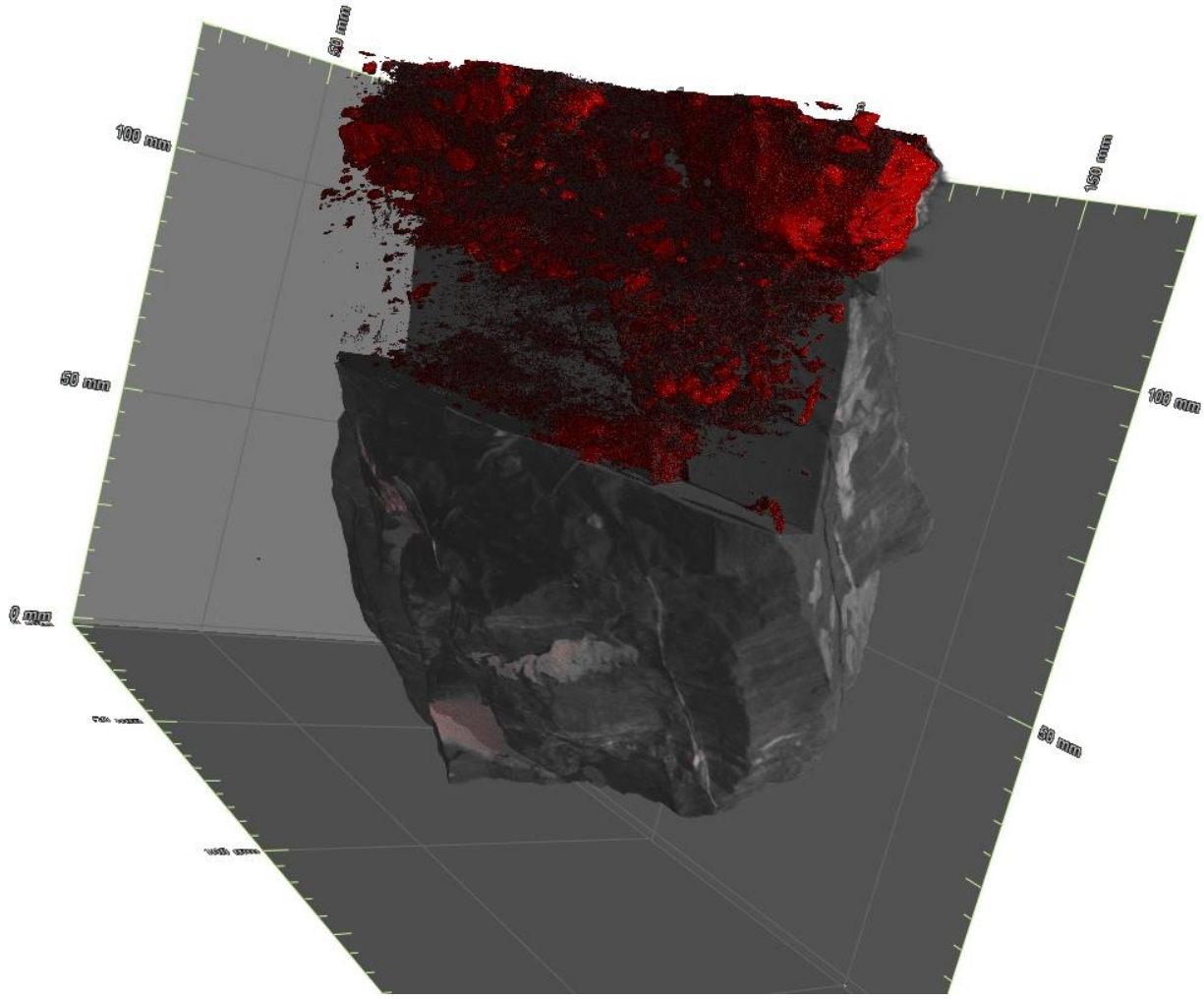

Figure 103: Three-dimensional tomographic image of coal at 11 m from the dyke. Highlighted in red is the inorganic material with the grey scale depicting the ORGANIC constituents.

At a distance of 11 m from the intrusion the sample hosts large concretions of inorganic matter cross-cutting the sedimentary layering. Seen in Figure 103, the large concretions are accompanied by smaller more granular material, in terms of volume the totality of the inorganic matter hosted in the sample is 17,24 %. The remaining volume corresponds to 1,31 % pore space and 77,72 % organic material.

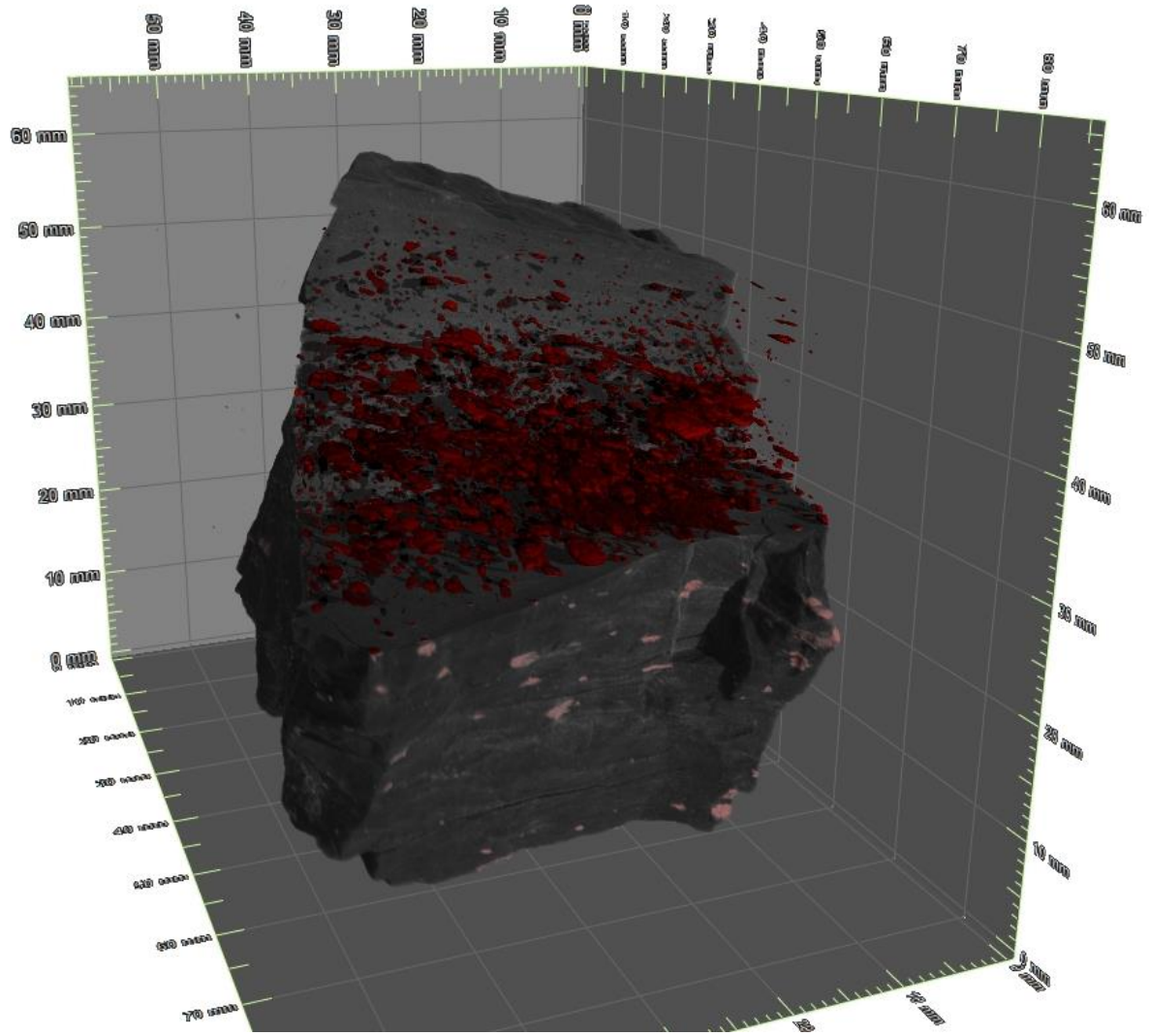

Figure 104: Three-dimensional tomographic image of coal at 12m from the dyke. Highlighted in red is the granular textured inorganic materials with the grey scale depicting the organic constituents.

The fine grained inorganic mineralization is noted in the samples at 0, 1, 2, 4, 6, 7, 9, 12, 14, 15, and 17 m from the intrusion. The inorganic material maintains a relatively constant position along the bedding plains, however there are a few instances where the inorganic material cross-cuts the sedimentary boundaries. The type example of this granular texture is displayed in Figure 104.

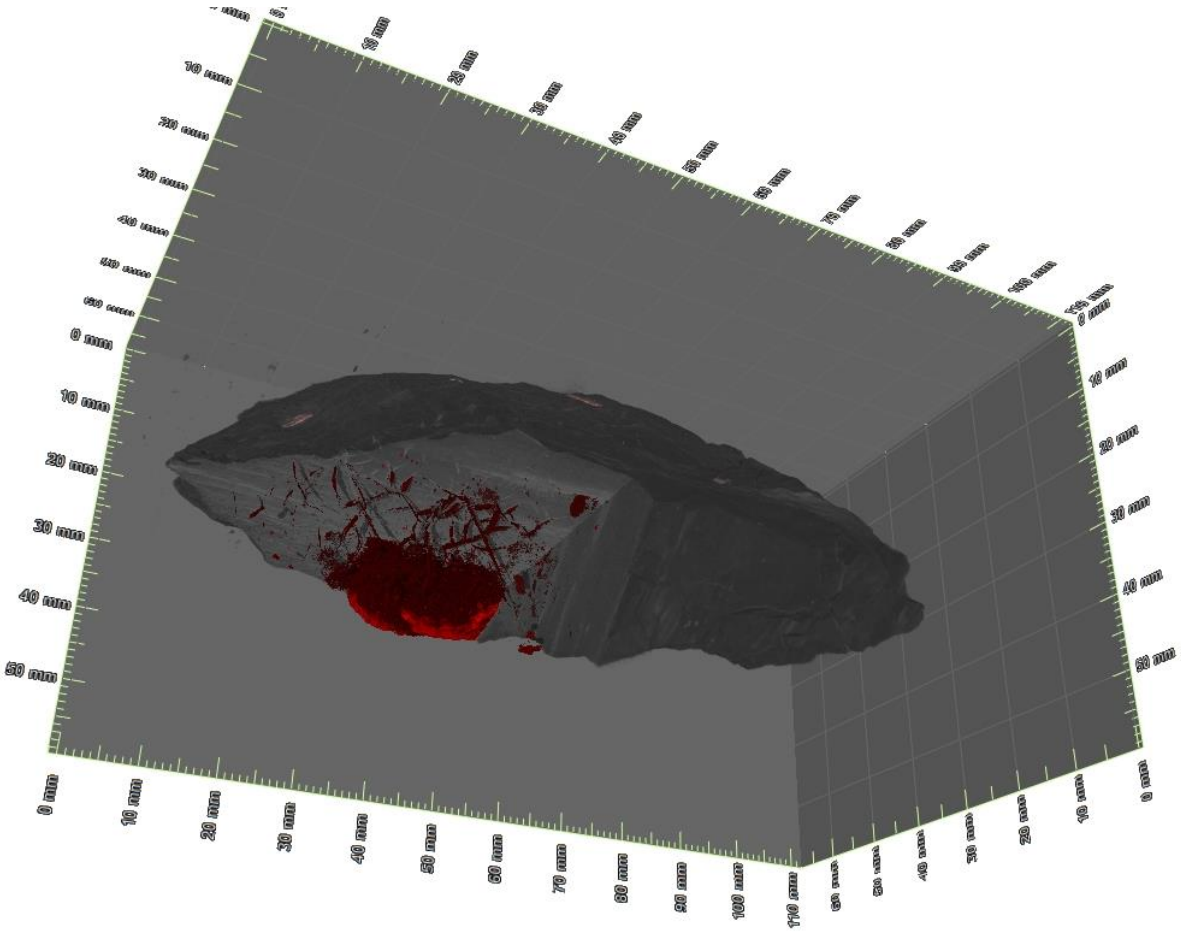

Figure 105: 3D tomographic image of sample DK 13 at 13 m from the dyke hosting sheet-like mineralization. Highlighted in red is the inorganic material's with the grey scale depicting the organic constituents.

At 13 m from the intrusion sampling shows a sheet like interior network of inorganic material. In Figure 105 further large concretions can be noted, these sheets and large inorganic clasts constitute 59,55 % of the volume of the sample. In accompaniment of the inorganics, the organic material and pore spaces constitute 40,15 % and 0,30 % of the volume of the sample.

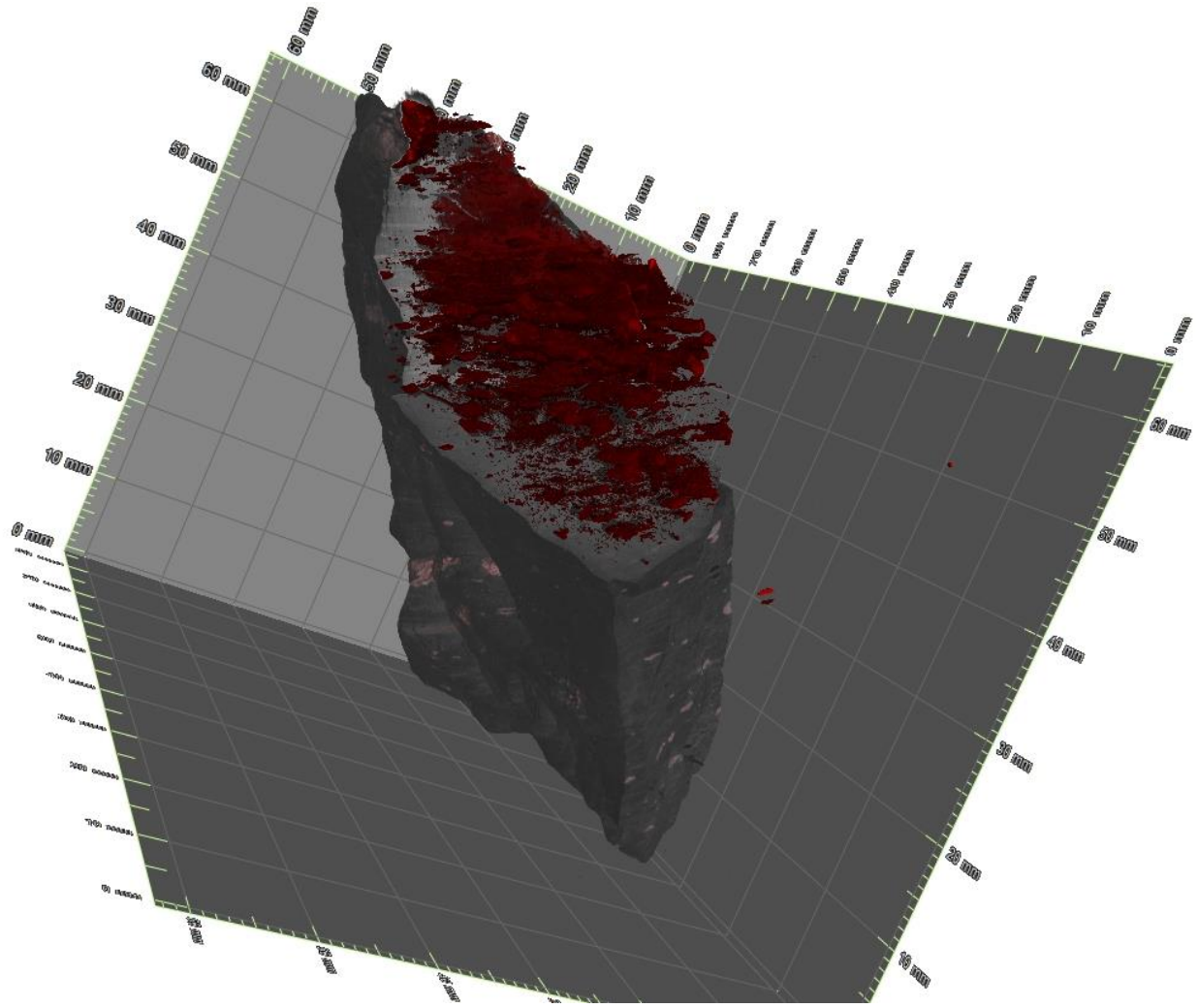

Figure 106: Three-dimensional tomographic image of coal at 14m from the dyke. Highlighted in red is the inorganic material with the grey scale depicting the organic constituents.

At 14 m from the intrusion, as seen in Figure 106, a complex network of cross-cutting fine grained inorganic material constituting 11,29 % of the volume of the sample. This is in comparison to the 88,27 % volume organic material and a low 0,44 % pore space volume.

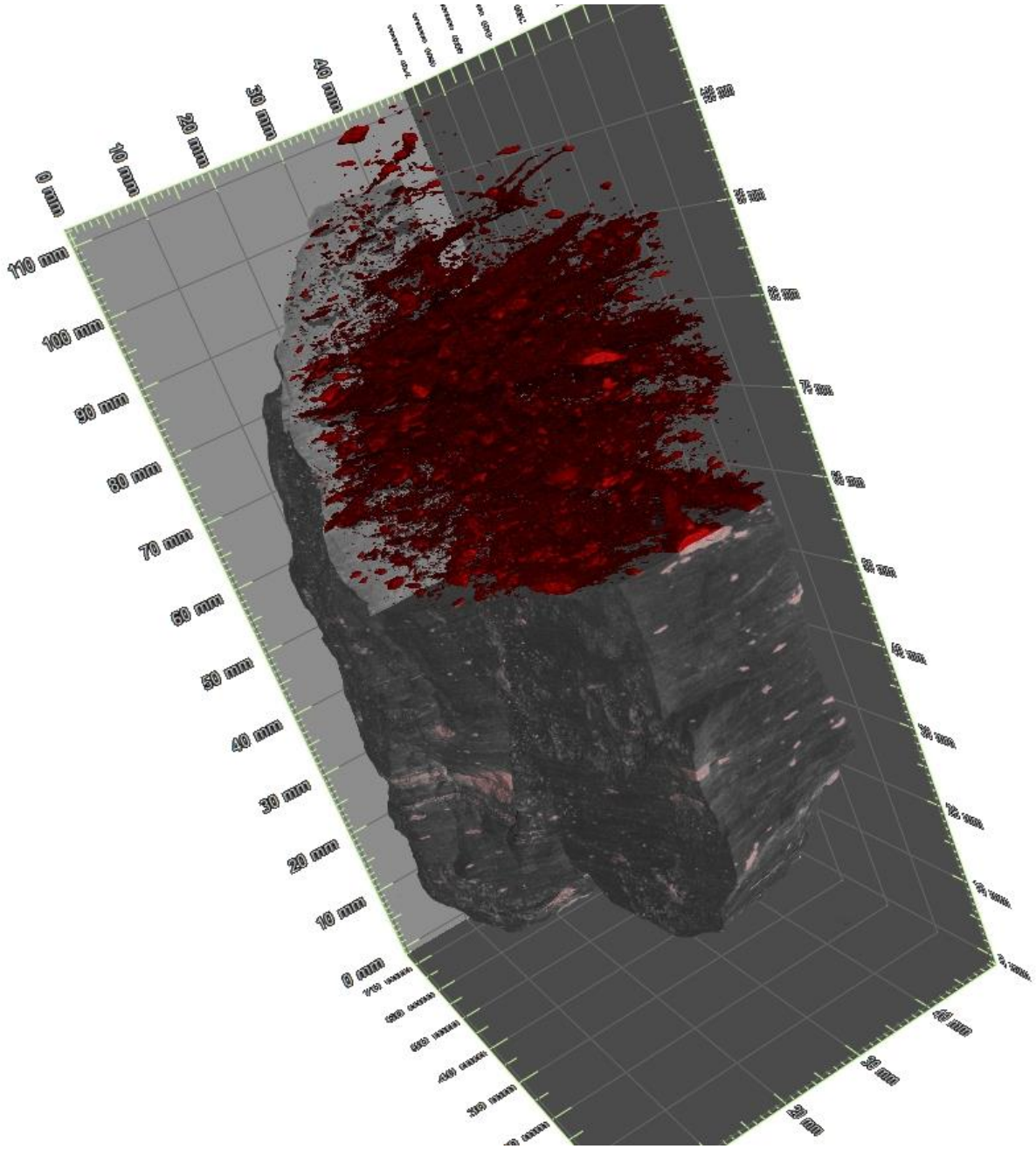

Figure 107: Three-dimensional tomographic image of coal at 15m from the dyke. Highlighted in red is the inorganic material with the grey scale depicting the organic constituents.

At 15 m from the dolerite intrusion, the sample exhibits complex cross-cutting network of inorganic material as seen in Figure 107. The inorganics form 8,98 % of the volume of the sample, while the organics and pore spaces form 73,85 % and 17,17 % of the volume respectively.

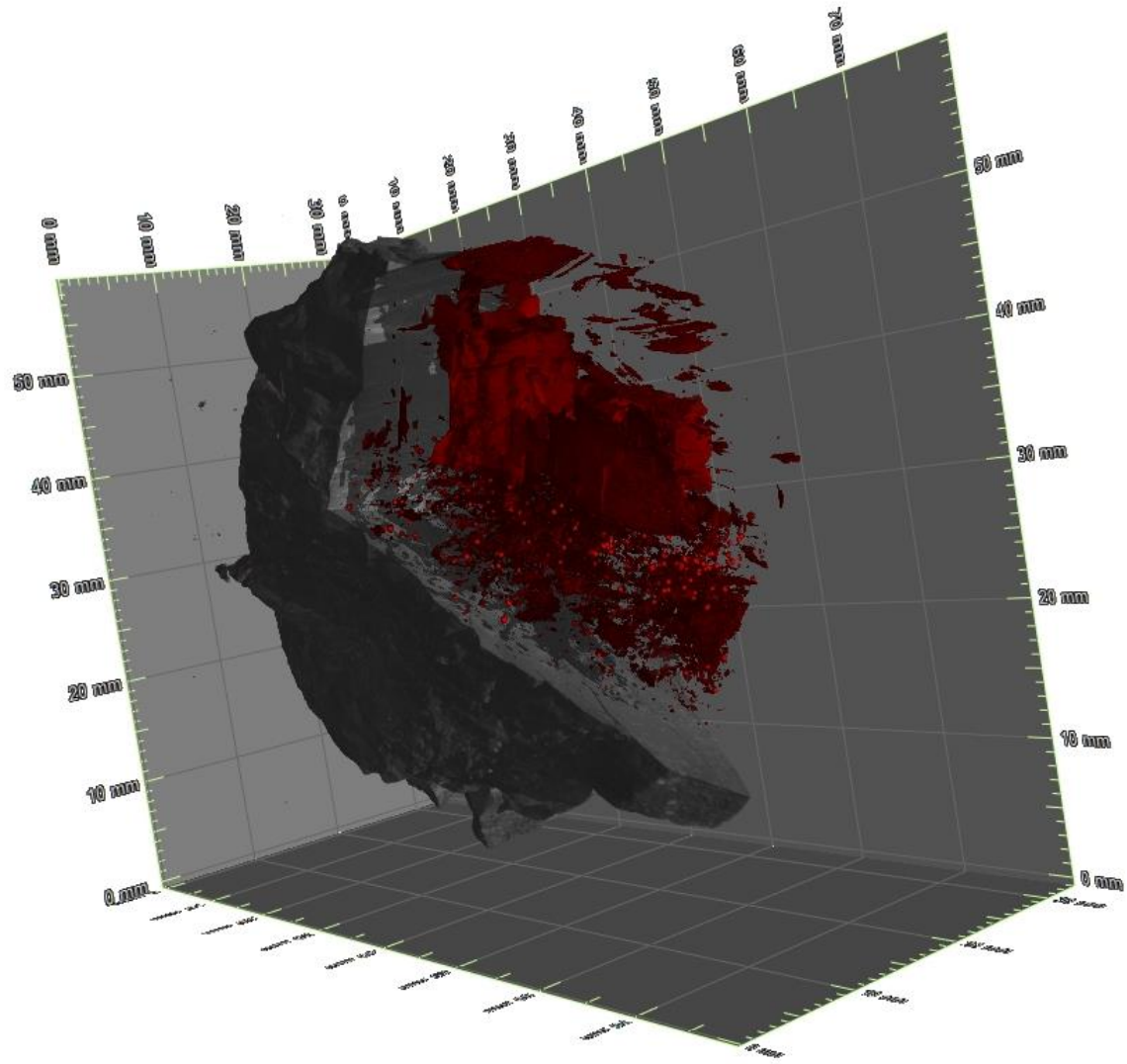

Figure 108: 3D tomographic image of sample DK 16 at 16 m from the dyke hosting sheet-like mineralization. Highlighted in red is the inorganic material's with the grey scale depicting the organic constituents.

Figure 108 displays the sample at 16 m from the dolerite intrusion. Within the tomographic image a complex network of inorganic sheet like structure cross-cut the sedimentary boundaries throughout the sample. This inorganic material constitutes 9,30 % of the volume of the sample, with the remaining volume being split between the organic material at 89,70 % and pore spaces of 1,00 %.

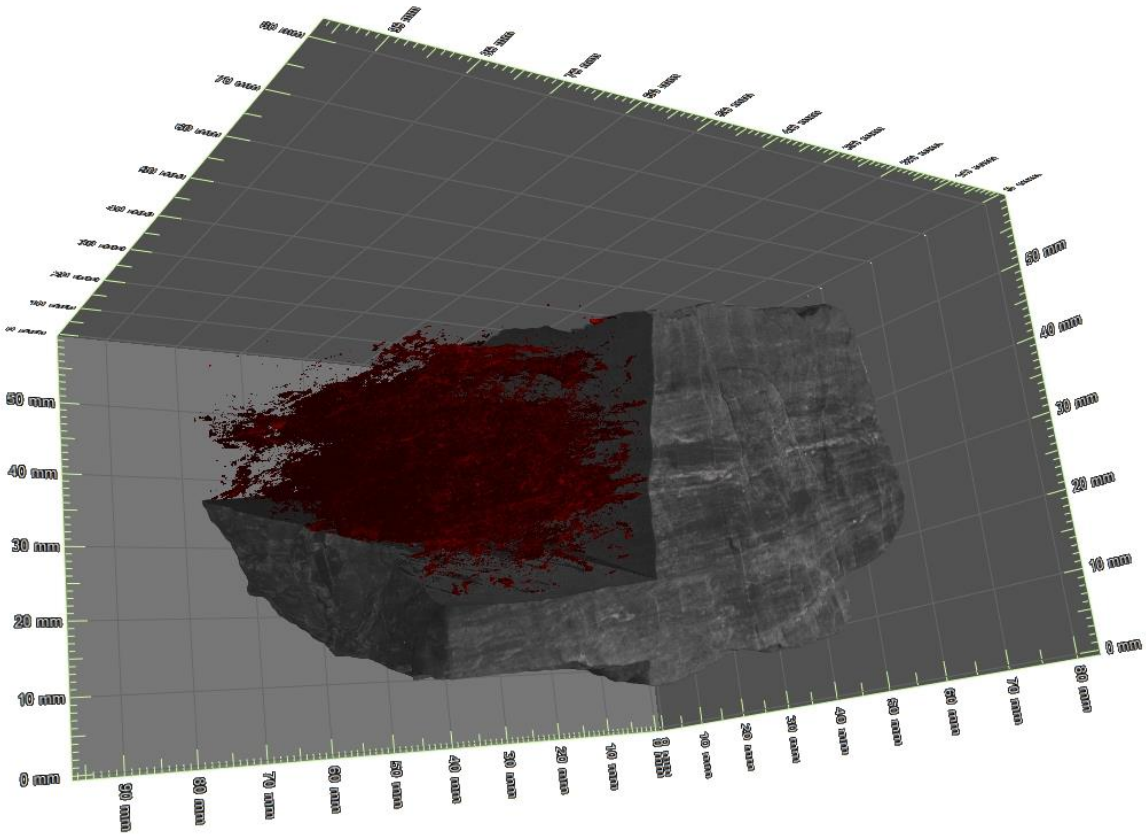

Figure 109: Three-dimensional tomographic image of coal at 17m from the dyke. Highlighted in red is the inorganic material with the grey scale depicting the organic constituents.

At 17m from the intrusion the tomographic image in Figure 109 displays a complex network of fine grained inorganic material cross-cutting the sedimentary layering of the sample. This inorganic material constitutes 12,77 % of the volume while the remaining volume is split between organic matter of 85, 25 % and pore spaces of 1,98 %.

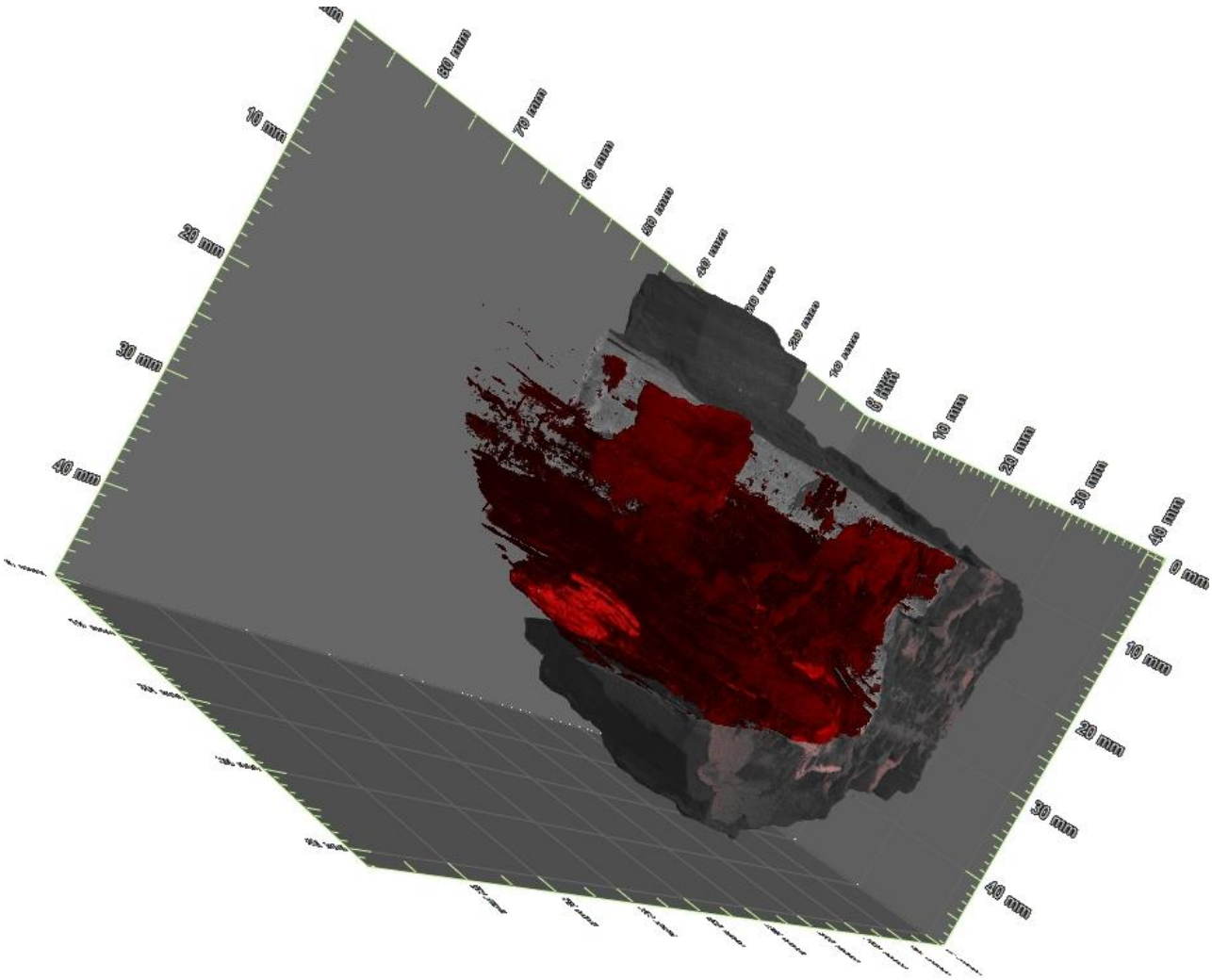

Figure 110: 3D tomographic image of sample DK 18 at 18 m from the dyke hosting sheet-like mineralization. Highlighted in red is the inorganic material's with the grey scale depicting the organic constituents.

In Figure 110 a complex network of inorganic sheet like structures cross-cutting the sedimentary boundaries can be noted. This inorganic material represents 43, 53% of the volume of the sample with pore spaces and organic matter accounting for 1,06 % and 55 and 41 % respectively.

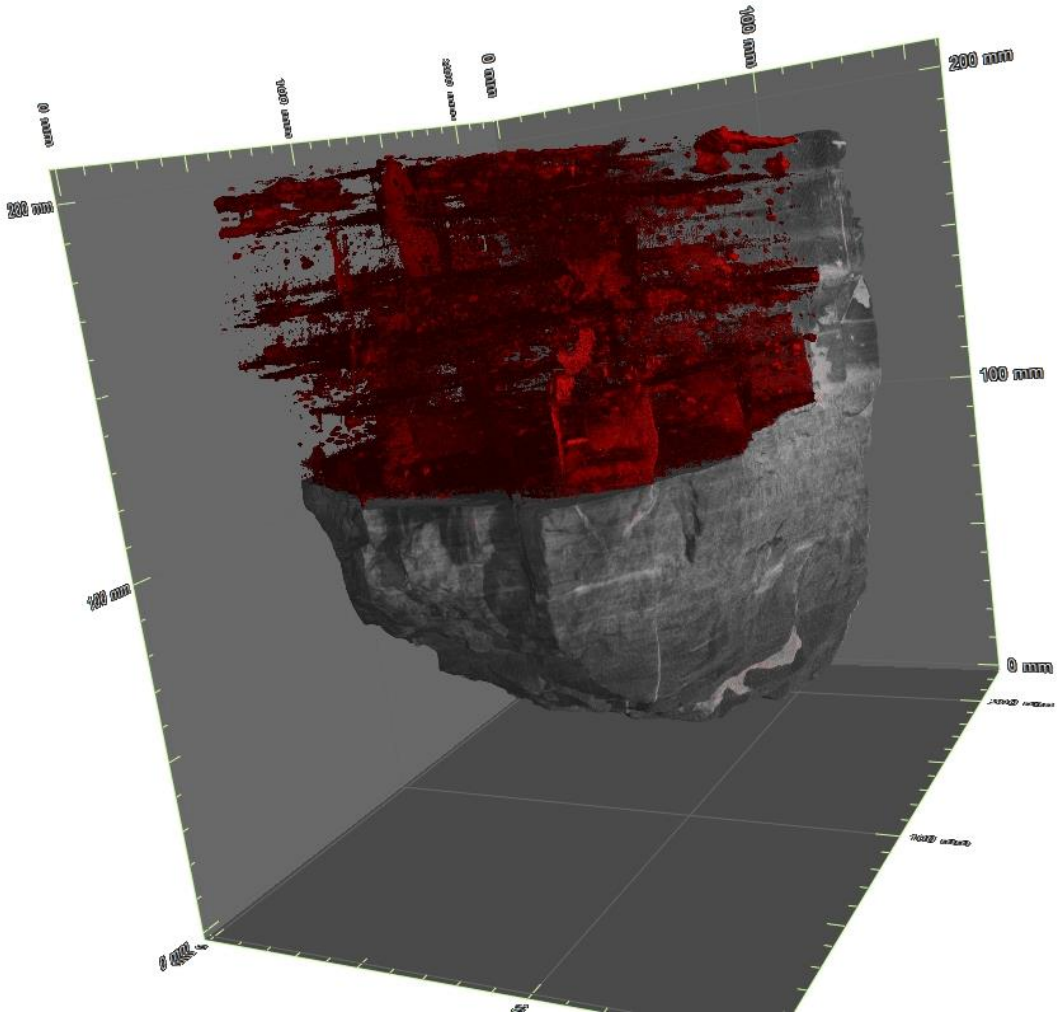

Figure 111: 3D tomographic image of sample DK 19 at 19 m from the dyke hosting sheet-like mineralization. Highlighted in red is the inorganic material's with the grey scale depicting the organic constituents.

At 19 m from the dyke, as seen in Figure 111 a mixed texture of sheet like and fine grained inorganic material is hosted in the sample, both of which exhibit a cross-cutting relationship with the sedimentary layering. The inorganic material represents 38, 79 % of the volume of the sample with organic matter accounting for 59,42 % and pore spaces only 1,80 %.

Table 13: Maceral Vitrinite Reflectance analysis histogram data

Specimen	DK 19		Specimen	DK 18		Specimen	DK 17		Specimen	DK 16		Specimen	DK 15	
Count	110		Count	117		Count	109		Count	130		Count	105	
Mean	0.644		Mean	0.644		Mean	0.726		Mean	0.661		Mean	0.666	
Std Deviation	0.057		Std Deviation	0.063		Std Deviation	0.085		Std Deviation	0.061		Std Deviation	0.069	
From	To	Percentage	From	To	Percentage	From	To	Percentage	From	To	Percentage	From	To	Percentage
0.45	0.5	2	0.5	0.55	4.3	0.55	0.6	5.5	0.45	0.5	1.5	0.45	0.5	1
0.5	0.55	3	0.55	0.6	26.5	0.6	0.65	14.7	0.5	0.55	4.6	0.5	0.55	3.8
0.55	0.6	11	0.6	0.65	23.1	0.65	0.7	20.2	0.55	0.6	10	0.55	0.6	11.4
0.6	0.65	41	0.65	0.7	23.9	0.7	0.75	15.6	0.6	0.65	21.5	0.6	0.65	29.5
0.65	0.7	32	0.7	0.75	17.1	0.75	0.8	22	0.65	0.7	37.7	0.65	0.7	21.9
0.7	0.75	7	0.75	0.8	4.3	0.8	0.85	13.8	0.7	0.75	20	0.7	0.75	21
0.75	0.8	2	0.8	0.85	0.9	0.85	0.9	7.3	0.75	0.8	4.6	0.75	0.8	8.6
0.8	0.85	2				0.9	0.95	0.9				0.8	0.85	2.9

Specimen	DK 14		Specimen	DK 13		Specimen	DK 12		Specimen	DK11		Specimen	DK 10	
Count	100		Count	100		Count	98		Count	99		Count	136	
Mean	0.676		Mean	0.659		Mean	0.678		Mean	0.693		Mean	0.68	
Std Deviation	0.061		Std Deviation	0.054		Std Deviation	0.067		Std Deviation	0.061		Std Deviation	0.058	
From	To	Percentage	From	To	Percentage	From	To	Percentage	From	To	Percentage	From	To	Percentage
0.5	0.55	4	0.5	0.55	2	0.5	0.55	3.1	0.55	0.6	5.1	0.5	0.55	1.5
0.55	0.6	5	0.55	0.6	10	0.55	0.6	10.2	0.6	0.65	25.3	0.55	0.6	5.1
0.6	0.65	26	0.6	0.65	32	0.6	0.65	25.5	0.65	0.7	24.2	0.6	0.65	25.7
0.65	0.7	31	0.65	0.7	38	0.65	0.7	23.5	0.7	0.75	24.2	0.65	0.7	33.8
0.7	0.75	25	0.7	0.75	15	0.7	0.75	23.5	0.75	0.8	18.2	0.7	0.75	22.8
0.75	0.8	6	0.75	0.8	1	0.75	0.8	10.2	0.8	0.85	3	0.75	0.8	8.1
0.8	0.85	3	0.8	0.85	1	0.8	0.85	4.1				0.8	0.85	2.9
			0.85	0.9	1									

Specimen	DK 9		Specimen	DK 8		Specimen	DK 7		Specimen	DK 6		Specimen	DK 5	
Count	105		Count	100		Count	100		Count	100		Count	100	
Mean	0.693		Mean	0.781		Mean	0.683		Mean	0.759		Mean	0.761	
Std Deviation	0.051		Std Deviation	0.064		Std Deviation	0.085		Std Deviation	0.074		Std Deviation	0.082	
From	To	Percentage	From	To	Percentage	From	To	Percentage	From	To	Percentage	From	To	Percentage
0.55	0.6	4.8	0.6	0.65	2	0.5	0.55	2	0.55	0.6	2	0.5	0.55	1
0.6	0.65	16.2	0.65	0.7	8	0.55	0.6	19	0.6	0.65	5	0.55	0.6	2
0.65	0.7	35.2	0.7	0.75	21	0.6	0.65	19	0.65	0.7	14	0.6	0.65	8
0.7	0.75	32.4	0.75	0.8	33	0.65	0.7	18	0.7	0.75	25	0.65	0.7	9
0.75	0.8	10.5	0.8	0.85	22	0.7	0.75	19	0.75	0.8	24	0.7	0.75	27
0.8	0.85	1	0.85	0.9	10	0.75	0.8	14	0.8	0.85	17	0.75	0.8	21
			0.9	0.95	4	0.8	0.85	6	0.85	0.9	11	0.8	0.85	15
						0.85	0.9	3	0.9	0.95	2	0.85	0.9	14
												0.9	0.95	3

Specimen	DK 4		Specimen	DK 3		Specimen	DK 2		Specimen	DK 1		Specimen	DK 0	
Count	100		Count	99		Count	124		Count	100		Count	109	
Mean	0.823		Mean	0.82		Mean	0.866		Mean	0.954		Mean	1.239	
Std Deviation	0.07		Std Deviation	0.074		Std Deviation	0.079		Std Deviation	0.068		Std Deviation	0.068	
From	To	Percentage	From	To	Percentage	From	To	Percentage	From	To	Percentage	From	To	Percentage
0.65	0.7	7	0.6	0.65	2	0.55	0.6	0.8	0.75	0.8	2	1.1	1.15	6
0.7	0.75	4	0.65	0.7	4	0.6	0.65	0.8	0.8	0.85	5	1.15	1.2	26
0.75	0.8	30	0.7	0.75	11.1	0.65	0.7	3.2	0.85	0.9	19	1.2	1.25	25
0.8	0.85	24	0.75	0.8	19.2	0.7	0.75	4	0.9	0.95	17	1.25	1.3	27
0.85	0.9	19	0.8	0.85	31.3	0.75	0.8	8.9	0.95	1	29	1.3	1.35	10
0.9	0.95	14	0.85	0.9	17.2	0.8	0.85	16.9	1	1.05	22	1.35	1.4	2
0.95	1	2	0.9	0.95	12.1	0.85	0.9	26.6	1.05	1.1	6	1.4	1.45	3
			0.95	1	2	0.9	0.95	30.6				1.45	1.5	1
			1	1.05	1	0.95	1	6.5						
						1	1.05	1.6						